DEVELOPMENT OF ADVANCED COMBUSTION STRATEGIES FOR DIRECT INJECTION HEAVY DUTY LPG ENGINES TO ACHIEVE NEAR-DIESEL ENGINE EFFICIENCY

Final Scientific/Technical Report

Colorado State University

Manav Sharma, Brye Windell, Reece Churchill, Colin Slunecka, Toluwalase Fosudo, Juan Felipe Rodriguez Rueda, Tanmay Kar, Bret Windom, and Daniel B. Olsen

Cummins Inc.

Hui Xu, Robert Sperry, Sujith Sukumaran, Muhammad Waqas, Mianzi Wang

Argonne National Lab

Sibendu Som, Lorenzo Nocivelli, Katherine Azstalos

Federal Agency and Organization	**Department of Energy, Energy Efficiency and Renewable Energy (DOE, EERE)**
FOA Name and Number	**Fiscal Year 2024 Advanced Vehicle Technologies Research Funding Opportunity Announcement, DE-FOA-0002197**
Nature of Report	**Research Performance Progress Report**
Award Number	**DE-EE0009198**
Award Type	**Cooperative Agreement**
Prime Recipient	**Daniel B. Olsen** **Professor of Mechanical Engineering** **Colorado State University** **Email:** daniel.olsen@colostate.edu **Phone: 970.214-9334**
Prime Recipient Type	**University**
Project Title	**Development of Advanced Combustion Strategies for Direct Injection Heavy Duty LPG Engines to Achieve Near-Diesel Engine Efficiency**
Principal Investigators	**Daniel Olsen and Bret Windom**
Prime Recipient's DUNS Number	**785979618**
Report Date	**10/28/2024**
Report Period	**10/1/2020 to 6/30/2024**

Abstract

The Vehicle Technologies Office funds early-stage, high-risk research to develop technology upon which industry can implement innovative transportation energy technologies that increase efficiency, decrease cost, and expand use of domestic energy sources, such as liquefied petroleum gas (LPG). To improve the viability of medium and heavy-duty vehicles the LPG engine efficiency must be closer to that of diesel. This work addresses fundamental limitations to achieve diesel-like efficiencies in heavy duty on-road LPG engines. The primary goal of this research is to achieve diesel-like efficiencies in heavy duty on-road LPG engines, focusing on the Cummins 15-liter engine platform (baseline diesel efficiency of 44% at peak torque). That goal has been achieved, though more work is needed to facilitate practical implementation of the developed technologies.

Disclaimer

Acknowledgment

This material is based upon work supported by the U.S. Department of Energy's Office of Energy Efficiency and Renewable Energy (EERE) under Award Number DE-EE0009198.

Table of Contents

Chapter 1.0. – Chemical Kinetic Model

1.1 Assemble and Validate Detailed Chemical Kinetic Mechanisms

Eight detailed chemical kinetic mechanisms were evaluated to determine which were the most accurate at reproducing experimental data from literature and to select the mechanism that represents the best starting point for LPG mechanism reduction. The mechanisms that were evaluated are summarized in Table 1.1-1.

Table 1.1-1: Detailed mechanisms selected for evaluation.

Detailed Mechanism	Origin	Species	Reactions
AramcoMech3.0	NUI Galway [1]	581	3,034
NUIGMech1.1	NUI Galway [2]	2,746	11,279
San Diego Mech	UC San Diego [3]	58	268
USC Mech Version II	University Southern California [4]	111	784
C1-C3 + NOx	Polytechnic University of Milan [5]	159	2,459
C1-C16 HT+LT+NOx	Polytechnic University of Milan [6]	537	18,250
Gaseous Fuels	ANSYS Chemkin-Pro [7]	1381	9,684
ARIES 82	Colorado State University [8]	82	519

Performance of the detailed chemical kinetic mechanisms was evaluated by comparing predicted ignition delay periods from constant volume, stoichiometric, 30 bar closed reactor simulations over a range of temperatures from 600-1000 K. The results of the simulations are shown in Figure 1.1-1.

All of the mechanisms showed reasonable agreement above 900 K. However, the USC Mech Version II mechanism and C1-C3 + NOx mechanism did not predict any low temperature reactivity and were eliminated as candidates for mechanism reduction. The San Diego Mechanism captured the NTC effect but appeared to be overly reactive at low temperatures. Both the C1-C16 HT+LT+NOx mechanism and the Gaseous Fuels mechanism predicted NTC behavior, but not in the same temperature range as the experimental data. ARIES 82 was developed for natural gas engines and lacks the propane chemistry necessary to fully predict NTC behavior. NUIGMech1.1 and AramcoMech 3.0 behave similarly with the former being slightly less reactive over the entire temperature range. Since NUIGMech1.1 contains recent updates to various sub-mechanisms and contains detailed NOx chemistry, it was decided to proceed with NUIGMech1.1 for mechanism reduction.

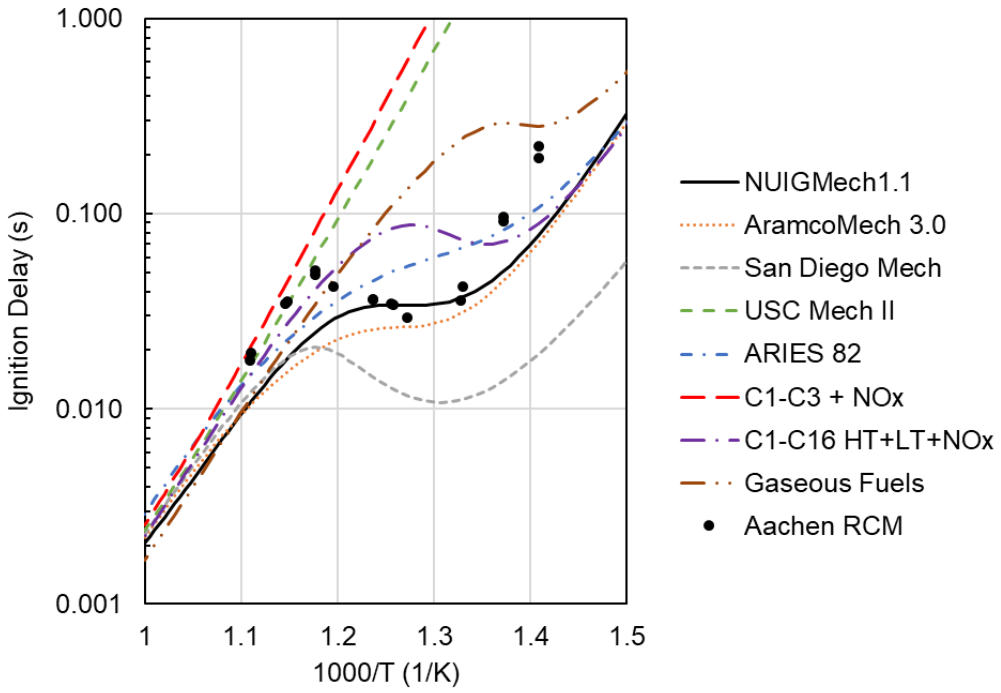

Figure 1.1-1: Fixed volume homogeneous autoignition of stoichiometric propane/air at 30 bar pressure as predicted by eight chemical kinetic mechanism (lines) in comparison with experimental results (black circles) from Ramalingam et al. [9].

References

1. Zhou, C.-W., Li, Y., Burke, U., Banyon, C., Somers, K. P., Ding, S., Khan, S., Hargis, J. W., Sikes, T., Mathieu, O., Petersen, E. L., AlAbbad, M., Farooq, A., Pan, Y., Zhang, Y., Huang, Z., Lopez, J., Loparo, Z., Vasu, S. S., and Curran, H. J., 2018, "An Experimental and Chemical Kinetic Modeling Study of 1,3-Butadiene Combustion: Ignition Delay Time and Laminar Flame Speed Measurements," Combustion and Flame, 197, pp. 423–438.
2. Ramalingam, A., Panigrahy, S., Fenard, Y., Curran, H., and Heufer, K. A., 2021, "A Chemical Kinetic Perspective on the Low-Temperature Oxidation of Propane/Propene Mixtures through Experiments and Kinetic Analyses," Combustion and Flame, 223, pp. 361–375.
3. "Chemical-Kinetic Mechanisms for Combustion Applications", San Diego Mechanism web page, Mechanical and Aerospace Engineering (Combustion Research), University of California at San Diego (http://combustion.ucsd.edu).
4. Wang, H., You, X., Joshi, A.V., Davis, S.G., Laskin, A., Egolfopoulos, F., and Law, C.K., USC Mech Version II. High-Temperature Combustion Reaction Model of H2/CO/C1-C4 Compounds. http://ignis.usc.edu/USC_Mech_II.htm, May 2007.
5. Ranzi, E., Cavallotti, C., Cuoci, A., Frassoldati, A., Pelucchi, M., and Faravelli, T., 2015, "New Reaction Classes in the Kinetic Modeling of Low Temperature Oxidation of N-Alkanes," Combustion and Flame, 162(5), pp. 1679–1691.
6. Bagheri, G., Ranzi, E., Pelucchi, M., Parente, A., Frassoldati, A., and Faravelli, T., 2020, "Comprehensive Kinetic Study of Combustion Technologies for Low Environmental Impact: MILD and OXY-Fuel Combustion of Methane," Combustion and Flame, 212, pp. 142–155.
7. Ansys® Chemkin-Pro, Release 2021 R1, ANSYS Chemkin-Pro Model Fuel Library Getting Started Guide, 2.1. MFL Full Mechanisms, ANSYS, Inc.

8. Mohr, J., 2020, "The Effect of Fuel Reactivity and Exhaust Gas Recirculation on Knock Propensity of Natural Gas," M.S. Thesis, Colorado State University, Fort Collins, CO.
9. Ramalingam, A., Fenard, Y., and Heufer, A., 2020, "Ignition Delay Time and Species Measurement in a Rapid Compression Machine: A Case Study on High-Pressure Oxidation of Propane," Combustion and Flame, 211, pp. 392–405.

1.2 RCM Experiments: Variable Composition, EGR

A full description of the CSU Rapid Compression Machine (RCM), as well as methods for experiments and simulations can be found in [1]. Homogeneous ignition delay results for lean, stoichiometric, and rich propane/air mixtures with an equivalence ratio of 0.75, 1.0, and 1.5 respectively for nominal TDC pressure of 24 bar and approximate temperature range of 700 to 900 K are plotted in Figure 1.2-1.

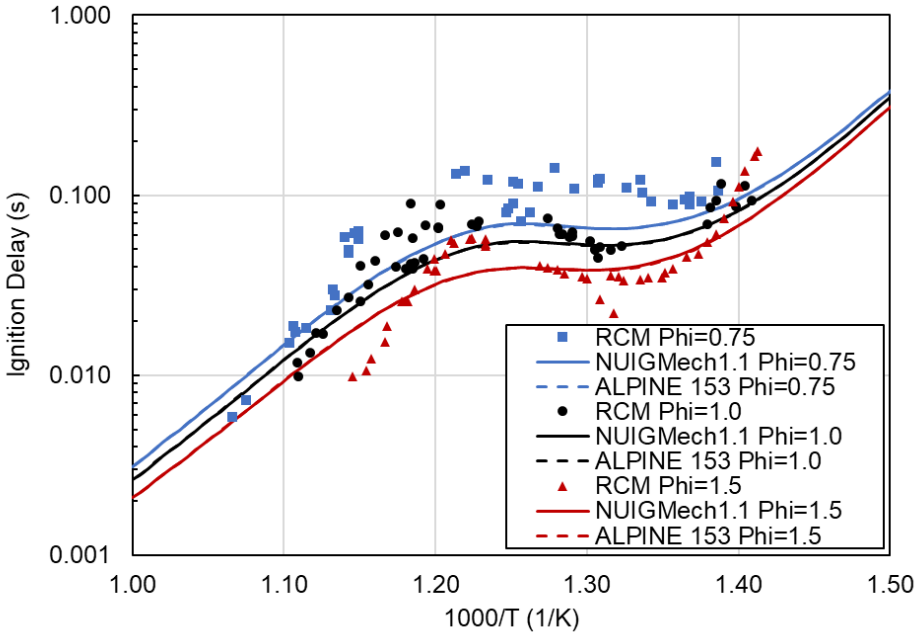

Figure 1.2-1: Experimental RCM ignition delay measurements (symbols) and simulated constant volume homogeneous autoignition delay of C_3H_8/inert/O_2 at 24 bar and varying equivalence using NUIGMech1.1 (solid lines) and ALPINE 153 (dashed lines).

Under these conditions, NTC behavior was observed for the rich, lean, and stoichiometric mixtures. The experimental results also showed that the rich fuel mixture exhibited the shortest ignition delay periods, and the lean mixtures the longest for the full temperature range. ALPINE 153 (described in Section 1.4) and NUIGMech1.1 both replicate these trends, as well as being almost indistinguishable from each other when plotted together.

The next set of ignition delay experiments shows the effect of the presence of NO_x in an EGR mixture. The R-EGR represents engine-out exhaust gas, which would be used for high pressure

EGR delivery to an engine cylinder. At 30% mass substitution, the R-EGR mixture contains approximately 1,000 ppm of NO_2 in the gas mixture, depending on the inert gas composition. The NR-EGR represents system-out exhaust gas which is used for low pressure EGR delivery. The results in Figure 1.2-2 show that NR-EGR increased ignition delay across the full temperature range as a result of mixture dilution and the lower heat capacity ratio from the CO_2 component gas. Again, the constant volume model does not predict the length of the IDT at the upper end of the NTC regime, but NUIGMech1.1 and ALPINE 153 predict the same values.

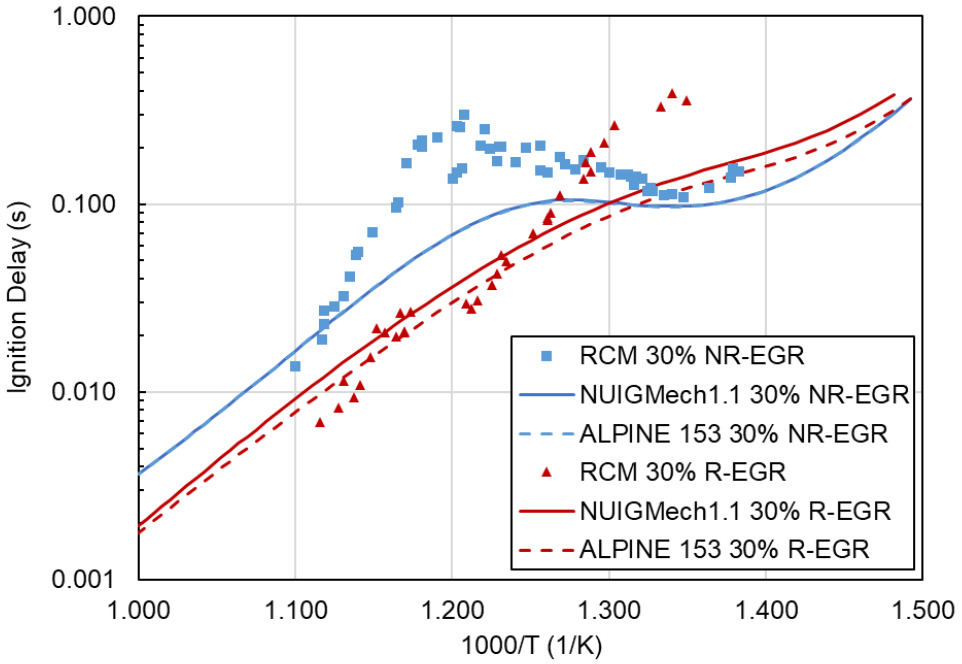

Figure 1.2-2: Experimental RCM ignition delay measurements (symbols) and simulated constant volume homogeneous autoignition delay of C_3H_8/inert/O_2/EGR at 24 bar and 30% EGR mass substitution using NUIGMech1.1 (solid lines) and ALPINE 153 (dashed lines).

The last set of IDT experiments were to determine the effect of variation in secondary fuel components of an LPG mixture. As discussed earlier, the amount of secondary fuels in HD-5 LPG is very small, but in the rest of the world LPG can be composed of over 50% C_4 hydrocarbons depending on location. To determine the impact of each secondary fuel type, stoichiometric mixtures of 80% propane with 20% of either ethane, propene, n-butane, or isobutane were used. The IDT for each mixture as well as the results of the constant volume model for NUIGMech1.1 and ALPINE 153 are shown in Figure 1.2-3. The mixtures show distinct differences in IDT with propane/ethane being the slowest, followed by propane/propene, propane/isobutane, and propane/n-butane in order of increasing reactivity. The propane/propene mixture showed a partial suppression of NTC behavior, which has also been displayed in other propane/propene mixtures in literature [67]. Both mechanisms predicted the same IDT values for the propane/ethane mixtures, while only deviating by a few milliseconds from each other for the

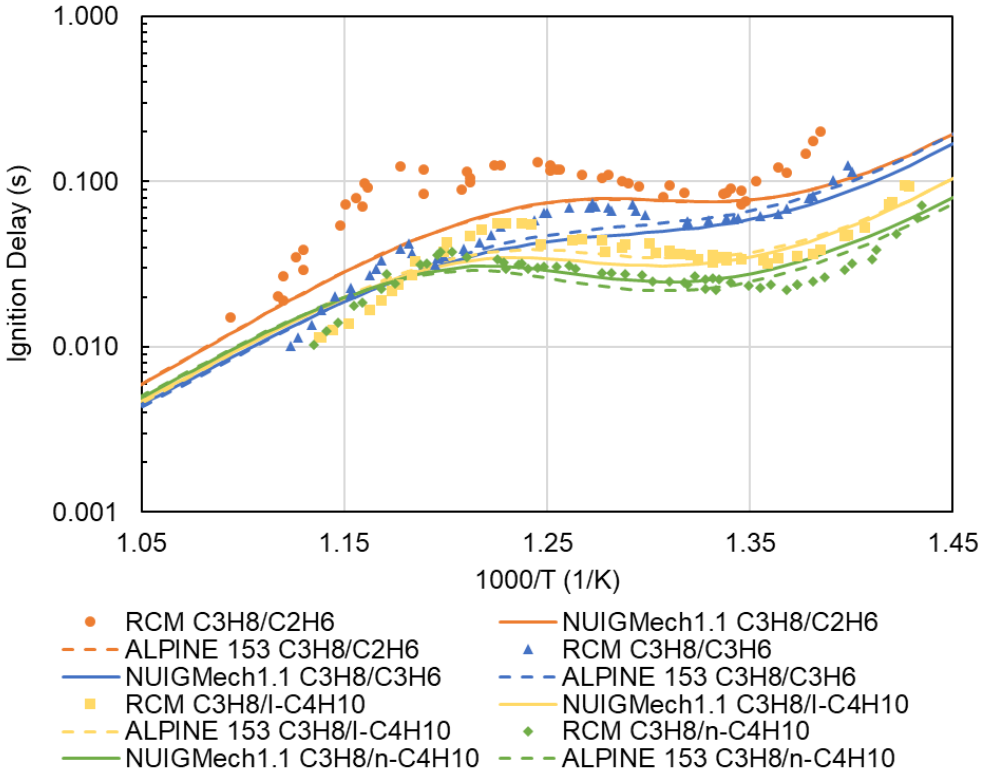

Figure 1.2-3: Experimental RCM ignition delay measurements (symbols) and simulated constant volume homogeneous autoignition delay of binary fuel/inert/O_2 at 24 bar and varying equivalence using NUIGMech1.1 (solid lines) and ALPINE 153 (dashed lines).

other mixtures. Due to the nature of mechanism reduction, it is expected that the error of ALPINE 153 in predicting IDT for LPG mixtures will go up if fuel composition does not consist of mostly propane.

Flame propagation rate was first tested as a function of equivalence ratio to determine if ALPINE 153 could predict lean, stoichiometric, and rich combustion scenarios as may be present in a stratified fuel injected engine. To ensure the effects of turbulence did not cause increasing flame speeds, all experiments with a piston offset greater than 2 ms were removed from the data sets. It has been shown previously that as piston offset increases, the measured flame propagation rate inside the RCM increases significantly [62]. To mitigate the effects of low temperature chemistry and ensure that the laser is igniting propane and not an intermediate species, a TDC temperature and pressure of 700 K and 24 bar was chosen for the equivalence sweep because propane will not autoignite in the CSU RCM at that condition. As observed in the spark timing matched schlieren images in Figure 1.2-4, the stoichiometric propane/air mixture was the fastest, with the lean flame moving slightly faster than the rich flame.

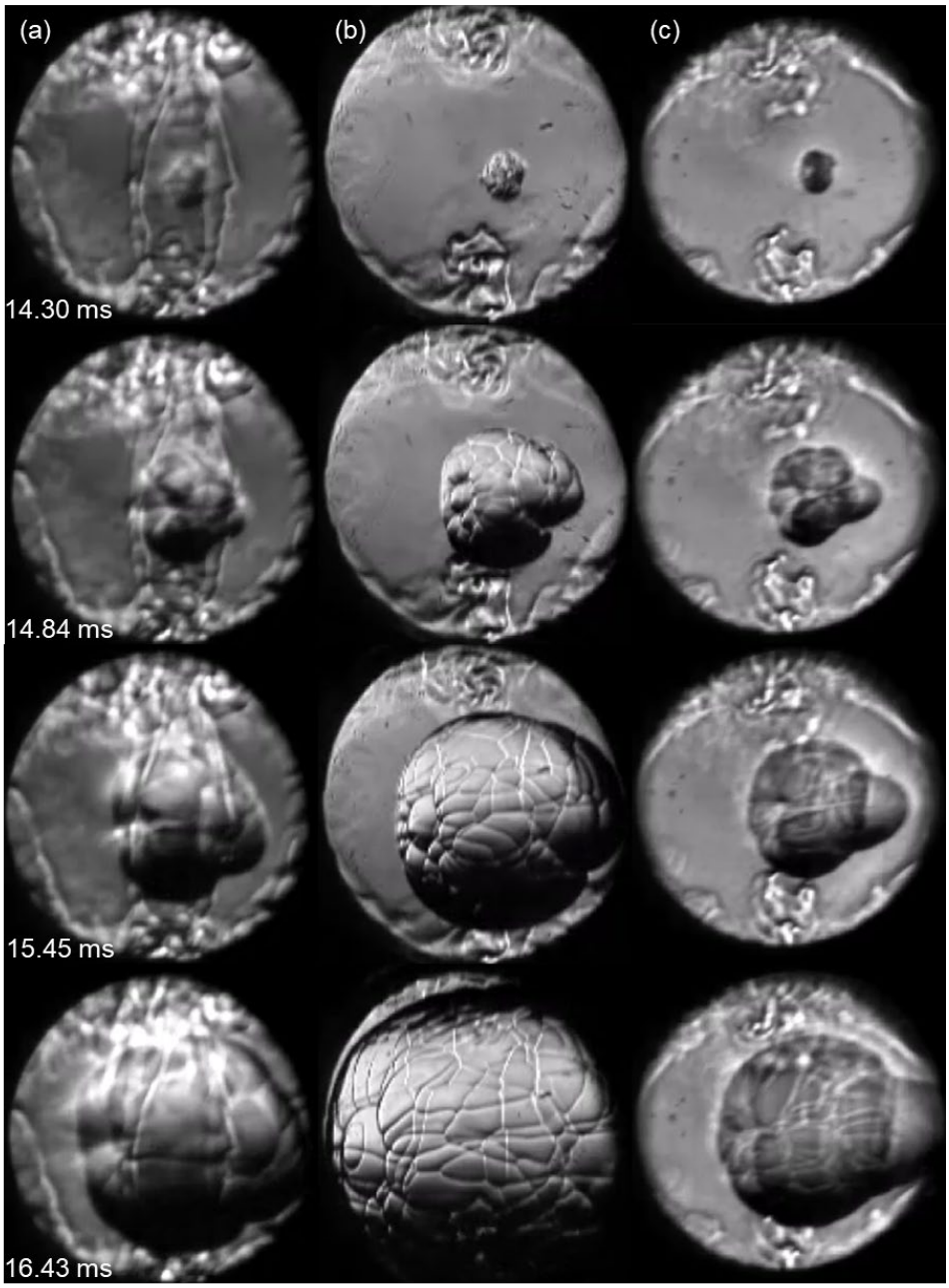

Figure 1.2-4: Schlieren images of flame propagation for propane with equivalence ratios of 0.75 (a), 1.0 (b), and 1.5 (c) at 24 bar, 700 K, and timestamps of 14.30, 14.84, 15.54, and 16.43 ms.

Measured flame propagation rates were compared to a 1-D Chemkin model using initial conditions that match the TDC conditions of the RCM. Both the full NUIGMech1.1_HT and the reduced ALPINE 153 mechanism accurately predict the flame propagation rate at stoichiometric and lean conditions, while overpredicting flame propagation in the lean region as shown in Figure 1.2-5. This same overprediction was observed for lean fuels in Figure 18 and the error appears to increase with increasing pressures. Error between the 1-D model and measured values of flame speed for stoichiometric propane was only 1.47%.

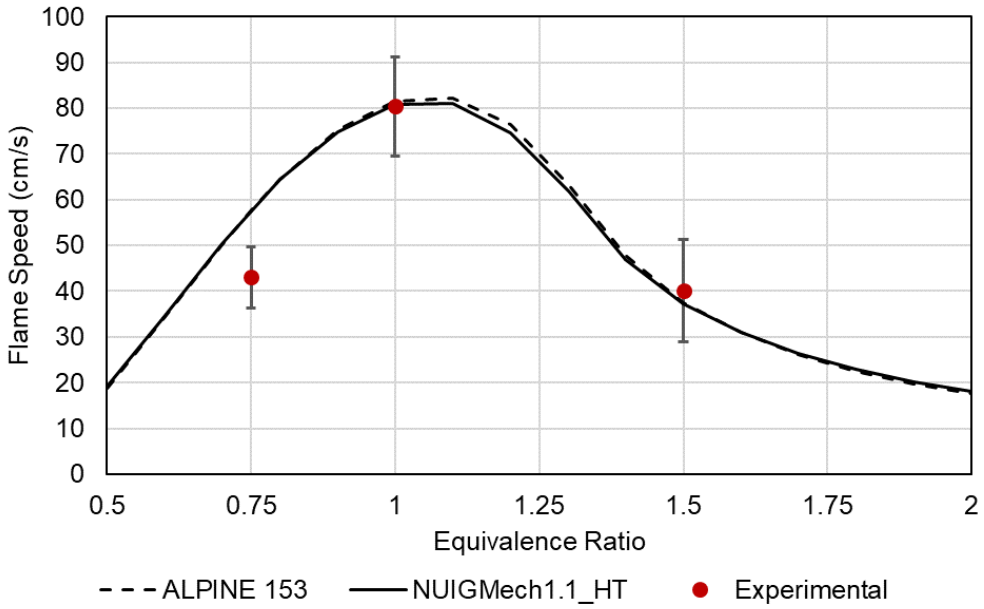

Figure 1.2-5: Experimental zero-stretch flame propagation rates at 24 bar and 700 K and simulated 1-D laminar flame speeds using NUIGMech1.1_HT and ALPINE 153 chemical kinetic mechanism for varying equivalence. Error bars represent standard deviation.

The next experimental parameter tested was the effect of increasing R-EGR amounts on flame propagation rates for stoichiometric propane/air mixtures. Again, a TDC condition of 24 bar and 700 K was used to prevent autoignition chemistry and the amount of R-EGR was increased from 0-30% by mass. The increasing R-EGR amounts decreases the flame propagation rate in an almost linear behavior due to dilution of the fuel/air mixture shown in Figure 1.2-6. The 30% R-EGR mixture in this data set contains 15% CO2 in the inert gas in order to maintain the 700 K TDC pressure and as such must be modeled as a discrete point because of the difference in thermal diffusivity from the other mixtures. Laminar flame speed models using NUIGMech1.1_HT and ALPINE 153 performed very accurately to the measured flame propagation rates except for the 20% R-EGR condition, although it is worth noting that the 20% R-EGR case also had much higher standard deviation than the others.

Since end gas autoignition had not been observed in the 700 K flame propagation experiments, a higher temperature data set was necessary. The results of the 30% R-EGR autoignition experiments and the significantly slower flame speeds provided by EGR dilution suggest that there is a conditional zone that would allow for visible EGAI in the RCM. The decreased flame speed because of EGR allows for a longer chemical induction period in the end gas which also has increased reactivity from high temperature NO_2. Based on a CFD model of the CSU RCM, 867 K was selected as the TDC temperature that was most likely to autoignite ahead of the flame front.

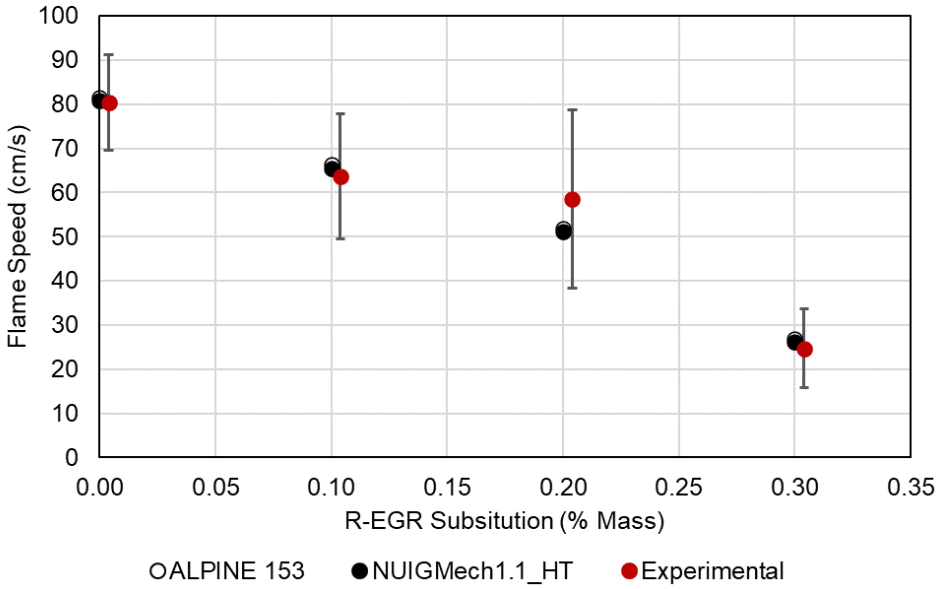

Figure 1.2-6: Experimental zero-stretch flame propagation rates at 24 bar and 700 K and simulated 1-D laminar flame speeds using NUIGMech1.1_HT and ALPINE 153 chemical kinetic mechanism for varying R-EGR amounts. Error bars represent standard deviation. Points staggered for clarity.

The 867 K flame propagation rates were significantly faster than the 700 K flame results but still exhibited the almost linear decline as a function of R-EGR mass substitution shown in Figure 28. Both the NUIGMech1.1 and ALPINE 153 mechanisms predicted the flame propagation rate within the standard deviation of the experiments until 20% R-EGR substitution, after which they began to diverge significantly. ALPINE 153 overpredicts flame propagation rate at 30% R-EGR as compared to NUIGMech1.1 and demonstrates that there is a conditional range where the reduced mechanism is no longer valid for accurate simulations. At R-EGR percentages of 20 and higher, it appeared that EGAI was visibly occurring, but not until the flame had spread beyond the windows of the combustion chamber. Recreating the 30% R-EGR experiment in a different combustion chamber design with larger windows, 25.4 mm as compared to 16.1 mm, did provide visual confirmation that EGAI was occurring.

References

1. Slunecka, C., 2023, “Autoignition and flame speed of premixed liquefied petroleum gas in a rapid compression machine: experimental results and reduced chemical kinetic mechanism,” M.S. Thesis, Colorado State University, Fort Collins, CO.
2. Ramalingam, A., Panigrahy, S., Fenard, Y., Curran, H., and Heufer, K. A., 2021, “A Chemical Kinetic Perspective on the Low-Temperature Oxidation of Propane/Propene Mixtures through Experiments and Kinetic Analyses,” Combustion and Flame, 223, pp. 361–375.
3. Zdanowicz, A., Mohr, J., Tryner, J., Gustafson, K., Windom, B., Olsen, D. B., Hampson, G., and Marchese, A. J., 2021, “End-Gas Autoignition Fraction and Flame Propagation Rate in Laser-Ignited Primary Reference Fuel Mixtures at Elevated Temperature and Pressure,” Combustion and Flame, 234, p. 111661.

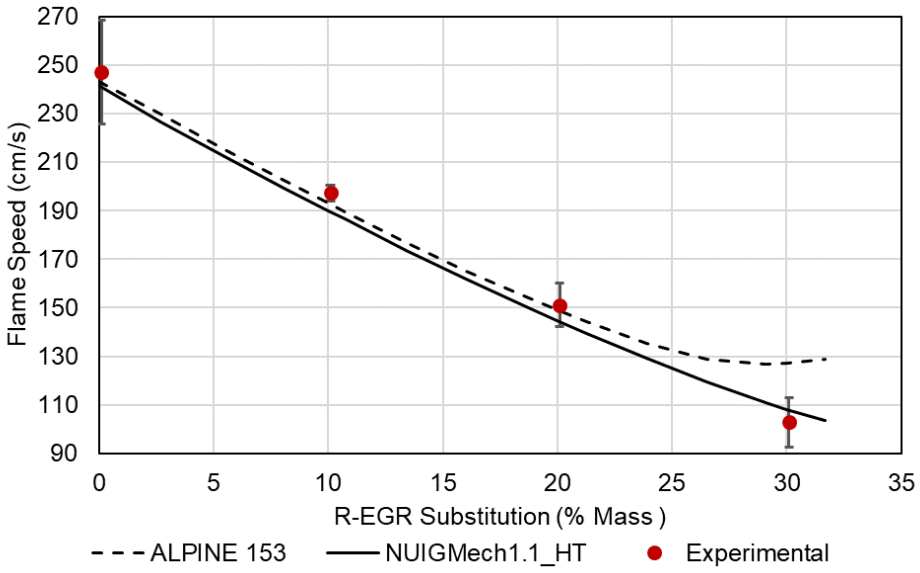

Figure 1.2-7: Experimental zero-stretch flame propagation rates at 24 bar and 867 K and simulated 1-D laminar flame speeds using NUIGMech1.1_HT and ALPINE 153 chemical kinetic mechanism for varying R-EGR amounts. Error bars represent standard deviation.

1.3 Engine Testing: Premixed LPG, Variable Composition, EGR

Section 1.3 was extracted from [1] in References.

Preliminary investigations involved operating the Cooperative Fuels Research (CFR) engine on premixed gaseous LPG. The CFR engine was designed as a single cylinder, 4-stroke CFR F-2 research engine capable of achieving different compression ratios. Details of the engine are presented in Table 1.3-1.

Table 1.3-1: CFR Engine Specifications

Displaced volume (L)	0.6117
Stroke (m)	0.1143
Bore (m)	0.0826
Connecting Rod (m)	0.254
Compression ratio	Adjustable 4:1 – 18:1 by cranked worm shaft – worm wheel drive in cylinder clamping sleeve
Number of Valves	2
EVO	140° ATDC
EVC	15° ATDC
IVO	10° ATDC
IVC	146° BTDC
Cylinder type	Cast Iron, Flat Combustion Surface, Integral
Ignition	Capacitive discharge through coil to spark plug

Several modifications were made to the original test engine to allow operation on gaseous fuels. This customization included the installation of several measuring instruments at specific locations to obtain accurate measurement of engine operating parameters and results. A detailed description of the measurement devices and methods used in this study is provided below. A few of these instrumentation upgrades include a Yaskawa U1000 regenerative variable frequency drive installed to ensure accurate speed control. All the tests in this preliminary study were performed at 900 RPM engine speed. A BEI model L25 incremental optical encoder was also installed on the crankshaft to provide crank angle position with a tenth of a degree resolution. Three Kistler high-speed pressure transducers were used in this study; a 6061B water-cooled piezoelectric transducer provided in-cylinder pressure readings, while dynamic intake and exhaust pressure measurements were made with the 4007D and 4049B piezoresistive transducers respectively. To maintain a constant vapor pressure inside the LPG cylinder irrespective of fluctuations in the ambient conditions, a heated blanket was wrapped around the tank and an electrically heated Swagelok K-series pressure regulator and heat trace were introduced on the fuel delivery line to preserve the fuel supplied to the engine in the gas phase. A Micromotion CMF series Coriolis mass flow meter downstream of the heated regulator was used to measure the flow rate of the fuel while a wide-band LSU 4.9 lambda sensor with operating range lambda (λ) 0.65 to ∞ and exhaust temperatures up to 930^{o}C located downstream of the exhaust buffer volume provided a measure of the air-fuel ratio in the engine. A schematic of the CFR engine test cell layout is presented in Figure 1.3-1. A National Instruments PCI 6251 high speed data acquisition card was used to collect in-cylinder pressure data. Combustion and manifold pressure data were logged at 54kHz (1/10th degree resolution) for 1000 cycles (2-3 min). Combustion data logged for 200 cycles on the Woodward LECM was used for ignition control. Other parameters such as temperatures, fuel flowrate, and electrical power were logged at 10 Hz for 3 minutes.

On the CFR engine, an NK APT-TH series 10kW power transducer was used to measure the electrical output from an induction motor connected to the engine. The generator efficiency of the motor was known, and the brake thermal efficiency was calculated using Equation 1.3.1.

$$\eta_b = \frac{\dot{W}_b}{\dot{m}_f * LHV} \tag{1.3.1}$$

Where:

η_b is the brake efficiency.

$\dot{W}_b$ is the brake power.

$\dot{m}_f$ is the mass flow rate of the fuel.

LHV is the lower heating value of the fuel.

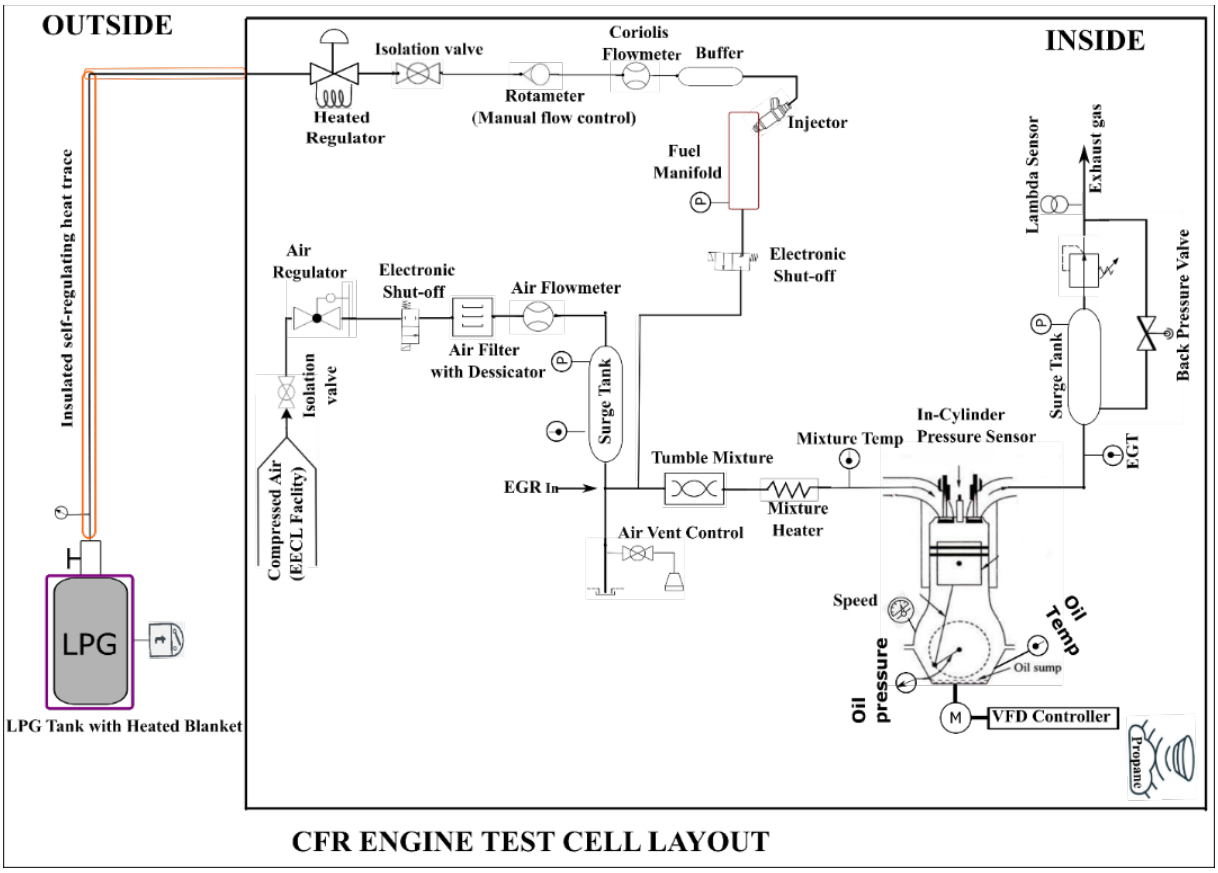

Figure 1.3-1: Schematic of the CFR engine test cell.

A time averaged approach was used to establish a knock index and to provide an objective and repeatable metric for comparison of the overall intensity of knock experienced with different fuels under the same engine operating conditions. The term knock integral was used to refer to the area under the curve bounded by FFT power spectrum magnitude over a set number of combustion cycles and was the first of the methods used throughout this work especially on the CFR engine. The KI summation is given by Eq. 1.3.2.

$$KI = Area_{bounded} = \sum_{i=0}^{n}\{KL(i+1) + KL(i)\}/2 \qquad (1.3.2)$$

Where:

n = number of combustion cycles in a data set

KL(x) = knock level magnitude for a given combustion cycle, x.

Engine-out emissions were measured with a Rosemount 5-gas emissions bench analyzer from Siemens Instruments and a Fourier transforms infrared (FTIR) spectrometer (an MKS Instruments, Inc. Model No. 2030) and were analyzed in brake specific terms calculated from the measured ppm values using Equation 1.3.3 below.

$$bsi = \dot{m}_i/\dot{W}_b = \frac{\dot{m}_f * \alpha * Y_i * M_i}{M_f * \sum(Y_j * \alpha_j) * \dot{W}_b} \quad (1.3.3)$$

Where:

bsi is the brake specific value of specie i

$\dot{m}_i$ is the mass flow of specie i

$\dot{W}_b$ is the brake power

$\dot{m}_f$ is the fuel flow rate

α is the fuel carbon number

Y_i is the mole fraction of species i

M_i is the molar mass of specie i

M_f is the molar mass of the fuel

$\sum(Y_j * \alpha_j)$ is the sum of all carbon carrying species j in the exhaust

Exhaust gases were cooled and then recirculated back into the intake. The mass flow rates of the measured and/or calculated quantities in Equation 1.3.4 were used to determine the EGR rate.

$$EGR\% = \frac{\dot{m}_{EGR}}{(\dot{m}_{EGR} + \dot{m}_{air} + \dot{m}_{fuel})} \quad (1.3.4)$$

where $\dot{m}_{EGR}$, $\dot{m}_{air}$, and $\dot{m}_{fuel}$ are the mass flow rates (g/s) of the recirculated exhaust gases, air, and fuel respectively.

Several LPG blends that broadly represent the present LPG market were chosen to study the effect of LPG composition on a premixed engine with EGR. Three LPG blends identified as a representative US blend (%vol ethane = 6.5), a representative European blend (%vol n-butane = 18) and an HD-5 blend (%vol propylene = 2.5) were selected for this study. Also, chemically pure propane was included to provide a base of comparison with the other blends. The LPG blends were delivered in the liquid state in cylinders and the fuel in gaseous form was drawn from the top of the cylinders during engine operation. The compositions of the gas stream supplied from the top of the cylinders were analyzed and presented in Figure 1.3-2 with fuel properties shown in Table 1.3-2.

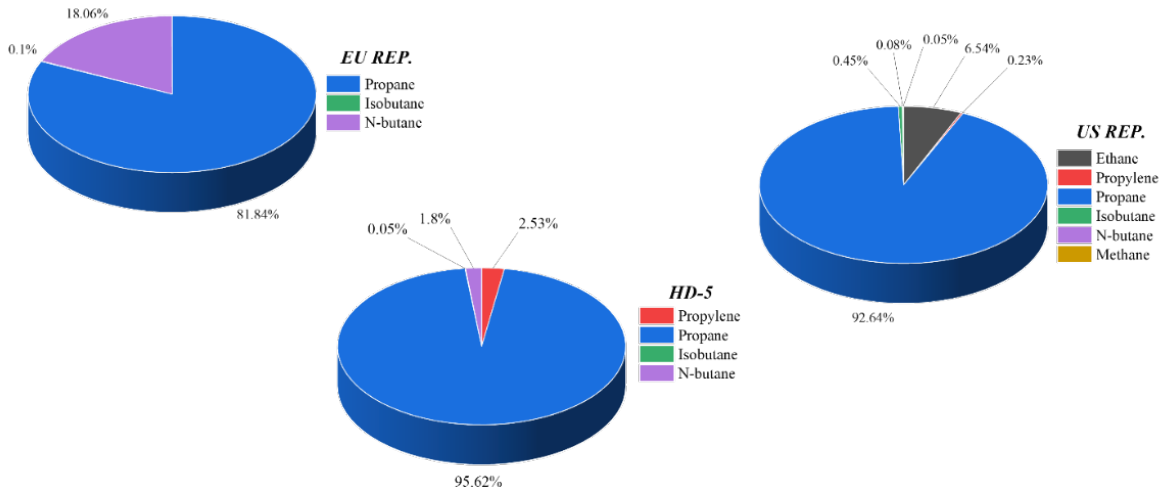

Figure 1.3-2: LPG blend composition showing other dominant constituents.

Table 1.3-2: Selected LPG blends composition details and their properties

LPG Blends	Chemically Pure Propane	US Representative (US Rep.)	HD-5	European Representative (EU Rep.)
LHV (MJ/kg)	46.36	46.4	46.31	46.2
Laminar Flame Speed (cm/s) at STP	40.18	40.3	40.24	39.54
Energy density (kJ/m^3)	3500	3503	3499	3488
H:C ratio	2.67	2.68	2.65	2.63
Density(kg/m^3)	1.9	1.82	1.87	1.97
Stoichiometric Air-Fuel ratio	15.57	15.59	15.54	15.52

The four LPG blends were tested across various engine compression ratios, loads and EGR rates while keeping other engine operating conditions constant. The CR was initiated from a point at which there was normal combustion for all blends i.e., without end-gas auto-ignition, and then swept by one-unit increments, through trace knock, and up to heavy knock for all blends. A baseline CR was then defined from the results of these tests. Spark timing was varied to maintain CA50 at ~ 9.5^0 aTDC for each test case (MBT for all cases was found to be between CA50 8.5-10^0 ATDC). Each test case was run at stoichiometric conditions and a constant speed of 900RPM, and all the experimental data taken at steady state engine operating conditions. The key findings are presented below.

Figures 1.3-3a and 1.3-3b show the brake thermal efficiency (BTE) for all tested LPG blends for the CR and load variations. The BTE increased with increasing CR from an average of ~20.2% at CR 7:1 to ~22.3% at CR 10:1, which was likely due to improved cycle efficiency and reduced burn duration at higher CR. For the load sweep, BTE was increased from an average of ~22.1% at

800kPa to 24.4% at 1100kPa for all blends. This increasing BTE trend with increasing load was as a result of higher fuel quantity required to maintain stoichiometric conditions at the higher intake manifold pressures, in agreement with results shown by Kumar et al. [2]. Fuel composition exhibited a minimal effect on BTE for a given load and demonstrated a more recognizable yet still minimal effect on BTE for a given compression ratio. The brake power and BTE trend can be attributed to the combined effect of a fuel's energy density and flame speed at a given engine operating condition. The laminar flame speeds (LFS) of the blends were calculated using the NUIG 1.1 high temperature mechanism in CHEMKIN [3] at standard temperature and pressure. The energy density was calculated using the blend properties in Table 2.3.2 and the measured fuel mass during stoichiometric engine operation at CR 7:1. Despite the difference in the composition of LPG blends, there was no distinct difference in the calculated laminar flame speed and energy density values among the LPG blends. This is likely responsible for the similar fuel efficiency trends shown in Figure 1.3-3.

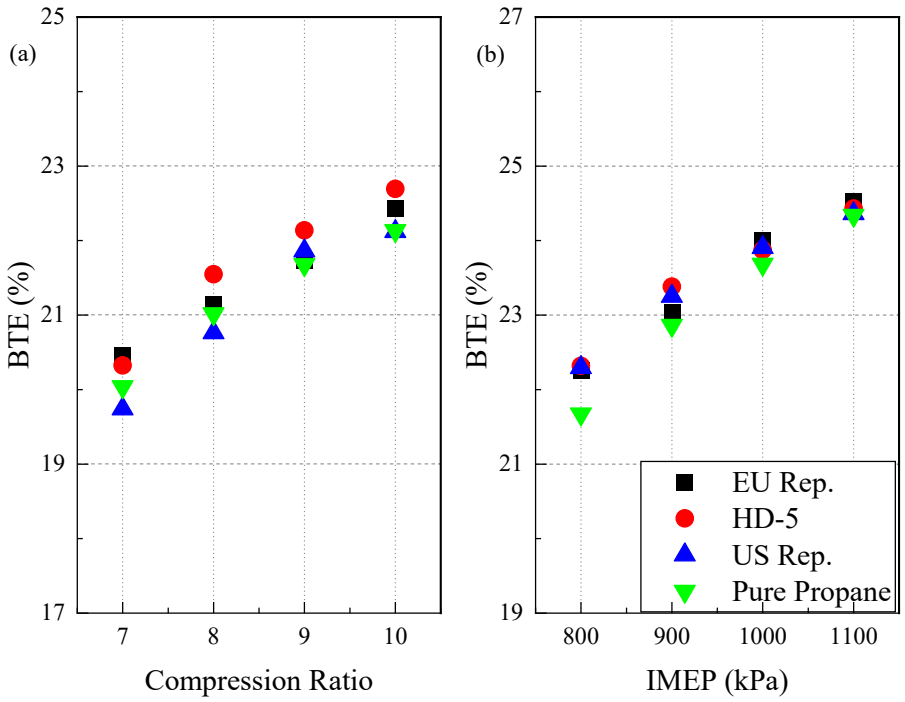

Figure 1.3-3: BTE for all LPG blends over the range of tested (a) CR (b) Engine loads.

The BTE and COV of peak pressure for all the blends at CR 8:1 and 800kPa engine load are presented in Figure 1.3-4: Firstly, the EGR limit is defined as the EGR% at a threshold $COV_{peak\ pressure}$ of 10%. All the tested blends indicated similar trends and demonstrated an EGR limit between 26 and 27%. After this point combustion became unstable and misfire was more likely to happen as the mixture became too diluted and heat release and combustion durations became longer to the detriment of engine stability and efficiency. Secondly, the BTE values are plotted in Figure 1.3-4. As EGR was introduced, the blend efficiencies started to converge, which indicated that there was also no significant fuel composition effect on performance with EGR. Maximum efficiencies were observed for all blends between 20 and 25% EGR rate with the HD-5 and US Rep. blends both achieving an overall maximum BTE of 23.2% among all the blends. Thirdly, all

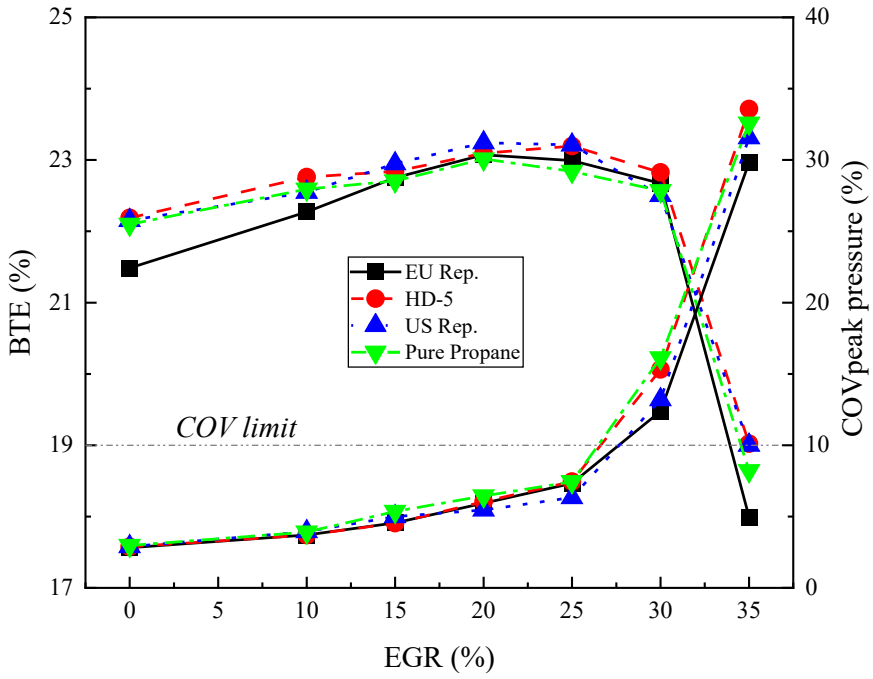

Figure 1.3-4: BTE and $COV_{peak\ pressure}$ (%) vs EGR (%) at CR 8:1, IMEP 800kPa

the tested LPG blends experienced a sharp drop in BTE beyond 30% EGR. In conclusion, these EGR results indicate that there is a window before and after the determined EGR limit where engine operation may be most beneficial in terms of BTE.

In terms of combustion and knock, a trace knock point KI_{limit} ~ 5kPa^2 was defined above which audible incipient knock began on the engine. In Figure 1.3-5a and b, at CR 7:1, the KI for all the blends was KI_{limit} and there was normal combustion. As CR was increased to 8:1, trace amounts of knock were noticed, particularly with HD-5 and EU Rep. As the CR increased to 9:1, the intensity of knock increased exponentially, and the fuel composition effect became more pronounced. The US Rep. blend and chemically pure propane also began to knock along with the other two blends. The ordering of the knock integral values among the blends was consistent with the reactivity of the components in the blends where n-butane > propylene > propane > ethane. Generally, increasing the length of the paraffin increases the knocking tendency of a hydrocarbon. However, propylene is an exception to the general rule of olefins as it knocks more readily than its corresponding paraffin, propane [4]. These effects coupled with the increased CR at 10:1 induced heavy knock and showed the most significant difference in KI observed among the blends. The KI for the US Rep. and the chemically pure propane blends were considerably lower than that of the EU Rep. blend at CR 10:1. Similar trends were observed as engine load was increased from 800kPa to the engine limit at 1100kPa albeit with slightly reduced intensities and with all blends exhibiting some level of trace-light knock at 800kPa.

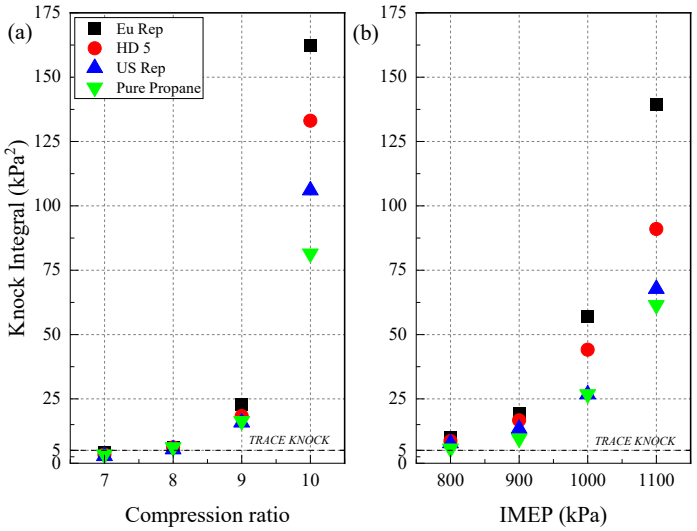

Figure 1.3-5: Plots of Knock Integral for all blends over the tested (a) Compression ratio (b) IMEP.

EGR had been shown to mitigate knock in the literature [4,5] so it was considered for this study to determine if there were LPG composition effects on its mitigation properties. Figure 1.3-6a demonstrates this mitigation effect as the engine was transitioned from varying levels of trace-light knock for all the blends to non-knocking combustion by 10% EGR rate. To properly demonstrate the mitigation potential, the compression ratio was increased to 9:1 shown in Figure 1.3-6b and consequently the engine transitioned into medium knock for all blends with EU Rep. exhibiting the strongest knock intensities. Encouragingly, as EGR was introduced up to the 20% mark, the US Rep and Pure Propane had transitioned into non-knocking combustion while the HD-5 and EU Rep. were barely exhibiting trace knock which was then completely dissipated by the 30% mark. This points to a potential for greater knock mitigation levels with lesser knock resistant fuels like the EU Rep. and HD-5 blends. The KI began to trend upwards again after the minimum at 30% believed to be as a result of the unstable combustion and misfire at those extremely diluted high CR conditions.

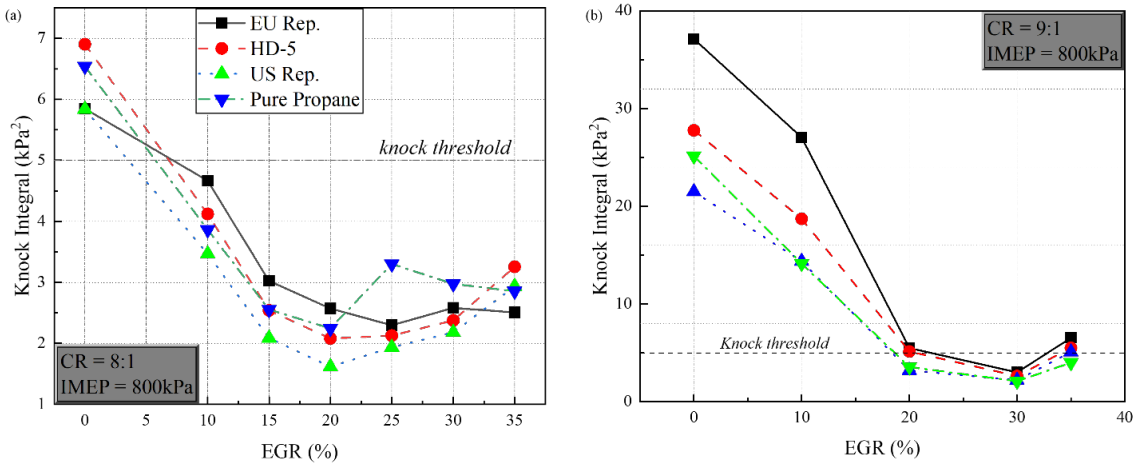

Figure 1.3-6: Knock intensity trends with increasing EGR rates for all blends at (a) 8:1 and (b) 9:1.

Finally, the bsNOx and bsTHC values are plotted as EGR was swept for all blends at CR 8:1 and 800kPa IMEP in Figure 1.3-7a and b. The introduction of EGR had a mitigating effect on NOx and no demonstrable effect on THC up until an inflection point. Between 25 and 30% EGR rates, bsTHC indicated a sharp rise due to incomplete combustion caused by partial burn and misfire while bsNOx continued to trend downwards creating a trade-off scenario where even lower NOx emissions could be achieved, but at the expense of HC emissions. Among the blends, the bsTHC emissions were not too dissimilar, however, there was a blend effect on the bsNOx emissions with US Rep. producing the least NOx emissions at almost all conditions. The bsCO_2eq emissions are presented in Figure 1.3-7b for all the LPG blends over the tested EGR range. There was some blend effect on these GHG emissions as EU Rep. which had the lowest H:C ratio as a result of its significant higher-alkane composition generated the highest bsCO2eq emissions at every EGR rate. Conversely, the US Rep. blend which had the highest H:C ratio of 2.68 generated the lowest bsCO2eq emissions at all EGR rates except at 30% EGR which was a highly unstable engine operation condition. At non-EGR conditions (0% EGR) there was a much as a 4% difference in the GHG emissions between the EU Rep. and US Rep. blends.

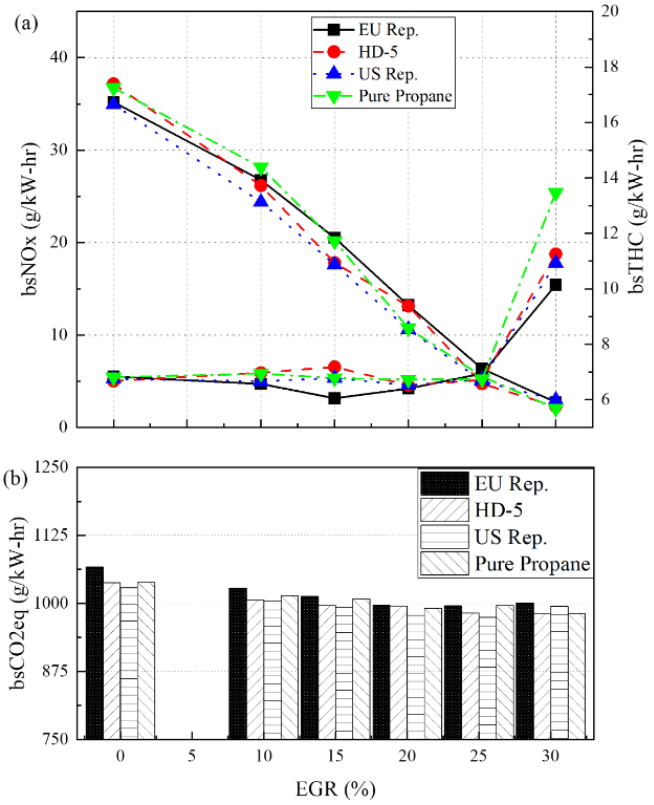

Figure 1.3-7: Variation of (a) bsNOx and THC (b) bsCO_2eq, at CR 8:1, IMEP 800kPa and for all blends, for the range of tested EGR rates.

The successful operation of the engine on premixed LPG was demonstrated and most importantly, the findings showed the importance of EGR in terms of performance, emissions and combustion. They also suggested that variable blend composition was not a significant determinant of engine performance. The results showed that perhaps the most critical

consideration when considering LPG blend composition would likely be the varying levels of knock intensity and how to design controls to accommodate this effect. This minimal effect of blend composition on performance informed the selection of the liquid LPG source for the remainder of the research.

References

1. Fosudo, T., "Development of Advanced Combustion Strategies for Heavy-Duty LPG Engines to Achieve Near-Diesel Efficiency", PhD Dissertation, Colorado State University, 2024.
2. Kumar, D., Sonawane, U., Chandra, K., & Agarwal, A. K. (2022). Experimental Investigations of Methanol Fumigation via Port-fuel Injection in Preheated Intake Air in a Single Cylinder Dual-fuel Diesel Engine. Fuel, 324, https://doi.org/10.1016/j.fuel.2022.124340
3. Ramalingam, A., Panigrahy, S., Fenard, Y., Curran, H., Heufer, K.A. (2021). A chemical kinetic perspective on the low-temperature oxidation of propane/propene mixtures through experiments and kinetic analyses. Combustion and Flame 223:361-37580.
4. J. B. Heywood, Internal Combustion Engine Fundamentals, 2nd Edition, McGraw-Hill Education, 2018.
5. Fosudo, T., Kar, T., Windom, B., Olsen, D. (2024). Low-carbon fuels for spark-ignited engines: A comparative study of compressed natural gas and liquefied petroleum gas on a CFR engine with exhaust gas recirculation. Fuel (360) 2024, 130456. https://doi.org/10.1016/j.fuel.2023.130456.

1.4 Generation of Reduced Chemical Kinetic Mechanism

Mechanism reduction was performed in Chemkin Reaction Workbench initially using the Directed Relation Graph with Error Propagation (DRGEP) method [1] with the autoignition results from stoichiometric propane combustion in air using NUIGMech1.1 as the target. The reduced mechanisms produced by this method became too inaccurate as the species count neared 100. In addition, both isobutane and n-butane were removed since they were not explicitly identified in the target model. Accordingly, more computationally intensive methods were used to improve the reduction results. A reduction operation sequence of DRGEP, Directed Relation Graph (DRG), DRG with Path Flux Analysis (DRGPFA), followed by the same three methods with added Sensitivity Analysis was used to achieve much greater accuracy in the reduced mechanisms [1]. This six-step reduction sequence was repeated until the reduced mechanism reached the specified error from the target mechanism. To ensure that the reduced mechanism contained all the needed reactions to predict ignition delay for the possible species present in LPG, autoignition of a fuel blend containing 60% propane, 10% ethane, 10% propene, 10% isobutane, and 10% n-butane was used as the target model. It was also necessary to constrain the mechanism reduction by the max NO mole fraction. Since NO created during the combustion event does not impact the IDT, Reaction Workbench will remove NOx chemistry from the reduced mechanism unless it is included as a target value. The details of the reduced mechanisms are listed in Table 1.4-1.

Table 1.4-1: Mechanism reduction schemes and reduction results for NUIGMech1.1.

Reduction Method	Fuel	Target	Tolerance	Species	Reactions
DRGEP	C_3H_8	IDT	5%	192	1,367
DRGEP	C_3H_8	IDT	10%	143	1,036
DRGEP	C_3H_8	IDT	15%	114	810
DRGEP, DRG, DRGPA, Sensitivity	Blend	IDT	1%	219	1761
DRGEP, DRG, DRGPA, Sensitivity	Blend	IDT	5%	128	965
DRGEP, DRG, DRGPA, Sensitivity	Blend	IDT	10%	102	717
DRGEP, DRG, DRGPA, Sensitivity	Blend	IDT / max NO mol fraction	1% / 10%	251	1,999
DRGEP, DRG, DRGPA, Sensitivity	Blend	IDT / max NO mol fraction	5% / 10%	153	1,227
DRGEP, DRG, DRGPA, Sensitivity	Blend	IDT / NO mol fraction	10% / 10%	100	670

Comparison of the reduced mechanisms to the NUIGMech1.1 target case showed that the 128 and 153 species reductions predicted IDT within 1 ms of the detailed mechanism at all but the lowest temperature point. The 219 and 251 species reductions were deemed too large to be computationally efficient in 3-D simulations. The 102 and 100 species reductions performed well at low and high temperatures but deviated to the maximum error allowed throughout the NTC regime. The 100 species mechanism also drastically underpredicted IDT for propane with 30% R-EGR, indicating that 100 species is simply too small for a mechanism required to accurately predict LPG reactivity across the full range of engine operating conditions. The 153 species reduction, hereafter referred to as ALPINE 153, was chosen as the optimal reduced mechanism.

ALPINE 153 was used to model the same experimental results from the RWTH Aachen University RCM in Figure 15, but this time using the more accurate variable volume modeling method with the effective volume profiles and initial conditions included in that study. Figure 1.4-1 shows the performance of ALPINE 153 and NUIGMech1.1 against the experimental IDTs. The IDTs predicted by the detailed and reduced mechanisms are never more than 1 ms apart and show good agreement with the experimental data.

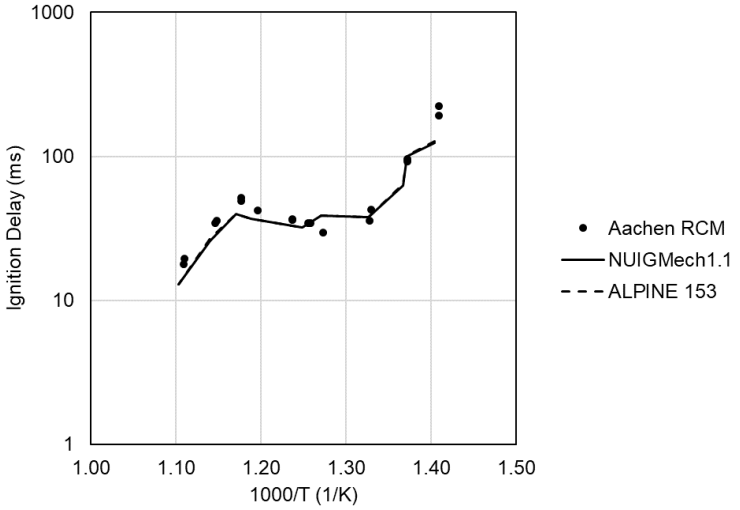

Figure 1.4-1: Variable volume homogeneous autoignition of stoichiometric propane/air at 30 bar pressure as predicted by NUIGMech1.1 and ALPINE 153 (lines) in comparison with experimental results (black circles) from Ramalingam et al. [2].

The RCM at RWTH Aachen University uses a single piston design, so it was also necessary to compare the reduced mechanism to a data set from a dual piston RCM, as they have different compression behavior and facility effects. The RCM at NUI Galway uses the same design as the RCM at CSU and has also been used to study propane combustion at the same pressure and similar temperatures. Again, the modeled IDTs for both mechanisms match very well with the experimental data in Figure 1.4-2, only deviating from each other at the coldest temperature but still within the experimental IDT variation.

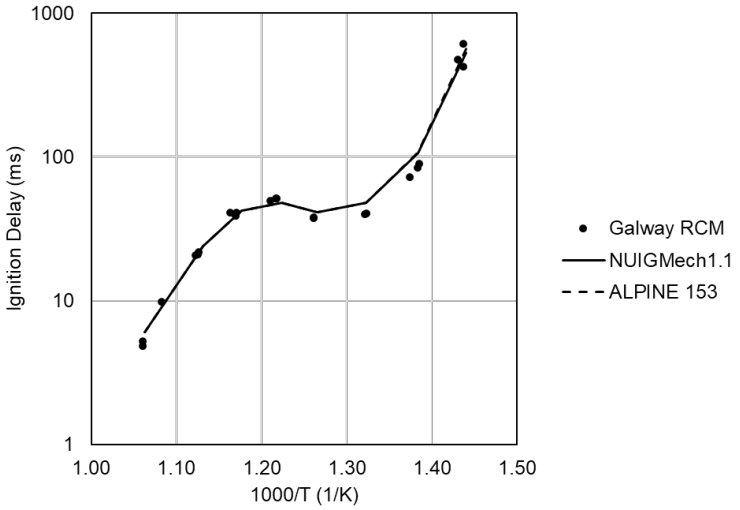

Figure 1.4-2: Variable volume homogeneous autoignition of stoichiometric propane/air at 30 bar pressure as predicted by NUIGMech1.1 and ALPINE 153 (lines) in comparison with experimental results (black circles) from Mohamed et al. [3].

Both NUIGMech1.1_HT and ALPINE 153 were compared to the same experimental data from literature used to validate NUIGMech1.1 for flame speed accuracy. NUIGMech1.1_HT is a high temperature version of NUIGMech1.1 that removes all the species and reactions that are not relevant to flame chemistry to be more computationally efficient. Both mechanisms perform very similarly to each other at low temperatures and pressures as seen in Figure 1.4-3, although it should be noted that as pressure increases, they also overpredict laminar flame speed in the lean condition.

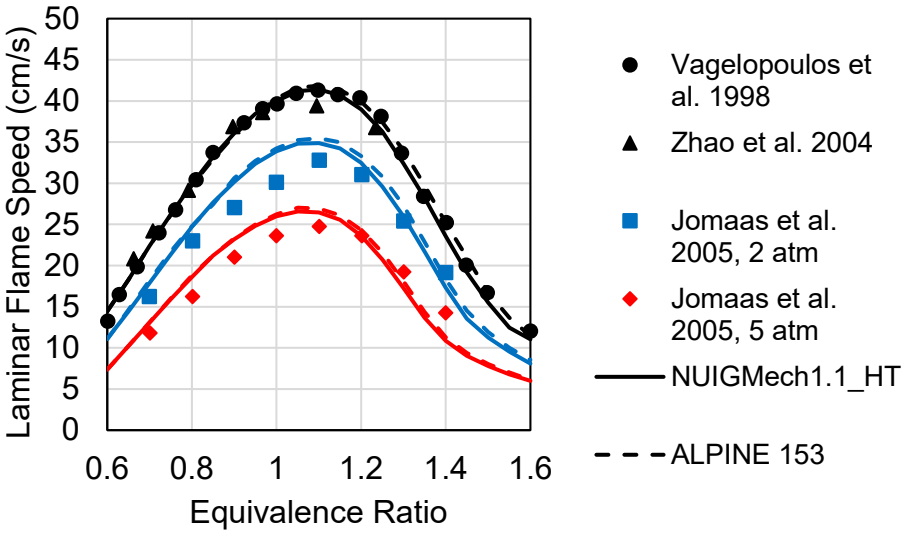

Figure 1.4-3: Simulated (lines) and experimentally measured (symbols) laminar flame speeds for pressures of 1, 2, and 5 atm at 298 K from literature [4-6].

References

1. Ansys® Chemkin-Pro, Release 2021 R1, ANSYS Chemkin-Pro Reaction Workbench User's Manual, 3.2. Mechanism Reduction Theory, ANSYS, Inc.
2. Ramalingam, A., Fenard, Y., and Heufer, A., 2020, "Ignition Delay Time and Species Measurement in a Rapid Compression Machine: A Case Study on High-Pressure Oxidation of Propane," Combustion and Flame, 211, pp. 392–405.
3. El-Sabor Mohamed, A. A., Sahu, A. B., Panigrahy, S., Baigmohammadi, M., Bourque, G., and Curran, H., 2022, "The Effect of the Addition of Nitrogen Oxides on the Oxidation of Propane: An Experimental and Modeling Study," Combustion and Flame, 245, p. 112306.
4. Vagelopoulos, C. M., and Egolfopoulos, F. N., 1998, "Direct Experimental Determination of Laminar Flame Speeds," Symposium (International) on Combustion, 27(1), pp. 513–519.
5. Zhao, Z., Kazakov, A., Li, J., and Dryer, F. L., 2004, "THE INITIAL TEMPERATURE AND N 2 DILUTION EFFECT ON THE LAMINAR FLAME SPEED OF PROPANE/AIR," Combustion Science and Technology, 176(10), pp. 1705–1723.
6. Jomaas, G., Zheng, X. L., Zhu, D. L., and Law, C. K., 2005, "Experimental Determination of Counterflow Ignition Temperatures and Laminar Flame Speeds of C2–C3 Hydrocarbons at Atmospheric and Elevated Pressures," Proceedings of the Combustion Institute, 30(1), pp. 193–200.

1.5 CFD Simulation of CFR Engine for Model Validation

As per Task 1.5, a CFR engine CFD model was developed to fundamentally study the effect of fuel composition and EGR on SI engine combustion according to **Error! Not a valid bookmark self-reference.**. The effect of compression ratio on engine knock with chemically pure propane had been presented (SAE technical paper 2022-01-0404). The CFD simulations were also performed with the EU representative LPG blend at different CR to validate the capability of the model while running with different LPG fuels. Also, the effect of EGR was simulated with pure propane.

Table 1.5-1: Engine operating cases analyzed using CFD

	Case	CR	Fuel	Conditions
CFR Study	Knocking	7	Propane (100%)	No knock
		10		Knock
	Effect of composition	7	EU rep (propane 82%, n-butane 18%)	No knock
		10		Knock
	EGR effect	8	Propane (100%)	EGR 0 (knock)
				EGR 25

Experimental data from the CFR was collected for the conditions listed above as per the engine operating conditions mentioned in Table 1.5-2. These results have been used for CFD simulation validation.

Table 1.5-2: Engine Operating Conditions.

Test type	Fuel	Compression Ratio	IMEP (kPa)	Intake Manifold Pressure (kPa)	Speed (RPM)	λ	EGR rate (%)	Others
Fuel composition effect	Pure Propane, EU rep, US rep	7, 10	Varied	101.2 (fixed)	900	1	–	Intake mixture Temp: 60 ^{0}C Coolant Temp: 95 ^{0}C Oil Temp: 57 ^{0}C
EGR effect	Pure Propane, EU rep	8	1000 (fixed)	Varied			0 - 30	

A numerical model of the CFR test engine was developed using a 3D CFD code, CONVERGE (version 3.0.18). The surface mesh generated from an X-ray scan of CFR engine cylinder/head assembly by Argonne National Laboratory was used as a computational domain geometry in this study. In this work, a base grid size of 4 mm was used outside the cylinder, whereas a grid size of 1 mm was implemented inside the cylinder. Three levels of fixed boundary embedding were specified near the cylinder head, piston, liner, and knockmeter (cell size of 0.5 mm), while four levels of fixed boundary embedding were assigned to intake and exhaust valve face (cell size of

0.25 mm). Furthermore, two fixed spherical embeddings were given near the spark plug to resolve the spark kernel and initial flame development. These are: (1) four levels (i.e., cell size of 0.25 mm) with spherical radius of 8 mm and (2) five levels (i.e., cell size of 0.125 mm) with 4 mm radius. In addition, adaptive mesh refinement (AMR) was implemented to refine the grid size down to 0.5 mm in the computational domain based on temperature and velocity subgrid scales of 2.5 K and 1 m/s, respectively. In-cylinder turbulence was modeled using the Reynolds-averaged Navier-Stokes (RANS) based renormalized group (RNG) k-ϵ model. Note that a minimum grid size of ~ 0.25 to 5 mm is sufficient for RANS simulations to perform both normal and knocking combustion studies in SI engines. Wall heat transfer was captured by using the model proposed by O´Rourke and Amsden. For combustion modeling, the SAGE detailed chemistry solver was implemented in the unburned zone to capture end-gas autoignition. The G-equation based chemical equilibrium model (CEQ) was incorporated on flame and the model tracks the turbulent flame front. Readers are referred to SAE Technical Paper 2022-01-0404 for any further details.

In this work, 3D CFD simulations were performed for three consecutive full engine cycles, out of which the first cycle was discarded for the analysis to remove any effect of initial conditions. Figure 1.5-1(a) and (b) show in-cylinder pressure traces for the second and third simulated engine cycles along with all the 1000 recorded cycles during propane experiments at CR 7 and 10, respectively. For both CRs, all the simulated in-cylinder pressure traces for closed part of the engine cycle are well within the spread of measured pressure traces.

At CR 7, on cycle average basis, it has been found that the simulated location of 50% MFB and peak pressure are within ± 2 crank angle degree (CAD) of corresponding experimental results. Additionally, the difference between the measured and simulated gross indicated mean effective pressure (g-IMEP) and peak pressure are 5% and 1%, respectively. At CR 10, the simulated cycles exhibit a sudden change in the slope of the in-cylinder pressure trace before the onset of high frequency pressure oscillations. This characteristic is very similar to that observed with experimental cycles. A quantitative comparison of important knock characteristics such as the location of knock point is also calculated. The average knock point predicted by the simulations is in good agreement with the experimental results with an error less than 1 CAD. Further, the simulated average pressure at knock point is also found within 3% of that obtained from experiments.

Finally, the evolution of in-cylinder intermediate species, radicals and thermodynamic properties are analyzed for fundamental understanding of end-gas autoignition in detail. Figure 1.5-2 presents the in-cylinder temperature and CH_2O distributions on a horizontal cut plane passing through the spark plug for CR 10 case, obtained from the third simulation cycle over different crank angle instances. At 10.5 deg aTDC, there is a considerable amount of CH_2O species build up, implying enhanced reactivity of the end-gas. Subsequently, CH_2O is consumed rapidly, raising the in-cylinder temperature. This leads to autoignition of the end-gas and finally knocking events. All of these confirm that the current CFR engine CFD model is capable to capture the combustion characteristics of propane reasonably well for both knocking and non-knocking conditions.

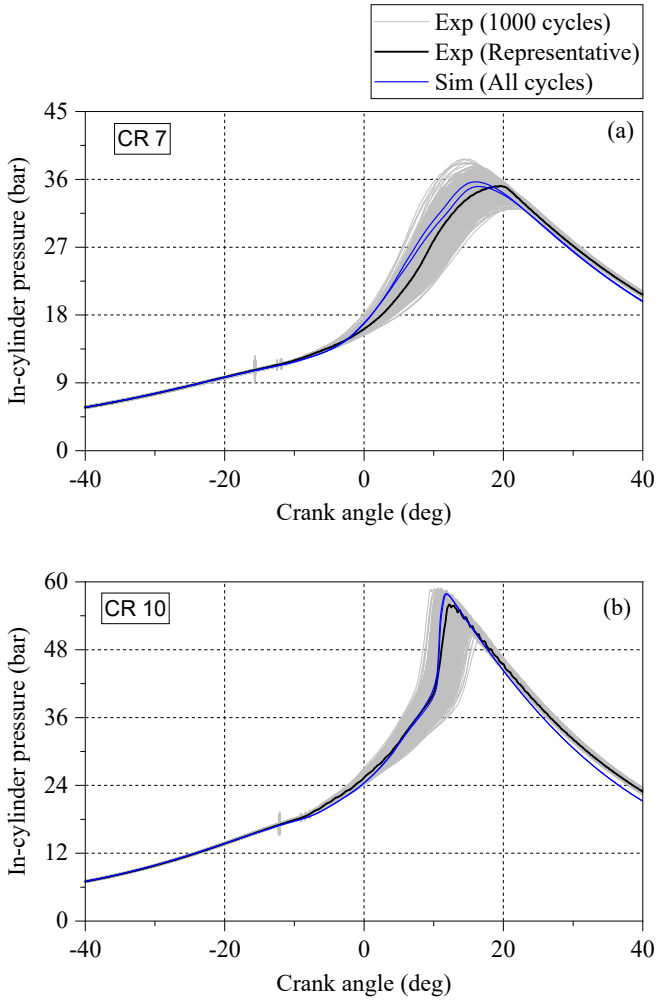

Figure 1.5-1: Comparison of in-cylinder pressure for both experiment and CFD simulation with pure propane for (a) CR 7 (non-knocking) and (b) CR 10 (knocking) at 900 RPM, λ = 1.

Figure 1.5-3 shows in-cylinder pressure traces for the simulated engine cycles along with the upper and lower limit of the recorded cycles during experiments at CR 7 and 10, respectively with EU rep fueling. For both CRs, all the simulated in-cylinder pressure traces for the closed part of the engine cycle are well within the spread of measured pressure traces. At CR 7, on a cycle average basis, it has been found that the simulated location of 50% MFB and peak pressure are within ± 2 crank angle degree (CAD) of corresponding experimental results. At CR 10, the simulated cycles exhibit a sudden change in the slope of the in-cylinder pressure trace before the onset of high-frequency pressure oscillations. This characteristic is very similar to that observed with experimental cycles. A quantitative comparison of important knock characteristics such as the location of the knock point is also calculated, as shown in Figure 1.5-4. The average knock point predicted by the simulations is in good agreement with the experimental results with an error of less than 1 CAD. Similar to propane simulations, EU rep fuel simulations are in close agreement with the experimental results.

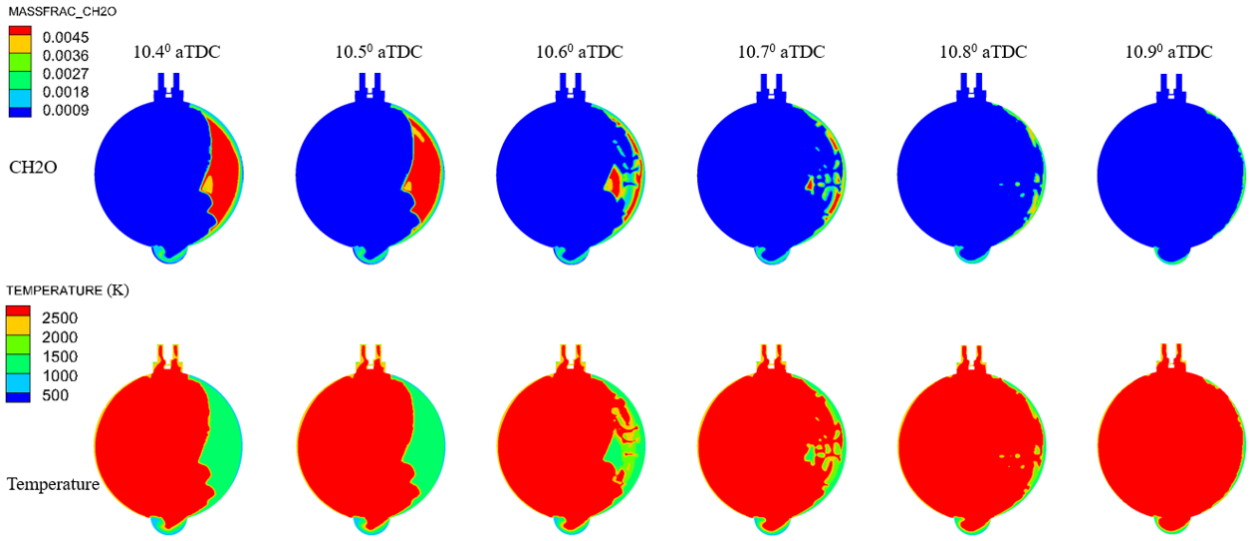

Figure 1.5-2: Evolution of CH2O mass fraction and in-cylinder temperature on a horizontal cut plane passing through the spark plug (obtained from the third simulation cycle). Intake and exhaust are located on the left and right sides, respectively.

Figure 1.5-5 (a) and (b) present the local evolution of in-cylinder temperature and chemical species (i.e., CH_2O and OH), respectively, for propane fueling without and with EGR at CR 8. These CFD results are obtained from the pressure transducer location in the model for the second simulation cycle. At the 0% EGR rate, a sudden consumption of CH_2O and an immediate formation of significant OH species along with the temperature rise in the end-gas indicates the autoignition event for propane fueling, similar to the results shown in **Error! Reference source not found.**. However, at the 25% EGR rate, CH_2O consumption is gradual and there is no substantial OH formation in the end gas. Also, the predicted peak in-cylinder temperature is lower with EGR than that with no EGR condition. These simulation results suggest that the introduction of EGR attenuates the activity related to the onset of end-gas autoignition, which is consistent with the EGR experimental results. All of these simulation results confirm that the current CFR engine CFD model is capable to predict both non-knocking and knocking combustion characteristics reasonably well for LPG fuels without and with EGR.

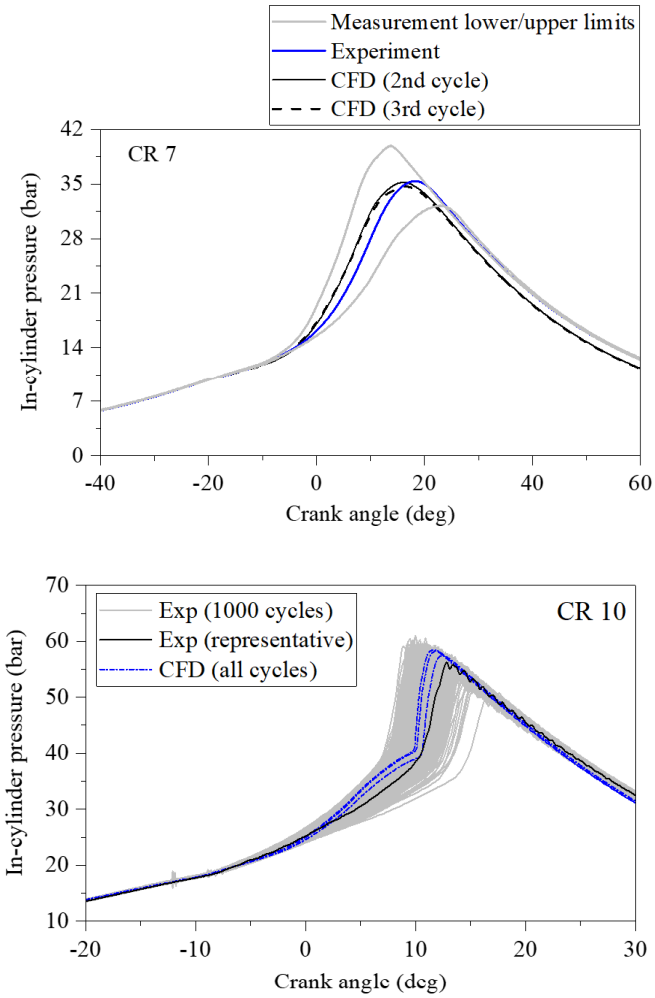

Figure 1.5-3: Comparison of in-cylinder pressure for both experiment and CFD simulation with EU rep LPG for CR 7: non-knocking (top) and CR 10: knocking (bottom) at 900 RPM, λ = 1.

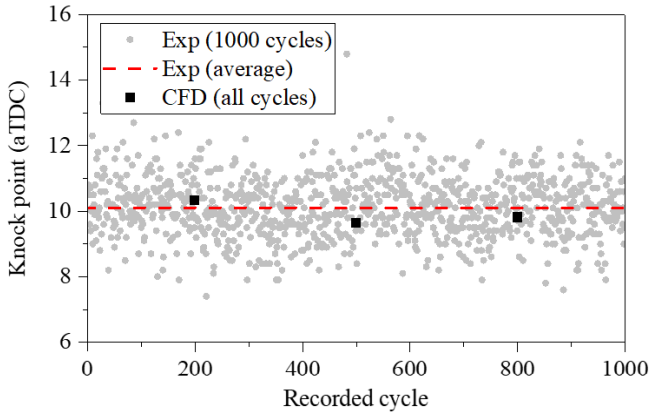

Figure 1.5-4: Knock points from experiments and CFD simulations at CR 10 with EU rep fueling.

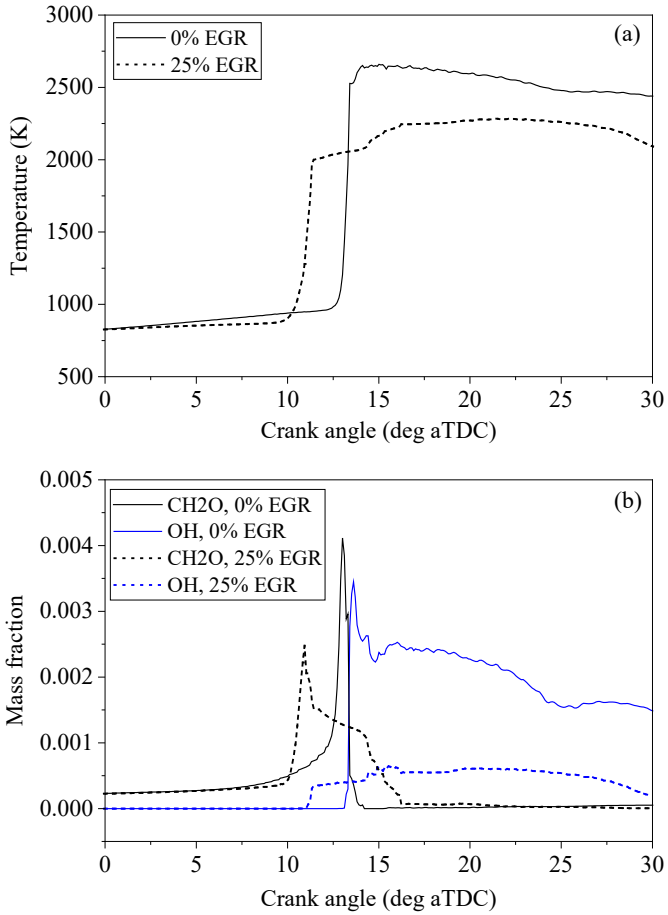

Figure 1.5-5: Local evolution of (a) in-cylinder temperature and (b) CH_2O and OH species for propane fueling without and with EGR at CR 8. CFD results corresponds to the pressure transducer location for the second simulated cycle.

2. LPG Fuel Injection System

2.1 System Design

Referring to Figure 2.1-1, a low-pressure lift pump (SC001) draws LPG from a tank at the saturation pressure for the existing ambient condition. After LPG exits the lift pump, it flows through heat exchanger (HXR001) into the high-pressure fuel pump (SC002). The heat exchanger cools the fluid to remove heat added by SC001. The fuel pressure at the injector (FCV001), downstream of the high-pressure fuel pump, is set with a back pressure regulator (PCV001). The high pressure pump flow rate is set so that roughly 150% of the required injector flow passes over this regulator. An accumulator (ACC001) also exists upstream of the injector to dampen the pressure fluctuations that result from the discontinuous flow demands of the injector such that a more constant pressure can be achieved throughout successive injection events. Finally, before returning to the tank, a second heat exchanger (HXR001) removes the heat added by the high-pressure fuel pump. During testing it was determined that the propane can reach its critical temperature inside the high-pressure fuel pump. To reduce the pump temperature and prevent vaporization of LPG inside the pump, a third heat exchanger (HXR003) was added to an oil loop that circulates oil through the high-pressure pump's cam housing.

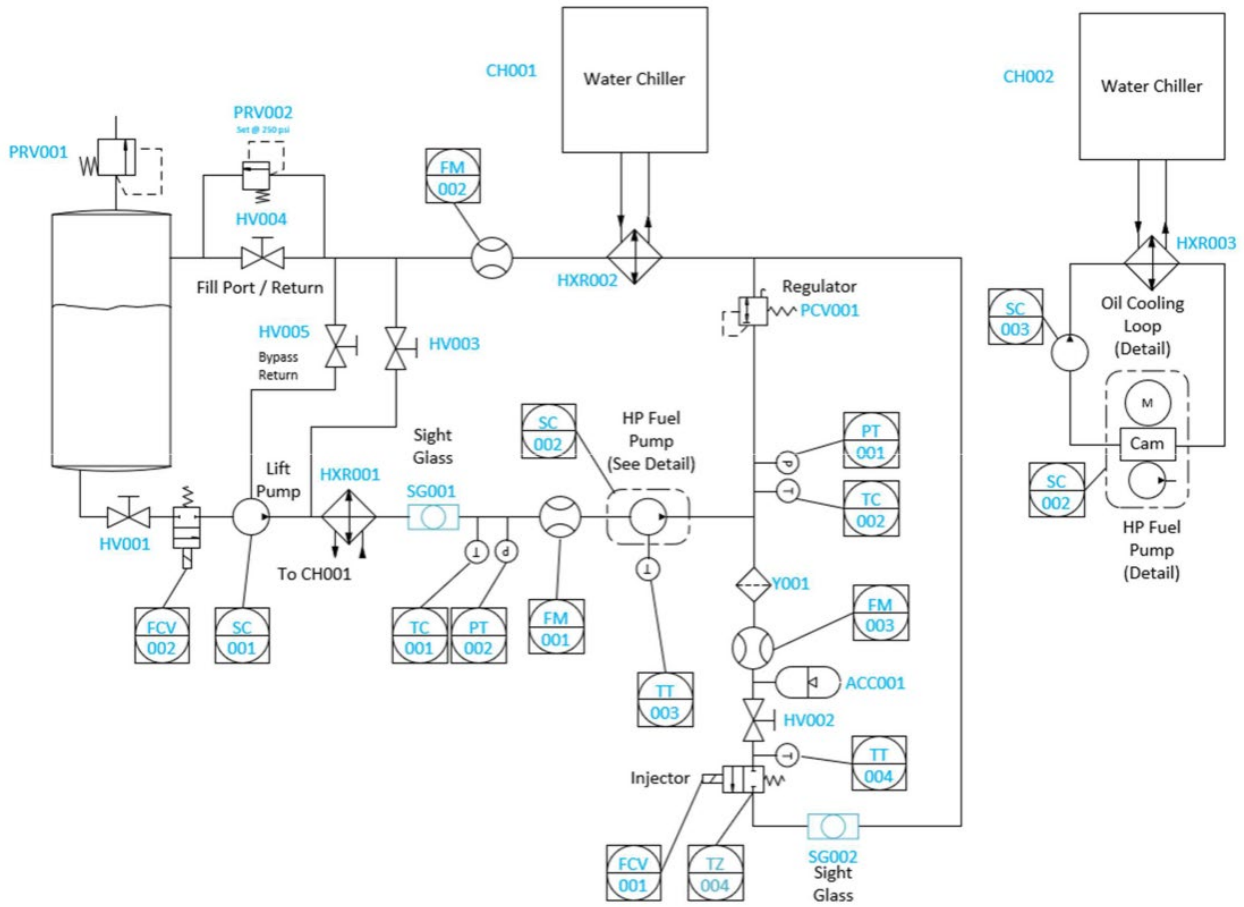

Figure 2.1-1: Fuel Delivery System Schematic

2.2 High Pressure Fuel Injector Nozzle Design

A commercially available fuel injector for a gasoline direct injection (GDI) engine, the Volkswagen 06M906036AE, was selected for modification for use with liquefied petroleum gas (LPG). Due to the larger volume of the X15 engine, as well as the lower energy density of LPG, modification of the injector is required to allow a higher fuel flow rate. Development of the injector was completed in three discrete phases. First, metrology of the stock injector was performed to understand the geometry of the injectors various flow restrictions as well as the nozzle orifice and seat dimensions. An injector nozzle was Electrical Discharge Machined (EDM) cut down the centerline of the injector to create a 3D scan as shown in Figure 2.2-1.

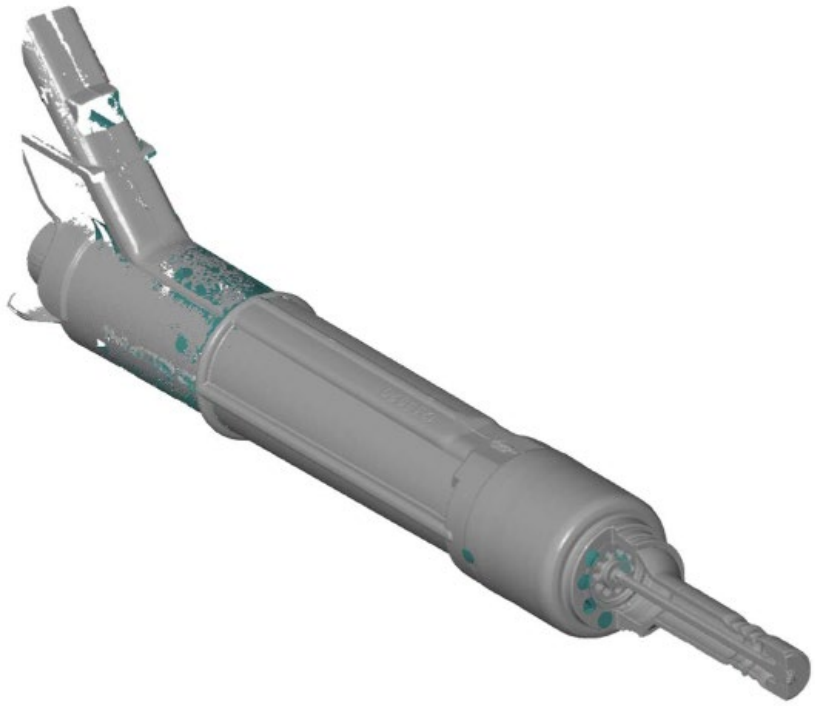

Figure 2.2-1: OEM injector 3D scan data

This dimensional information was used to develop the dynamic model of the injector. A detailed injector model was built in MATLAB/Simulink using previously validated hydraulic and dynamic blocks taken from Czero's extensive library. The model includes all the moving components in the injector, the separate fluid passages and volumes within the injector, and the injector control circuit. This model identified areas of high pressure drop that needed to be modified to achieve the flow targets. Using design modifications made to the OEM injector in the Simulink model, it was determined that the injector LPG flow rate could be increased roughly 25-40% depending on injection pressure. Based on the dynamic model, two locations of flow restriction were identified: the nozzle holes and the needle skirt area (Figure 2.2-2). The needle skirt area could not be increased with impacting operability which made increasing the injector nozzle orifice the primary option.

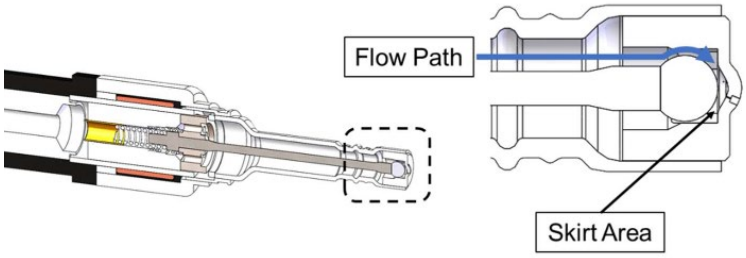

Figure 2.2-2: Needle skirt flow restriction.

Design of the updated nozzles focused in two areas: increasing flow area and ensuring even distribution of the fuel within the cylinder. These two design criteria had to occur while ensuring the injector needle can seal and that the nozzle has sufficient strength to withstand the impact of the needle. To achieve this, a 5-hole design was selected, the dimensions of which are given in Table 2.2-1. Ignoring other restrictions in the system, this flow area was estimated to yield an instantaneous flow rate of .030 kg s^{-1} at 172 bar. This would correspond to an 85 crank angle degree (CAD) injection duration at 1100 RPM in the X15 engine.

Table 2.2-1: 5-hole nozzle design dimensions.

Parameter	**N**	**D1 [in]**	**D2 [in]**	**L1 [in]**
Description	Number of Holes	Nozzle Diameter	Counterbore Diameter	Counterbore Depth
Value	5	0.012	0.023	0.014

An impact study between the needle and the nozzle was performed on this design using static finite element analysis in Solidworks 2020. This was done by extracting the impact velocity from the dynamic model and using the mass of the moving components to calculate the kinetic energy. Next, a calculation was performed where a static force was applied to the nozzle and the resulting displacement was used to find an equivalent spring rate. By assuming that all the kinetic energy from the impact is converted to potential energy, a maximum displacement and "spring force" of this impact can be determined. This force is then used in the FEA software to determine a maximum stress. The maximum stress is then used in a modified Moody diagram to estimate life. Using this method, the life of the injector is estimated to exceed 10^9 cycles which is sufficient for this project scope.

2.3 Fabrication and Hardware Integration

To install the updated nozzle a simple adapter, shown in Figure 2.3-1 and Figure 2.3-2, was developed. This adapter was designed to replicate the outer geometry of the stock injector to ensure that the stock injector nozzle seal can be re-used. The adapter is designed for the nozzle to first be welded onto the nozzle adapter and then assembled to a step cut that is machined

onto the injector. As the adapter assembly is pressed onto the step cut on the injector, the location of the backside of the needle is measured. When a displacement of 0.0005" is measured, the second weld is made to attach the nozzle adapter to the rest of the injector. This is done to ensure the needle makes sufficient contact with the nozzle seat and results in a spring preload of approximately 27 N. The needle sealing diameter is approximately 1.47 mm. Therefore, in-cylinder pressure would need to be approximately 160 bar above fuel pressure before the needle would open unintentionally.

The nozzle spray pattern was chosen based on the LPG injection models created at Argonne National Lab to enable the most uniform distribution of fuel within the X15 cylinder. The orientation of the spray pattern relative to the engine cylinder is shown in Figure 2.3-3.

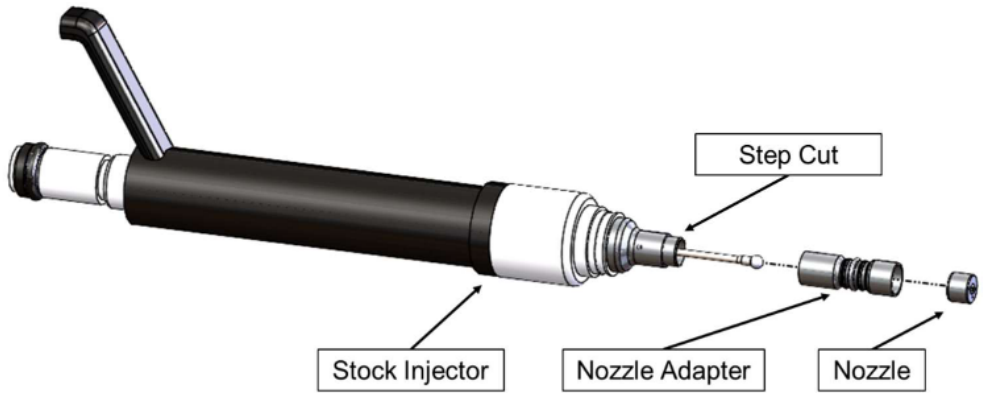

Figure 2.3-1: Injector modification and nozzle adapter

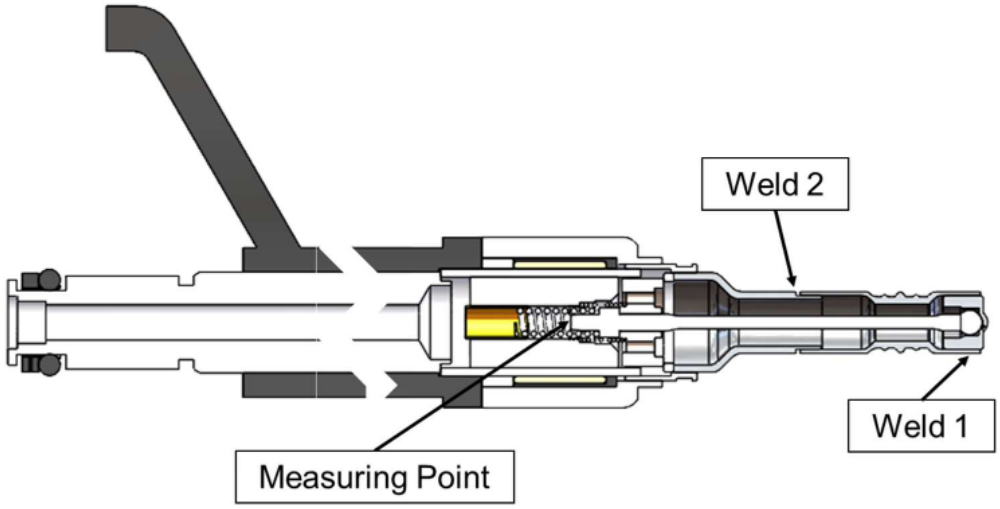

Figure 2.3-2: Modified injector assembly steps

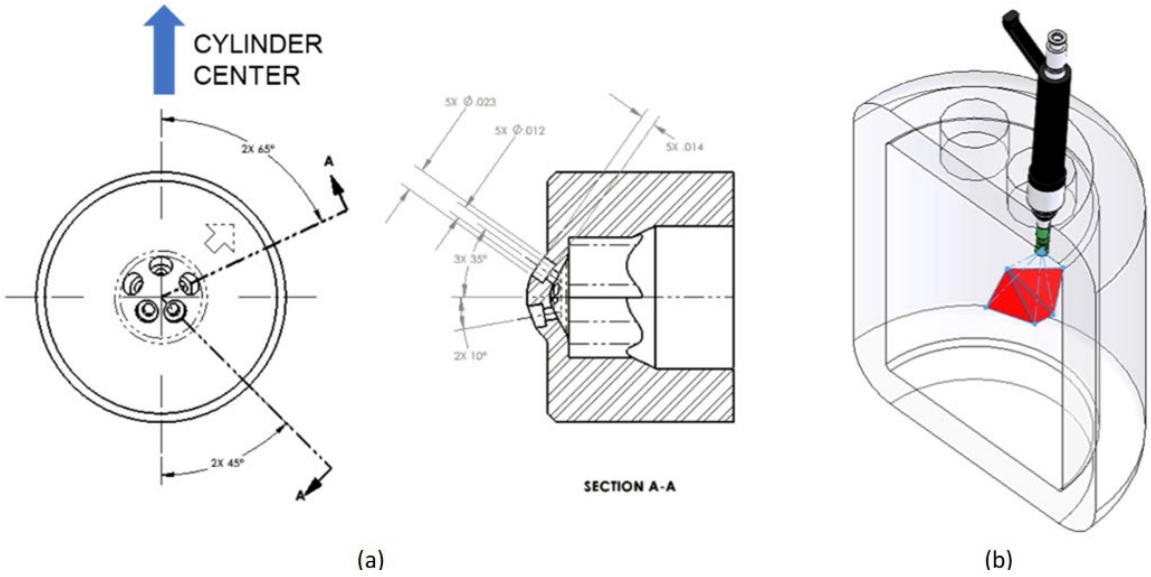

Figure 2.3-3: 5-Hole nozzle orientation (a) and hole centerline distribution in cylinder (b)

2.4 LPG Fuel Injection System Bench Testing

Flow rates were measured for a range of injection pressures using LPG. The injection pressure was set by the back pressure regulator PCV001 (See Figure 2.1-1). Injection flow rate comparisons between the stock and modified injectors are shown in Figure 2.4-1. These are instantaneous flow rates calculated from the flow rate measured at the flow meter (FM003) which is an averaged flow rate due to the accumulator in the system. Flow rates for the modified injectors were greater than the OEM injector across the full range of injection pressures.

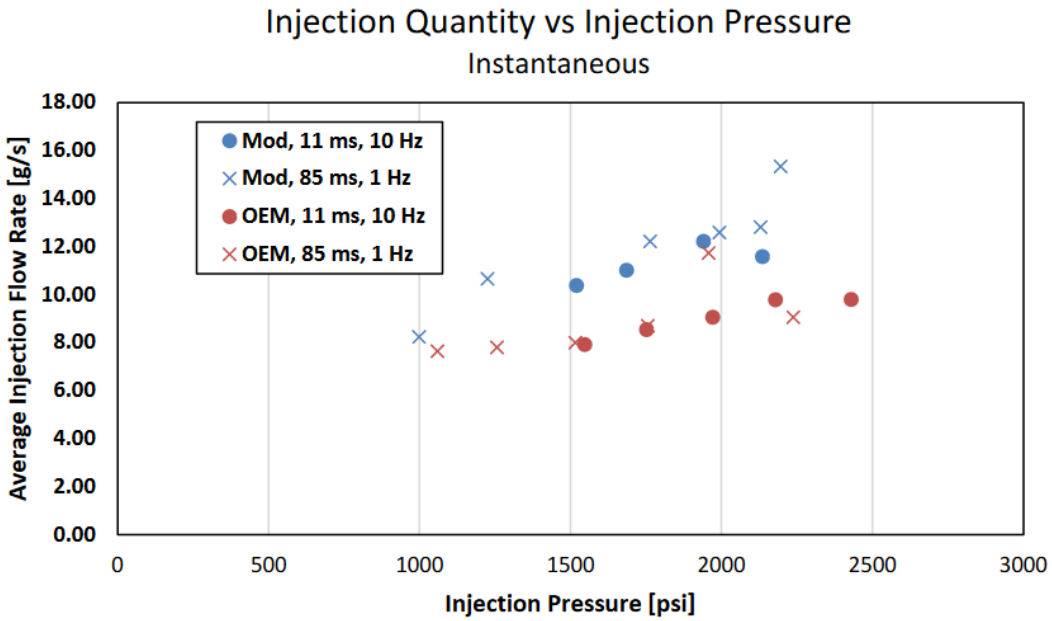

Figure 2.4-1: Measured injection rate for modified (mod) and stock (OEM) injector

The original plan was to conduct an ~8 million cycle durability test on the modified injector at 11 Hz for 200 hours. The actual test was conducted for 122.9 hours at 18 Hz which still equaled the 8 million cycles. Both the OEM injector and a 5-hole modified injector were used in durability testing. Injection rate testing was conducted again after durability testing and the 5-hole modified injector and OEM injector showed no signs of diminished flow rate.

3.0 Fuel Injection Visualization in HPSC

3.1 HPSC System Design/Updating

Chamber Assembly

The chamber is fully functional and can replicate engine-like conditions by changing chamber and fuel pressures and temperatures. High-speed Schlieren and Planar Mie imaging were carried out for Engine Combustion Network's (ECN), Delphi manufactured, solenoid driven, 8-hole, axisymmetric, GDI injector (Spray-G). As shown in Figure 3.1-1 (a), the defined testing conditions include sub-atmospheric conditions to replicate a homogenous, full-load, early injection event observed in the direct injection engines, and high-pressure cases that correspond to late injections or boosted engines. These conditions are also marked on the in-cylinder pressure trace (Figure 3.1-1 (b)), corresponding to different regimes of engine operations. Testing was carried out at various engine relevant temperatures for iso-octane (a surrogate for gasoline) and propane (surrogate of LPG).

Control Parameters	
Fuel	Propane and Iso-octane
Fuel Injector	ECN Spray-G and Delphi 5-hole
Electronic Injection Duration	680 µsec
Electronic Injection Duration	870 µsec
Imaging Techniques	Schlieren and Mie
Data Range	0 µsec ASI – 1200 µsec ASI
Time Interval (Δt)	33 µsec (= 30,000 fps)
Test Conditions	45 tests
Trials	5 for each test

a)

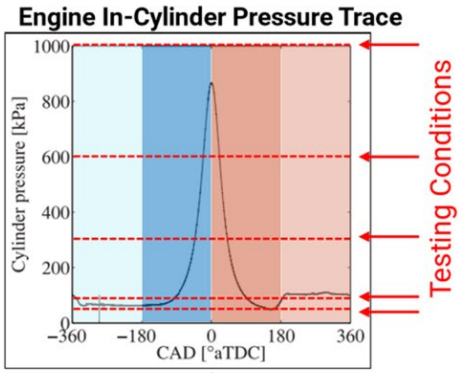

b)

Figure 3.1-1: a) Extended test matrix including Engine Combustion Network's identified experimental conditions and high-pressure engine relevant conditions. b) Testing conditions indicated on an in-cylinder pressure case to demonstrate the range and applicability of the testing conditions.

The HPSC has been updated with aluminum flanges to accommodate various direct injection fuel injectors and thermocouples. The aluminum water jacket flange retains the fuel injector of choice and can cool or heat the injector to a desired temperature with an accuracy of ± 0.5 K. Fuel injector adapters for each injector have been manufactured for specific design conditions, each capable of withstanding around 350 bar. With the help of O-rings and gaskets, the HPSC is able to hold pressures up to 11 bar. Cartridge heaters, tape heaters, and insulation are able to heat the chamber and maintain the chamber temperature up to 400 K. With the procurement of square windows, the HPSC is able to allow a Nd:YAG laser sheet through the chamber for Mie and PLIF imaging techniques. The Large Engine Control Module (LECM) can produce multiple injection profiles for a given injector. The last update to the HPSC would be integration of acetone doping system to the nitrogen supply. Apart from this, the chamber is fully functional for a multitude of testing conditions. An acetone loop was installed in the HPSC assembly that included an acetone bubbler which can handle high pressures and temperatures to allow for controllable

doping of acetone in nitrogen gas. Acetone doped nitrogen is required to perform planar laser-induced fluorescence imaging of the spray which will be used to quantify the planar vapor penetration lengths and plume specific data.

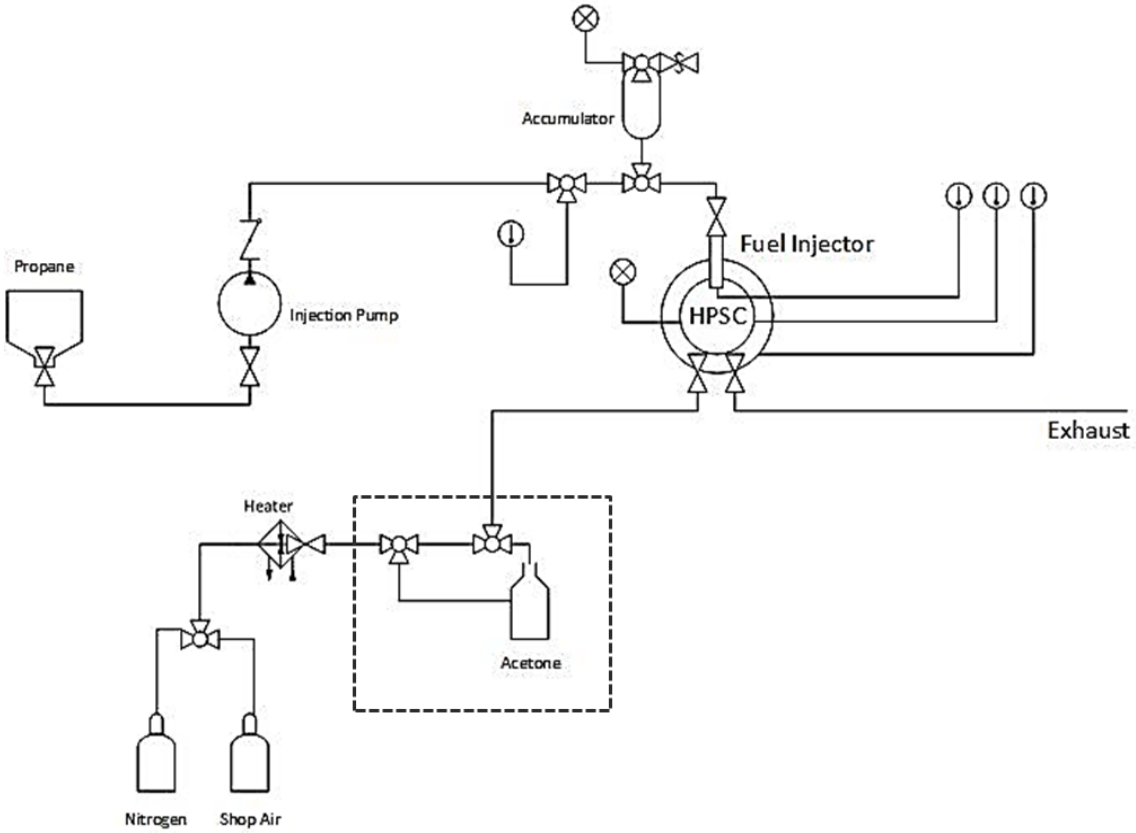

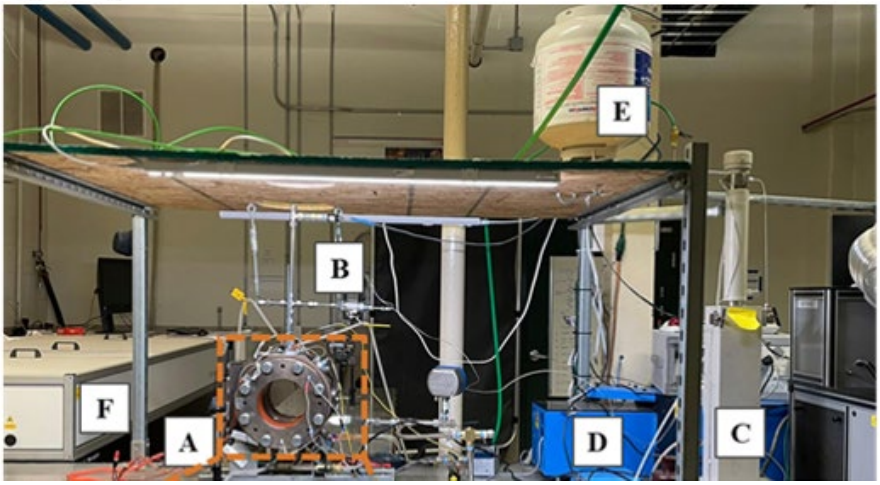

Figure 3.1-2: Piping and instrumentation diagram of the high-pressure spray chamber including the injection lines, chamber pressurization and temperature controls, and acetone bubble loop in the dashed rectangle.

3.2 Visualization Technique Development

Schlieren Imaging

Schlieren imaging is a well-established, line-of-sight technique that is commonly used to visualize inhomogeneities in the refractive index of a transparent medium, created by gradients in the corresponding density field. This technique is commonly used in literature for both qualitative visualization and quantitative fuel spray measurements, such as vapor phase. Schlieren provides a good visualization of the global spray dynamics. But it does not provide all the details that are needed to fully understand the spray. As seen in the images (Figure 3.2-1) the darker regions in the spray correspond to higher densities than the lighter portions of the spray. The darker regions

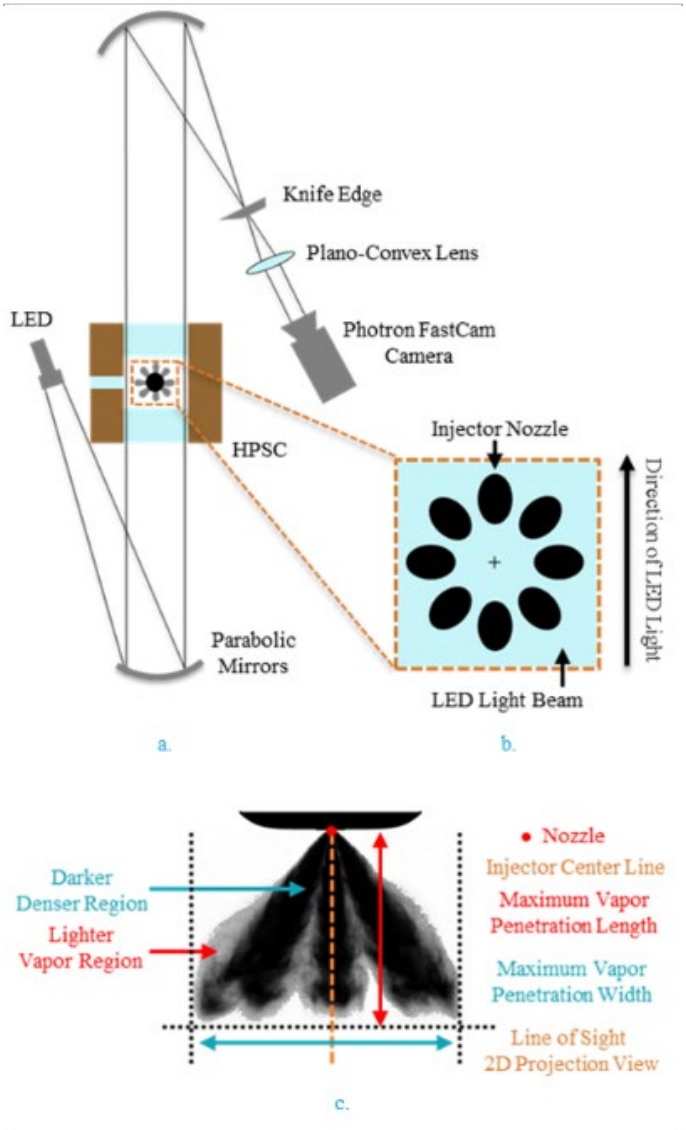

Figure 3.2-1: (a) Schematic of the top-view of Schlieren imaging setup, (b) Spray-G injector nozzle-alignment relative to the LED light, and (c) resulting Schlieren spray image, features, and nomenclature.

encapsulate both high-density gas and liquid; but there is no distinct difference that can be visually examined. Hence, there is a need of a sophisticated imaging technique like Mie Scattering to identify the difference within these structures.

Mie Scattering Imaging

Mie scattering imaging is an elastic light scattering technique used extensively in prior literature to measure liquid penetration through a medium. When a spray is exposed to a specific wavelength of light, the liquid region scatters light in all directions, but the vapor regions do not illuminate. Hence, Mie scattering imaging is often used to capture the liquid regions of the spray. Coupled with Schlieren imaging, Mie can provide a strong comparison amongst the liquid regions, high density vapor regions, and low-density vapor regions. Like Schlieren, Mie scattering captures the liquid regions of the spray globally, i.e., no clear distinction between each plume can be observed. This study utilizes planar Mie scattering to increase the plume-to-plume distinction and enhance the resolution of individual plume penetration morphology. A custom Nd: YAG laser was used to produce a 532 nm beam with 25 ns pulse width and 7 mJ of energy per shot. The setup for Mie testing consisted of two 50 mm Nd: YAG mirrors designed to reflect 532 nm light to the height of the injector tip. The setup also included two cylindrical optics: a converging lens with a focal length of 1000 mm, and a diverging lens with a focal length of -75 mm as shown in Figure 3.2-2a, to create a thin laser sheet, 100 µm thick, bisecting the front nozzle of the fuel injector as seen in Figure 3.2-2b. The Mie laser sheet in Figure 3.2-2c was used to precisely image the spray structure of the individual plumes injected by the front and back nozzles in the plane of the laser sheet, represented in Figure 3.2-2d. Additional optics and equipment were used to regulate and measure the energy of the laser sheet, to finely tune the amount of energy delivered to the spray. An Andor iStar sCMOS camera was used along with a Vivitar 75-300 mm macro focusing camera lens to capture the spray image with a spatial resolution of 49 µm/px and image size of 2560 x 2160 pixels at various instances of time, ranging from 25 µs to 1200 µs ASI. Like the Schlieren timing setup, the camera, the fuel injector, and the laser were synchronized using the external delay generator triggered by the LECM. The actual laser and camera shot timings relative to the start of injection were measured using an oscilloscope and was found to be within ± 15 µs. The Andor camera was gated for 15 ns to capture the center of the laser pulse.

3.3 Spray Angle Penetration Testing for Model Development

The effect of fuel temperature variation on the spray for Bosch EU6 injector is shown in Figure 3.3-1. The darker region in the spray indicates liquid propane droplets, whereas less dark or white region in the spray is vaporized fuel. A difference in the light intensity is distinctly visible between the two injector tip temperature conditions, which is likely due to the flash boiling of propane at higher injector temperature.

Figure 3.3-2 shows the effects of increasing fuel injection pressure on the spray behavior for the Bosch EU6 injector over time for a given chamber pressure and fuel injection temperature. It is observed that the spray penetration length and penetration speed are directly proportional to the fuel injection pressure. The measured spray angles, however, behave differently as the pressure is increased.

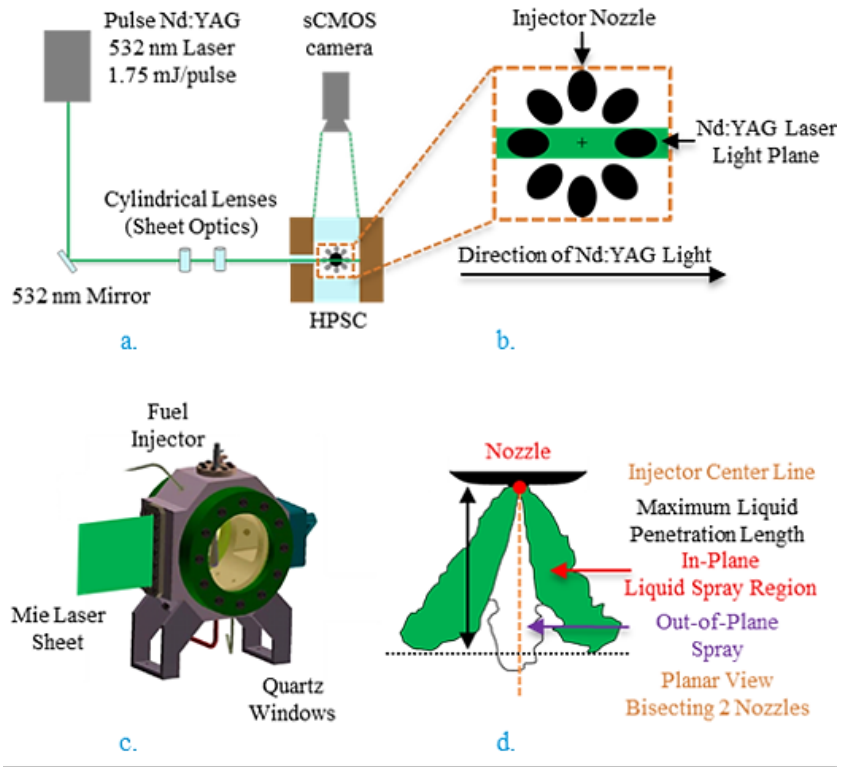

Figure 3.2-2: (a) Schematic of the top-view of planar Mie scattering imaging setup, (b) Spray-G injector alignment relative to the laser sheet bisecting the front and back nozzles, (c) isometric 3-D rendering of HPSC and Mie laser sheet, and (d) schematic of corresponding Mie image with illuminated liquid spray plumes in the plane of the laser sheet, and associated nomenclature.

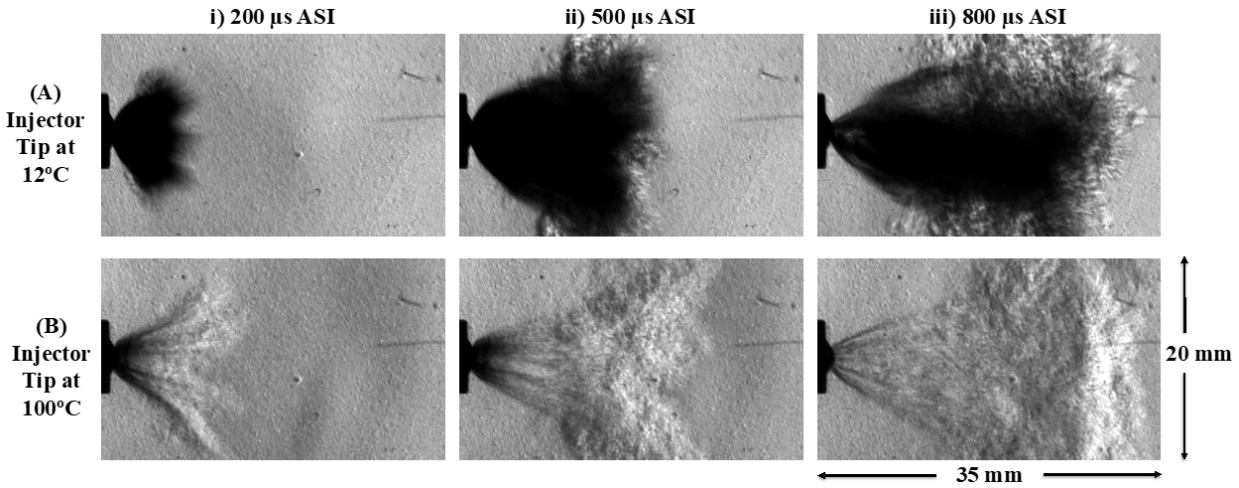

Figure 3.3-1: Schlieren images recorded at 50,000 frames per second with Bosch EU6 at injection pressure of 1000psi and a chamber temperature of 100°C.

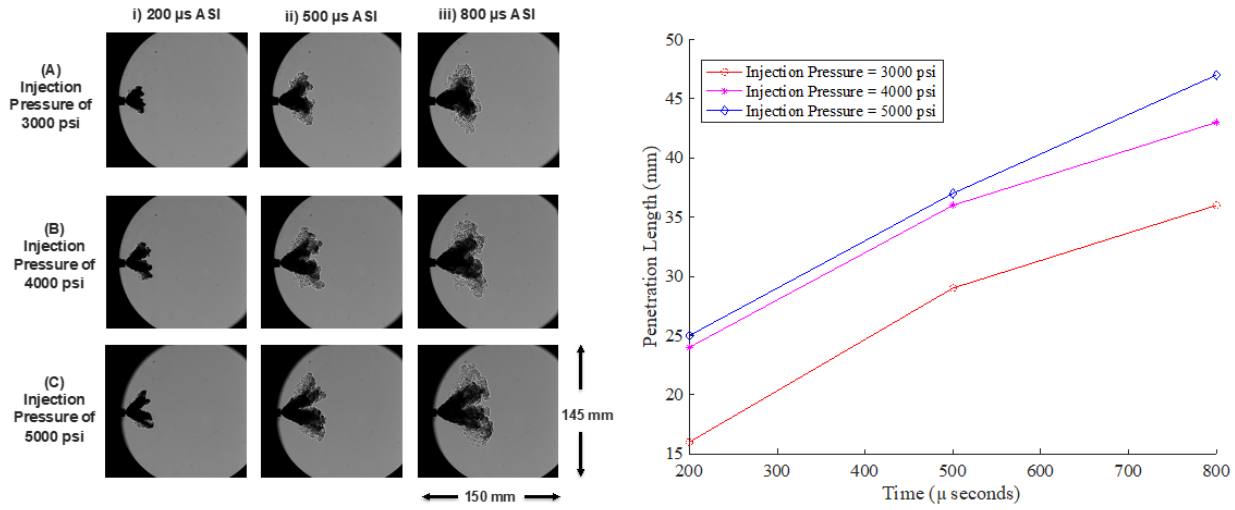

Injection Pressure	Average Spray Angle	Average Penetration Speed
A) 3000 psi	85.85°	92.6 m/sec
B) 4000 psi	86.75°	113.6 m/sec
C) 5000 psi	80.57°	124.6 m/sec

Figure 3.3-2: Schlieren images for Propane at various injection pressures and corresponding spray measurements using Bosch EU6 Injector.

Figure 3.3-3 shows the effects of chamber pressure on the spray behavior for the Delphi injector over time for a given fuel injection pressure and temperature. The penetration length decreases with the increase of chamber pressure. The angle of the spray increases significantly from 0 to 5 bar chamber pressure as the vapor is less super-heated and the jets able to sustain their individual forms. Some optical blurring is observed in the images, which are due to the scratches on the surface of the quartz window. This was taken care of with sanding and polishing work, and the quartz windows are now optically clear.

Measurements such as vapor penetration length, width, and speed are used to characterize the spray structure. These measurements provide good insight into spray dynamics and the dependencies the spray has on temperature and pressure. High-speed Schlieren imaging has been utilized to image both iso-octane and propane at previously stated conditions. These images are recorded at 30,000 frames per second to obtain high-speed videos with a 33 µsecond difference between two frames. For simplicity, images only at 600 µsecond timestamp after the start of injection are shown in Figures 3.3-5 and 3.3-5. Spray collapse results from two phenomena: plume-to-plume interaction and flash boiling. The plume-to-plume interaction between individual jets can be seen as the jets combine, resulting in further penetration depths. In these interactions the transverse component of the jet is canceled with another jet leaving

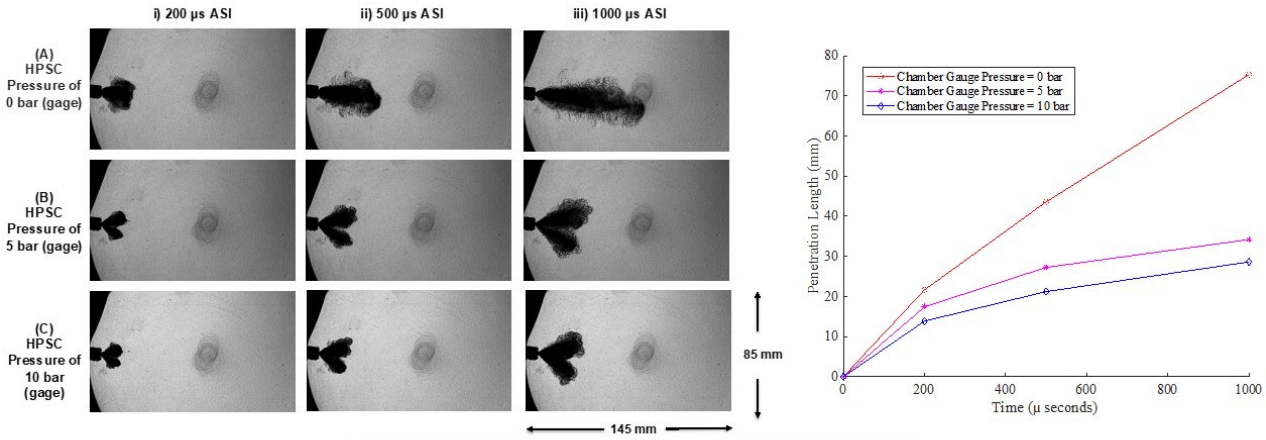

Chamber Gauge Pressure	Average Spray Angle	Average Penetration Speed
A) 0 bar	25.85°	115.1 m/sec
B) 5 bar	78.47°	66.4 m/sec
C) 10 bar	71.39°	53.1 m/sec

Figure 3.3-3: Schlieren images for Propane at various injection pressures and corresponding spray measurements using Delphi Injector.

only the vertical component. The jets merge, resulting in greater momentum to penetrate deeper into the chamber. Another critical feature observed in the collapsed jet is the darker central core indicating higher density (more liquid) due to the shielding effect. The flash boiling collapse can be characterized by increased plume interaction and less defined plume boundaries. Like plume-to-plume collapse, flash boiling collapse also contributes to increased penetration depth and liquid depth.

Schlieren images of iso-octane sprays and propane sprays at various chamber pressures (columns) ranging from 0.5 bar to 10 bar absolute are shown in Figures 3.3-4 and 3.3-5, respectively. The top row contains spray for 20C for fuel and chamber temperatures, the middle row for 60C for both, and the bottom row for 90C for both at an injection pressure of 170 bar. For iso-octane, in Figure 3.3-4, it observed that the spray collapse increases with temperature and chamber pressure. In contrast, for propane, observed in Figure 3.3-5, spray collapse due to flash boiling increases with temperature while increasing chamber pressure shifts the collapse to plume-to-plume interactions. Schlieren gives a good visualization of the global spray dynamics. Spray development of propane is sensitive to chamber pressures and fuel and chamber temperatures. The liquid-vapor boundary is unclear in Schlieren. Schlieren is a 2D projection of a 3D phenomenon that makes it difficult to parse out individual plume behavior to develop high-fidelity spray models. Hence, a sophisticated imaging technique like the plane Mie scattering imaging is needed to define the difference within these structures.

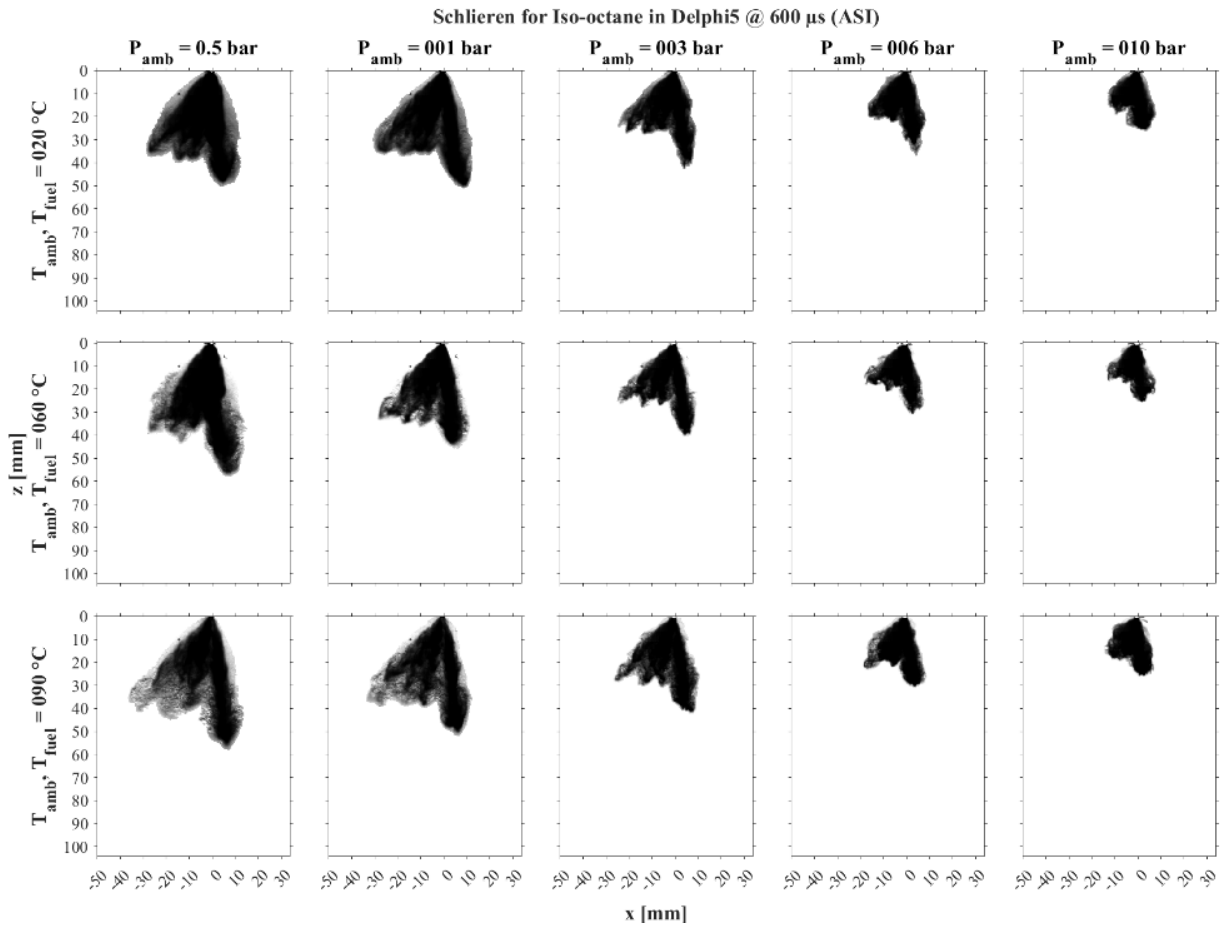

Figure 3.3-4: High-speed Schlieren images for iso-octane at various denoted chamber pressures (columns) and fuel/chamber temperatures (rows) at 600 µseconds after the start of injection for modified Delphi 5-hole injector.

Mie images of iso-octane and propane sprays at various chamber pressures from 0.5 bar to 10 bar absolute are shown in Figure 3.3-6 and 3.3-7, respectively. For iso-octane, observed in Figure 3.3-6, greater liquid concentrations are maintained throughout the spray duration for higher temperatures and pressures. Conversely, propane spray, shown in Figure 3.3-7, liquid concentrations permeated longer for higher temperatures and lower pressures.

The increased duration of liquid present in the spray is associated with the dominating collapse phenomenon. For iso-octane, the plume-to-plume interaction at higher temperatures and pressures leads to larger concentration gradients in the center of the collapsed jets. Due to the geometry of the injector, three spaced holes and two clumped holes, there are two distinct regions of liquid that form. The propane behavior is opposite of iso-octane, as the flash boiling is present under different conditions. The shielding of the flash boiling at lower pressures and high

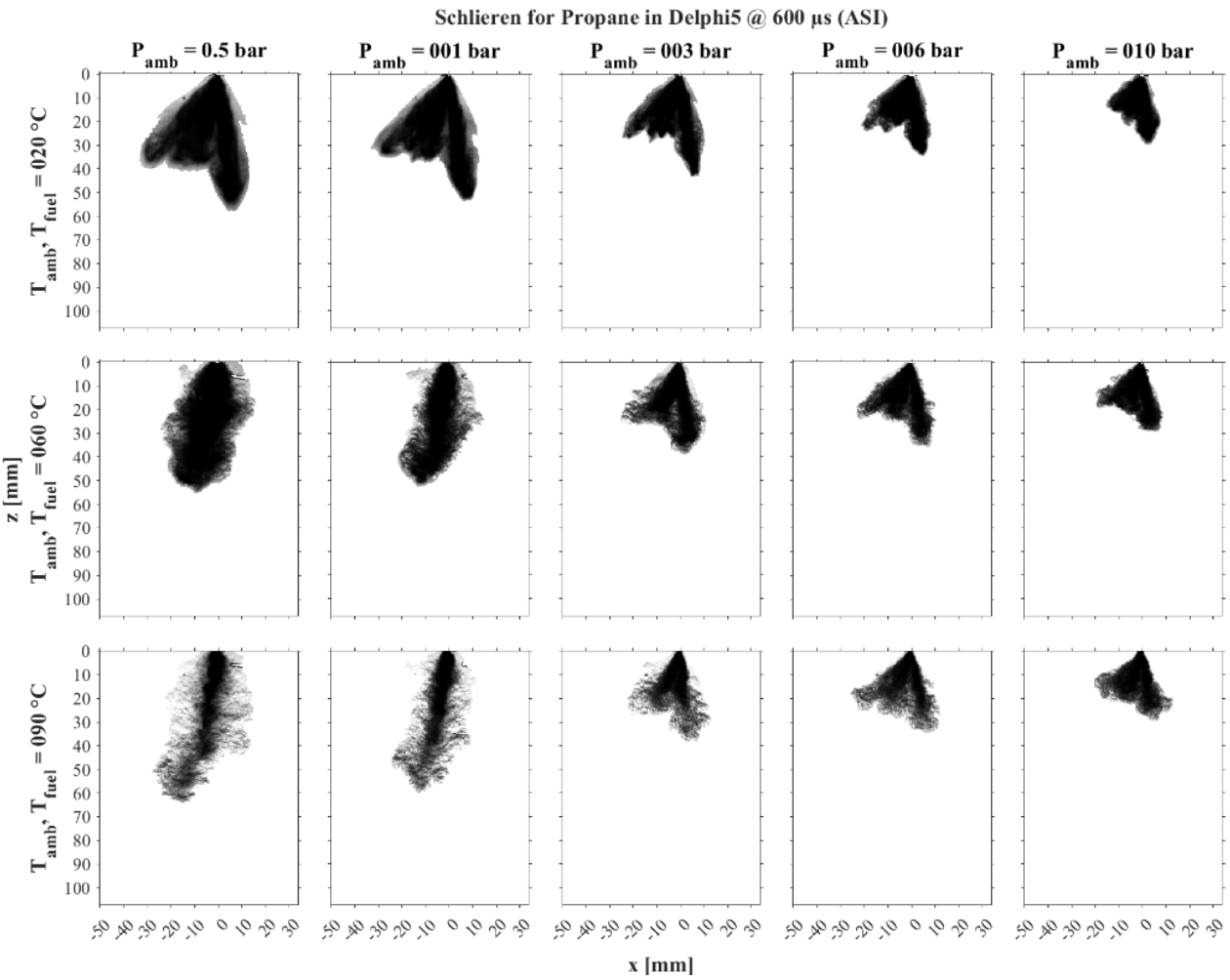

Figure 3.3-5: High-speed Schlieren images for propane at various denoted chamber pressures (columns) and fuel and chamber temperatures (rows) at 600 µseconds after the start of injection for modified Delphi 5-hole injector.

temperatures protects liquid regions throughout the injection duration. Shown in Figure 3.3-8 is a direct comparison between the maximum axial liquid and vapor penetration lengths for propane and isooctane at both hot and cold temperature conditions. At cold temperatures, both the liquid and vapor penetrate the same distance compared to hot conditions where the vapor achieves maximum penetration length while the liquid cannot reach the same distance due to rapid vaporization.

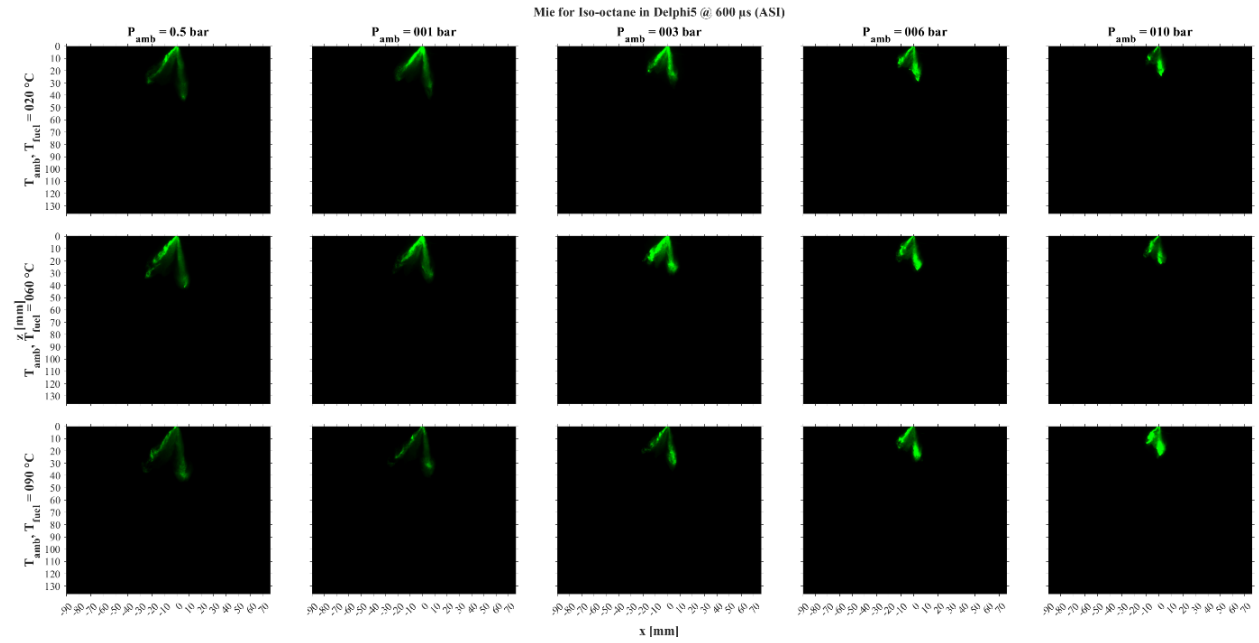

Figure 3.3-6: Planar Mie images for iso-octane at various denoted chamber pressures (columns) and fuel and chamber pressures at 600 µseconds after the start of injection for modified Delphi 5-hole injector.

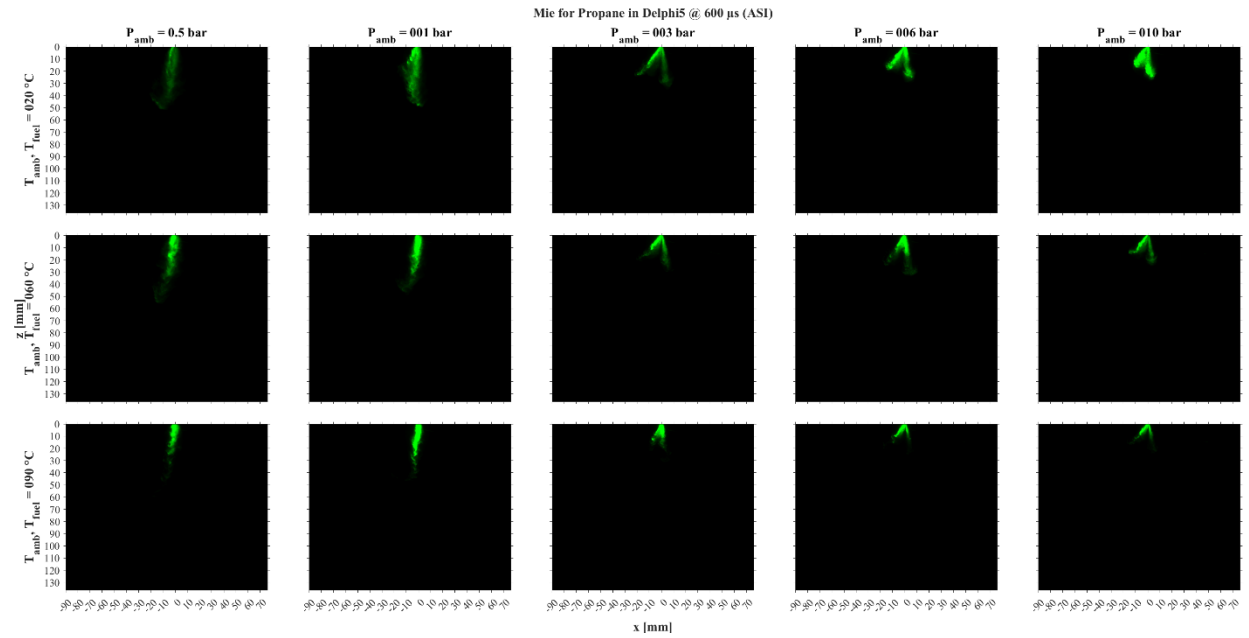

Figure 3.3-7: Planar Mie images for propane at various denoted chamber pressures (columns) and fuel and chamber pressures at 600 µseconds after the start of injection for modified Delphi 5-hole injector.

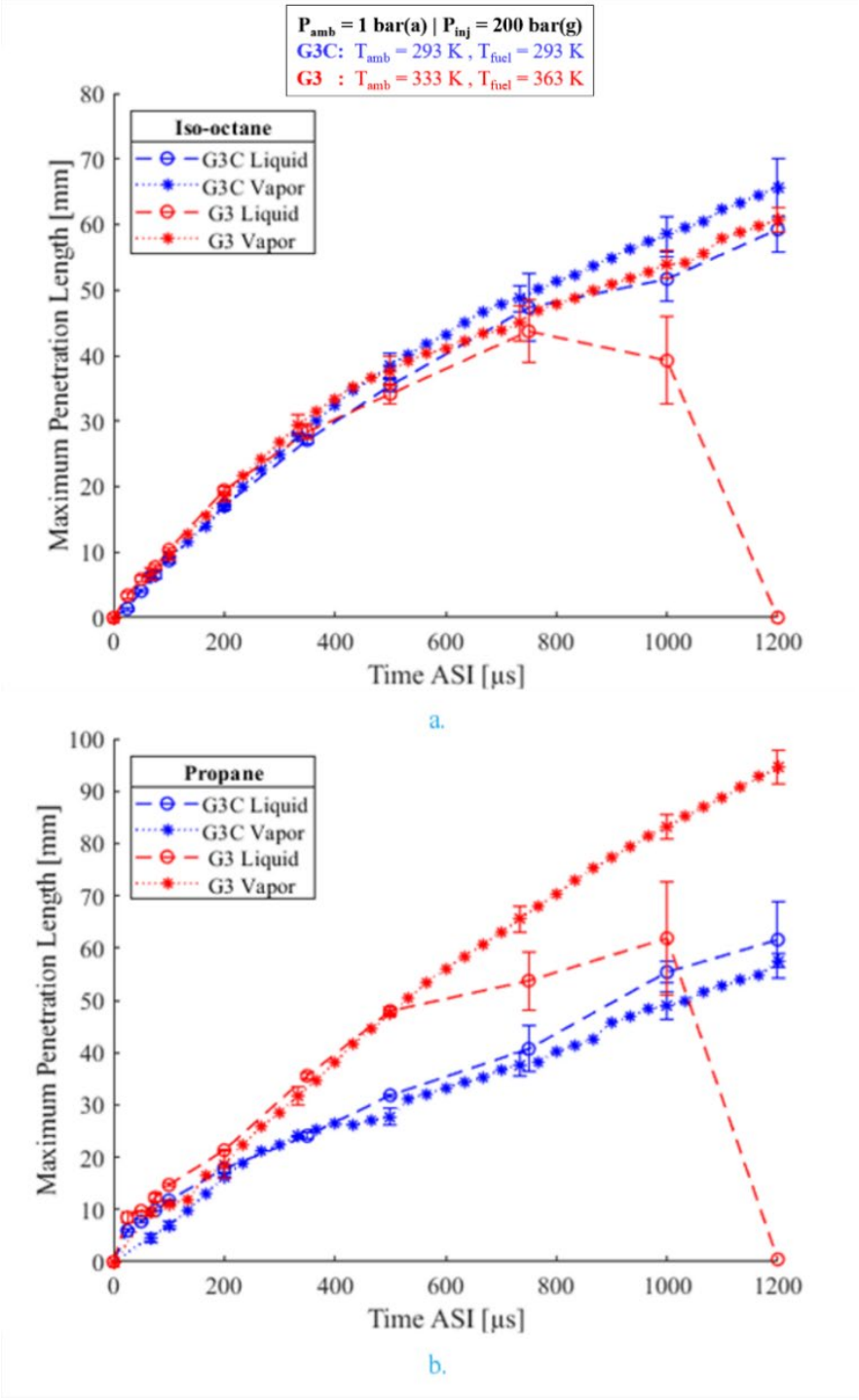

Figure 3.3-8: A comparison of maximum axial liquid vs. vapor penetration length for a) iso-octane, and b) propane at corresponding conditions and timesteps as a combined effort of high-speed Schlieren and planar Mie scattering imaging techniques. Error bars are included at suitable timestamps for improved legibility and comparison. The error ratios are same as observed in corresponding single phase experimental results.

3.4 Exploration of Injection Profiles and Strategies

Four injectors including the Bosch BMW 325i EU5, Delphi 7-hole stock injector, ECN Spray-G injector, and modified 5-hole Delphi injectors have been tested at various engine-like conditions and high-speed Schlieren and planar Mie imaging for propane and iso-octane fuels were carried out. The data was processed and sent to Argonne National Lab for model tuning and validation. To further analyze the performance of 5-hole injectors manufactured using different machining techniques, leak testing and injection rate testing were done for an array of engine relevant pressures. Leak and injection testing was done using high-speed Schlieren imaging to qualitative visualize the fuel leaks as shown in Table 3.4-1. It was found that Injector 2 from the first batch was the best performing injector with the lowest leak rates and highest injection fuel rate at 200 bar. Injector 2 was followed by injector 7 and 4 in terms of leak rates. Injector 3 from the new batch was getting stuck while injecting and no injection rate could be measured for it. For further testing in the Cummins X-15 engine, Injector 2, 7, and 4 were used.

Table 3.4-1: Leak rates, volumetric injection flow rates, and injection mass flow rates for various Delphi 5-hole injectors modified by Czero at relevant injection pressures.

Leak Rate (mL/sec)					
	INJ 2	INJ 7	INJ 3	INJ 4	INJ 8
Pressure (bar)	Best Performance and Used for Spray Testing	Second Best Injector	New (Gets Stuck Open)	New (Lowest Leak Rate Among the New Injectors)	New (Leaks More, Higher Fuel Injection Rate)
30	8.33E-05	1.17E-03	3.33E-03	2.50E-03	2.25E-02
60	1.17E-03	1.83E-03	6.00E-03	3.00E-03	3.50E-02
100	1.00E-03	1.83E-03	7.67E-03	1.83E-03	4.70E-02
130	8.33E-04	1.30E-03	8.00E-03	2.33E-03	4.92E-02
170	8.33E-04	1.17E-03	8.33E-03	3.00E-03	3.83E-02
200	6.67E-04	1.50E-03	8.50E-03	3.17E-03	3.58E-02
Injection Rate @ 1200 RPM (mL/s)					
150	18.67899425	17.09325402	Leaks (Sticks Open)	26.55405747	Not Tested
170	19.44527778	17.26170307	Leaks (Sticks Open)	26.47809579	25.53641762
200	26.74396169	15.1547567	Leaks (Sticks Open)	Not Tested	Not Tested
Injection Rate @ 1200 RPM (g/s)					
150	9.796011746	8.96438614	Leaks (Sticks Open)	13.9260099	Not Tested
170	10.26399542	9.111417346	Leaks (Sticks Open)	13.97619808	13.47914268
200	14.24436887	8.071726516	Leaks (Sticks Open)	Not Tested	Not Tested

Table 3.4-2: Test Matrix of Current Profile Optimization

Injector	Delphi 5-hole #2
Fuel	Propane
Injector Pressure	172 bar
Chamber Pressure	0.855 bar
Injection Duration	11 ms
Peak Current	10 A - 25 A
Hold Current	2 A - 15 A
Peak Duration	0 - 11 ms

To further analyze the performance of 5-hole injectors manufactured using different machining techniques, additional injection rate testing was done for an array of engine relevant conditions and timing to optimize the current profile and injection pressure. Table 3.4-2 contains the test matrix for the empirical testing for current profile optimization. As seen in Table 3.4-2, all parameters except the peak current, hold current and peak duration were held constant. Only one input of the current profile was varied at a time and the injection rates were measured at those conditions. First the peak current was optimized, then the hold current, and finally the peak duration of the current profile was optimized to maximize the injection rate of propane.

Figure 3.4-1 includes the injection rate measured at various current inputs. As seen in 1a, the maximum flow rate was achieved at peak current of 15 A. Figure 3.4-1b shows that flow rates saturate for hold currents greater than 3 A, with a maximum injection rate at 7 A. When these optimized peak and hold currents were used to measure the variability in the injection rate as a function of peak duration, as seen in Figure 3.4-1c, the variability was minimal, hence the 500 µs was considered as optimized peak duration.

A few other injectors: Bosch BMW 335 I injector, Bosch Jaguar Injector, and XDI +65 injector, were also tested along with the previously mentioned injectors and these injectors are shown in Figure 3.4-2. Injection testing was performed and a comparison of injection rate in grams per second are plotted in Figure 3.4-3.

As seen in the plot in Figure 3.4-3, the XDI injector outperformed all the other injectors and approximately had twice the injection rate compared to the second-best injector: Bosch BMW for pressures ranging from 100 to 240 bar. XDI injector, however, stops injecting for pressures higher than 240 bar. This maximum limit of injection is also seen for Delphi 5-hole injector, and Spray G injector where their injection rate drops after 200 bar and 250 bar, respectively. The best to worst performing injectors are: XDI, Bosch BMW, Delphi 5-hole, Bosch Jaguar, Spray G, and Delphi stock injectors.

High speed schlieren imaging was conducted for the XDI LT4 +65% injector. Two different orientations were considered to obtain a full profile of the spray for an updated injector model. The experiments were conducted at the same injection pressure of 172 bar as the chamber pressure was swept for each orientation. As the chamber pressure increased, the individual jets could be discerned between each other shown in both the 5 bar and 10 bar cases before the increased mass flow rate from the center nozzle causes all the individual jets to collapse into one plume.

High speed schlieren imaging was conducted for an OEM LT4 injector, which is the 6-hole injector on which the XDI LT4 +65% injector is based. Imaging of the OEM injector was performed to capture the influence of the 7th hole on the XDI +65% injector and to gain further insight into the individual cone angles for each nozzle to create an accurate 3-D CFD model to implement into simulations for both engine combustion and the high-pressure spray chamber. Displayed in Figure 3.4-4 are the experimental results from the high speed schlieren imaging. Snapshots at different time stamps are considered for two spray pattern orientations to the chamber window; in line with the imaging and rotated perpendicular to the imaging

path. The same orientations were used at each pressure condition. The experiments were conducted at an injection pressure of 172 bar, the same as used in the X15 test cell, and chamber pressure was swept from .85-10 bar. As the chamber pressure increased, the individual jets could be discerned in the spray pattern as shown in both the 5 bar and 10 bar cases before the individual jets collapse into one plume. For the OEM LT4 injector, the individual jets can be seen at 100 and 200 microseconds before the momentum causes collapses. Further analysis is required to implement these findings into the CONVERGE CFD simulations.

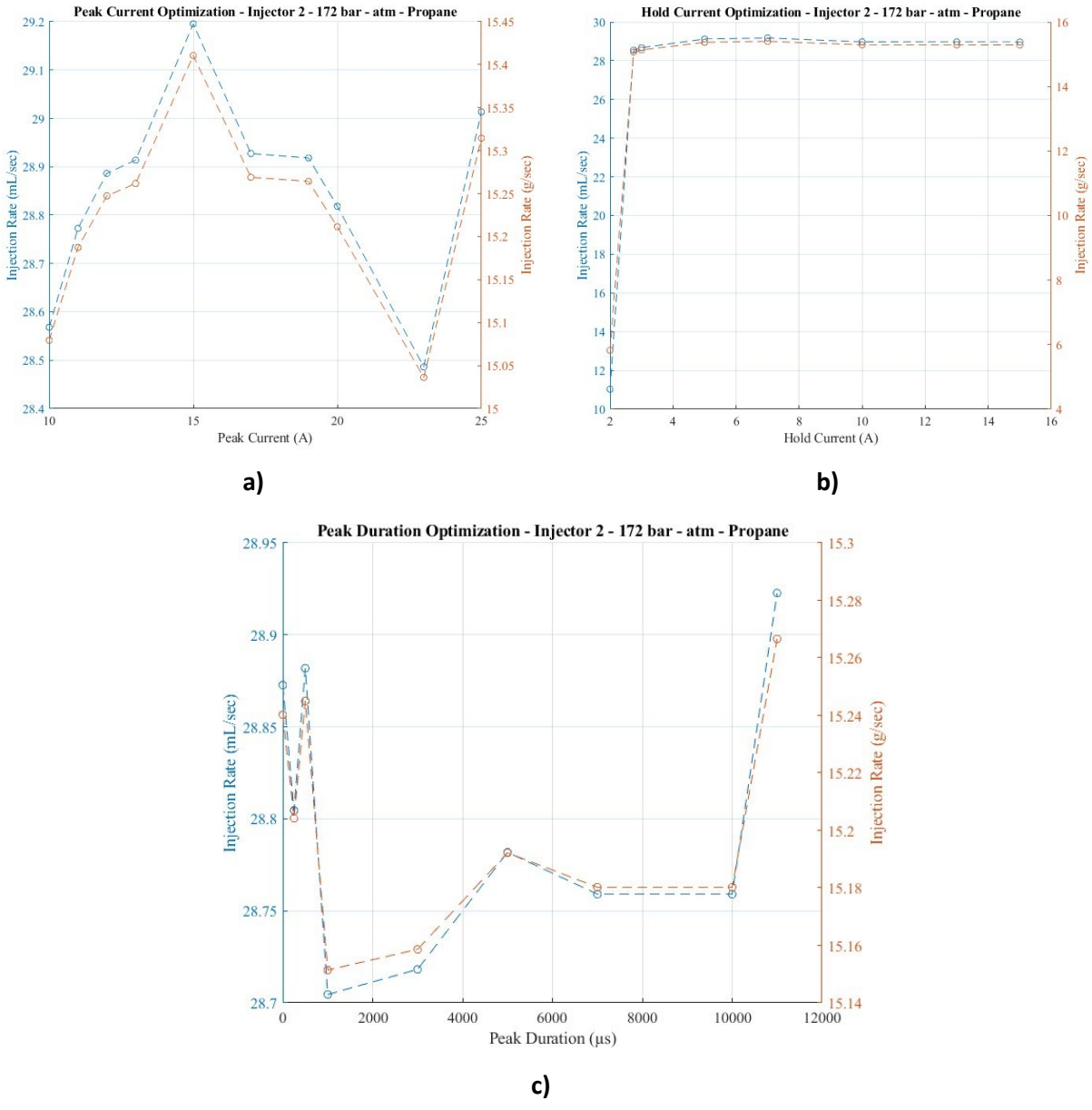

Figure 3.4-1: Injection rates of propane at various a) Peak current, b) Hold current, and c) Peak duration.

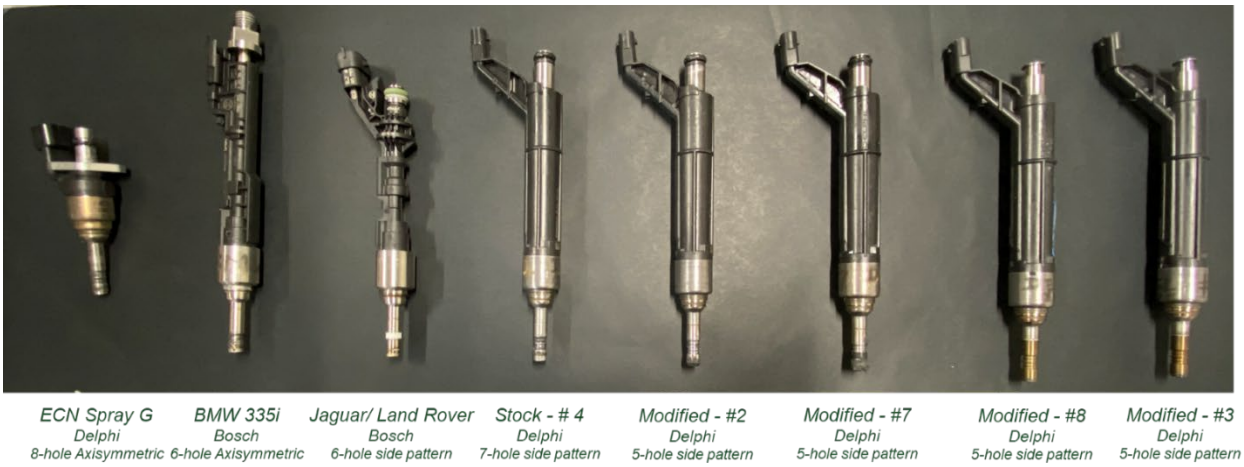

Figure 3.4-2: Various injectors, and their manufacturer and hole pattern, tested in the spray chamber for injection testing.

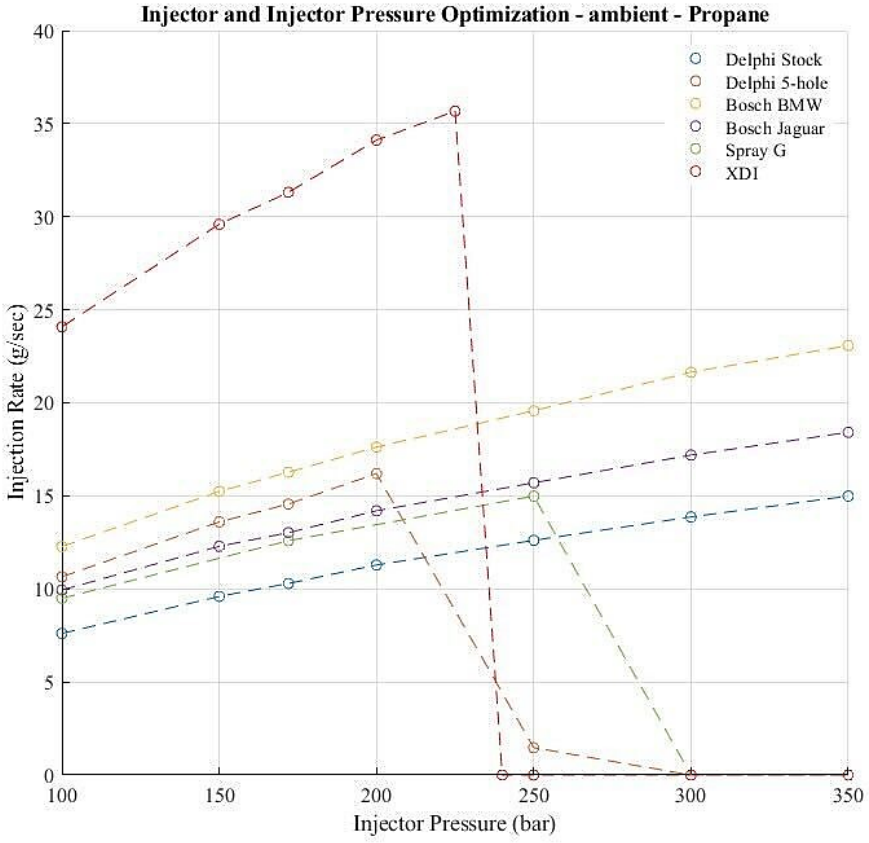

Figure 3.4-3: Injection rate as a function of injection pressure of Propane for various injectors at atmospheric conditions.

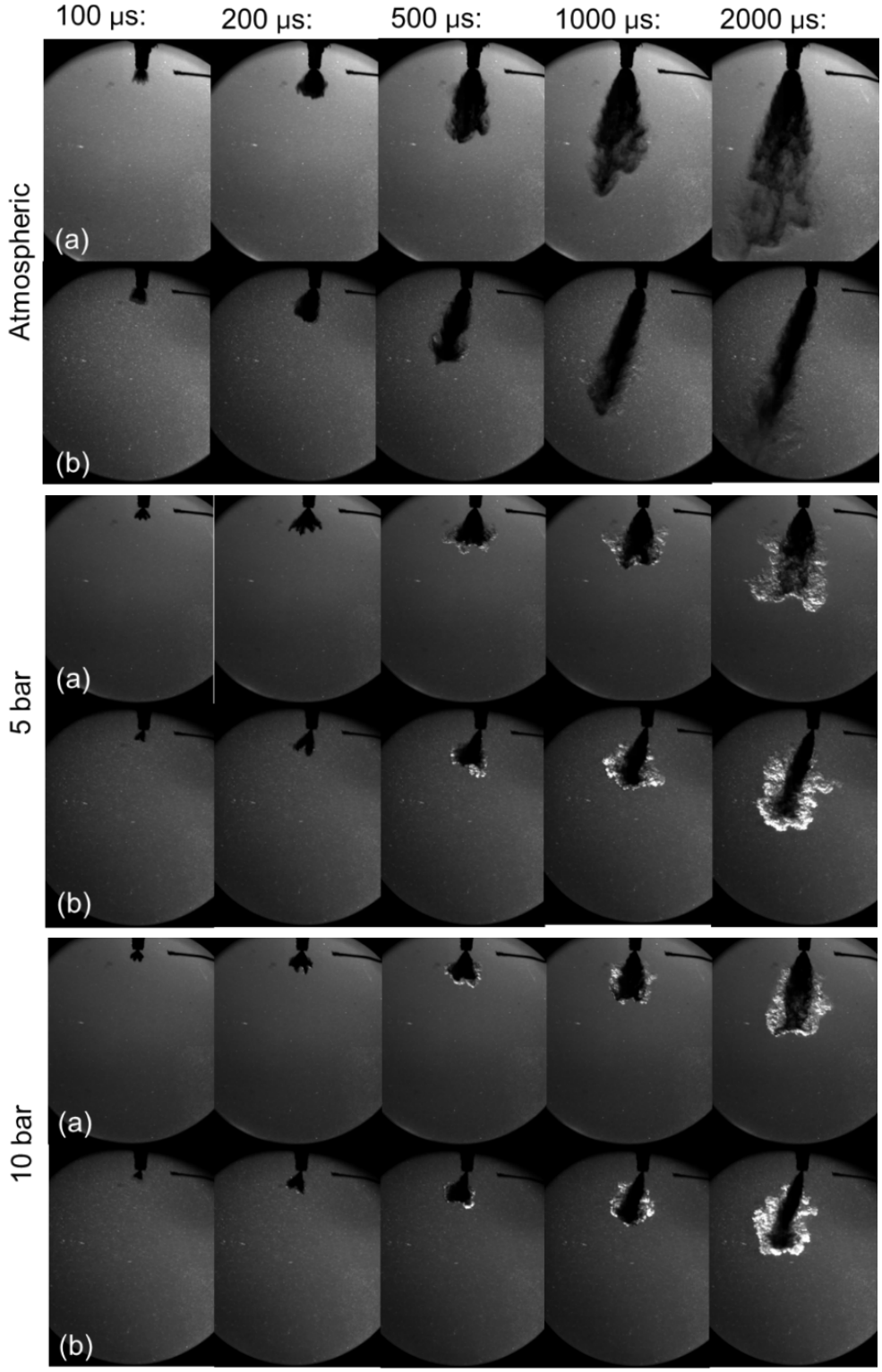

Figure 3.4-4: Snapshots over the initial 2000 µsec of schlieren imaging comparing penetration length and width for the OEM LT4 injector rotated (a) in line and (b) perpendicular to the imaging at atmospheric pressure (top) 5 bar (middle) and 10 bar (bottom)

4.0 Development of Fuel Injection Spray Model

This work carried out in this task aimed to develop and validate a comprehensive spray model, capable of simulating the behavior of LPG injection at realistic engine conditions to enable CFD simulations of advanced LPG fueling strategies. The model is based on the Lagrangian-Eulerian spray framework, because of its CPU affordability on engine-sized domains, and because of its robust coupling with complex moving geometries (e.g., piston) and with combustion dynamics.

The Lagrangian-Eulerian framework models the spray as a set of stochastic discrete parcels that are representative of liquid droplets and are tracked in the gas domain and coupled with the gas phase (which is described in a conventional finite-volume approach) through source terms. The coupling is two-way between the phases and strongly relies on semi-empirical submodels, which are developed for high-speed Diesel and Gasoline sprays, and assume incompressible and sub-cooled liquid. For this reason, its applicability to LPG injection requires extensive model adaptation and validation against experimental results.

The focus of this task is to modify and adapt the L-E modeling approach to LPG injection for realistic injectors at realistic engine conditions and to deliver a spray-model that can be imported in 3D engine CFD simulations to support the development of the advanced combustion strategies proposed by this project. Because of its extensive application to reacting spray and engine simulation, and because of the broad expertise of project team with the tools, we chose the commercial CFD software CONVERGE(-v3.0) to model the injection dynamics, and we validated its behavior against experimental measurements carried out in high-pressure spray chamber within the project.

4.1 Initial Spray Model Design

The spray model is developed taking advantage of the availability of the internal geometry of the injectors, which are used to define CFD models of the two-phase flow inside the injector and in the vicinity of the nozzle exit. This model, which is based on a volume of fluid (VoF) approach, is too expensive to be applied to full-size engine domains, because of the spatial and temporal scales to be resolved to characterize the two-phase flow dynamics. The model is based on a single-fluid multi-phase approach, in which the two-phases are tracked as species in the system. The phase-change dynamics are characterized with the homogeneous relaxation model (HRM), which determines mass transfer between the two species based on a characteristic time-scale that is a function of the super-heat degree of the fuel entering the system.
As visible from the graph in Figure 4.1-1, the high vapor pressure of propane, which is the predominant component of LPG and it is used as test fuel for the simulations, is always above the ambient pressure of the system, determining a condition of high-super degree.

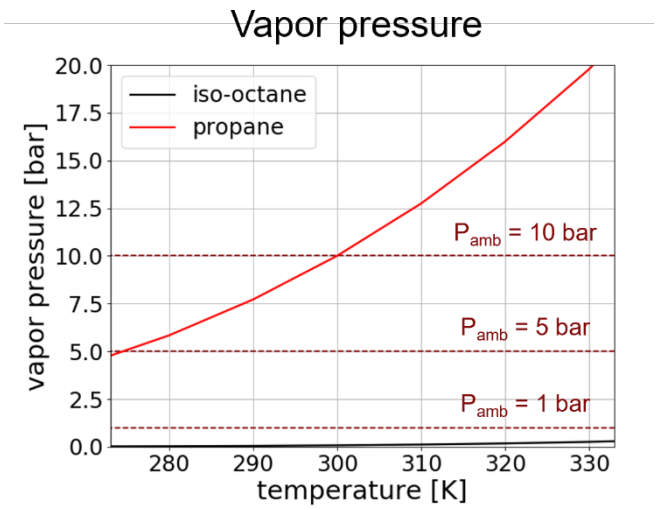

Figure 4.1-1: Graph showing the vapor pressure trends as a function of fuel temperature for propane and conventional iso-octane.

In this condition, fuel phase-change strongly affects the spray morphology in the vicinity of the nozzle, leading to under-expanded jet dynamics, which are shown in Figure 4.1-2 for a multi-hole injector.

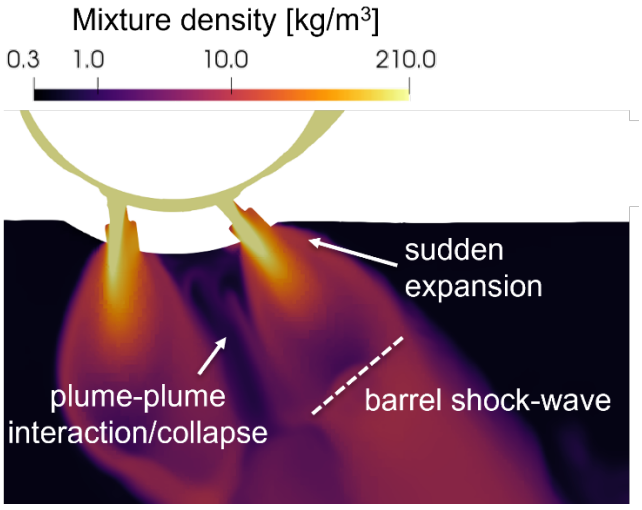

Figure 4.1-2: Characteristic dynamics of super-heated fuel injection in the vicinity of the nozzle exit.

The initial model development was carried out with Engine Combustion Network's (ECN) SprayG injector, which is an 8-hole axi-symmetric injector derived from direct gasoline injection applications, which is operated with a maximum injection pressure P_{inj}=200 bar. The injector has been installed in the HPSC and operated with iso-octane and pure propane, assessing the influence of P_{inj}, P_{amb}, and T_{fuel} on the spray morphology. This choice is motivated by the large availability of experimental data on this injector, which has been also extensively characterized numerically.

High-fidelity VoF nozzle flow simulations have been carried out matching the experimental measurements, showcasing a strong response of the model to the operating conditions. Figure 4.1-3 reports a summary of the results, for injection in constant volume chamber.

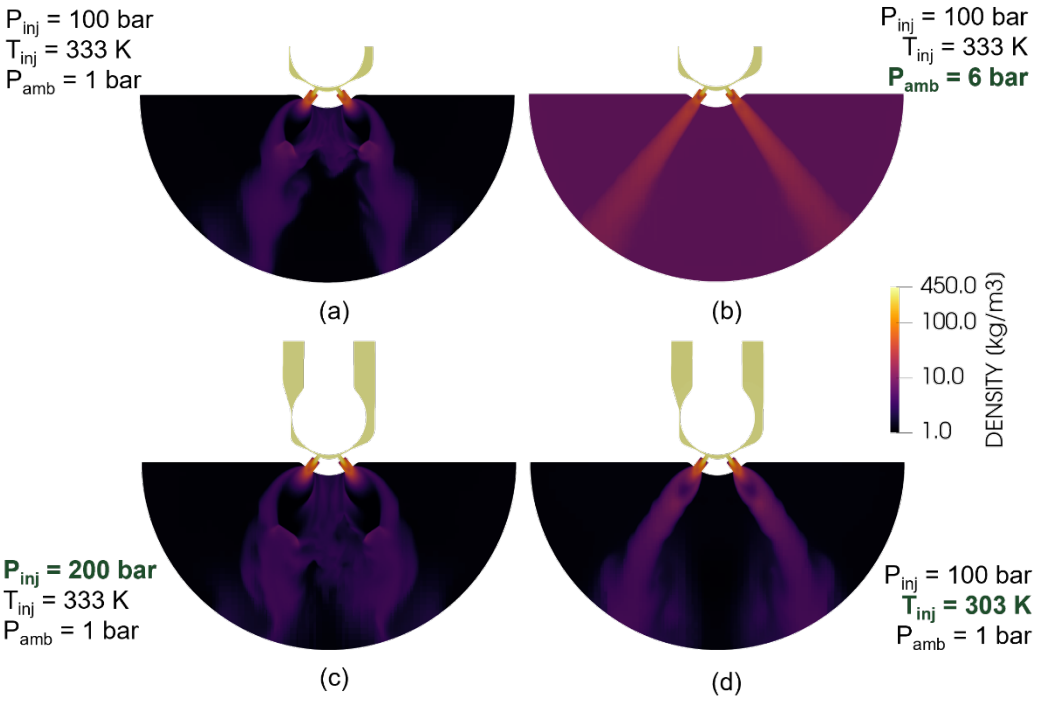

Figure 4.1-3: Mixture density profiles at the centerline slice of quasi-state solution of the injection of propane in constant volume chamber, changing operating conditions.

Figure 4.1-3a shows barrel shocks and strong plume interactions in the vicinity of the nozzle tips. The axi-symmetric structure of the injector generates a collapse of the single spray plumes towards the axial direction and a strong vaporization of the liquid fuel. Increasing the ambient pressure (Figure 4.1-3b) reduces the super-heat degree of the fuel, generating a conventional spray structure, in which the single plumes are injected in a direction that is consistent with the nozzle geometrical axes. When increasing injection pressure and maintaining low ambient pressure (Figure 4.1-3c), the dynamics of under-expanded jets are still visible, and the location of the barrel shocks are shifted downstream because of the faster injection velocity. Decreasing the injection temperature also reduces the phase-change propensity of the fuel, which results in more concentrated plumes with negligible interaction, as shown in Figure 4.1-3d.

An extensive campaign has been performed to capture initial spray trends in terms of spray direction, cone angles and plume temperature to initialize the Lagrangian-Eulerian spray model. The target of initial model development has been set to ECN's G3 (P_{inj}=200bar, P_{amb}=1bar, T_{fuel}=363K, T_{amb}=333K) and G3-cold (P_{inj}=200bar, P_{amb}=1bar, T_{fuel}=293K, T_{amb}=333K), as they were found to be the most sensitive conditions to tune injection and semi-empirical Lagrangian models to match the experimental results. This initial campaign explored the effect of: (i) cone angle, (ii) inclusion angle, (iii) flash-boiling phase-change modeling, and (iv) aerodynamic breakup

modeling, obtaining the following major results: (i) large cone angles (>40°) can reproduce the initial jet lateral expansion and mimic the flashing fuel dynamics. (ii) stronger super-heat degrees generate stronger collapse, and this can be simulated by reducing the plume inclusion angle to 30°. (iii) additional flash-boiling-based phase-change models are not applicable to extremely super-heated fuels such as propane, and they are too disruptive for the spray morphology and not responsive to small changes in the operating conditions of the system. (iv) adapting aerodynamic breakup (KH-RT) parameters is key to represent the effect of flash boiling on the atomization and vaporization of the fuel. Specifically, the focus is set to the RT part of the KH-RT framework, using different time and size constants, which are modified according to the super-heat degree of the injected fuel. For $P_{amb}/P_{sat} < 0.3$ (corresponding to flash-boiling conditions), we set the time constant to 0.1 and the size constant to 0.25, while for subcooled or moderate flashing fuel, we set the time constant to 1.0 and the size constant to 0.6. Figure 4.1-4 reports images of the fuel vapor morphology both from experimental Schlieren images and from CFD results, which are processed integrating the vapor phase density gradient along the line of sight, to mimic the Schlieren phenomenon. The CFD model is capable of representing the response of the spray to the operating conditions, here reported for SprayG injector at flare and moderate flash-boiling.

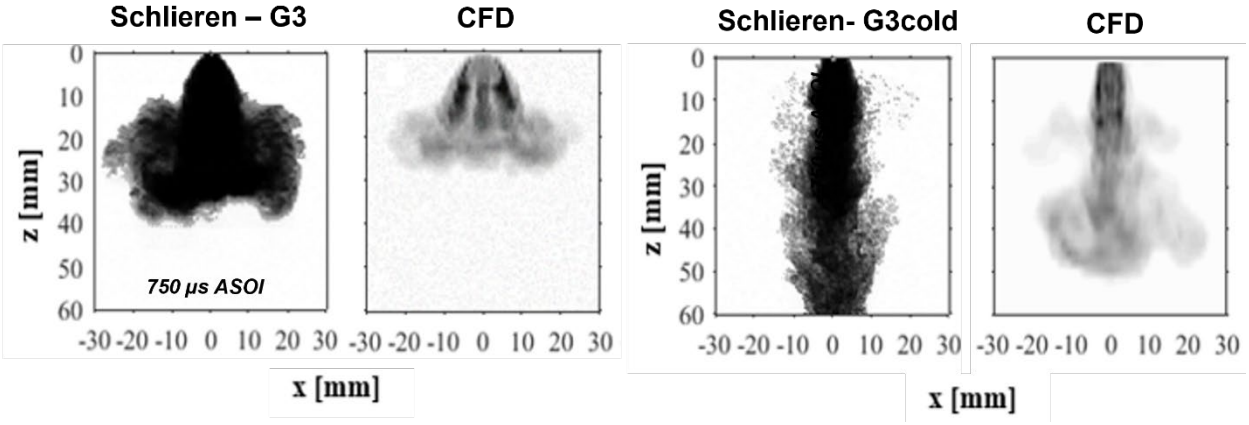

Figure 4.1-4: Validation of the CFD spray model in constant volume chamber in terms of vapor fuel morphology. Experiments and simulations are performed with ECN's SprayG injector at G3 (left) and G3-cold (right) conditions.

This simulation effort represents the baseline model to be applied to injectors that are relevant to the project and that have been measured experimentally and then applied to the engine platform.

4.2 Run Matching HPSC Cases and Compare with Experiment

During the project, multiple injectors have been proposed, designed, and tested to match the fuel delivery requests and the spray simulation effort adapted the modeling strategy developed in Task 4.1 to obtain Lagrangian spray CFD models capable of reproducing the behavior of the

proposed multi-hole injector at realistic conditions. Figure 4.2-1 shows the injectors that have been characterized experimentally and numerically during the project.
The simulation framework is based on preliminary high-fidelity VoF simulation of the multi-phase flow inside and in the vicinity of the injector exit, and on the definition of effective Lagrangian-Eulerian spray models.

We reproduced with good accuracy the morphology of the spray behavior in constant-volume chamber, as reported in Figure 4.2-2, where the simulation of the 7-hole injector, with the 'mid' nozzle diameter has been compared with experimental Schlieren images. The plume collapse is obtained in strongly flashing conditions, at the temporal evolution of the spray is reproduced.

The setup developed in Task 4.1 has proven to be accurate and responsive to different injectors and a broad range of realistic operating conditions, reported in Table 4.2-1, and therefore has used to refine final spray model recipe for the selected injector to move forward in the engine, the 5-hole optimal injector developed by Czero.

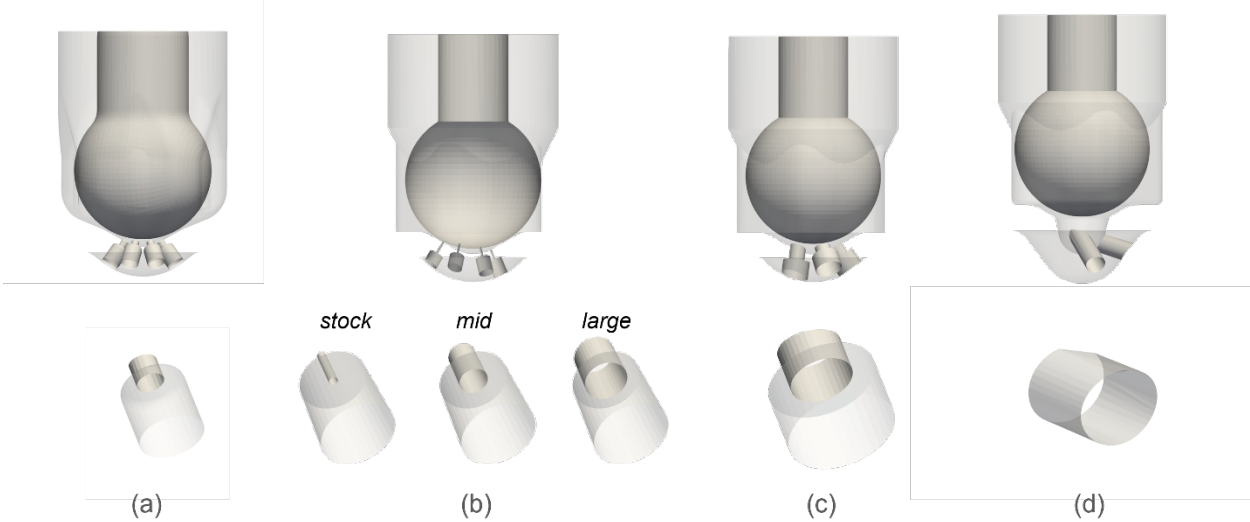

Figure 4.2-1: Images of the internal nozzle geometry and of the single orifice characteristics of the injectors measured and modeled in the project. a) ECN's SprayG, b) stock 7-hole injector with 3 different nozzle variations, c) optimal 5-hole injector, and d) prototype of 3-hole injector.

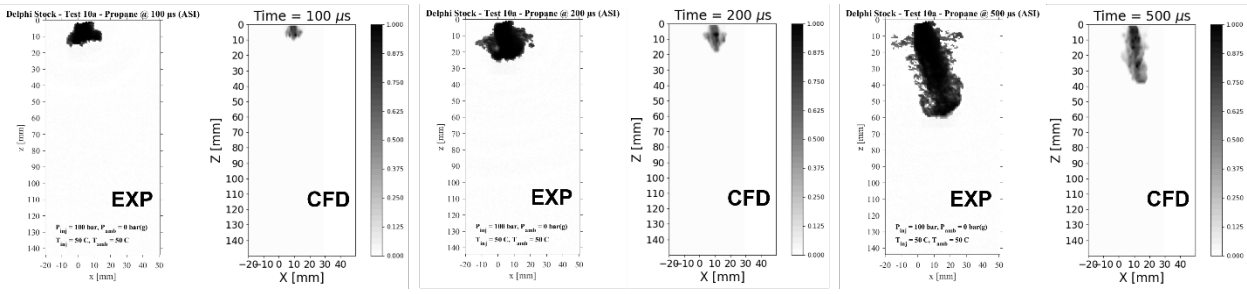

Figure 4.2-2: Temporal evolution of the spray vapor during one injection event in constant volume chamber. Operating conditions: P_{inj}=100bar, T_{fuel}=323K, P_{amb}=0.852bar, T_{amb}=323, fuel=propane.

Table 4.2-1: Summary of operating conditions tested and validated during the spray model development.

Operating condition	#1	#2	#3	#4	#5	#6	#7	#8
$T_{inj}(K)$	293	363	293	363	293	363	293	363
$P_{amb}(bar)$	0.5	0.5	6.852	6.852	3.852	3.852	10.852	10.852
$T_{amb}(K)$	293	363	293	363	293	363	293	363
SH degree	0.06	0.01	0.89	0.20	0.50	0.11	1.41	0.31

4.3 Refine Model to Match Experimental Data

The extensive validation against experimental data collected within the project for the 5-hole injector has been carried out, focusing on matching fuel vapor penetration against measured Schlieren profiles, to provide an accurate model to be exported to engine simulations.

The previously developed setup, involving large cone angles (>40°), inclusion angles shifted toward the average axis of the multi-hole injector by 5°, and adapting aerodynamic breakup constant to the super-heat degree condition, proved to be well capable of capturing the penetration trends, as reported in Figure 4.3-1 for a broad range of operating conditions. Specifically, Figure 4.3-1a reports a flare flashing conditions – condition #1 from Table 4.2-1, Figure 4.3-1b reports a slightly super-heated injection – condition #3 in Table 4.2-1, and a fully subcooled condition – condition #7 – is shown in Figure 4.3-1c.

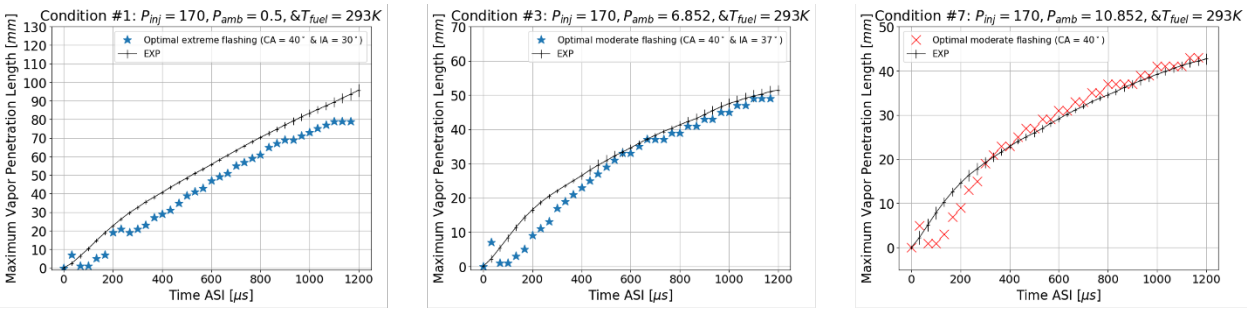

Figure 4.3-1: Vapor penetration profiles for the optimized 5-hole injector developed during the project.

The model has been transferred to the engine DI simulation task as a spray.in dictionary which is compatible with reacting simulation and can be easily modified to test multiple injector configurations in terms of injector location, orientation and start-of-injection timings.

The finale 3-hole injector design has been analyzed in its internal and near-nozzle operation and it has shown consistent behavior with the 5-hole injector in terms of plume development. The simulated mass flow rate is consistent with the 5-hole injector, enabling the fueling strategy envisioned for optimal operation of the engine.

5.0 Design of Advanced Combustion Strategy

5.1 Converge CFD Modeling of Cummins X15 SCE

The key objectives of Combustion CFD Modeling of X15 SCE are stated below

1. Spray Optimization
    a. The LPG spray pattern optimization is aimed at improving the mixture-homogeneity, improving the turbulent kinetic energy at TDC and reducing any wall impingement. The models developed by ANL using the constant volume chamber data will be used here on the X15 SCE model for analyzing the spray quality
2. Baseline Engine model calibration
    a. The combustion CFD model with PFI-LPG X15 SCE test data. The calibration will be targeting to predict the combustion efficiency, GITE, knock limit at a high load operating condition, which will be further optimized using a DI-LPG system.
3. Optimization of DI-LPG SCE
    a. The optimization analysis would look at changing the compression ratio, Swirl ratio, bowl shape and EGR fractions to improve the GITE and make hardware recommendations.
4. Wall heat transfer predictions
    a. The primary aim of wall heat transfer prediction using X15 combustion CFD analysis is to predict any structural concerns on the new head designed for the LPG system. This will be performed using a previously calibrated Natural Gas SCE high load CFD model
    b. The predicted wall temperatures will also be useful for LPG combustion optimization analysis. Hot spots on the walls often results in auto-ignition of unburned mixture adjacent to the walls. To predict the engine knock (EGAI) accurately, it is vital to predict the combustion wall temperature closer to the reality.

Spray Optimization

The operation of modern on-road stoichiometric SI engine requires effective fuel air mixing for uniform mixture upon combustion. The mixture homogeneity is quantified using a parameter named equivalence ratio standard deviation (PHI-StdDev). In this study, the injection parameters and spray pattern are optimized for: a) (primarily) low PHI-StdDev, and b) (secondarily) conserve swirl and tke.

The baseline injector specifications are listed in Table 5.1-1 and baseline injector spray pattern is as shown in Figure 5.1-1.

A one-factor variation study was performed for start of injection (SOI), and injection duration. For the start of injection, the SOI was varied as -300 aTDC, -320 aTDC and -340 aTDC. The SOI

Table 5.1-1: Baseline Injector Specifications.

Baseline Injector Specifications	
# Holes	5
Hole Exit Diameter (µm)	584
Flow Rates (mg/ms)	11.3
Injection Pressure (bar)	150

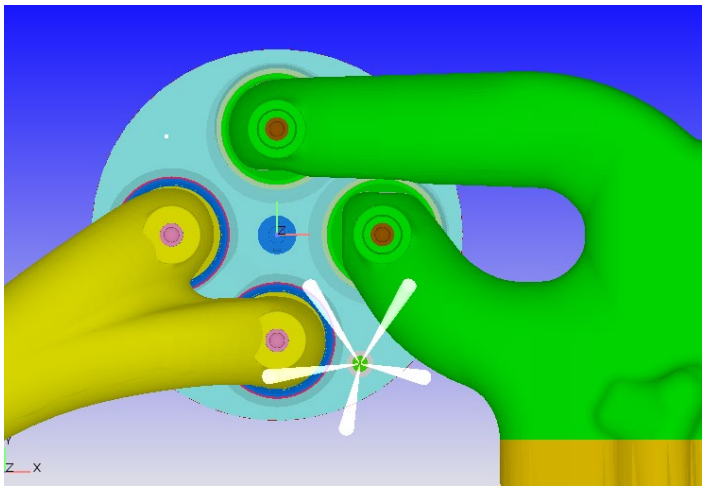

Figure 5.1-1: Top view of Cylinder#6, Intake (R) and Exhaust (L) sides and injector placement and spray pattern of baseline injector.

The engine details and operating condition for the injector performance CFD analysis is provided in Table 5.1-2.

Table 5.1-2: Engine details and Operating Conditions for injector performance optimization.

Engine Details and Operating Conditions	
Bore (mm)	137
Stroke (mm)	169
Swirl Ratio (-)	1.1
IVC (aTDC)	-149
EVO (aTDC)	+153
Speed (rpm)	1196
Injection Quantity	286 mg
Lambda (-)	1
Fuel	Liquid Propane

could not be advanced further as the exhaust valve closes at -340 aTDC. The injection duration was fixed at 180 degree crank angles to inject 286 mg fuel, which corresponds to a GMEP target of 21 bar. For comparison, PHI-StdDev is compared at -20 aTDC for each SOI from the analysis. It can be observed that, retarding the SOI to -300 aTDC increases the PHI-StdDev significantly. Although the flash boiling of propane spray evaporates faster, the mixture does not get sufficient time to mix in the cylinder when the SOI is late. As a result, the PHI-StdDev result in a higher value when injection is retarded. An SOI of -340 aTDC is ideal to improve the mixture homogeneity.

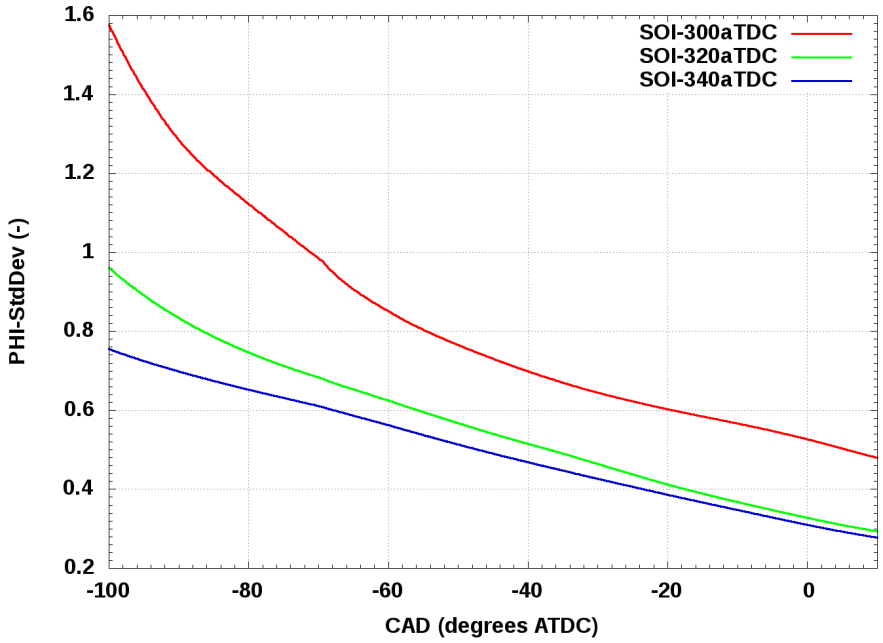

Figure 5.1-2: Crank angle evolution of in-cylinder PHI-StdDev with different SOI timings.

The injection duration sweep consisted of durations of 180, 160 and 140 degrees. With the maximum flow rate achievable with the baseline injector being tested, the injection of 286 mg propane requires 182 degree of injection duration at the tested operation point. This analysis provides a “what-if” evaluation assuming faster injection was achievable. The injector pattern is kept same as baseline and SOI is kept at -340 aTDC. A shorter duration of injection to inject the same quantity is shown to have a better homogeneity in the mixture at close to firing TDC. The shorter injection duration mainly results in faster injection velocities, which helps to spread the fuel vapors to farther regions in the cylinder. It also results in longer residence time for fuel vapors to mix with the charge air. Shorter injection duration is preferable to optimize the injection performance.

The spray patter optimization was performed with intake manifold pressure of 1.2 bar, corresponding to medium load engine operation. Stoichiometric operation requires 203 mg fuel per cycle. With the existing injector flow rate capacity, the injection has 128 degree crank angle of duration at 1200 rpm.

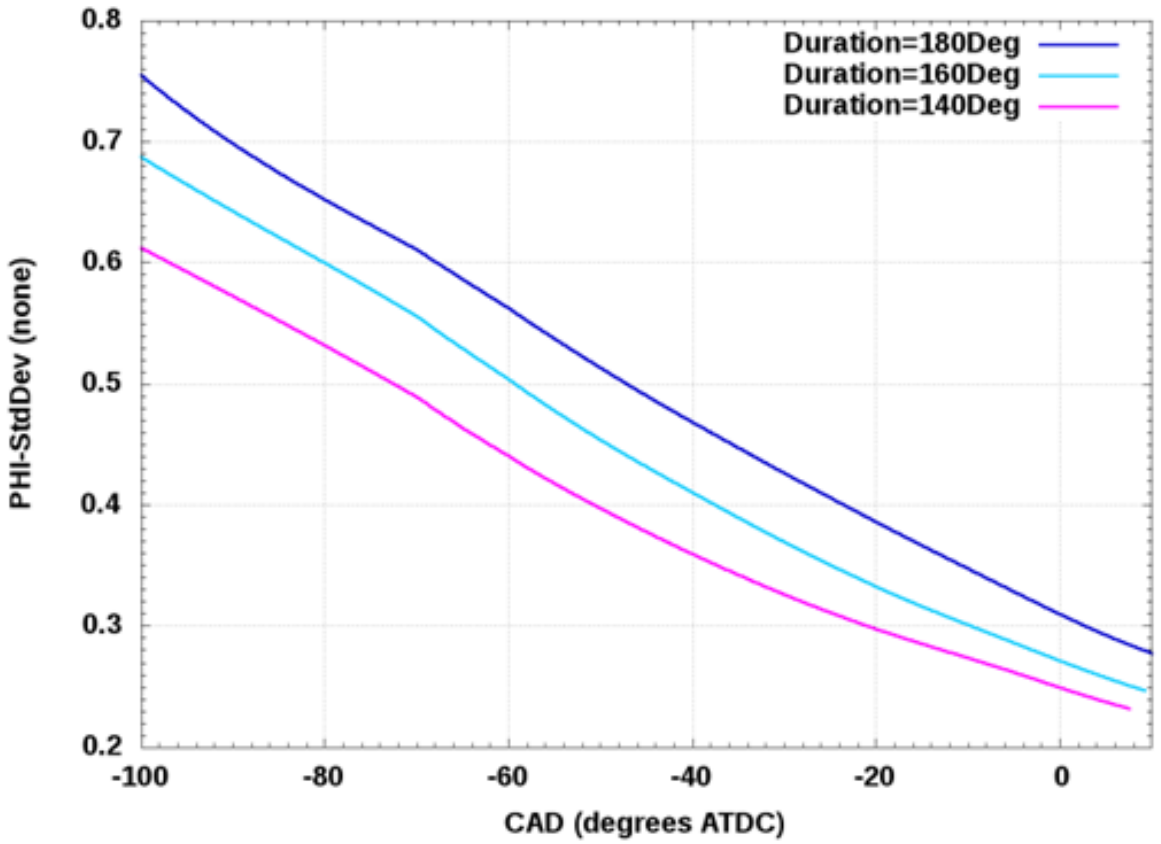

Figure 5.1-3: Crank angle evolution of in-cylinder PHI-StdDev with different injection durations.

With a trial of 1 to 5-hole designs, the analyst quickly limited the scope to 3-hole designs. 3-hole designs strike a good balance between fuel spreading and spray penetration. With more than 3 holes, the spray momentum of a single jet is not strong enough to deliver fuel to places far away from the injector. With less than 3 holes, the fuel is spread to less directions. 3-hole designs avoid significant drawbacks in both aspects and is believed to be appropriate at both high load and low load conditions.

Around twenty 3-hole designs are generated and tested. Four 3-hole designs were selected to continue testing. As shown in Figure , the four design candidates are revision 4, 12, 15, and 17. The four designs fall into two concepts. Revisions 4 and 12 have two lateral jets and one downward jet, while revisions 15 and 17 have two downward jets and one lateral jet. The one-downward concept is good at keeping the jets separated under a wider range of conditions, while the two-downward concept enables more effective fuel delivery to the lower part of the combustion chamber.

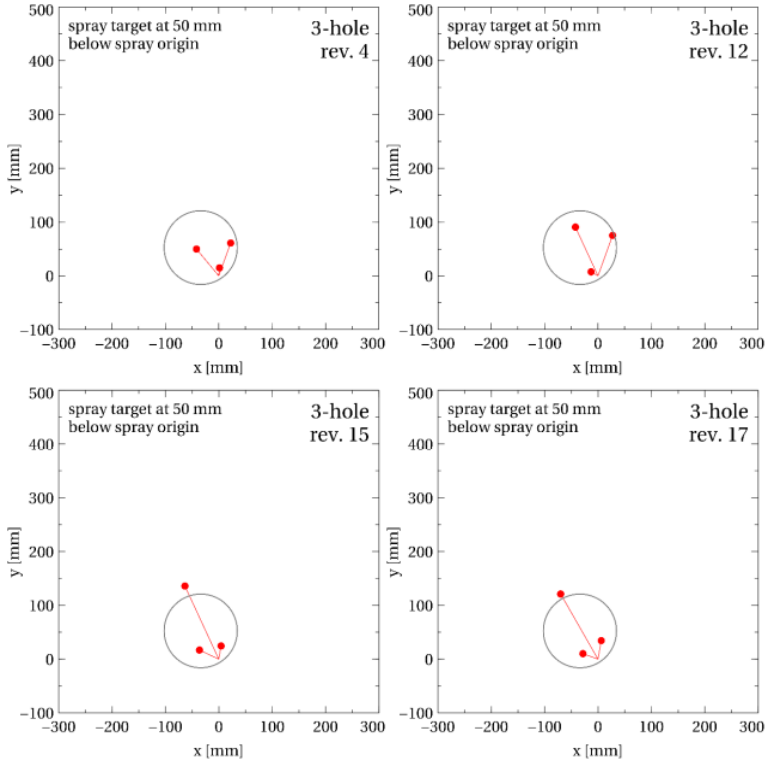

Figure 5.1-4: Four good performing 3-hole spray pattern design candidates.

To make the final selection out of the four design candidates, more operation conditions must be considered. The optimal final design could deliver good performance with different injector flow rates. It should also be accounted for that the initial liquid parcel temperature and droplet flashing breakup parameters might be inaccurate. Seven additional cases were created to find the best overall design that is also robust to variabilities. The variation of the cases is presented in Table . The cases are designed to pose vastly different impedance to the spray traveling and fuel distribution.

Table 5.1-3: Engine operation conditions used for final design selection.

Case	Speed (rpm)	Intake Pressure (bar)	Injection Rate	Flashing Breakup Parameters	Liquid Temperature (oC)
0	1200	1.2	Default	“extreme”	50
1	1200	2.2	2x	“extreme”	50
2	1200	2.2	2x	“moderate”	50
3	1200	0.5	Default	“extreme”	50
4	1200	0.5	2x	“moderate”	50
5	1200	1.2	Default	“extreme”	65
6	1200	2.2	2x	“extreme”	65
7	1200	2.2	1.5x	“moderate”	65

The performance (PHI-StdDev) of the four design candidates under the eight operation conditions is summarized in **Error! Reference source not found.**. The 3-hole revision 15 is the clear winner in four out of the eight cases. Cases 3 and 4 are where the revision 15 suffers most. Cases 3 and 4 have intake manifold pressure of only 0.5 bar, corresponding to a low load operation condition. Based on experience, 0.5 bar is only about 10 kPa higher (if at all) than the intake pressure needed to maintain SI engine idling at 1200 rpm. Such operation is not knock-limited. And DI does not provide significant benefit over PFI at this level of load. In fact, PFI is preferred at this load level for better mixing, and reduced use of throttling. Given that the current exploratory study does not need to provide overwhelmingly convincing justification for including both PFI and DI, it would not be a significant concern that revision 15 does not perform well in case 3 and 4.

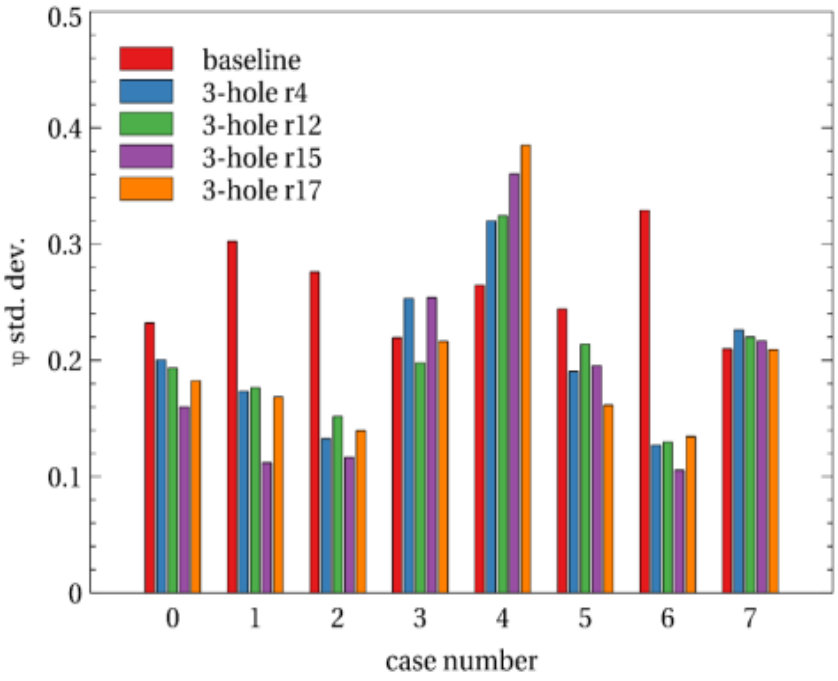

Figure 5.1-5: Local equivalence ratio standard deviation of the baseline and four design candidates under eight operation conditions.

Another benefit of revision 15 is, as shown in Figure , the avoidance of the liner impingement. Liner impingement is known to be responsible for symptoms like oil dilution, high PM and HC emissions, premature engine wear, etc.

The 3-hole spray pattern revision 15 can be defined in the coordinate system of the cylinder. As shown in Figure 5.2-1, the x+ points to the intake side, the z+ points to the upward direction and is parallel with the cylinder axis (not necessarily parallel with the injector axis). In such a coordinate system, the direction vectors of the three jets are listed in Table 5.1-3.

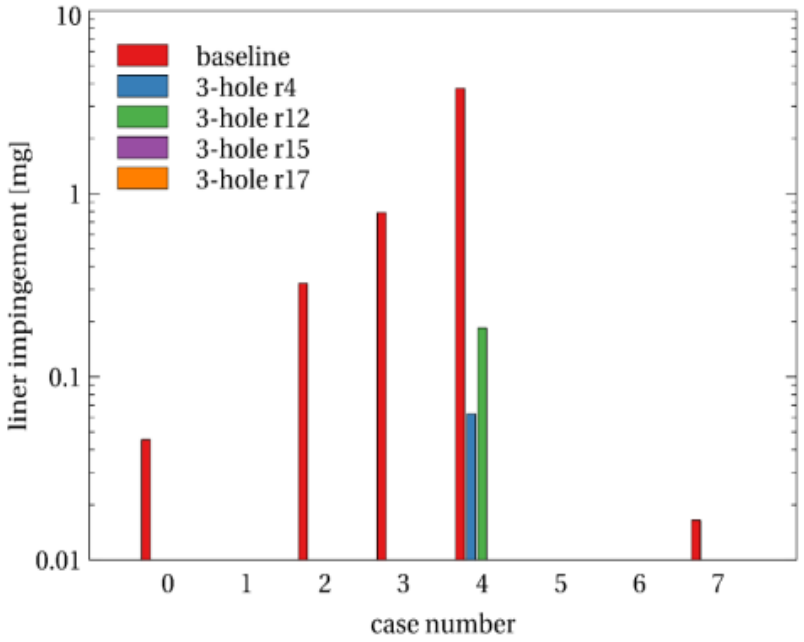

Figure 5.1-6: Liner impingement of the baseline and four design candidates under eight operation conditions.

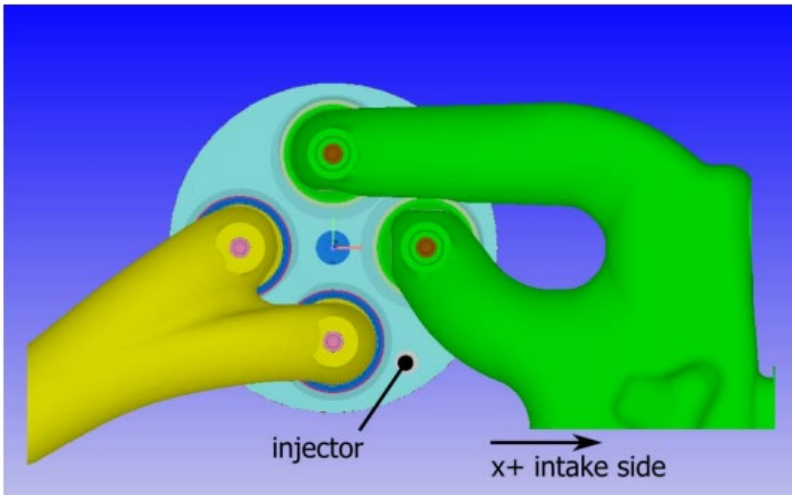

Figure 5.2-1: Injector in engine cylinder coordinate system.

Table 5.1-3: Direction vectors of the three jets in 3-hole revision 15.

	x	y	z
Nozzle 1	0.077658277	0.440419489	-0.894427116
Nozzle 2	-0.400929983	0.859799305	-0.316228247
Nozzle 3	-0.566165702	0.264008572	-0.780868665

Due to manufacturability issue, the 3-hole revision 15 design cannot be directly used. Czero altered the 3-hole revision 15 design and provided a manufacturable 3-hole design. Combustion CFD was performed to evaluate the performance of Czero's design. Czero's deign of the 3-hole injector enjoys significant improvement of mixing over the 5-hole baseline, but is still not as good as the 3-hole revision 15. 3-hole r15 only has marginal efficiency advantage over Czero's design. Both 3-hole injectors enjoy about 2 points of efficiency advantage over the 5-hole baseline injector. Base on the result, Czero's design is selected as the prime path design.

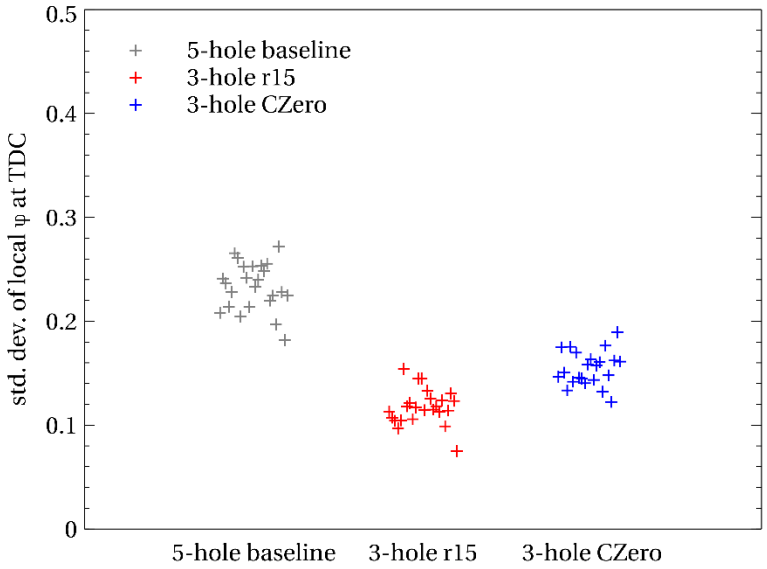

Figure 5.1-2: PHI-StdDev of the three spray patterns.

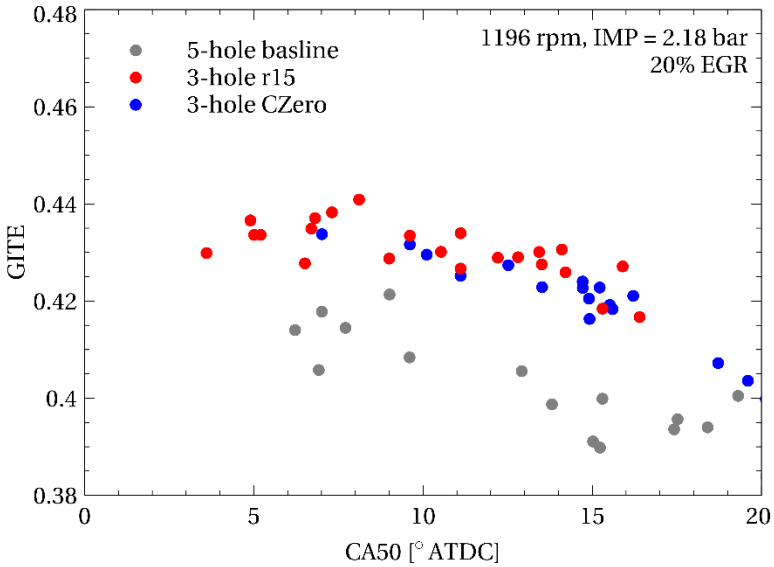

Figure 5.1-3: GITE as a function of CA50 with the three spray patterns.

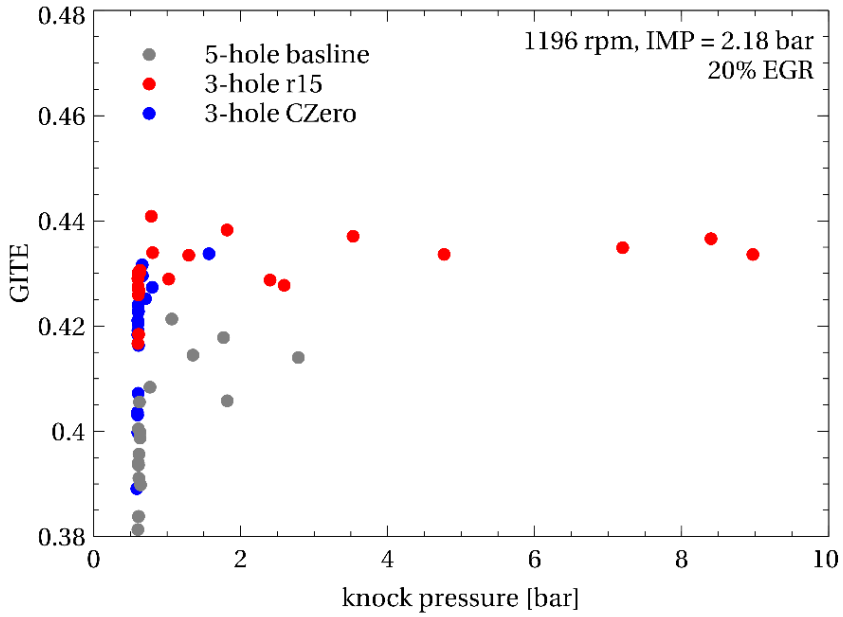

Figure 5.1-4: Knock-limited GITE with the three spray patterns.

Baseline engine model calibration

The combustion CFD calibration is initially done for a PFI case. The operation condition of the case is presented in Table 4. The condition has about 10.4 bar nominal GIMEP at 1200 rpm, corresponding to the medium load operation of a turbocharged engine. With the low compression ratio (9.3), medium load level around 10.4 bar, and propane fuel, the operation is expected to be slightly (if at all) knock limited. At this condition, the intake pressure and exhaust pressure are close to atmospheric pressure. The turbo charger is not actively creating boost. The charge enters the intake manifold at 318.5 K, a temperature easy to achieve under all reasonable boost conditions with a typical charge air cooler.

The CFD simulation domain includes a single cylinder, intake and exhaust ports, and part of the intake and exhaust manifold adjacent to the cylinder. In the simulation, the stoichiometric charge

Table 4.1-5: Engine operation conditions of the PFI calibration case.

PFI calibration case operating conditions	
Speed (rpm)	1200
Intake manifold pressure (kPa)	96
Intake manifold temperature (K)	318.5
Exhaust manifold pressure (kPa)	100
Nominal GIMEP (bar)	10.4 (fluctuation allowed with fixed intake manifold pressure)
Lambda (-)	1.0
Fuel	propane vapor

is assumed to be perfectly mixed upon entering the intake manifold. Each simulation covers three full consecutive cycles, as well as the exhaust stroke immediately prior to the first full cycle. Due to the inclusion of the extra exhaust stroke, as well as the premixed inlet assumption, the charge condition of the first full cycle is accurately estimated. Hence the data from the first full cycle does not need to be discarded. Spark timing sweep is also executed to cover a range of CA50. Considering that accurate modeling of spark plug operation provides almost no practical benefit (due to spark plug clock angle control, spark plug wear, manufacturing variability, etc.), it is allowed that the spark timing for a certain CA50 is different between simulation and experiment. The timing of a simulated cycle is only characterized by CA50, but not with spark timing. The spark timing is swept only to cover a range of CA50. The spark timing sweep includes four spark timings separated by 3 crank angle degree intervals. In total, the calibration case includes data from twelve simulated cycles (four spark timings by three consecutive cycles). Among the twelve cycles, the fuel mass, GIMEP, GITE, etc. are allowed to fluctuate.

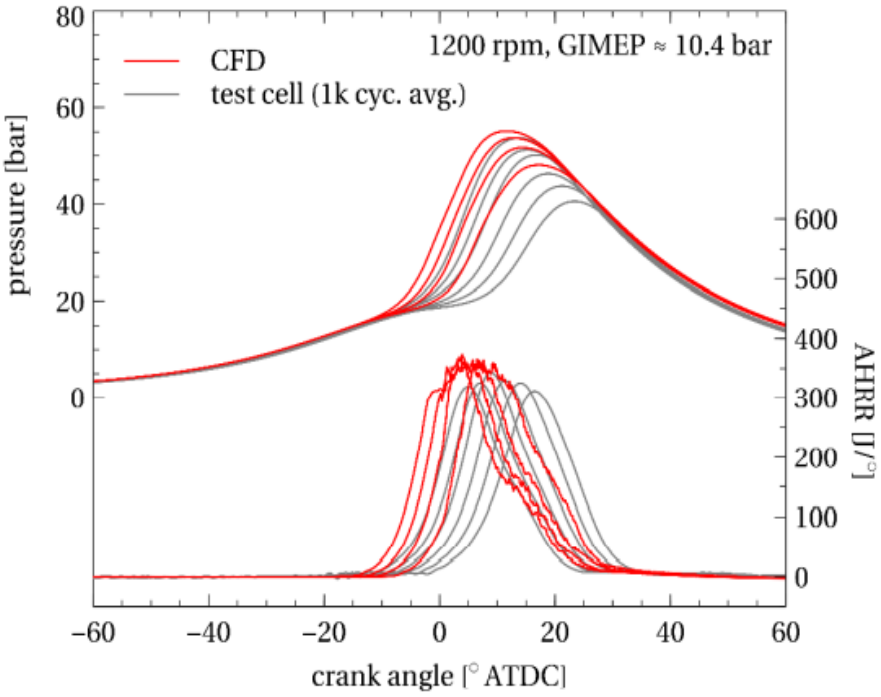

Figure 5.1-5: Cylinder pressure and AHRR prediction compared with experiment. The CFD curves are from the first cycles of the spark timing sweep. The test cell curves are from 1000 cycle averages with six different spark timings.

Figure 5.1-5 shows the comparison between CFD and experiments. Each of the experiment curves is an average of 1000 cycles. Both cylinder pressure and AHRR match reasonably well given that the CA50 is similar. The comparison using individual cycle data in both CFD and experiment, as shown in Figure 5.1-6, confirms the accuracy of the combustion simulation.

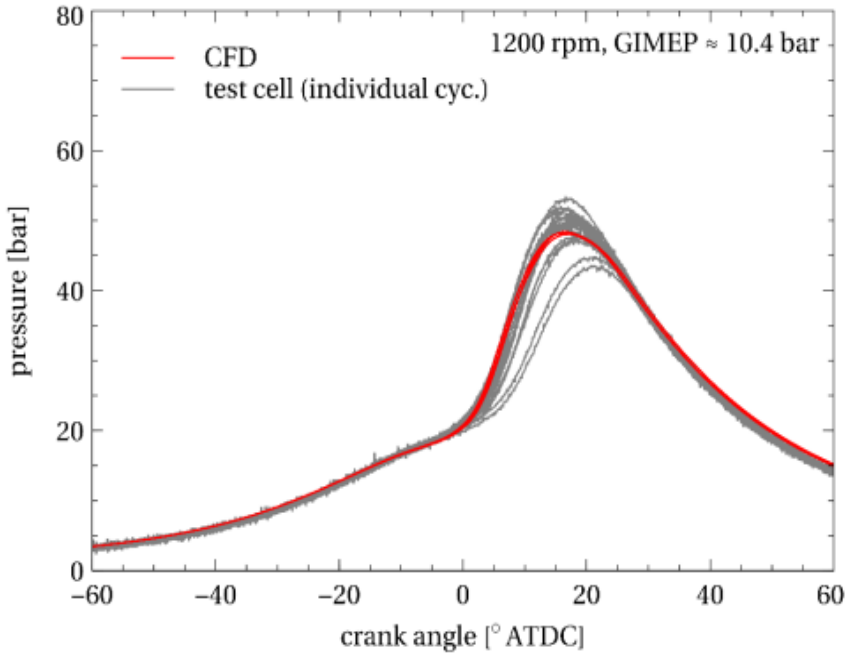

Figure 5.1-6: Cylinder pressure and AHRR prediction compared with experiment. The CFD curves are from three consecutive cycles of a certain spark timing. The test cell curves are from 20 consecutive individual cycles of a single operation point.

One important purpose of combustion CFD is to predict the knock behavior of the engine. The knock propensity at a certain condition is characterized by the CA50 around which the engine operation changes between knocking and non-knocking. With CA50 more advanced than such value the engine knocks, while later CA50 results in non-knocking operation. In combustion system optimization for SI engines, effort should be made to move such transitional CA50 to a more advanced value.

The knock strength of a single cycle is evaluated by a process used internally at Cummins. This process takes local pressure trace(s) and pass it (them) through a high-pass filter. The magnitude of the high-frequency pressure variation (with unit of bar) is used to characterize the knock strength of a single cycle. A threshold value can be selected to mark the boundary between knocking and non-knocking operation.

Figure 5.1-7 plots the CA10 and CA90 versus CA50 for all 12 CFD cycles. A collection of representative experimental data (1000 cycle averages) is also included for comparison. The vertical distance between a CA10 and CA90 pair is the combustion duration of a simulated cycle (or an experimental point). Figure 5.1-7 confirms again the prediction accuracy of the combustion timing and duration. For both CFD data and experimental data, solid markers are used to represent non-knocking cycles, while hollow markers are used to represent knocking cycles. In both CFD and experiment, the chance of knocking clearly increases once the CA50 is advanced beyond 9 degrees ATDC, demonstrating the model's capability of knock prediction.

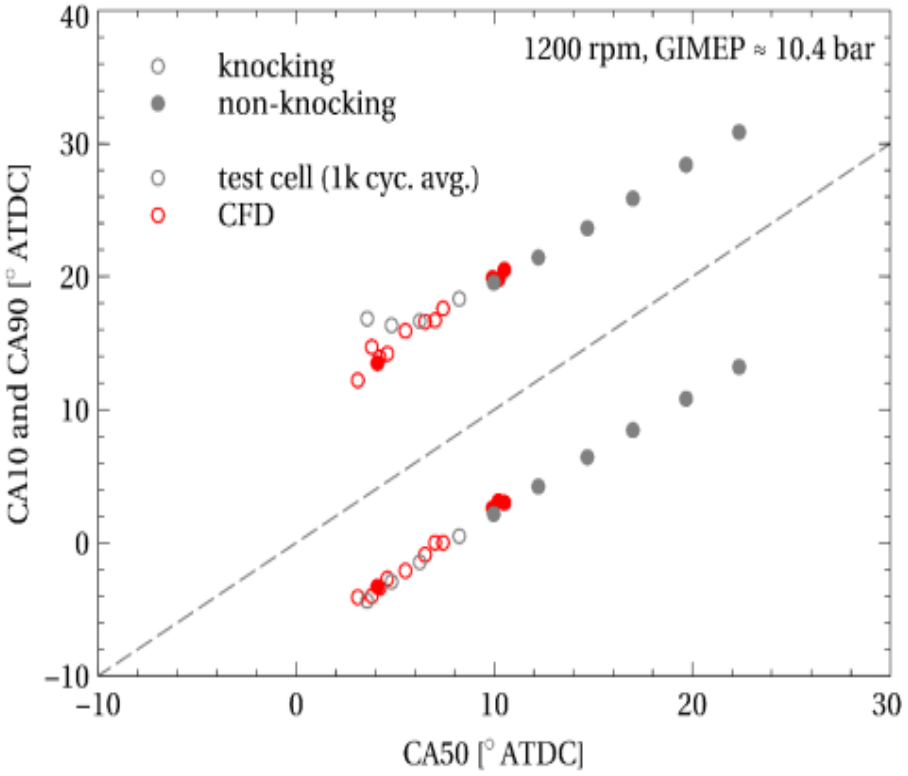

Figure 5.1-7: The combustion phase, duration, and transition between knocking and non-knocking operation.

With DI engine test data became available, the combustion CFD model calibration were updated accordingly. DI simulations were performed with the baseline injector with 5 holes. An SOI timing of -340 aTDC was used in the simulations with a duration of 97 CAD assuming a flow rate of 11.3 mg/ms. With an IMP of 96 kPa, a stoichiometric mixture was achieved by a 153 mg/stroke injected quantity of propane. The fuel temperature was specified as 50° C. This would yield a superheat degree of 0.06. The extreme flashing model parameters suggested by ANL were employed to model the spray break-up under these conditions. The test dataset which was closest to the simulated conditions was the SOI at -360 aTDC data at manifold pressure of 101 kPA.

Figure 5.1-8 compares the preliminary CFD predictions with the DI test data. The test data in the plot shows the envelope of pressure traces from 1000 cycles and the mean pressure trace. The Apparent Heat Release Rate (AHRR) is calculated from the mean pressure trace. The CFD data in the plot is from the 2nd and 3rd cycle of the simulation. Compared to the test data, the CFD is able to predict the pressure and AHRR reasonably well. However, the CFD simulations show considerable cycle to cycle variations between the cycles which makes a comparison with the test mean cycle difficult in this case.

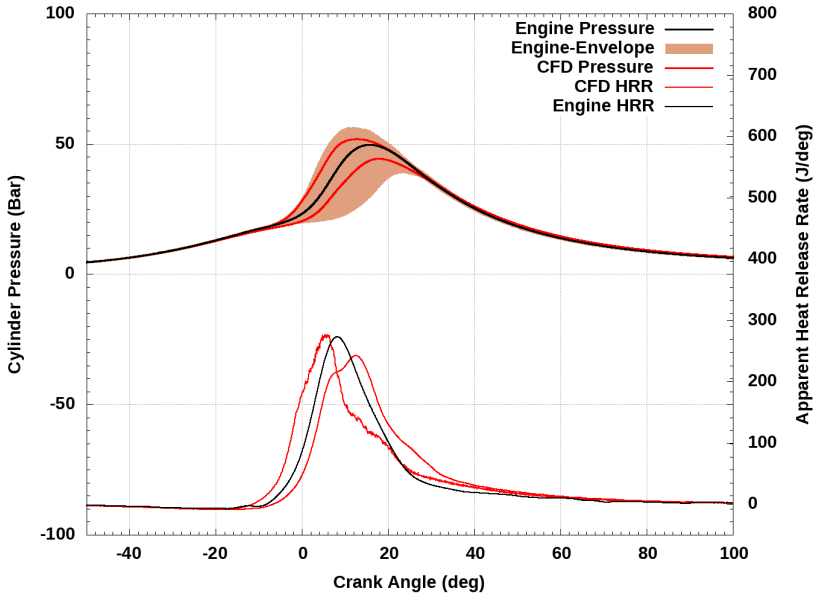

Figure 5.1-8: In-cylinder pressure traces and AHRR from CFD model predictions and measurements using the LPG-DI engine.

Optimization of DI-LPG SCE

It was proposed that EGR is the enabler for high CR, and high knock-limited efficiency. combustion CFD analysis was performed to investigate the benefits of adding EGR to advance the knock limited CA50 and GITE on the CR11.9:1 compression ratio design. The analysis was performed using the baseline injector with 5 holes. In the simulation the engine speed was set as 1200 RPM, and the fueling conditions were set as direct injection (DI) of 276 mg propane starting from -340° aTDC, corresponding to a high load level with a few bars (BMEP) of head room from the final peak torque. The EGR fraction varies from 0, 15, 21, and 25%. EGR is introduced at the intake boundary premixed with the fresh charge. As the EGR is increased, the IMP is also increased from 1.73 bar up to 2.18 bar to maintain a stoichiometric mixture at firing TDC.

Figure 5.1-9 plots the predicted knock intensities at different EGR levels. For each EGR level, the simulation is performed for five consecutive cycles. The result from the first cycle is ignored to avoid the effect of initialization estimates and the results are evaluated from the other four cycles. Also, a spark sweep is performed for each EGR level until the knock limit is reached. As each cycle generates slightly different mixture distribution at spark timing, there is cycle-to-cycle variation in these predictions albeit the use of RANS turbulence models. The multiple knock values at similar CA50s are a result of these cycle-to-cycle variations in predictions. However, a general trend of knock with CA50 can be deduced from these scatter data. A knock limit of 1 bar is used to compare the effectiveness of different EGR levels to reduce knock. This limit is based on historical data and does not translate to a non-operable regime in the engine. A knock level of 1 to 2 bar is considered mild knock and anything above 3 bar is severe knock. The knock-trade off plot shows the benefit of EGR on reducing knock.

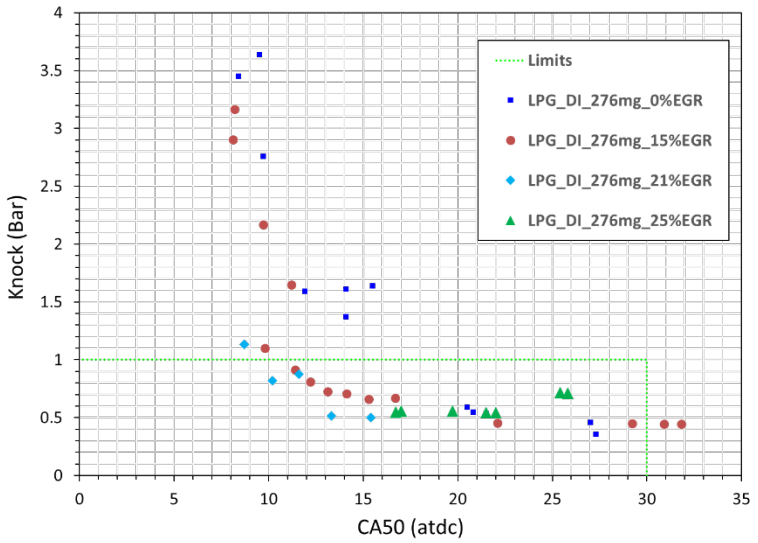

Figure 5.1-9: Predicted knock-CA50 trade-off with different EGR levels.

At the operating point analyzed, the non-EGR condition knocks at CA50 of 15° aTDC whereas 15% EGR can operate without significant knock at the same CA50. The knock limited CA50 can be further advanced using 21% EGR. Increasing the EGR further to 25% made the ignition delay too long and resulted in very delayed combustion phasing even with the most advanced spark timing used. Also, it made combustion very unstable with multiple cycles misfiring. This can be observed as the points with very low GITE in the GITE scatter plots in presented in Figure 5.1-10.

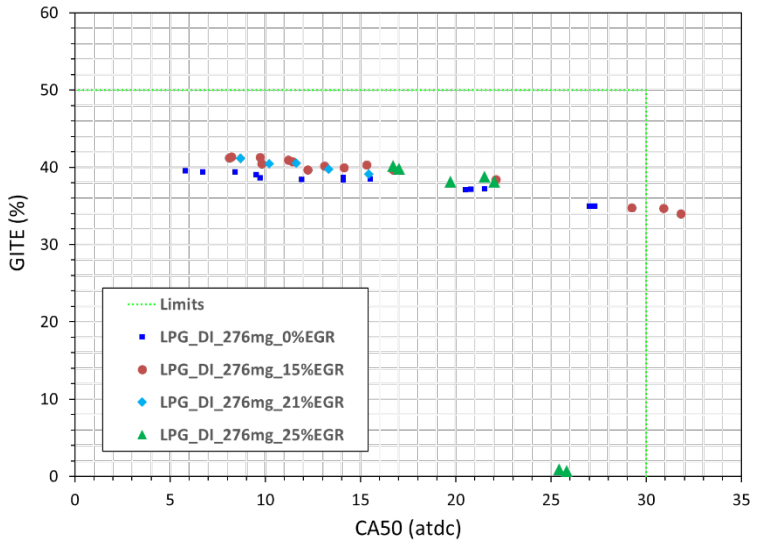

Figure 5.1-10: Predicted GITE with different EGR levels.

As the CA50 is advanced with higher EGR, GITE will improve to ~41% at knock limited conditions. One of the drawbacks of higher EGR is the increased burn duration as shown in Figure 5.1-11. The burn duration limit is based on the baseline non-EGR burn duration and does not limit the engine to operate at higher values.

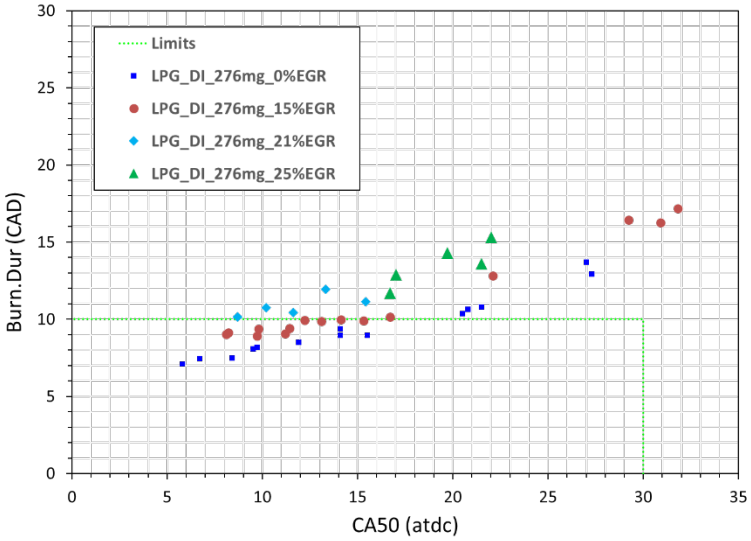

Figure 5.1-11: Predicted burn duration with different EGR levels.

At advanced CA50s with the EGR conditions, the engine is able to complete the combustion in a similar duration as that of non-EGR operation at a retarded CA50. Hence the increased burn durations with these EGR levels are not considered significantly detrimental to performance.

Once 20% is identified as a good level of EGR, CR study is done to explore potential of using higher CR. The study covers CR of 11.9, 13, 14, and 15. The CR variation is done by varying the piston bowl depth in the triangulated geometry (Sophisticated CAD modeling is used for the bowl study for the CR of 14, which turned out to be the recommended CR from this study). The analysis is performed assuming perfectly mixed stoichiometric mixture at the inlet (Initially, DI spray modeling for the 5-hole baseline injector was used, but the cycle-by-cycle variation of mixing overwhelms the effect of CR and prevents us from reaching conclusion confidently regarding CR). In the simulation, the engine speed is set as 1196 RPM, and the intake pressure is selected to match 276 mg propane mass and 20% EGR. The spark timing is swept to cover a range of CA50, and a few consecutive cycles are included for each spark timing.

Figure 5.1-12 shows the knock-limited CA50 with different CR. With higher CR, the CA50 must be more retarded to keep the operation within the knock limit (around 1 – 2 bar), offsetting part of the efficiency benefit of higher CR. As shown in Figure 5.1-19, increasing CR from 11.9 to 13 results in about 1 point of higher GITE, while another half point improvement can be achieved by elevating the CR further to 14. Marginal efficiency improvement less than half point is possible with CR of 15, despite of about 1.5° more retarded CA50 comparing to CR of 14 suggested by Figure 5.1-12.

For robust engine operation, it is important to keep a reasonably wide timing window, i.e. the space between knock-limited CA50 and COV-limited CA50, up to the full load operation. In order to protect for the potential of higher load than the one used in the CFD study, CR of 14 is

recommended over 15 because of wider operative window, hence robust engine operation, and higher load capability.

Once 14 is chosen as the recommend CR, multiple bowl design candidates are considered. The shape of the bowls is shown in Figure 5.1-14. The “high swirl” bowl has the smallest overall bowl diameter for swirl enhancement near TDC. The “high squish” bowl has the largest squish area with its contracting opening. The “raised pip” bowl has a raised center pip and looks similar to diesel bowls. The “step lip” bowl has a step lip at the edge of the bowl. The “nebula” bowl has a ridge across the bowl to dissipate swirl energy into turbulence energy near the TDC. All five bowls have the correct volume to achieve CR of 14, and are compatible with the piston blanks with valve pockets possessed by CSU. The simulation setup is the same as the CR study except that the 5-hole baseline injector spray modeling is recovered to include bowl’s effect on mixing.

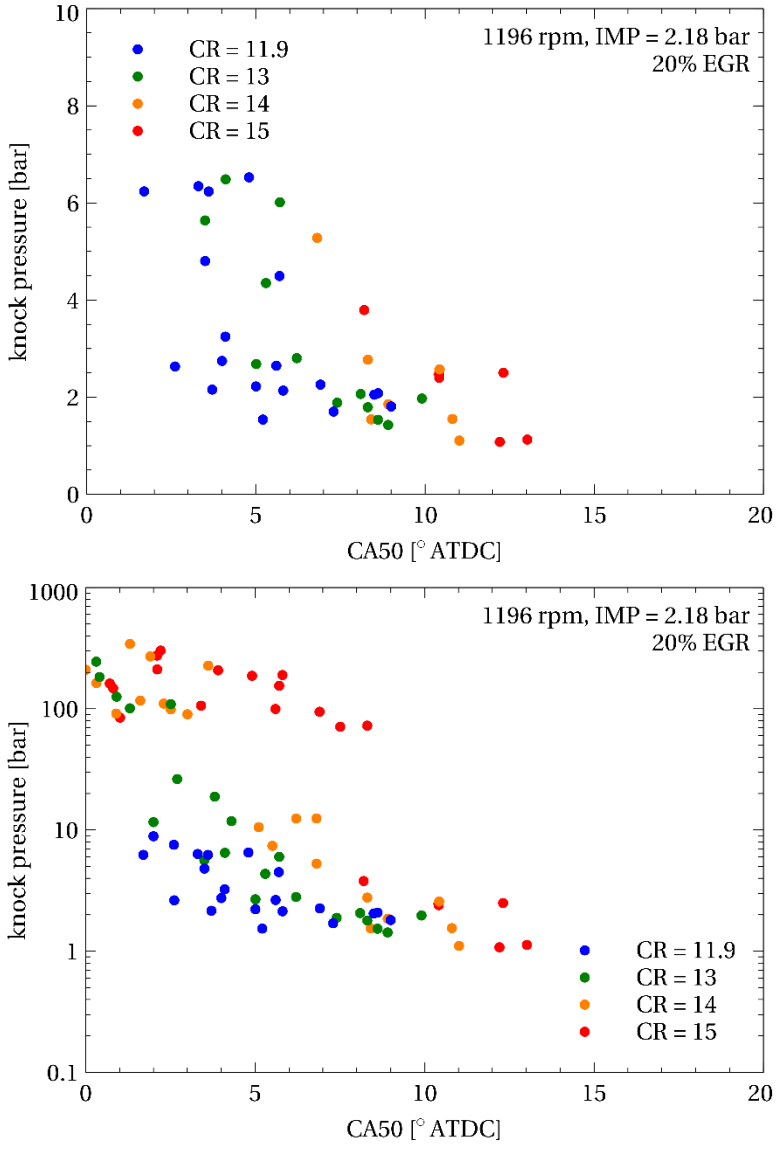

Figure 5.1-12: Knock pressure as a function of CA50, in linear scale (top) and logarithm scale (bottom).

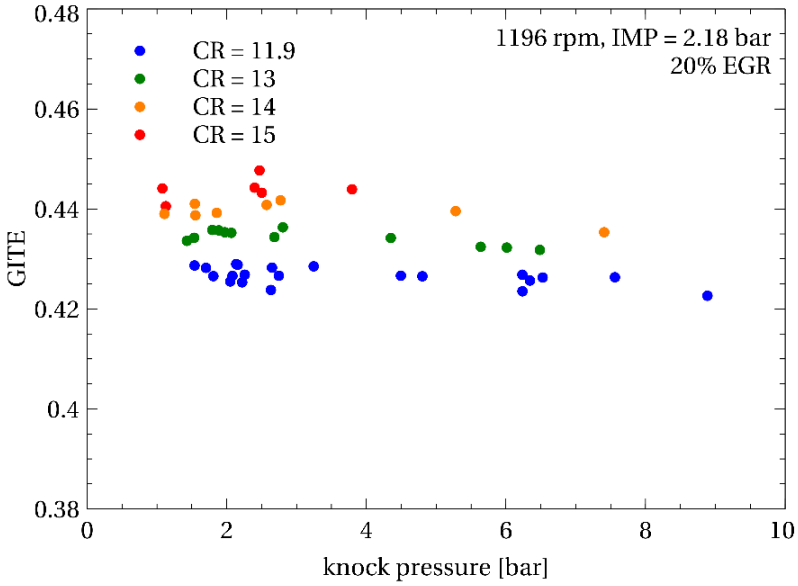

Figure 5.1-13: Knock-limited GITE with different CR.

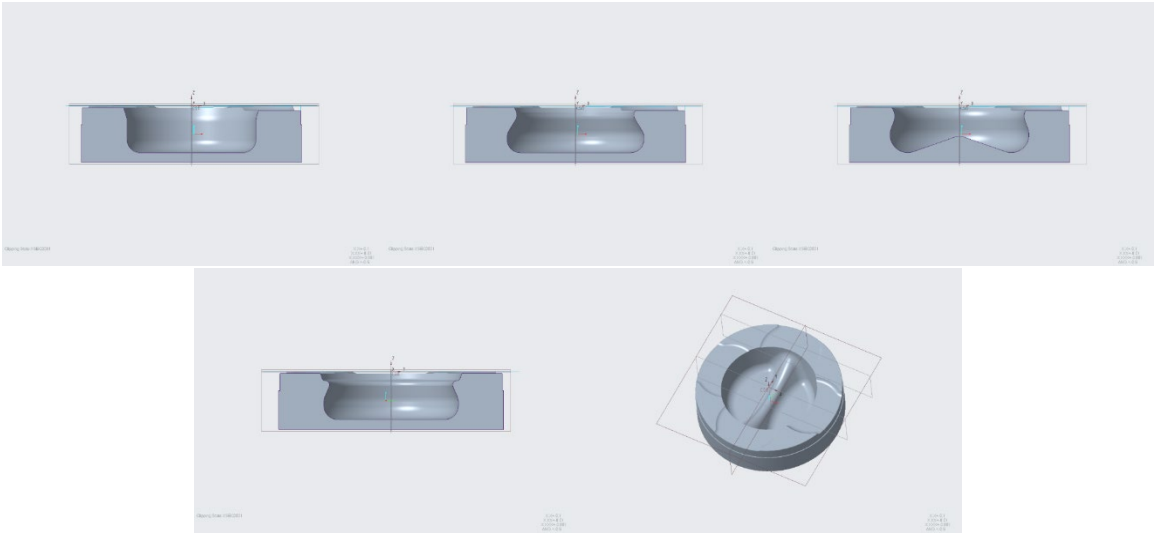

Figure 5.1-14: The five bowl design candidates: high swirl (1st row left), high squish (1st row center), raised pip (1st row right), step lip (2nd row left), and "nebula" (2nd row right).

Figure 5.1-15 to Figure **5.1-17** compare the knock-limited CA50, knock-limited GITE, and combustion duration among the five bowls. The difference among the five bowls is not significantly more pronounced than the stochastic cycle-to-cycle variation. Considering the overall performance of all cycles, the high squish design is recommended for its slightly more advanced knock-limited CA50, and slightly shorter combustion duration (at a given CA50), both features are important for tolerating high EGR level (i.e. around 20%). The high squish design also enjoys relatively better manufacturability and is well within the machining capability of CSU.

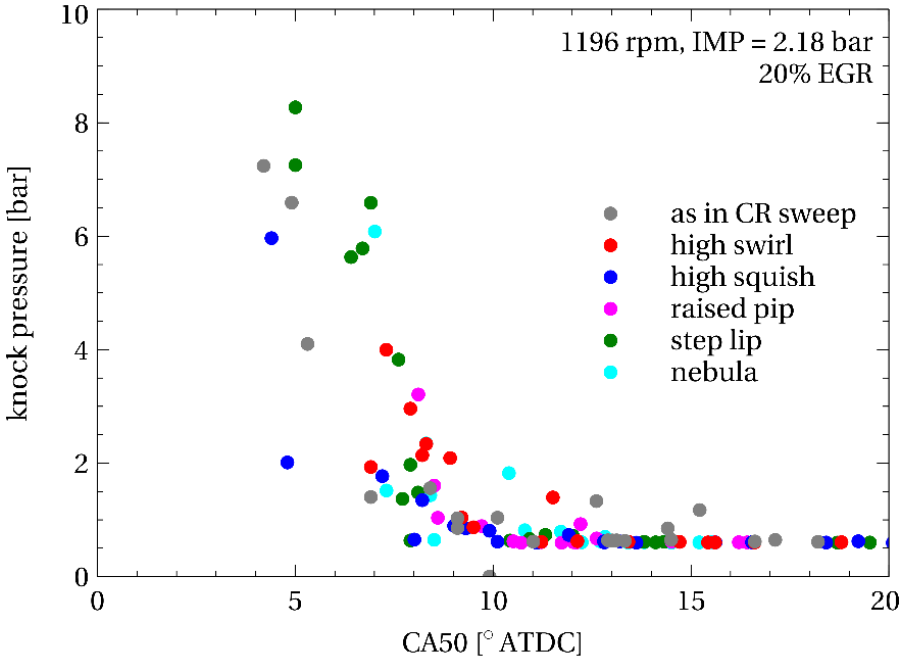

Figure 5.1-15: Knock-limited CA50 with the five bowl design candidates.

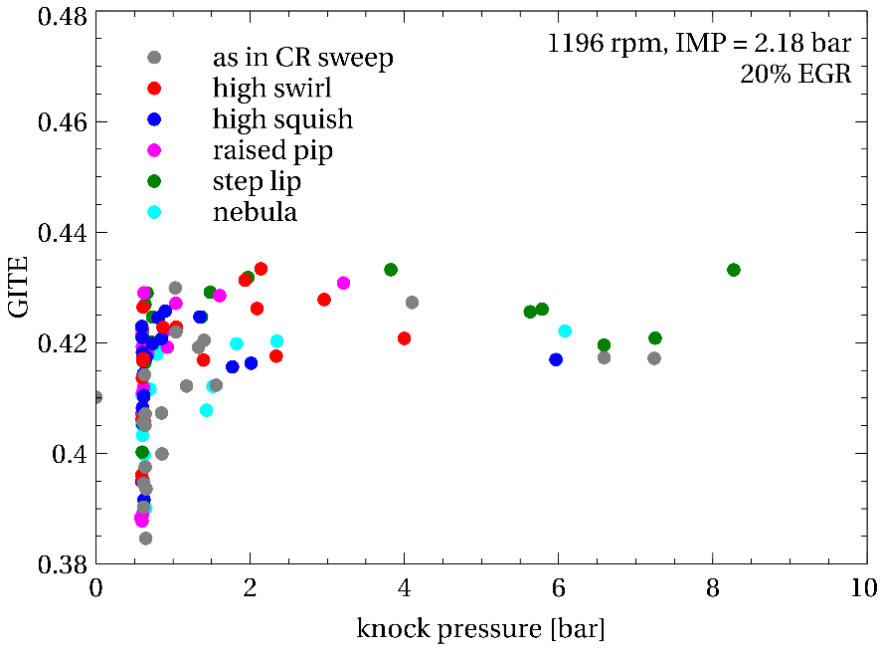

Figure 5.1-16: Knock-limited GITE with the five bowl design candidates.

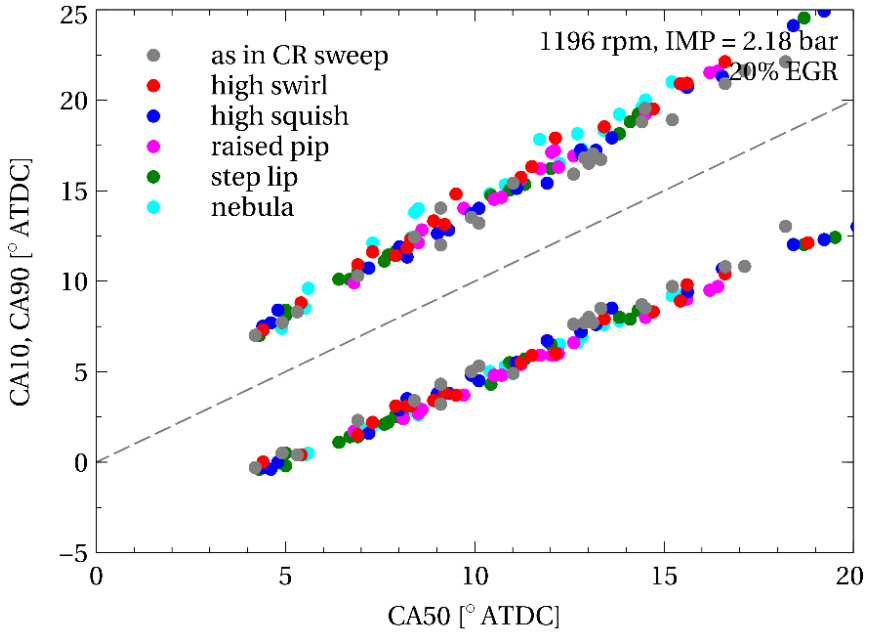

Figure 5.1-17: CA10 and CA90 as functions of the CA50 with the five design candidates.

Wall heat transfer predictions

In this study, conjugated heat transfer (CHT) simulation is performed for the single-cylinder ALPINE LPG SI engine to estimate its component temperature during steady operation under the proposed maximum load. The result is not meant to be confirmed by thermocouple measurement and provides only ballpark estimation. This CHT study predicts the temperature of the head (including valves, seats, and guides), liner, and piston.

In this CHT study, instead of employing another simulation software for solid heat conduction and coolant CFD, an "all-Converge" approach is applied. The CHT problem is decomposed into four Converge simulations. Figure 5.1-18 shows the four simulations and data transfer among them. The three simulations on the top are CFD simulations, while the lower one is solid heat conduction simulation. The three CFD simulations are independent of each other within an iteration and can be executed concurrently. The three CFD simulations are only directly coupled with the solid heat conduction simulation in the same and previous iteration. In general, CFD simulations take the wall temperature (T_{wall}) predicted by the solid heat conduction simulation in the previous iteration and generates free-stream fluid temperature (T_{ref}) and heat transfer coefficient (HTC) maps. The T_{ref} and HTC map is loaded into the current iteration solid heat conduction simulation, which updates the solid temperature T_{solid}, an overset of T_{wall}.

A combustion CFD study was done to evaluate the effectiveness of the increased mass flow rates achieved by the XDI 7-hole injector when compared to the baseline 5-hole design. The increased mass flow rate from the XDI 7-hole injector provides enough fuel such that the injection duration

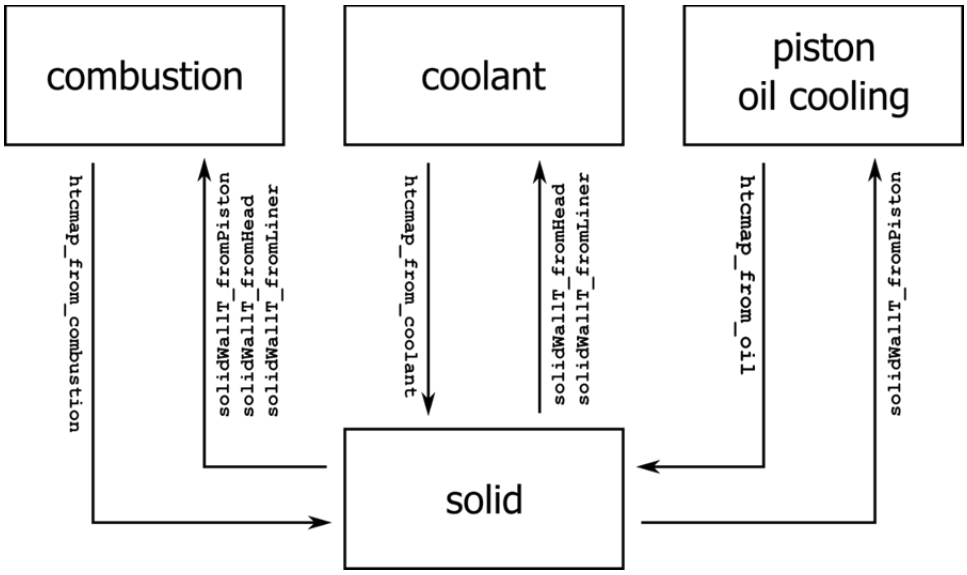

Figure 5.1-18: Four Converge simulations and data transfer among the simulations.

Figure 5.1-25 shows the final T_{wall} predicted by the solid heat conduction simulation of the final iteration. The head monitor point temperature and maximum temperature of each component are listed in Table 5.1-5.

may be reduced which can allow for different start of injections (SOI) to be considered. The comparison study was conducted utilizing the baseline conditions, start of injection for both cases is at -340° ATDC at 1200 rpm and a compression ratio of 9.3. The XDI 7-hole injector geometry is unknown at this point, for this comparison, the same injector geometry was used but the injector flow rates were varied to match the injection rates observed from the spray chamber testing.

Table 5.1-5: Combustion parameter and component temperature during C-EGAI and regular knock operation.

		EGAI	regular knock
monitor point temperature	1	478 K	470 K
	2	516 K	511 K
	3	526 K	520 K
	4	538 K	535 K
	5	542 K	527 K
	6	536 K	527 K
maximum temperature	piston	611 K	578 K
	liner	588 K	559 K
	head deck	591 K	572 K
	IVs	754 K	720 K
	EVs	786 K	766 K
CA50		13.2°	17.6°
KP		9.65 bar	0.627 bar

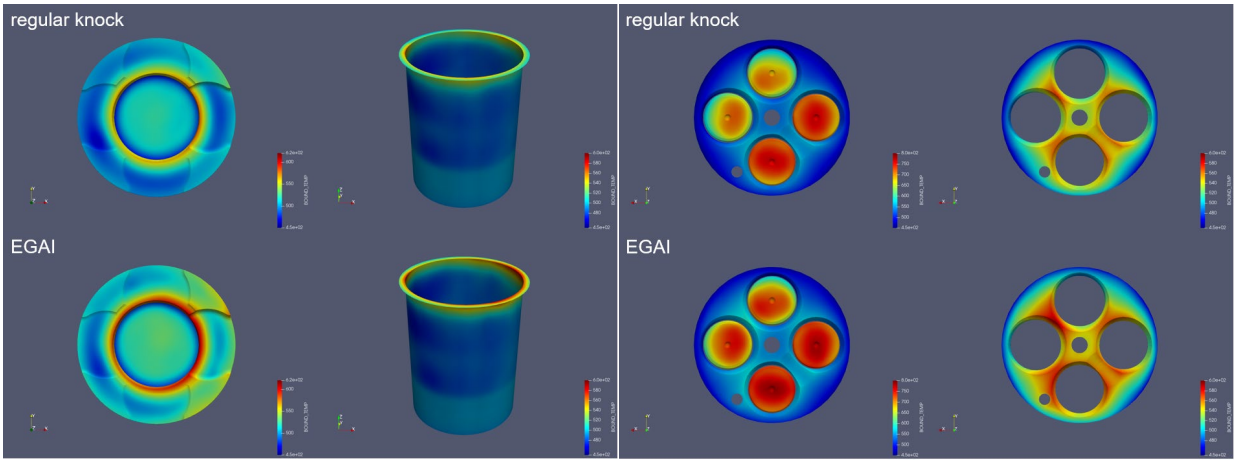

Figure 5.1-19: In-cylinder wall temperature during normal knock and C-EGAI operation.

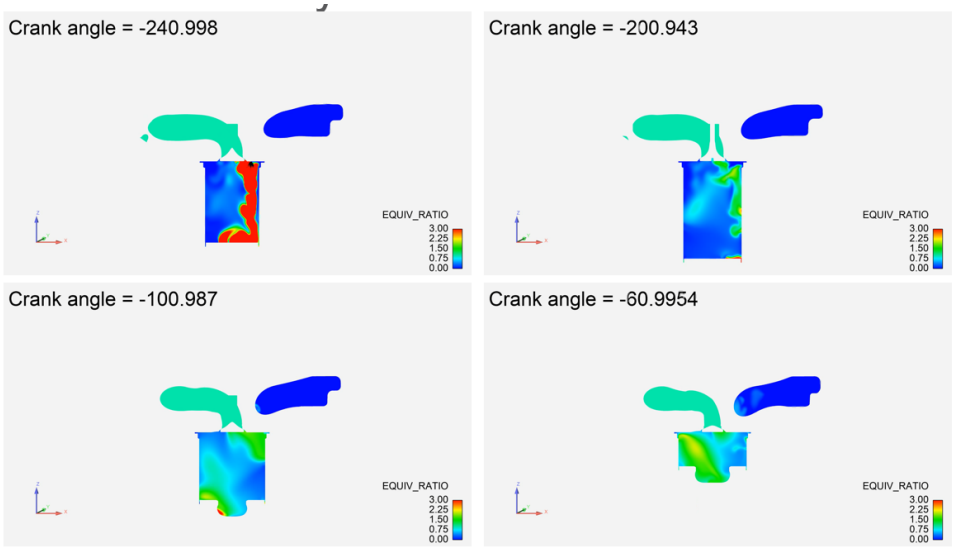

Figure 5.1-26: Crank angle degree resolution of the equivalence ratio for the baseline 5-hole injector.

Figure 5.1-26 displays a snapshot of a cut-plane through the cylinder located at the region of the spark plug. The contours show the difference in equivalence ratio observed in the cylinder at different crank angle degrees. An equivalence ratio of 0 is represented by the blue regions while the red represents higher equivalence ratios above 3. The color is interpreted between red and blue to showcase the intermediate regions of equivalence ratios. The snapshots from the baseline case in Figure Mixing-1 show how the fuel/air mixture progresses as the compression stroke occurs. For the baseline case, a stratified area is created, or a richer region is present around the spark plug when compared to the XDI 7-hole simulations shown in Figure 5.1-27.

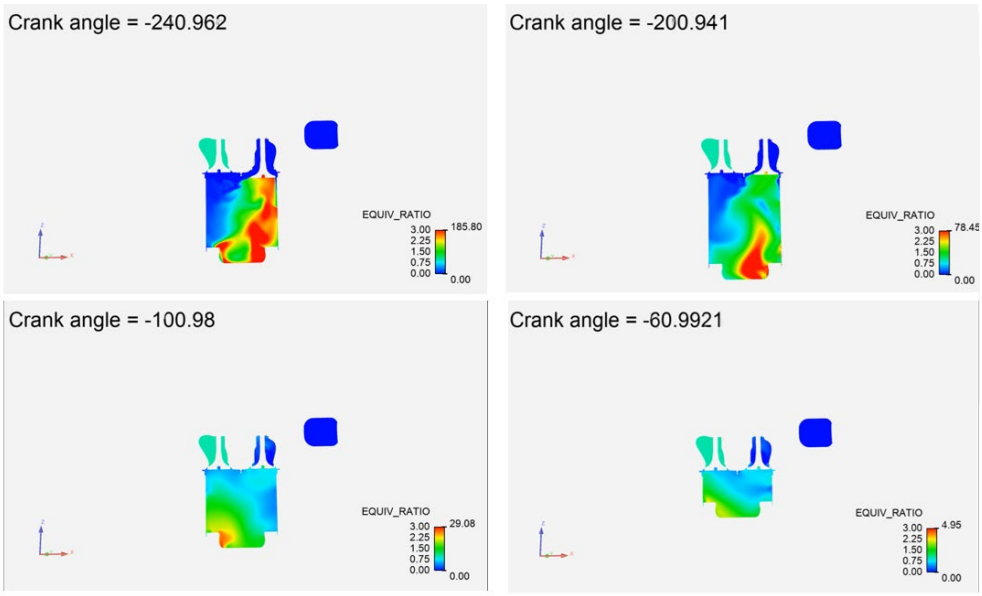

Figure 5.1-27: Crank angle degree resolution of the equivalence ratio for the XDI 7-hole injector.

As shown in Figure 5.1-27, there are more regions with rich pockets that are not being fully mixed when implementing the XDI 7-hole injector. Comparing crank angle -100° ATDC to the baseline, the XDI 7-hole case experiences a rich pocket or region located at the bottom of the piston bowl. From the increased mass flow rate, more LPG gets trapped in the bowl and the swirl or tumble motion is not enough to promote mixing in this region. As the compression stroke continues, the concentration of fuel in this corner does not dissipate and this is seen at -60° ATDC and further into the cycle around the spark timing which is highlighted in Figure 5.1-28.

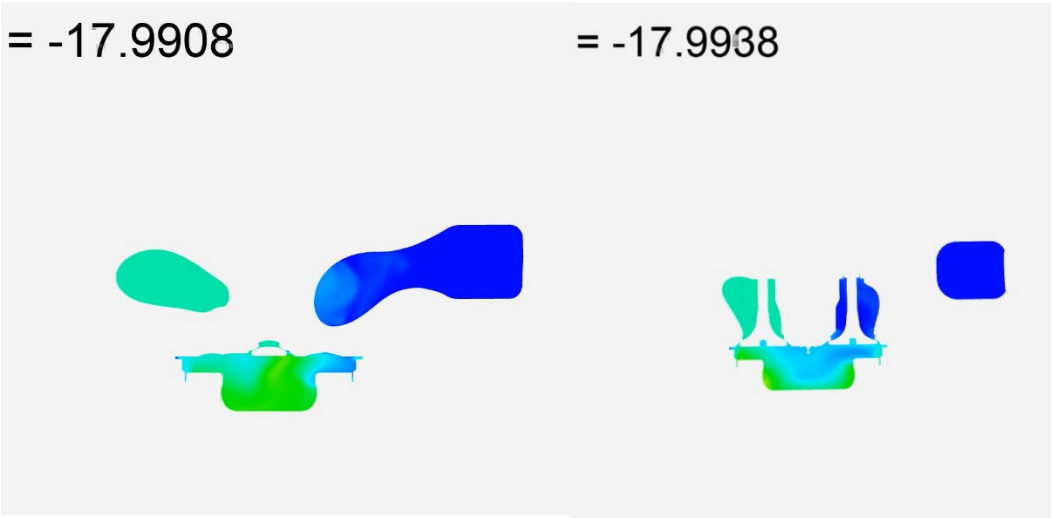

Figure 5.1-28: Direct comparison between the XDI 7-hole (right) and baseline injectors (left) near spark timing.

Observing a snapshot around the spark timing shows the vast differences between the two cases. The baseline case shown in the left of Figure 5.1-28 achieves a slightly rich region where phi is around 1.5 in the spark plug area. This is desirable for engine operation to achieve a flame that propagates from the spark plug outward into the lean regions of the cylinder. The XDI 7-hole injector is shown in the right image of Figure 5.1-28. For the XDI 7-hole case, the area around the spark plug contains very low amounts of fuel shown by the blue region which impedes combustion. Due to the mixture properties around spark timing, combustion was not present for all the simulated cycles for the XDI 7-hole injector case.

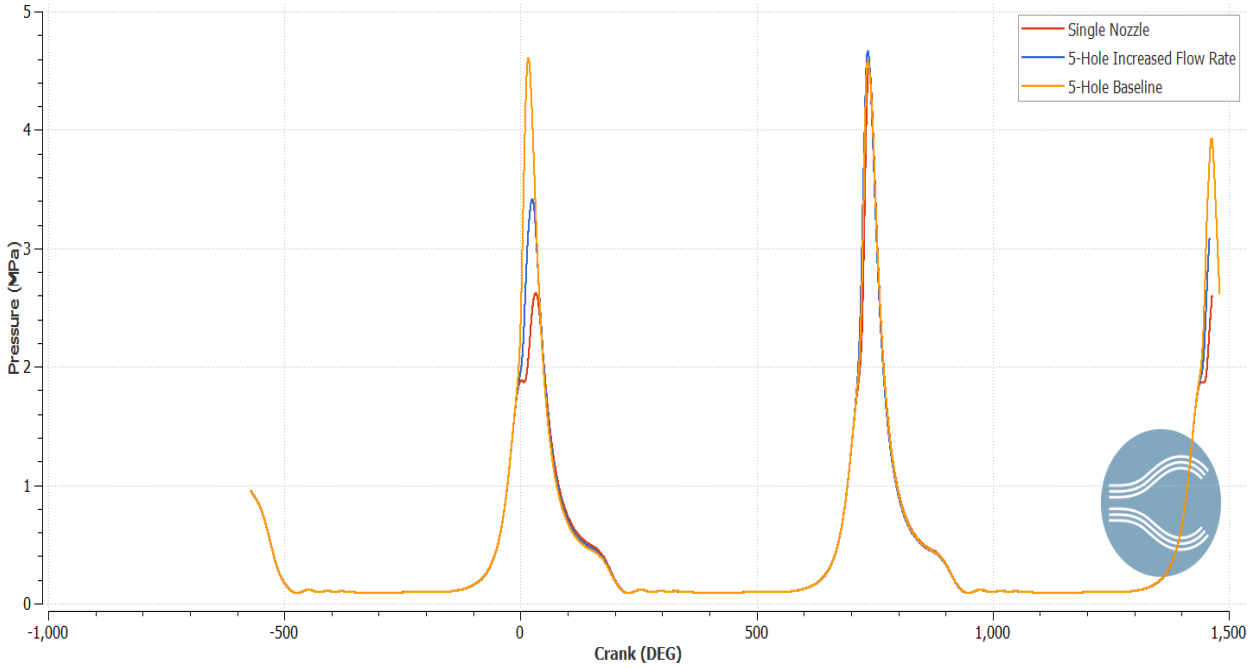

Figure 5.1-29: XDI Injector single nozzle model vs baseline pressure trace.

In continuation with the injector imaging, a start of injection (SOI) sweep for the initial compression ratio cases of 9.3 was conducted with the goal to capture the full mixing effect present in the experiments as the SOI is changed. The In-Cylinder pressure traces for some of the SOI sweeps are shown in Figure 5.1-30, these results indicate that the earlier injection times allow more time for mixing resulting in a uniform charge around the spark plug at TDC which creates better combustion shown with a higher peak pressure. The late SOI resulted in delayed combustion seen in pressure traces of both SOI 150 and 180, while for SOI 180, combustion was not obtained in the simulations. Experimentally, as the SOI was advanced, the combustion performance decreased until it crossed a threshold bring back the mixing performance closer to the earlier SOI cases such as SOI 330. The CONVERGE simulations were able to capture this phenomenon which is displayed in Figure 5.1-31. At TDC or around 0 CAD, the standard deviation of Phi is compared between SOIs where a lower standard deviation indicates better mixing performance. The lowest standard deviation of Phi resulted from the earliest SOI 330, next as

the SOI is advanced, the mixing performance suffers shown by the remaining results where the standard deviation increases from 330, 330< 260< 150< 180. The mixing continues to decrease with advancing the SOI until around SOI 150 where an improvement is seen bringing the mixing performance closer to earlier injection timings as the standard deviation of Phi is under 1. The improvement in mixing performance could be due to the bowl position when it is coming back to TDC in the compression stroke as this would cause different fluid velocities to be present in-cylinder changing the mixing performance, but more investigation is required to determine the true cause of the phenomenon.

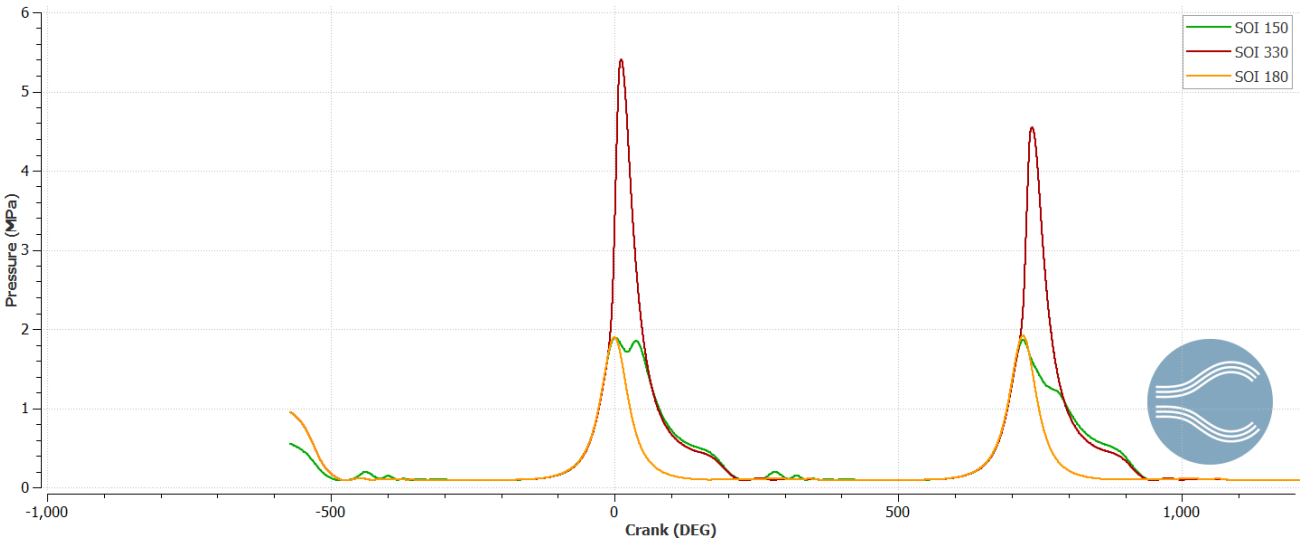

Figure 5.1-30: In-cylinder Pressure traces for Start of Injection (SOI) sweep.

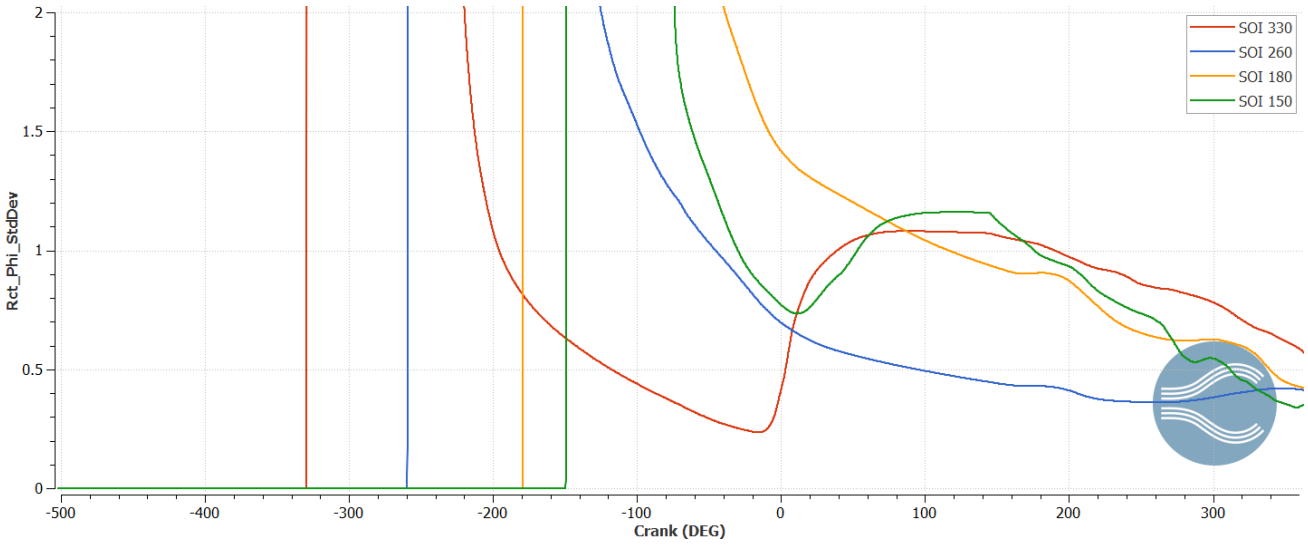

Figure 5.1-31: Standard deviation of Phi vs Crank angle for different Start of Injections.

CONVERGE simulations of the new experimental conditions were conducted, utilizing a compression ratio (CR) of 12, engine operating speed of 1200 rpm, phi of 1, and a CA50 of 12. In addition, high speed schlieren imaging was conducted for the unmodified 6-hole XDI injector at two orientations 90 degrees from each other. Imaging of the unmodified injector was performed in order to capture the influence of the 7th hole on the modified XDI injector and to gain further insight into the individual cone angles for each nozzle to create an accurate 3-D CFD model to implement into simulations for both engine combustion and the high-pressure spray chamber. In conjunction with the imaging experiments, the results from the initial start of injection sweep are displayed in Figure 5.1-32. A start of injection sweep was implemented in CONVERGE conducted with the goal to capture the full mixing effect present in the experiments as the SOI is changed at higher compression ratios. Figure 5.1-32 highlights the in-cylinder pressure traces for the initial SOI sweep; as the SOI is advanced closer towards TDC, the combustion performance is hindered exhibited in the pressure trace. The SOI 120 simulation did not obtain complete combustion, but this could be a spark timing issue leading to the simulation to be at a different combustion phasing than experimentally. Even though the experimental COV performed well at this operating condition, if there were any slight deviations, the engine went out of the acceptable operating range which is seen in the simulations.

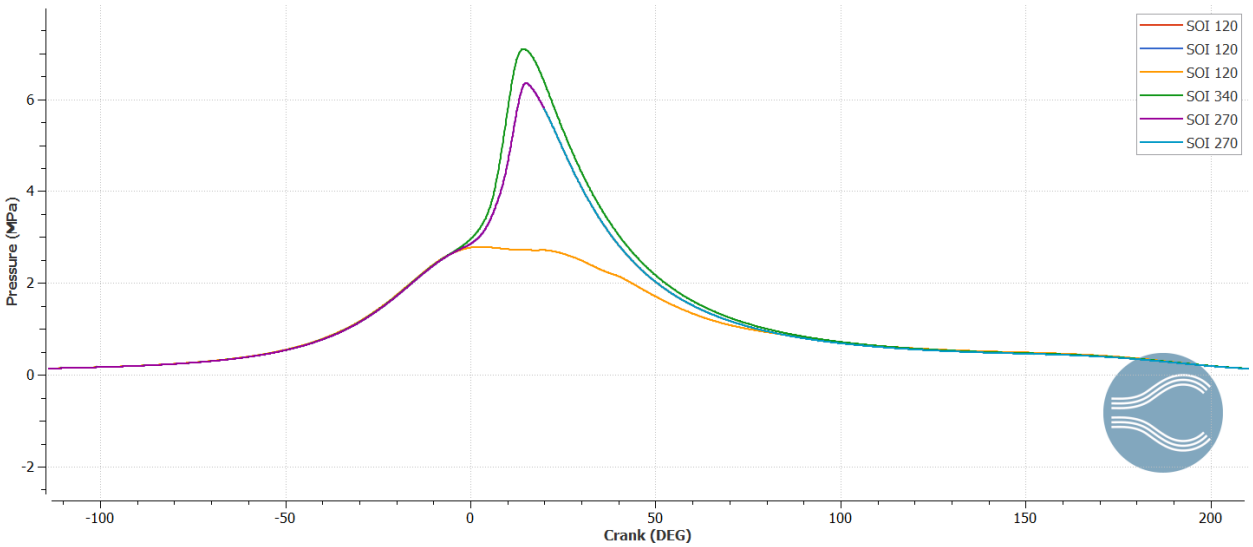

Figure 5.1-32: In-cylinder Pressure traces for Start of Injection (SOI) sweep at CR12.

The same mixing behavior was observed at the higher CR12, but the phase was shifted by 30 crank angle degrees resulting in performance coming back to an acceptable level at SOI 120 compared to an SOI 150 at CR 9.3. Further investigation is required to understand the fluid dynamics that are dominating mixing, influencing combustion, and straining engine operation.

A solid model for the XDI injector was created. The 3D model is to be implemented into both the Converge engine and High-pressure spray chamber set ups to update the geometry utilized in

simulations to match the most recent engine and spray chamber experiments. Figure 5.1-33 showcases an isometric and a front view of the SolidWorks model which was created from high resolution electron microscope imaging with a representative picture from that work shown in the far right of Figure 5.1-33. CSU is working in collaboration with Argonne National Laboratory on the implementation of the updated model into HPSC simulations to eventually be able to compare the simulation to the experimental results obtained from the high-speed camera schlieren imaging of both the LT4 six- and XDI seven-hole nozzles. The updated models will be used to explain the injection behavior observed with changing start of injections (SOI) as the COV drastically increases for the XDI injector with earlier SOIs following a similar trend observed with the Delphi 5-hole injector while being seen experimentally at every test condition).

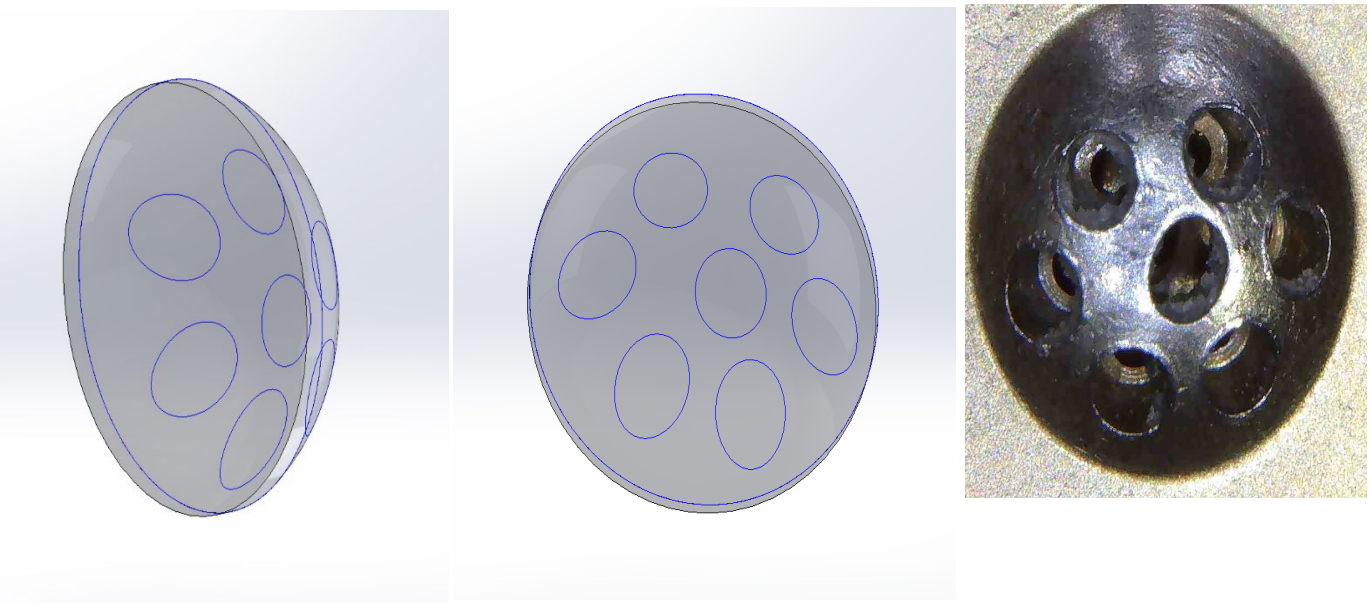

Figure 5.1-33: XDI Injector single SolidWorks model for implementation into HPSC.

Optimizations and updates were made to the CONVERGE 3-D simulations for the updated piston geometry resulting in a compression ratio (CR) of 12. At a CR 12, engine operating speed of 1200 rpm, phi of 1, and a CA50 of 12 an SOI sweep was conducted in order to compare the simulation and experimental results in tandem with investigating the spray dynamics. Figure 5.1-34 displays the results for SOI 90, 240, 270, 300, and 340 CA bTDC or the first iteration of the simulations where the earliest SOI's timing, 340 and 300 agreed with the experimental data and follows the same trend observed experimentally whereas the SOI is retarded and brought closer to TDC the peak in-cylinder pressure decreases with each iteration shown with SOI 340 and 300. The SOI 90, 270, and 240 simulations did not result in combustion differing from the experimental results.

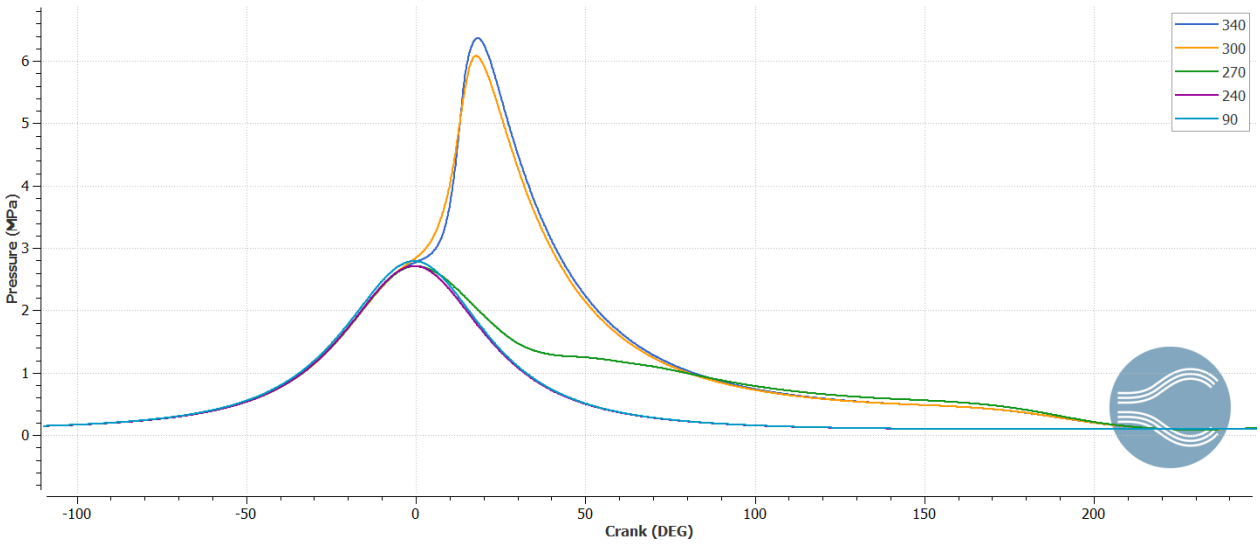

Figure 5.1-34: CONVERGE In-cylinder pressure traces of an SOI sweep at CR12.

After analyzing the results from the initial simulation run, tuning of CONVERGE's parameters was required to match the simulations to the experiments. Earlier work conducted by Cummins encountered a similar issue where the delayed start of injection conditions was not properly captured by CONVERGE and the injector parameters that were being utilized. To get around this problem, Cummins decreased the nozzle size to obtain better spray performance that matched closer to experiments. Following this approach, the nozzle size of the Delphi-5-hole injector was decreased to the same diameter used for the CR 9.3 baseline case and an SOI sweep at delayed injection conditions was conducted with the results of that study shown in Figure 5.1-35. Simulations of SOI 120, 150, 210, and 240 all agree with the experimental results which showed as the injection timing is retarded, the performance is hindered until the engine finds a sustainable operating point and then if the timing is retarded any further the engine cannot operate. CONVREGE was able to fully capture this behavior shown in Figure 5.1-35 as SOI 240 performs the best followed by SOI 210, 120, and 150. SOI 120 follows the same trend as the CR12 experiments functioning as the best operating point for delayed injection timings. SOI 90 simulations results were shown in Figure 5.1-34 where ignition did not occur thus highlighting SOI 120 as the turning point for stable operation both in simulations and experimentally.

5.2 LECM Development/Programming

Section 5.2 was extracted from [1] in References.

To achieve the baseline port-fuel and the intended direct injection operation of the heavy-duty engine, the LECM was programmed for single injection event strategies in both injection configurations. The single injection event strategy was chosen as a starting point due to its simplicity and ease of programming. Other injection strategies were developed, to be tested in the event that the single injection event strategy fell short of the target efficiency, for example,

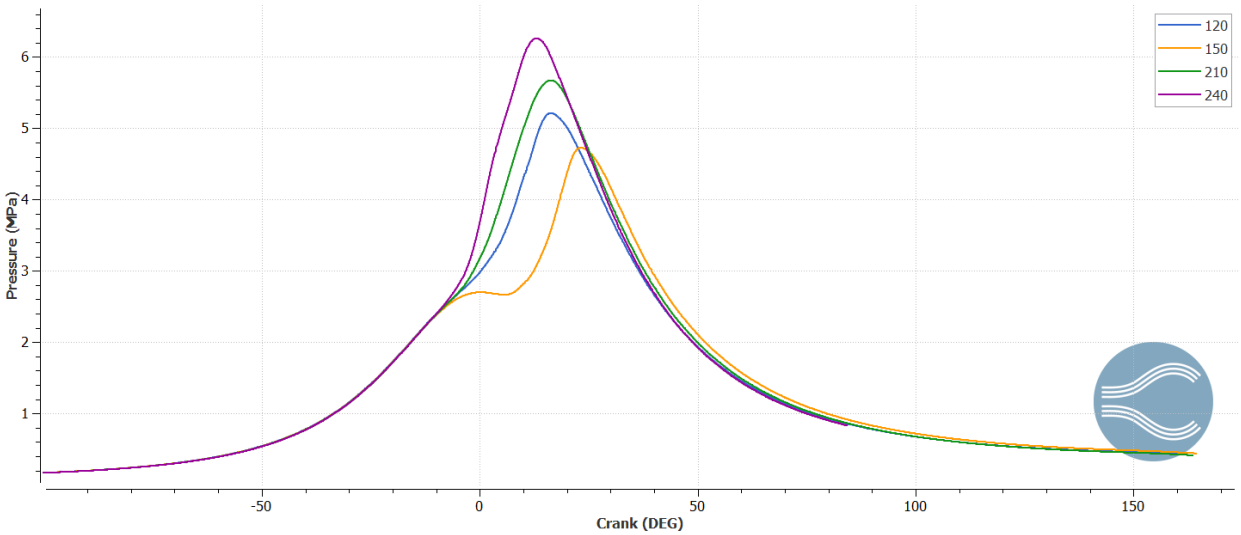

Figure 5.1-35: CONVERGE In-cylinder pressure traces of an SOI sweep at CR12.

a stratified injection strategy with direct injection or a mixed PFI/DI strategy guided by initial spray diagnostics and engine results. However, as will be shown later, the project goals were achieved with the designed single, high-flow, early injection strategy and these other strategies were considered as possible directions for future studies. Snapshots of the baseline port-fuel injector behavior on an oscilloscope as well as the developed injection profile on the LECM interface are shown in Figure 5.2-1.

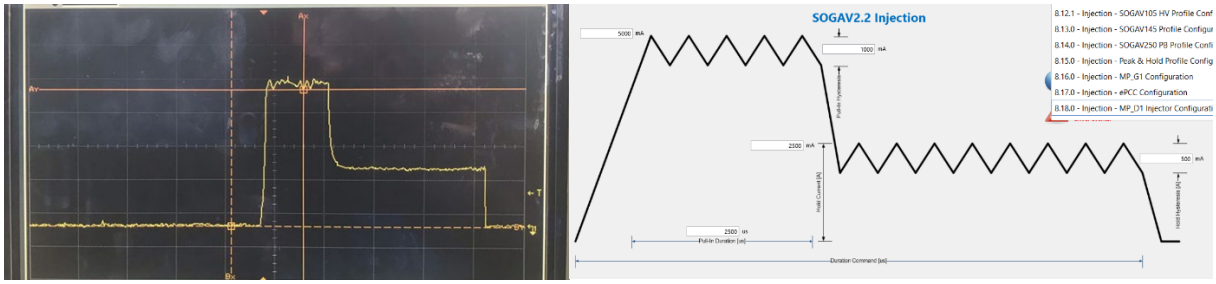

Figure 5.2-1: Snapshot of the port-fuel injection profile development.

Further algorithm development was required for the Combustion Intensity Metric (CIM) programming and calibration. The CIM is an advanced combustion tool which monitors the effects of several key combustion metrics in real-time to detect and control end gas auto-ignition in the cylinder to a desired fraction [2]. The CIM is native to the Woodward LECM and had been shown to control the fraction of end-gas auto-ignition (f-EGAI) to a desired amount in previous CFR natural gas tests [3,4]. This f-EGAI was reliably controlled by the CIM which is a linearly scaled combination of the metrics shown in equation 5.2.1 with respect to a reference value. The CIM tool was then programmed for LPG operation on the CFR engine and on the heavy-duty engine at compression ratio 14 due to the strong fuel effects on these five metrics. The programming involved calibrating the relevant combustion metrics shown in equation 5.2.1 for the control of the end-gas auto-ignition fraction (f-EGAI).

$$CIM = A_1 \frac{P_{max}}{P_{max_{ref}}} + A_2 \frac{BD}{BD_{ref}} + A_3 \frac{PRR}{PRR_{ref}} + A_4 \frac{HRR_S}{HRR_{S_{ref}}} + A_5 \frac{KI}{KI_{ref}} \quad (5.2.1)$$

Where:

A_x are calibration constants,

P_{max} is the peak pressure (bar),

BD is the burn duration (CAD),

PRR is the pressure rise rate (bar/deg),

HRR_s is the heat release rise rate slope (J/deg/deg), and

KI is the knock intensity.

A picture of the LECM-CIM programming interface is shown in Figure 5.2-2.

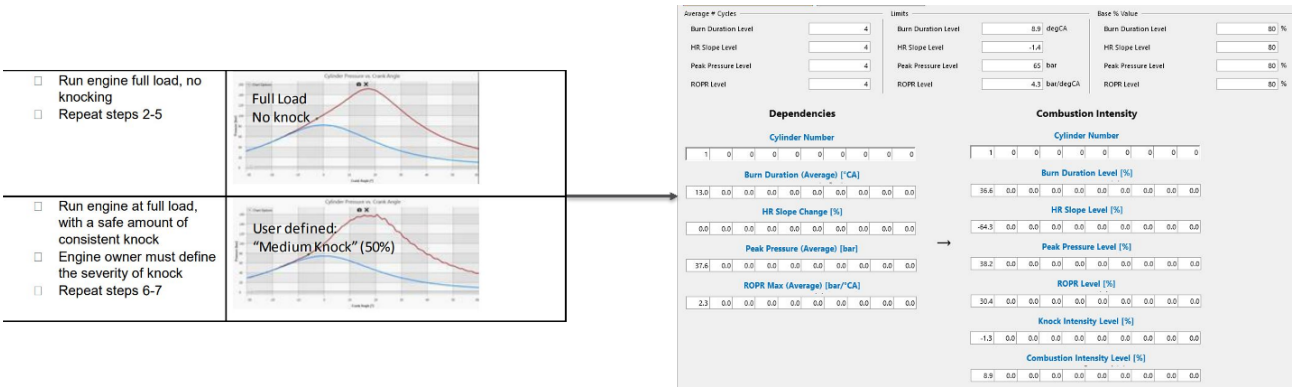

Figure 5.2-2: LECM Interface

The relationship of the CIM tool with end-gas auto-ignition, quantified by the knock ripple sum (KRS) in this section is shown in Figure 5.2-3. As the CIM was increased, in effect causing the CA50 to be advanced, it exhibited a notable relationship with the KRS, following a similar trendline with the knock metric, and allowing the engine to operate steadily in the tighter advanced regions. This suggested the possibility of controlling the knock intensity/end-gas auto-ignition occurrence while maintaining peak pressures and heat release durations to the desired amounts. Following the successful programming of the CIM, it was then applied in the response surface method as one of the factors for optimization. However, the CIM was found to be susceptible to signal noises such as spark plugs may induce, and further development of this tool will be considered in the future.

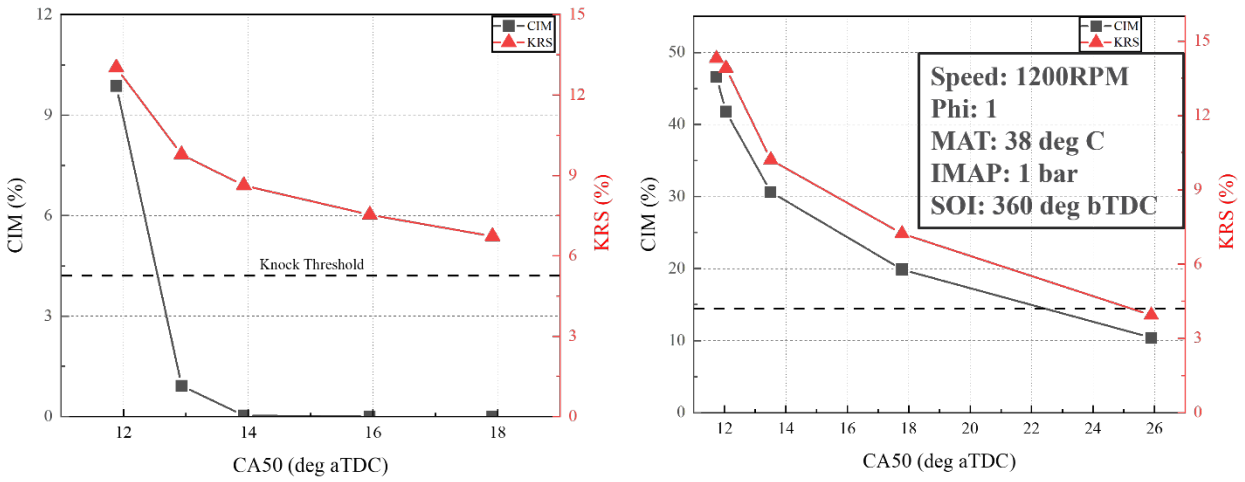

Figure 5.2-3: CIM (%) trend with KRS (%) on the engine, left – Before programming, right – After programming.

References

1. Fosudo, T., "Development of Advanced Combustion Strategies for Heavy-Duty LPG Engines to Achieve Near-Diesel Efficiency", Dissertation, Colorado State University, 2024.
2. Hampson, High efficiency natural gas engine combustion using controlled auto-ignition, in: Internal Combustion Engine Division Fall Technical Conference, Vol. 59346, American Society of Mechanical Engineers, 2019, p. V001T03A019.
3. S. M. Bayliff, Evaluation of controlled end gas auto ignition with exhaust gas recirculation in a stoichiometric, spark ignited, natural gas engine, master's thesis (2020)
4. Bayliff, S, Windom, B, Marchese, A, Hampson, G, Carlson, J, Chiera, D, & Olsen, D. (2020). Controlled End Gas Auto Ignition with Exhaust Gas Recirculation on a Stoichiometric, Spark Ignited, Natural Gas Engine. Proceedings of the ASME 2020 Internal Combustion Engine Division Fall Technical Conference. ASME 2020 Internal Combustion Engine Division Fall Technical Conference. November 4–6, 2020. V001T03A011. ASME. https://doi.org/10.1115/ICEF2020-2979

6.0 LPG Hardware Integration on X15 Cummins SCE

6.1 Cylinder Head Design/Fabrication

Cummins provided CSU with a 2.5L singe cylinder engine (SCE) based on a current production ISX15 (15 liter) diesel engine that is converted into a 2.5 liter (bore x stroke of 137 x 169 mm). Figure 6.1-1 shows the installed Cummins X15 SCE engine in the test cell. Cylinders one to five were deactivated by replacing the pistons and injectors with “dummy parts” to maintain the balance of the crankshaft system and the functionality of the lube oil system. The Cummins X15 SCE was designed and fabricated by Cummins and delivered to CSU in June 2019.

Figure 6.1-1: Cummins X15 SCE Installed engine in test cell.

A new modified cylinder head compatible with spark ignited platform was designed, fabricated, and delivered to CSU. The new head included a sleeve for the modified 5-hole Delphi injector, pressure transducer and a spark plug. Figure 6.1-2 illustrates the new modified cylinder head delivered to CSU. Initially two GDI injectors were selected: Bosch 0261-500-260 and Delphi 09M-906-036AE. Figure 6.1-3 illustrates the Bosch and Delphi injectors. However, the Bosch injector was down selected due to complexities in modifying the nozzle design. Additional parts such as a fuel tube and injector clamp were also included for easy connection of the injector.

In addition to the cylinder head and injectors, Cummins also delivered other parts such as fuel pumps and blank pistons to help with the LPG DI experiments. The Delphi pump (HM10016) was procured and shipped to Czero along with a pump housing assembly shown in Figure 6.1-4.

The pump housing was previously used on another Cummins program and was adapted from a gear train mounted design to a standalone configuration through addition of an oil seal and drain port. In addition to the pump housing modifications, a shaft adapter on Figure 6.1-4 was

procured and designed to convert the tapered shaft on the cam nose to a 5/8" keyed shaft needed to mate with the isolator coupling and electric motor selected by Czero. A hydraulic motor housing adapter was also ordered and modified to allow direct bolting to the electric motor.

Figure 6.1-2: X15 SCE new modified head.

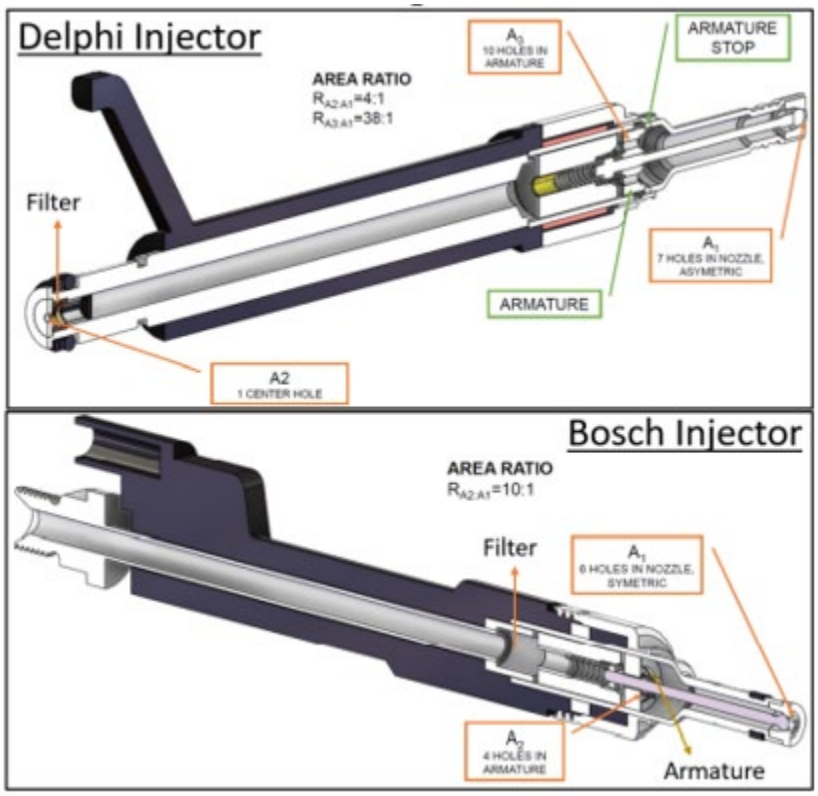

Figure 6.1-3: GDI Injectors.

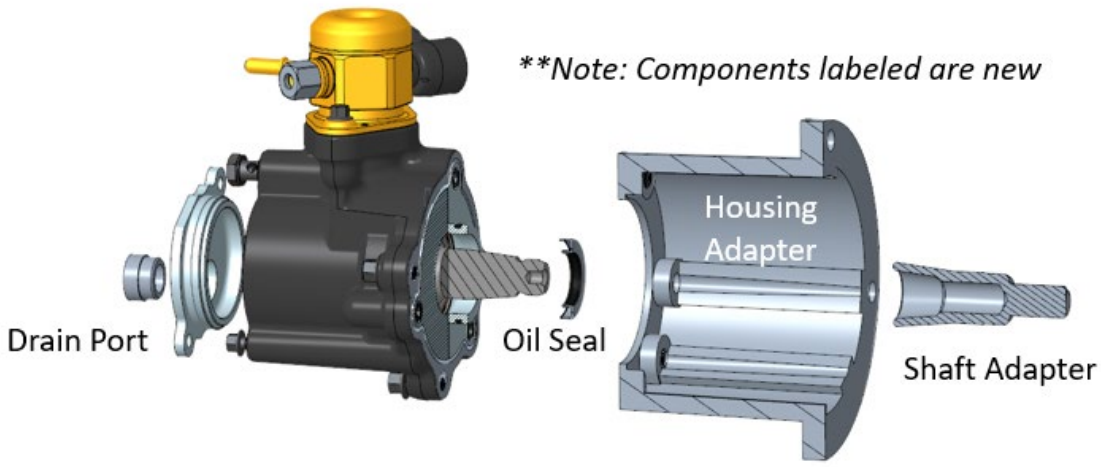

Figure 6.1-4: Fuel pump housing assembly.

6.2 Fuel Blending System Design/Installation

Fuel Blending was never implemented as it was more cost effective to buy different LPG mixtures directly from a gas supplier for the amounts of gas necessary for testing on the CFR engine. A 10-gallon refillable HD-5 propane tank was used for all X-15 testing since that is the LPG that is commercially available on a large scale in the United States and variable LPG composition had been shown to not have a significant effect on engine performance.

6.3 LPG Fuel Injection System Assembly

Section 6.3 was extracted from [1] in References.

The LPG fuel injection system was designed for the baseline operation of the engine in the port-fuel configuration and then for the direct injection of the engine on high-pressure liquid LPG. The system assemblies of both fuel delivery systems are described below.

Port Fuel Injection (PFI) System

The fuel injection system in Figure 6.3-1 was designed to ensure a steady supply of liquid LPG to an injector just upstream of the intake valve on the SCE. The LPG injector used in this configuration was the Siemens DEKA injector also used on the Roush Cleantech Ford 6.8L-V10 engine. The high impedance injector was controlled by the LECM and delivered the required amount of liquid fuel at all operating conditions. The liquid fuel delivery system consisted of a high-pressure nitrogen cylinder connected to the vapor port of an LPG tank. The nitrogen enters the LPG tank, through two sets of pressure regulators, at a pressure of ~1.6MPa. Several studies have shown that this pressure is sufficiently above the LPG vapor pressure to ensure liquid LPG all through the system [2,3].

The system was designed to incorporate the possibility of alternative fueling options on the SCE with a 3-way valve installed just upstream of the Coriolis flow meter. Two accumulators were installed up and downstream of the Coriolis flow meter to dampen any pressure fluctuations and

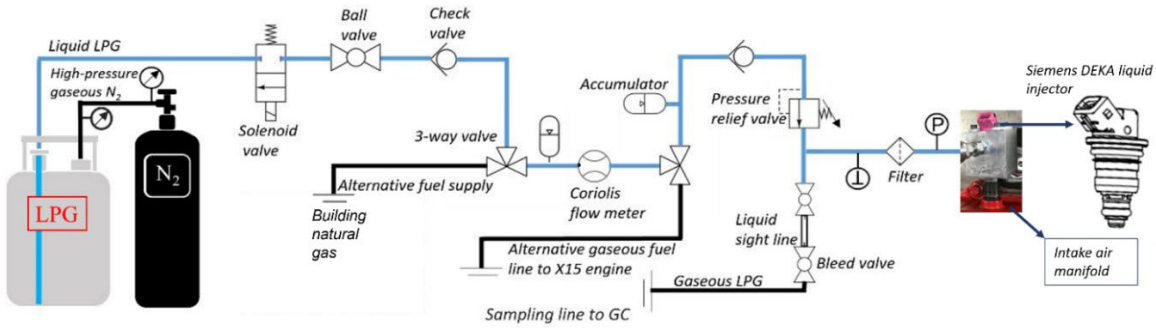

Figure 6.3-1: The schematic of the PFI system

ensure a reliable fuel flow rate measurement with the flow meter. Density measurements were displayed by the visual interface of the Coriolis flow meter, and this was a useful tool to confirm the state of the LPG in the fuel line. A sight tube installed upstream of the engine also provided visual confirmation of the phase of the fuel. Downstream of the liquid sight tube and bleed valve, the fuel line was connected to an INFICON Micro gas chromatograph to give the real-time composition of the fuel entering the injector. Battino et al. [4] showed that nitrogen is soluble over time in LPG, so particular care was taken to eliminate this possibility in this work. The empty LPG tanks were purged of nitrogen before each refill and its contact time with the LPG minimized by only initiating the flow of the nitrogen gas into an LPG tank at the beginning of the test day.

Direct Injection (DI) System

The direct injection fuel delivery system expanded on the design and successful operation of the baseline PFI fuel delivery system. The schematic is shown in Figure 6.3-2.

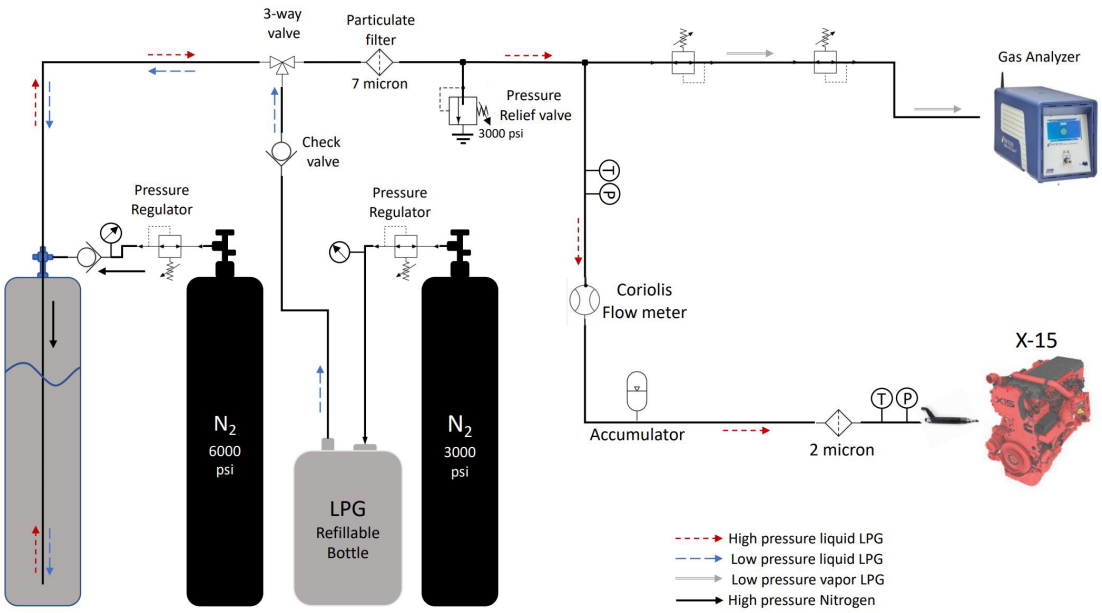

Figure 6.3-2: A schematic of direct injection system.

The direct injection system was designed with the capability to supply high-pressure liquid LPG at pressures up to 20MPa. Medium pressure liquid LPG is delivered into a cylinder rated to pressures as high as 41.36MPa and a secondary nitrogen supply at the desired injection pressure is flowed to compress the medium pressure liquid to the required injection pressure. Due to the higher nitrogen solubility at the higher DI pressures [4] compared to the PFI system, the DI system included a continuous fuel supply line to the Micro GC to provide real-time fuel composition data. A braided tube was also installed upstream of the injector to dampen any vibrations from the engine into the rigid high-pressure fuel supply line.

Both the PFI and DI systems reliably delivered liquid LPG to the engine in their respective configurations. Three main injector configurations were tested on the heavy-duty engine. Firstly, the baseline configuration as well as other high compression ratio configurations involved port-fuel liquid LPG injection using a Siemens DEKA injector. The initial set-up for the baseline study had one DEKA injector slightly upstream of the intake ports, however, this design was optimized for high-load engine operation to a double-injector set-up with valve targeting. Secondly, a Delphi 7-hole gasoline direct injector (Volkswagen 06M906036AE) was modified for LPG use as the baseline DI injector on the engine. The modification involved a metrology of two choice gasoline direct injectors (GDI) to understand seat dimensions, nozzle orifice dimensions, flow restrictions associated with the injectors. The Delphi injector was then chosen for its ease of modification and form (long-body type injector). Next, a dynamic model of the injector was created and recommended only injector nozzle orifice modification to achieve the desired high LPG flow rate required for high load operation of the heavy-duty engine and mitigate pressure losses. Based on the injector off-center location constraint and the required flow rate at peak load, 1200RPM, target efficiency conditions, a new 5-hole nozzle was machined and welded onto the stock Delphi injector to replace the 7-hole tip. The 5-hole nozzle pattern was designed to guarantee LPG spray distribution to the center of the combustion chamber despite the off-center location constraint. Finally, a commercially available high-flow LPG short-body injector (XDI LT4 +65% 7-hole injector) was physically modified for operation on the heavy-duty engine. The nozzle and spray pattern remain unchanged; however, the injector was tweaked to ensure installation was possible on the Cummins SCE. Details of the injectors and the injection configurations are presented in Table 6.3-1 and Figure 6.3-3.

The 3-hole injector was developed using CONVERGE CFD to optimize mixture homogeneity and achieve effective LPG distribution in the combustion chamber. This 3-hole design emerged as the best at different engine operating conditions in terms of intake pressure, fuel temperature, injection rates, and spray break-up or flashing tendency after simulations with other designed patterns. There were errors in the fabrication of the 3-hole injector resulting in poor injector functionality and extremely low flowrates. The problem was not able to be resolved before the contract end date. Actual testing of the 3-hole injector on the engine was designated as future work and will not be discussed further.

References

1. Fosudo, T., “Development of Advanced Combustion Strategies for Heavy-Duty LPG Engines to Achieve Near-Diesel Efficiency”, PhD Dissertation, Colorado State University, 2024.

2. Mizushima, N., Sato, S., Ogawa, Y., Yamamoto, T. et al., "Combustion Characteristics and Performance Increase of an LPG-SI Engine with Liquid Fuel Injection System," SAE Technical Paper 2009-01-2785 (2009), https://doi. org/10.4271/2009-01-2785.
3. Kim, Y., Lee, Y., Kim, C., and Shin, M., "Effects of Shape and Surface Roughness on Icing and Condensation Characteristics of an Injector in a Liquid Phase LPG Injection System," Fuel 132 (2014): 82-92, https://doi. org/10.1016/j.fuel.2014.04.010.
4. Battino, R., Rettich, R., and Tominaga, T., "The Solubility of Nitrogen and Air in Liquids," Journal of Physical and Chemical Reference Data 13, no. 2 (1984): 563-600, https:// doi.org/10.1063/1.555713

6.4 Commission X15 SCE Operation on LPG

Section 6.4 was extracted from [1] in References.

The single cylinder engine was commissioned for operation on LPG in port-fuel configuration. The engine used was a converted Cummins ISX15L 6-cylinder diesel engine. The conversion involved replacing five of the six original pistons with carefully machined dummy pistons to provide balance on the crankshaft as the active piston, the piston in cylinder number 6 in this case, was operated. The cylinder head was modified to accommodate a spark plug in the location originally intended for the diesel direct injector. The turbocharger, fuel pump, exhaust gas recirculation (EGR) components, and other diesel-allied components were also uninstalled from the original engine. The SCE is water-cooled and has the capability to run at higher loads using compressed air from the research facility. A friction model which was based on an analysis of the production diesel engine was used to account for the other cylinders thus allowing brake mean effective pressures to be calculated from the indicated mean effective pressures. Exhaustive details of the conversion and required modifications that were carried out on the original ISX15 diesel engine can be found in the experimental studies done by Rodriguez et al. [2]. A detailed specification of the SCE is presented in Table 6.4-1.

Table 6.3-1: Injection configuration details

Injector Type	**Hole Number**	**Injection duration @ nominal conditions***	**Current Profile**		**Average flow rate (g/s) at relevant injection pressures (MPa)**			
			Peak (A) [duration (ms)]	Hold (A)	1.6	14	16	17
Delphi	5	9ms	15 [3]	10	N/A	16.24	17.74	18.95
XDI	6	4.8ms	17 [3]	4		30.87		33.97
Siemens DEKA	1	11ms	5 [2.5]	2.5		N/A		

*** Nominal conditions are 1200RPM, naturally aspirated, phi: 1, injection pressure: 17MPa for Delphi, 13MPa for XDI and 1.6MPa for the Siemens DEKA injector.**

Figure 6.3-3: Injector configuration details showing all the essential features and considerations for Top: The modified Delphi 5-hole injector, its designed nozzle and spray schlieren image, Next: The high-flow XDI injector modified to long body form and its unmodified spray pattern, Next: The disassembled Delphi stock injector and a CFD optimized 3-hole spray pattern, Bottom: The PFI set-up showing the DEKA injector, both locations considered for this project, the optimized double-injector PFI mount and location designed for this engine.

Table 6.4-1: The single cylinder engine specifications.

Displacement volume (L)	2.5
Stroke (mm)	169
Bore (mm)	137
Connecting Rod (mm)	261.5
Compression ratio	9.3:1
Number of Valves	4
Exhaust Valve Open	19° BBDC
Exhaust Valve Close	2° BTDC
Inlet Valve Open	11° BTDC
Inlet Valve Close	155° BTDC

Apart from the modifications that were made to the engine hardware, several upgrades were made to the SCE and its test cell to facilitate the collection and analysis of combustion data, and determination of the performance of the engine under different operating conditions. In-cylinder pressure measurements were made with an AVL GH14DK pressure transducer (range 0-300bar) installed in the active cylinder. High speed manifold pressure measurements were performed using a Kistler 4007D piezoresistive pressure transducer and a water-cooled Kistler 4049B piezoresistive pressure transducer for intake and exhaust pressures, respectively. A BEI H25 series encoder with 0.1 crank angle resolution and LabView based high-speed National Instrument hardware (NI PXIe 6363) were used to record and analyze combustion and manifold pressure signals. A Woodward large engine control module (LECM) was used to control injection, ignition, combustion, and air-fuel ratio while giving real-time updates on the state of combustion in the cylinder. The LECM received a lower resolution position signal using a hall effect crank sensor. A model of the original X15 engine showing the converted single cylinder is shown in Figure 6.4-1.

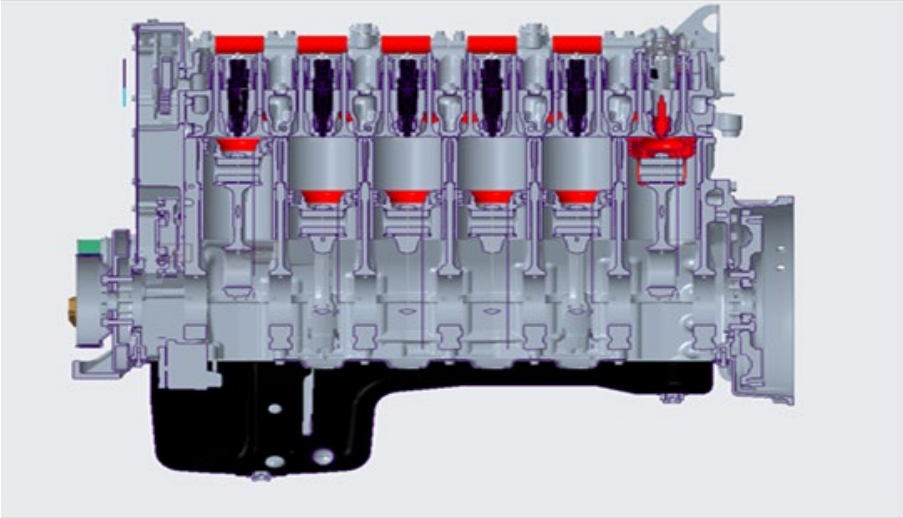

Figure 6.4-1: A CAD model of the X15 engine showing the 5 deactivated cylinders and the rightmost cylinder with the spark plug installed.

Key performance parameters were also recorded on LabView software platform using the NI 6224 and 6704 modules and on the LECM. These measurements include fuel flow rate measured using a Bronkhorst M15 Coriolis flow meter, air-fuel ratio measured with a wide-band lambda sensor LSU 4.9 (application range: lambda 0.65 to ∞), and pressure and temperatures measurements made at the required locations using absolute pressure transducers and K-type thermocouples. The engine speed was controlled by an Eaton SVX variable frequency drive (VFD) which turned the engine during motoring and applied a load during combustion. This VFD was controlled by LabView, and its value recorded in LabView as well. The high-speed combustion and manifold pressure data were logged for 1000 cycles, while 200 cycles of combustion data were logged on the LECM. Other parameters such as the fuel flowrate, engine speed, and fuel pressure were logged at a slower rate of 2Hz for 2 minutes.

A 9.3:1 compression ratio (CR) baseline piston was designed with CAD software and was fabricated at the research facility using a 3-axis computer numerical control (CNC) milling machine. The 9.3:1 CR piston was chosen to enable the baseline operation of the SCE on liquid LPG described in this paper replicate the performance of current LPG engines. Two of such identified LPG engines currently on the market are the Power Solutions International 8.8L-V8 engine and the Roush Cleantech Ford 6.8L-V10, used in the Navistar 44 CE Series and Blue Bird school buses, respectively. These engines have compression ratios of 9.1:1 and 9.2:1 respectively. A blank stock piston with the required cooling gallery was provided by Cummins and then machined to achieve 9.3:1 CR. Cummins also provided technical assistance on the minimum recommended piston crown and bowl thickness for an assumed maximum peak pressure of 7MPa. The target brake mean effective pressure (BMEP) to match the Blue Bird LPG engine at naturally aspirated conditions was 900kPa. The 9.3:1 CR was achieved by milling material off the blank piston to obtain the required clearance volume (V_c) shown in Equation 6.4.1.

$$Vc = \frac{Vd}{(CRt - 1)} \tag{6.4.1}$$

Where:

V_d is the displacement volume = 2.49 x 10-6mm^3

CR_t is the target compression ratio = 9.3

Figure 6.4-2 shows the CAD model of the final 9.3:1 CR piston. The research engine was run at 1200RPM for the best torque performance. A sweep of SOI timing tests was done with liquid LPG to evaluate the effect of closed (after IVC) and open valve (after IVO) port injection on performance, emissions, and combustion, and to select the optimal SOI for the rest of the

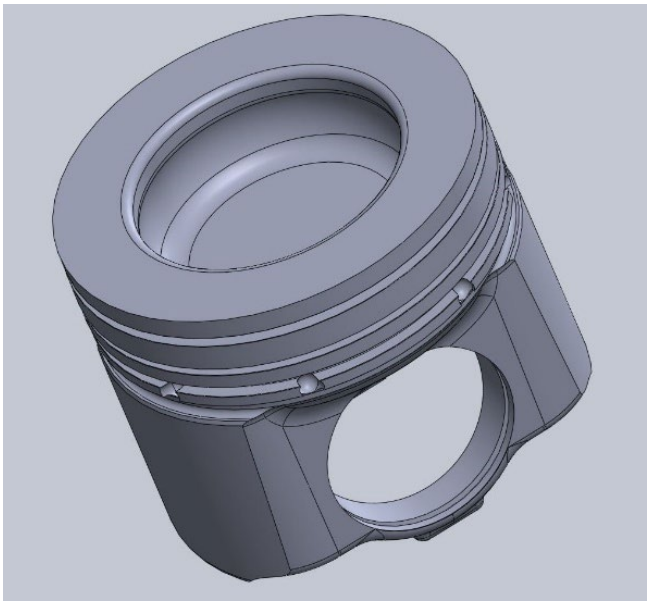

Figure 6.4-2: A CAD model of the baseline 9.3:1 piston.

experiments. With the optimal SOI determined, a spark timing sweep was carried out to establish the optimal combustion phasing, described as the MBT, with liquid LPG on the SCE. The effect of further advancing the spark timing past the MBT was also investigated to determine the effect of knock on the SCE. The MBT CA50 was then documented and utilized for the rest of the baseline study. The IMAP was increased from the naturally aspirated condition until a knock-limited load was achieved. Finally, the effect of equivalence ratio was explored from lean to rich engine operation regimes. The test matrix is presented in Table 6.4-2.

Table 6.4-2: Baseline test matrix.

ENGINE OPERATING PARAMETERS			
CR = 9.3:1, Manifold air temperature (MAT) = 38 deg C, Speed = 1200RPM, Injection pressure ~ 1.6MPa, Target BMEP ~ 900kPa			
SOI (deg bTDC)	Spark Timing (deg bTDC)	IMAP (kPa)	Equivalence Ratio
120, 150, 330, 360	6 – 18	100 – 140	0.83 – 1.25
Φ = 1 IMAP = 100kPa CA50 ~ 11 deg aTDC	SOI = 120 deg bTDC Φ = 1 IMAP = 100kPa	SOI = 120 deg bTDC Φ = 1 CA50 = MBT	SOI = 120 deg bTDC IMAP = 100kPa, CA50 = MBT
**SOI 120 and 360 deg bTDC were also evaluated at a knocking condition of CA50 = 3 deg aTDC	**The spark timing was advanced from 18 to 24 deg bTDC to investigate the occurrence and effect of knock		

Knock, emissions and BTE were quantified as described in section 1.3. Heat release analysis was conducted using the single zone equation shown in Equation 6.4.2. The specific heat ratio, γ, was deduced in real-time by the LECM using the polytropic relation. The γ of compression was calculated from 30 deg bTDC to 10 deg bTDC and the γ of expansion was determined from 10 deg after the location of peak pressure to 60 deg after the location of peak pressure for that particular engine operating condition. The average of the compression and expansion γ was then used in Equation 6.4.2 to evaluate the apparent heat release rate (AHRR).

$$\frac{dQ}{d\theta} = \frac{\gamma}{\gamma-1} P \frac{dV}{d\theta} + \frac{1}{\gamma-1} V \frac{dP}{d\theta} \quad (6.4.2)$$

Where:

P is the in-cylinder pressure

Q is the heat release

V is the cylinder volume

Uncertainty analysis was performed in this section by calculating the standard deviation (SD) of independent variables at each engine operating point. The data points used were ~3-minute averages (1000 consecutive cycles) for high-speed pressure data and ~2-minute averages for other independent variables. The root of summation of squares (RSS) technique shown in equation 6.4.3 was then applied to calculate the propagation of the SD from the independent variables to the results. However, only random errors were considered in this uncertainty analysis, as experiments were conducted on the same test cell over a relatively short period of time with the fixed errors assumed to be constant.

$$S_R = (\sum_{i=1}^{n} [S_{x_i} \frac{\partial R}{\partial x_i}]^2)^{1/2} \quad (6.4.3)$$

Where:

S_R is the total uncertainty of the result,

S_{x_i} is the uncertainty of the independent variable x_i

LPG tanks were filled at a local LPG supplier before the tests and the composition of the fuel was measured using a gas chromatograph. The composition of LPG used in this study and its properties are shown in Table 6.4-3.

Table 6.4-3: LPG properties.

Composition (%vol)	
Propane	98.473
Ethane	0.95
I-butane	0.49
N-butane	0.07
Propylene	0.01
Nitrogen	0.007
Properties	
LHV (MJ/kg)	46.36
H:C ratio	2.67
Stoichiometric AFR	15.57
Density (kg/m3)	493

The preliminary set of tests in this baseline evaluation were carried out to determine an optimal start of injection (SOI) timing. Figure 7.4-3 shows that 120 deg bTDC produced the highest brake torque, but there was no significant improvement in BTE between the closed intake valve injection SOI timings at 120 and 150 deg bTDC and the open intake valve SOI timings at 330 deg bTDC and 360 deg bTDC. Therefore, the optimal SOI that would be used in this study would mostly consider the combustion and emission characteristics at these injection timings.

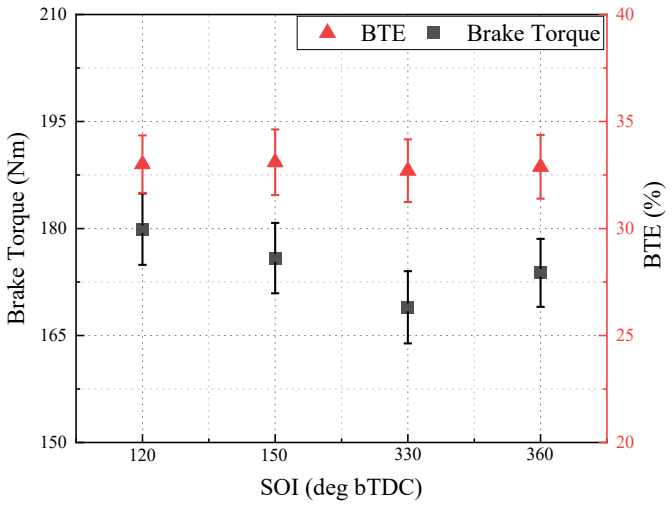

Figure 6.4-3: Brake Torque and BTE at open and closed valve injection timings.

The average in-cylinder pressure trace and apparent heat release rate indicated similar trends with the BTE. This trend is captured in Figure 6.4-4a. Further investigations were then conducted into the possible advantages of open valve timings over closed valve timings in the shape of charge cooling and its effect on knock. Spark timing was advanced to a knocking condition and the knock integral (KI) compared at this condition. Figure 6.4-4b presents the KI and COV of peak pressure, a measure of combustion stability, at the various injection timings. There was no observed difference in the knock integral values at all injection timings. However, the COV indicated that the close valve timing, 120 deg bTDC indicated a slightly more stable combustion at knocking conditions compared to open valve timing 360 deg bTDC. This is most likely due to the increased time for mixture preparation at closed valve injection timings and its promoting effect on the homogeneity of the fuel-air mixture entering the cylinder.

Finally, the engine-out emissions were compared to determine an optimal injection timing. The engine-out emissions were normalized with brake power and the brake specific results are

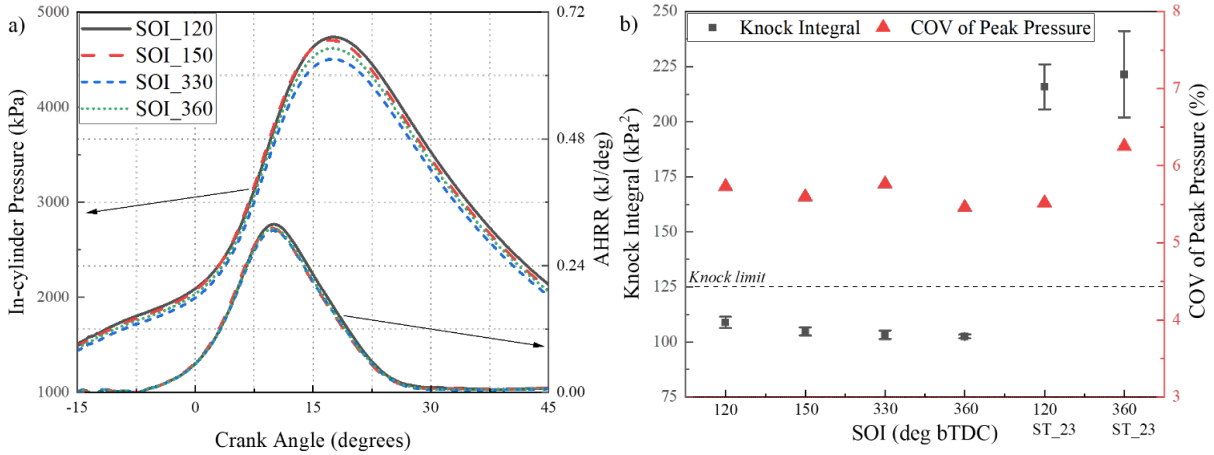

Figure 6.4-4: Comparison of (a) 1000-cycle averaged in-cylinder pressure trace and apparent heat release rates (b) knock integral and COV of peak pressure for all injection timings at knocking (spark timing 23 bTDC) and non-knocking conditions.

plotted in Figure 6.4-5. In Figure 6.4-5a, the brake specific NOx remained fairly constant across the open and closed valve timings. The brake specific CO trends indicated a 6% increase in magnitude between the lowest value at closed valve timing 150 deg bTDC and at open valve timing 360 deg bTDC for non-knocking conditions, and a 10% increase between closed valve timing 120 deg bTDC and open valve timing 360 deg bTDC for knocking conditions. This CO increase was a result of a greater degree of combustion incompleteness at the open valve timings possibly linked to mixture preparation time. In Figure 6.4-5b, while closed valve timing 150 deg bTDC indicated similar bsTHC and bsNMHC emissions to the open valve timing 330 deg bTDC, closed valve timing 120 deg bTDC produced the lowest bsTHC and bsNMHC at all non-knocking conditions. The closed valve timing (120 deg bTDC) producing the lowest hydrocarbon was similar to results presented by McGee et al. [3]. Therefore, owing to its slight advantage over the other timings especially in terms of brake torque, bsTHC and bsNMHC, 120 deg bTDC was selected as the optimal SOI for the rest of the baseline study.

The brake specific emissions plotted in Figure 6.4-6 described interesting trends as the spark timing was varied at SOI 120 deg bTDC and naturally aspirated, stoichiometric engine operating

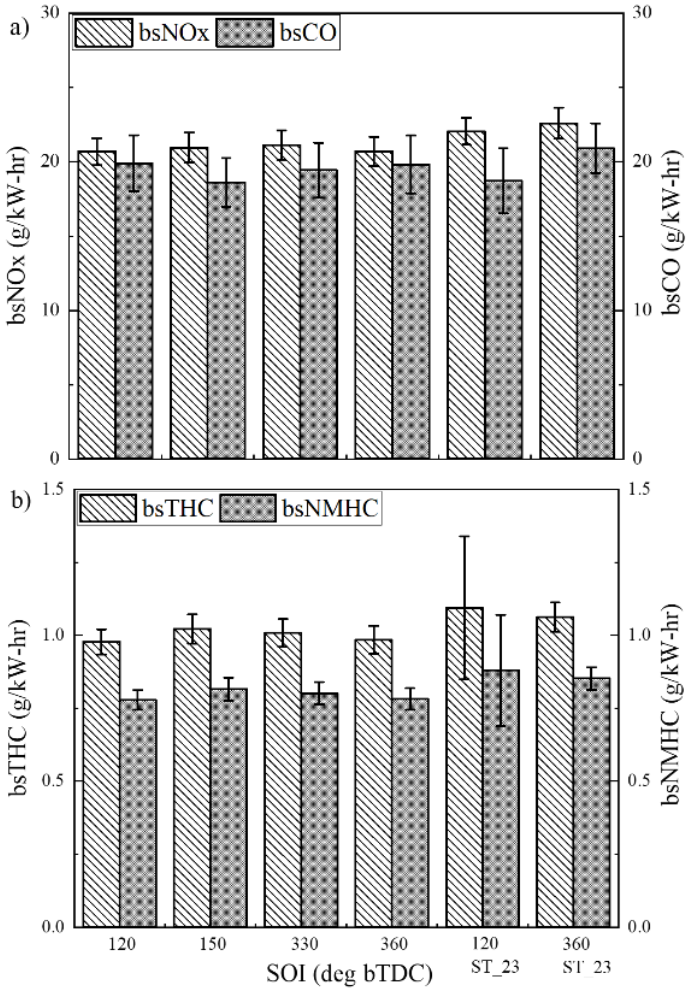

Figure 6.4-5: Brake power normalized engine-out (a) bsNOx and bsCO (b) bsTHC and bsNMHC, at the various start of injection timings and at knocking and non-knocking conditions.

conditions. As spark timing was advanced, bsNOx, shown in Figure 6.4.6a increased marginally from 19.9g/kW-hr at 6 deg bTDC to 20.7g/kW-hr at 18 deg bTDC, while there was a decreasing bsCO trend with spark timing except for the outlier at spark timing 16 deg bTDC. The normalization by brake power was responsible for the marginal increase in bsNOx as NOx ppm values (not shown) increased significantly with advanced spark timing. This increasing NOx ppm trend was also observed in the literature [4, 5]. This uptick in NOx values is due to the increase in average in-cylinder temperatures which occurred as more of the combustion and heat release occurs closer to TDC. Figure 6.4-6b shows a more consistent and pronounced increase in bsTHC and bsNMHC as spark was advanced, corroborated by the findings of Wendeker et al [4]. This is likely due to the dual effect of increased in-cylinder pressure described earlier forcing more of

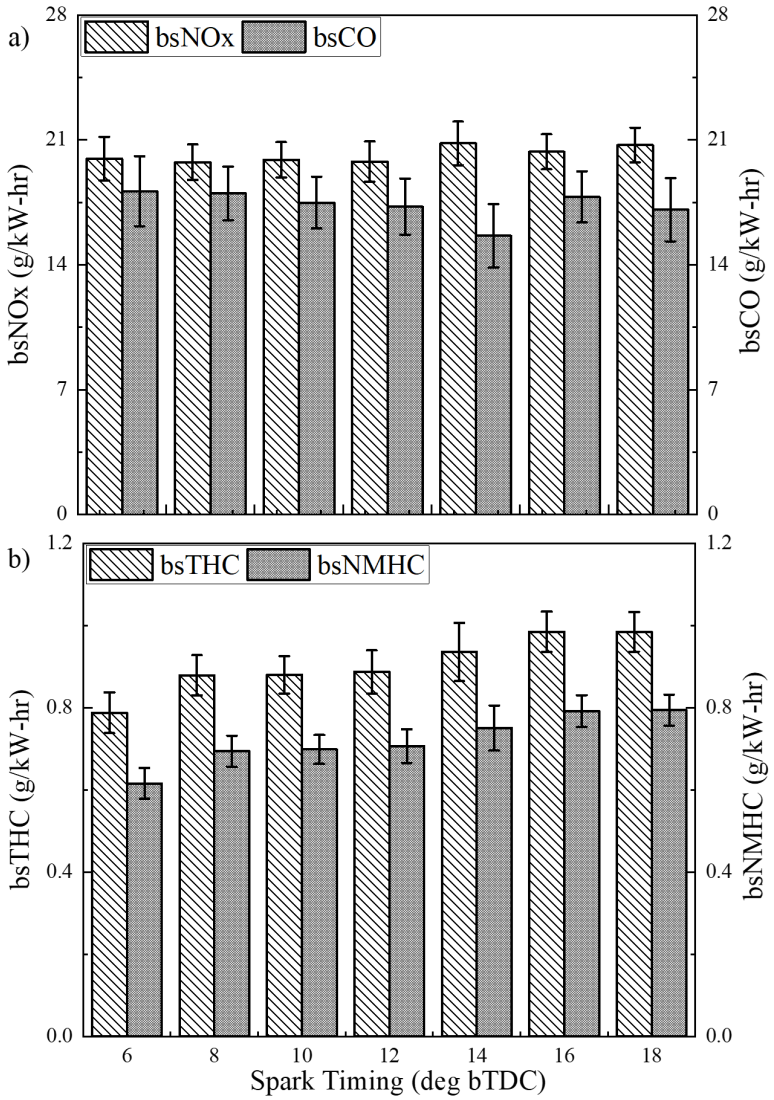

Figure 6.4-6: Comparison of engine-out emissions (a) bsNOx and bsCO (b) bsTHC and bsNMHC, for the spark timing sweep 6 -18 deg bTDC.

the fuel-air mixture into the crevice volumes and, possibly to a larger extent, the effect of in-cylinder temperatures on the oxidation of HC. Retarded timings produce higher late-cycle temperatures as more of the combustion is happening later in the cycle. Therefore, as the hydrocarbon-air mixture that was pushed into the crevice volumes reenters into the combustion chamber, the higher temperatures at retarded timings cause more of the HC-air mixture to be oxidized.

The load on the engine was increased from the initial 900kPa BMEP target, by increasing the IMAP, to a knocking operating condition. The knock limit was determined to be at an IMAP of 140kPa with a BMEP of ~1.3MPa. The results are presented in Figure 6.4-7. Two representative single cycle in-cylinder pressure traces at IMAP 100kPa and 140kPa along with their bandpass filtered values are plotted in Figure 6.4-7. The pressure oscillations as a result of knocking combustion are visible on the IMAP 140kPa line. An increase of over 40% was recorded in peak pressure values between both operating conditions. The bandpass filtered pressure plots indicate the magnitude of the pressure oscillations observed at the increased load point of IMAP 140kPa. This represented >40% increase compared to the IMAP 100kPa condition.

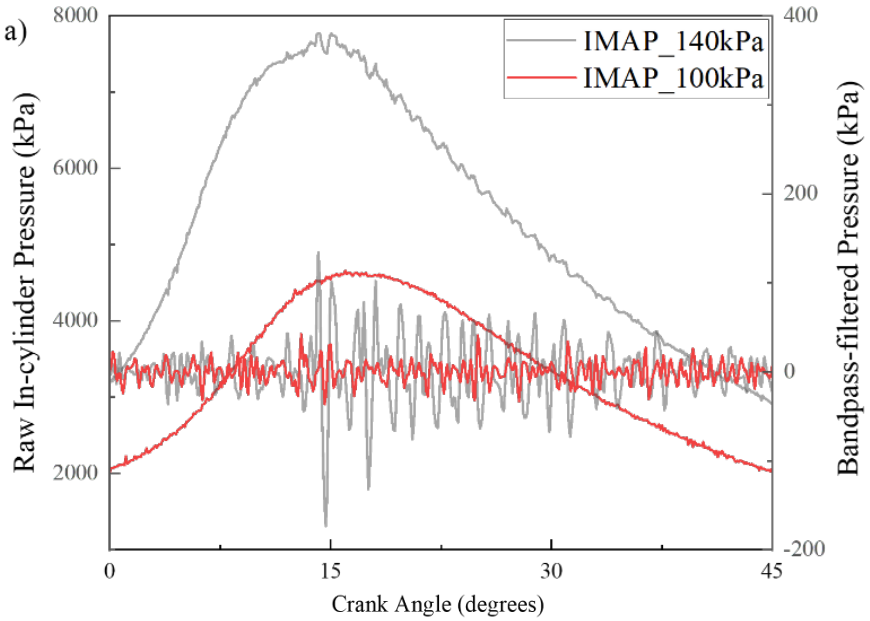

Figure 6.4-7: Plots of (a) representative single cycle in-cylinder pressure traces and bandpass filtered pressures at IMAP 100 and 140kPa.

Figure 6.4-8 demonstrates the influence of increasing load on BTE and BSFC. As the amount of fuel and air inducted into the combustion chamber and the heat release rate increased with IMAP, a greater BTE was produced by the engine and an attendant reduction in BSFC was also observed. This desired trend was also observed in previous studies [6, 7]. The BSFC was reduced by over 5% to ~221g/kW-hr at the knocking condition of IMAP 140kPa. There was also a corresponding ~5% relative improvement in BTE as load was increased to the knock limit from the naturally aspirated conditions.

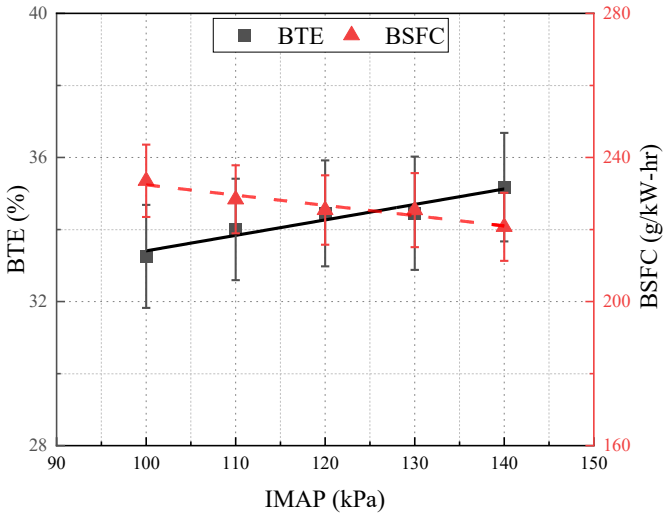

Figure 6.4-8: Plots of BTE and BSFC against IMAP at 1200RPM, ϕ = 1, and MBT

The highest efficiency recorded for the baseline PFI tests were achieved at lean conditions. Figure 6.4-9 shows the relationship between the brake torque, the BTE, and the equivalence ratio. The brake torque increased until an equivalence ratio just rich of stoichiometric at which point peak temperatures are typically experienced. Despite the relatively lesser brake torque values at the leanest operating condition (ϕ value of 0.83) investigated, the BTE was highest at this point, and this accounted for a ~22% relative improvement in BTE compared to the richest operating condition (ϕ value of 1.25). Several studies have also observed this trend of increasing efficiency with reducing equivalence ratio [8, 9, 10]. The BTE at lean conditions is higher due to the combustion products being at lower temperatures causing lower heat transfer and therefore, more expansion work to be extracted by the piston, while at rich conditions the combustion inefficiencies from an overly rich mixture dominate [10] and this severely diminishes the BTE at these conditions.

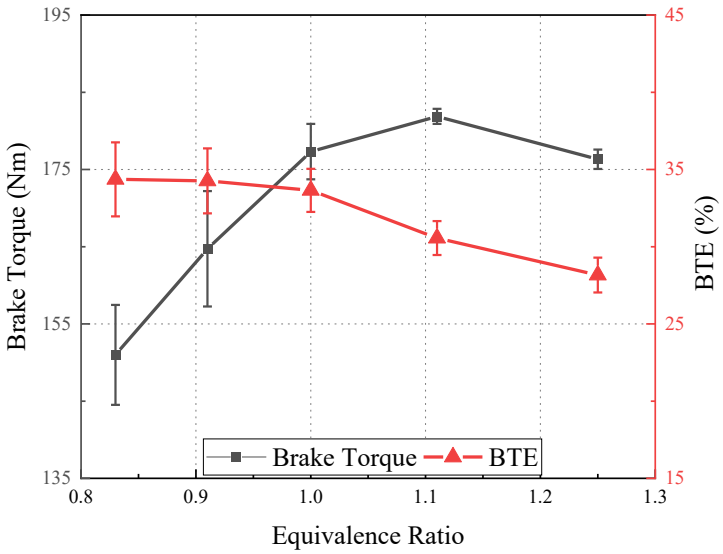

Figure 6.4-9: Comparison of brake torque and BTE for equivalence ratios 0.83 – 1.25 at engine operating condition: 1200RPM, IMAP - 100kPa, IMAT - 38 deg C and CA50 10 deg aTDC.

The commissioning of the SCE heavy-duty engine on liquid LPG was successful and the baseline results showed that:

- The PFI system consistently delivered liquid LPG at an injection pressure of 1.6MPa. This set-up guaranteed excellent control of the combustion and air-fuel ratio during the baseline experiments.
- An optimal SOI was determined by investigating the effect of open and closed valve injection timings on the engine. The closed valve timing, 120 deg bTDC, produced the lowest bsTHC and bsNMHC emissions. There was no significant improvement in BTE and knocking intensity across the injection timings. At knocking conditions, combustion stability was slightly improved by the closed valve timing, 120 deg bTDC, which also produced 10% lower bsCO than the open valve timing, 360 deg bTDC. 120 deg bTDC was selected as the optimal SOI for this study.
- The engine exhibited knocking combustion at a BMEP of 1.3MPa, corresponding to an IMAP of 140kPa. This operating condition indicated a 40% increase in peak pressure, ~5% relative improvement in BTE and over 5% reduction in BSFC compared to the naturally aspirated condition.
- There was a 6% increase in BTE between the lean condition at equivalence ratio 0.83 (34.4%) and the rich condition at equivalence ratio 1.25 (28.2%).
- Finally, the baseline LPG BTE on the heavy-duty engine platform was established as 34% i.e., at naturally aspirated, MBT, and stoichiometric conditions with PFI LPG.

References

1. Fosudo, T., Kar, T., Windom, B., Schlagel, J. et al. (2023). Performance, Combustion and Emissions Evaluation of Liquid Phase Port-Injected LPG on a Single Cylinder Heavy-Duty Spark Ignited Engine. SAE Technical Paper 2023-01-0245. doi:10.4271/2023-01- 0245
2. Rodriguez, F., Xu, H., Hampson, G., Windom, B. et al., “Heavy Duty Natural Gas Single Cylinder Research Engine Installation, Commissioning, and Baseline Testing,” Energy and Power Engineering, 14, 217-232, 2022, https://doi.org/10.4236/epe.2022.146012
3. McGee, M., Curtis, W., Russ, G., Lavoie, A., “The Effects of Port Fuel Injection Timing and Targeting on Fuel Preparation Relative to a Pre-Vaporized System,” SAE Technical Paper 2000-01-2834, 2000
4. Wendeker, M., Jakliński, P., Czarnigowski, J., Boulet, P. et al., “Operational Parameters of LPG Fueled SI Engine-Comparison of Simultaneous and Sequential Port Injection,” SAE International, 2007-01-2051, 2007
5. Sierens, R., “An Experimental and Theoretical Study of Liquid LPG Injection,” SAE Technical Paper 922363, 1992, https://doi.org/10.4271/922363.
6. Fosudo, T., Kar, T., Windom, B., and Olsen, D., “Comparative Analysis of a Spark-Ignited CFR Engine Operation on Compressed Natural Gas and Liquefied Petroleum Gas at Stoichiometric Conditions,” Proceedings of the Western States Section of the Combustion Institute Spring Technical Meeting, 2022.
7. Singh, S., Dhar, A., and Agarwal, A., “Technical feasibility study of butanol-gasoline blends for powering medium-duty transportation spark ignition engine,” Renewable Energy, 76, 706–716, 2015, https://doi.org/10.1016/j.renene.2014.11.095
8. Pradeep, V., Bakshi, S., and Ramesh, A., “Direct Injection of Gaseous LPG in a Two-Stroke SI Engine for Improved Performance,” Applied Thermal Engineering, 89, 738–747, 2015, https://doi.org/10.1016/j.applthermaleng.2015.06.049

9. Dube, A., Vivekanand, M., and Ramesh, A., “Experimental Studies on Liquid Phase LPG Direct Injection on a Two-Stroke SI Engine,” SAE International Journal of Engines, 12(3), 2019, https://doi.org/10.4271/03-12-03-0023.
10. Heywood, J.B., “Internal Combustion Engine Fundamentals,” McGraw-Hill, New York, USA, 1988

7.0 System Optimization for Near-Deisel Efficiency on X15

Section 7.0 was extracted from [1] in References.

7.1 Direct Injection Testing

The engine operation on DI mode required a more involved process as the engine cylinder head had to be redesigned to accommodate the direct injector due to the centrally located sparkplug. The redesigned cylinder head was fabricated by Cummins and installed on the engine along with the direct injectors developed for high-pressure LPG injection. A picture of both cylinder heads used in this project during a cylinder head swap is presented in Figure 7.1-1.

Figure 7.1-1: Engine cylinder head and manifolds swap in progress

Three pistons were installed on the heavy-duty Cummins engine for direct injection tests namely.

1. The baseline 9.3:1 piston
2. The 11.9:1 “Natural Gas” piston
3. The CFD-optimized high-squish 14:1 piston

The pistons were designed with CAD software and fabricated at the Colorado State University powerhouse research facility using a 3-axis computer numerical control (CNC) milling machine. The 9.3:1 CR piston was chosen to enable the baseline operation of the Cummins SCE on liquid LPG replicate the performance of current LPG engines. The 11.9:1 piston was designed for natural gas operation on the X15 engine and adopted for LPG applications to provide useful data on the performance of the engine at compression ratios higher than the baseline piston. The high-squish 14:1 piston was then developed using combustion models calibrated and validated with engine data obtained at 9.3 and 11.9 compression ratio to computationally optimize combustion

chamber design, piston bowl shape, in-cylinder charge motion and homogeneity and compression ratio for peak thermal efficiency and knock mitigation. Figure 7.1-2 shows the CAD model and pictures of the piston configurations used on the X15 LPG engine. The cooling galleries have been filled out in the CAD section views.

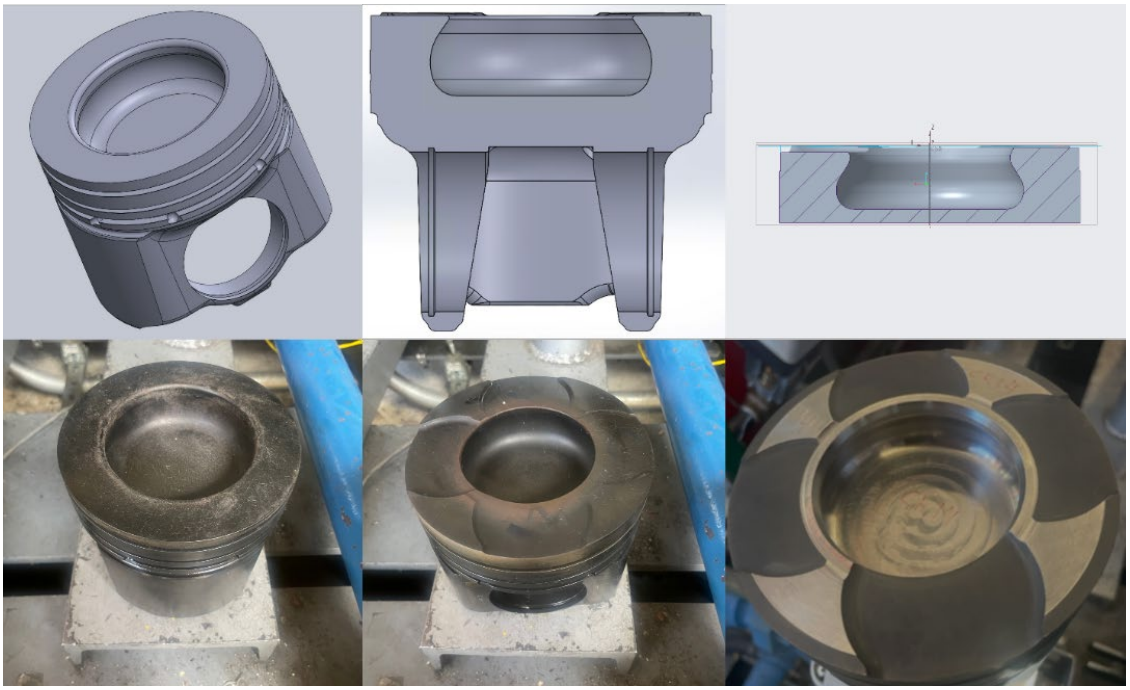

Figure 7.1-2: Compression ratio optimization direction on the X15 LPG engine showing the CAD model (top) and pictures (bottom) of the pistons for Left: The baseline 9.3:1 piston, Middle: The 11.9:1 "Natural Gas" piston, Right: The CFD-optimized high-squish 14:1 piston.

Three sparkplug options shown in Figure 7.1-3 were considered for the heavy-duty engine operation. The Altronic L1863B massive 3-prong nickel sparkplug was used as the baseline sparkplug. The sparkplugs were designed for large, and medium bore stoichiometric and lean-burn engines [2]. One of the key advanced combustion strategies used in this work was the passive pre-chamber combustion enabled by the Woodward FTI pre-chamber sparkplug. The FTI igniter which was developed for large bore lean-burn engines and designed for high in-cylinder pressures generates a multi-jet flame front from the holes on its surface to provide a faster, more stable combustion in these large bore engines [3]. The pre-chamber FTI sparkplug was especially important in this work in mitigating misfire and knock thus extending the EGR tolerance limit and increasing engine efficiency at high EGR-diluted in-cylinder mixture operation. A regular J-gap sparkplug was also tested to demonstrate the improvements with the 3-prong and FTI sparkplugs.

For these sets of tests, knock intensity calculation was mostly based on the Woodward LECM operation called the knock ripple sum (KRS). The KRS considers the 50 previous pressure traces of engine operation and takes an average of these traces to set as the reference. Knocking traces and their intensities can then be analyzed by subtracting the reference trace from the knocking trace in real-time, generating a history of pressure fluctuations vs crank angle degrees.

A composite picture of the heavy-duty Cummins ISX15L engine test cell and a few of its integral details are presented in Figure 7.1-4.

The knock ripple sum is scaled on a 0 to 100% basis and thresholds of transition from no knock to light, medium and heavy knock were determined and set during engine operation. Also, nominal repeat tests were conducted for every day of testing at the same engine operating condition to determine the random uncertainty. The random uncertainty for each measured

Figure 7.1-3: Spark plug options for the heavy-duty LPG engine operation Left: The Woodward Fast Turbulent Igniter (FTI) Pre-chamber sparkplug, middle: The Altronic L1863B 3-prong massive nickel sparkplug, right: The regular J-Gap sparkplug.

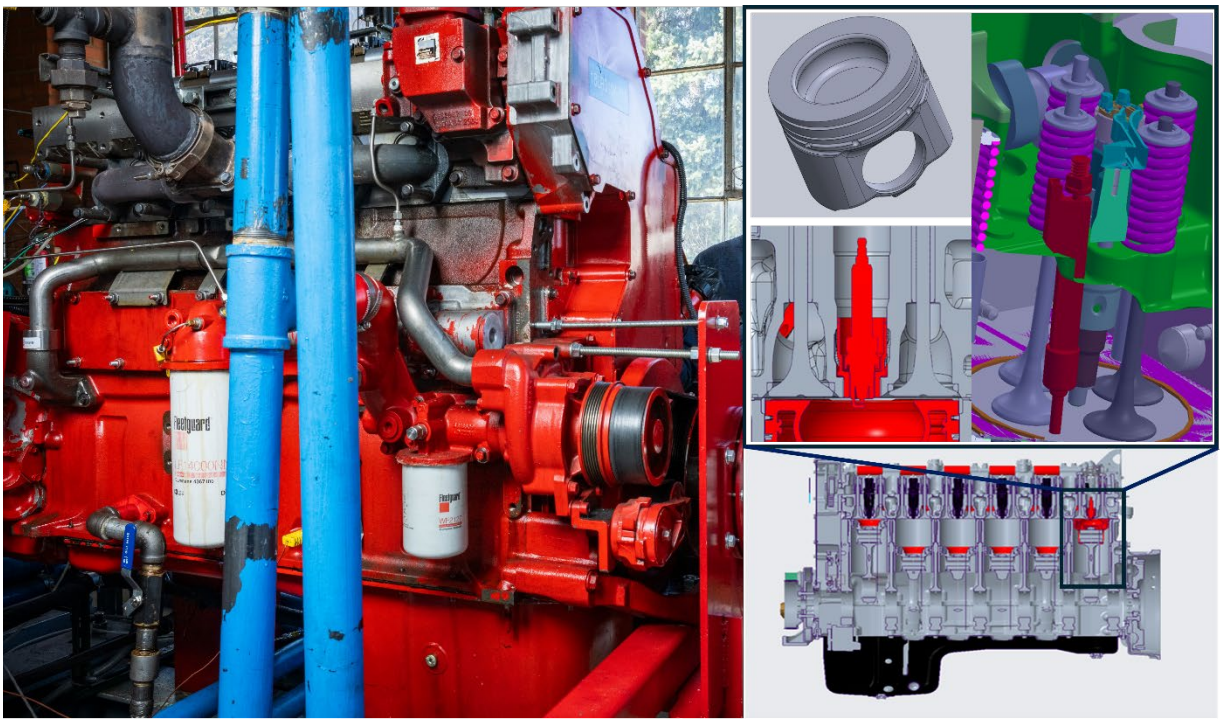

Figure 7.1-4: Left - X15 SCE; Top Right – Cut-out of key sections of the cylinder head showing the valves and the centrally located spark plug, off-center installed direct injector and baseline 9.3:1 piston; Bottom Right – CAD of the six-cylinder engine showing the active single cylinder, cylinder 6.

variable was then propagated to the results of interest using the root of summation of squares equation [4] in Equation 7.1.1

$$w_R = (\sum_{i=1}^{n}[w_{x_i}\frac{\partial R}{\partial x_i}]^2)^{1/2} \quad (7.1.1)$$

Where:

w_R is the total uncertainty of the result

w_{x_i} is the uncertainty of the independent variable x_i

A summary of the direct injection tests using the 5-hole LPG injector is presented below. Start of injection and combustion phasing in terms of CA50 are varied on the engine at all tested compression ratios in DI mode. The 3-D plots in Figure 7.1-5 demonstrate the relationship between compression ratio and key engine combustion, performance and emission metrics. Figure 7.1-5a indicates that combustion is mostly stable (COVimep < 3%) in the early start of injection timings for all CR configurations due to the maximized mixture preparation time. There were islands of relative stability encountered at a few late SOI timings, while the region between 240 and 300 deg bTDC suffered from higher combustion instability than some later SOI timings pointing to the possible influence of other in-cylinder factors such as piston and valve position, combustion chamber design and spray dynamics on combustion stability. For example, the high squish 14:1 piston did not indicate any late SOI region of combustion stability with as high as 40% COVimep at the most retarded SOI timing. Figure 7.1-5b showed that the direction of improving efficiency is at higher compression ratios as backed by the literature [5, 6] and earlier SOI timings. For example, the 14:1 piston improved BTE by ~13% relative to the baseline 9.3:1 piston at 360 deg bTDC. Figure 7.1-5c described very interesting results for the bsNOx emissions as the maximum region was found at earlier SOI timings due to the reduced effect of the LPG spray charge cooling but not exactly at the earliest SOI times which would have the most reduced charge cooling effect. The minima also found as expected at retarded SOI timings due to the increased effect of the LPG spray vaporization cooling the charge and reducing combustion temperatures but not exactly at the most retarded SOI times. Even more interesting was the observed trend of CR 14:1 piston producing the lowest bsNOx while the CR 11:9 piston generated the highest bsNOx emissions. This was believed to be as a result of the superior design of the CR 14:1 piston specifically for LPG combustion and for better thermal management as despite the higher in-cylinder pressures and consequently temperatures the piston was exposed to, the CR 14:1 piston indicated similar exhaust gas temperatures (not shown) as the CR 11.9 piston at all tested CA50s. This led to comparatively better bsNOx emissions at this high compression ratio. Finally, the bsTHC emissions are presented in Figure 7.1-5d. The bsTHC plot demonstrates a distinct dependence on the COVimep as the regions of severe combustion instability (retarded SOI timings, high 14:1 compression ratio) were also the regions of high THC emissions. This misfires and partial burns associated with the retarded injection timings were most likely responsible for this trend. Another possible contributor was the design of the 14:1 piston. The

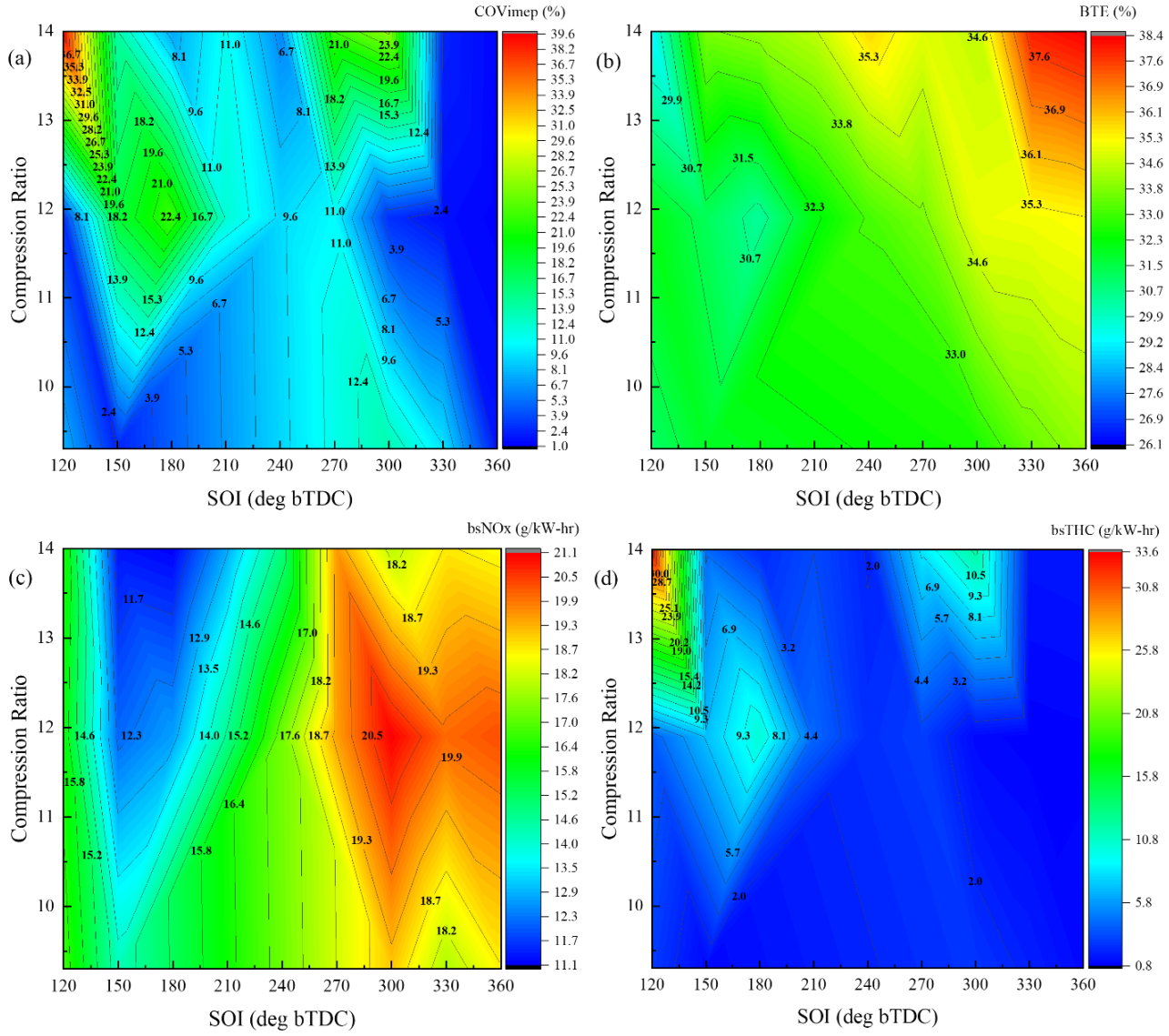

Figure 7.1-5: 3-D plots showing the relationship between compression ratio and (a) COVimep (%) (b) BTE (%) (c) bsNOx (g/kW-hr) (d) bsTHC (g/kW-hr) and SOI (deg bTDC) with the 5-hole DI configuration.

high squish design likely forces more charge into the crevice regions especially at the late SOI timings which is then reintroduced into the cylinder, and for the fraction that escapes low temperature oxidation, into the exhaust stream as HC emissions.

Upon conclusion of the SOI tests, the combustion phasing was advanced for all tested pistons from a retarded CA50 timing to the MBT combustion phasing. If the spark cannot be advanced until MBT before the occurrence of knock, the engine is said to demonstrate knock limited spark advance or be knock limited. The limits on the left of the 3-D plots in Figure 7.1-6 are the knock limits on the engine as compression ratio was increased, implying that the engine will transition into uncontrollable, abnormal combustion if the spark was advanced into that region. While there was some play left in this knock region for further slight advances of combustion phasing,

these tests were limited to safe intensities of medium knock as the knock limit. To further demonstrate the relationship of compression ratio with knock and combustion phasing, the knock ripple sum (KRS) is plotted in Figure 7.1-6a. As the center of combustion is advanced towards TDC leading to higher peak pressures and temperatures, the KRS increases. A similar effect was observed as compression ratio was increased up from 9.3 to 14 with a maximum KRS at CA50 10 deg aTDC for the CR 14:1 piston. A subjective KRS threshold of 4.2% was determined as the value above which the engine began to exhibit incipient knock in this study. The 4.3 line on Figure 7.1-6a shows that the higher compression ratios would require significant combustion phasing retardation to completely avoid knock with the LPG fuel on the heavy-duty engine. Next, the MBT timing was determined from the brake torque trends in Figure 7.1-6b. The MBT timing points to the combustion phasing where the combination of work done on the gas by the piston and work done by the gas produce the highest torque for a particular engine configuration. The lower compression ratios (9.3:1 and 11.9:1) showed that maxima somewhere between CA50 7 and 9, but then the engine began to exhibit knock limited spark advance as compression ratio was increased further as can be observed from the change of slope on the left limit of the 3-D curve. Nevertheless, CR 14:1 achieved the highest brake torque and BTE with the compression ratio configurations with 193.7Nm, ~4% higher than the peak torque at CR 9.3:1, and 39.1% BTE. The bsNOx trends in Figure 7.1-6c demonstrate similar patterns to those discussed earlier in Figure 7.1-5c in terms of their relationship with compression ratio. Combustion phasing had the effect of increasing bsNOx as phasing was advanced owing to the higher in-cylinder pressures as combustion is moved closer to TDC and the consequently higher temperatures which then promote the NOx formation chemistry. Figure 7.1-6d presents the relationship between bsTHC, combustion phasing and compression ratio. As combustion phasing is retarded, the engine experiences higher late cycle temperatures which then improves the low temperature oxidation of the reintroduced charge from the crevices. This effectively reduces the bsTHC emissions as is shown in Figure 7.1-6d. On the other hand, as compression ratio is increased the in-cylinder peak pressures are also increased (demonstrated in the next figure), this increased pressure forces more charge into the crevices. This, along with the possibility of the high squish design forcing more charge into the crevices, was likely responsible for the increase in the peak bsTHC, from 1.13g/kW-hr at the baseline 9.3:1 compression ratio to 1.37g/kW-hr at the high squish CR 14:1 compression ratio configuration at the most advanced CA50 tested for each CR.

Finally, the in-cylinder pressures and apparent heat release rate curves are shown in Figure 7.1-7 for the three compression ratio configurations and the same engine operating condition. The CR 14:1 piston exhibited the highest peak pressures as mentioned earlier and the steepest rate of pressure rise amongst the three tested configurations. The CR 14:1 piston also indicated the highest peak rate of heat release and the shortest heat release duration of the three pistons. A significant observation in this plot is the presence of the distinctive shoulder on the AHRR curve for the CR 14:1 piston which pointed to the presence of a secondary combustion event or some end-gas auto ignition at this operating condition on the engine. Considering all factors, the CR 14:1 was shown to be a successful design and was moved forward for the rest of the EGR, BMEP and BTE optimization tests.

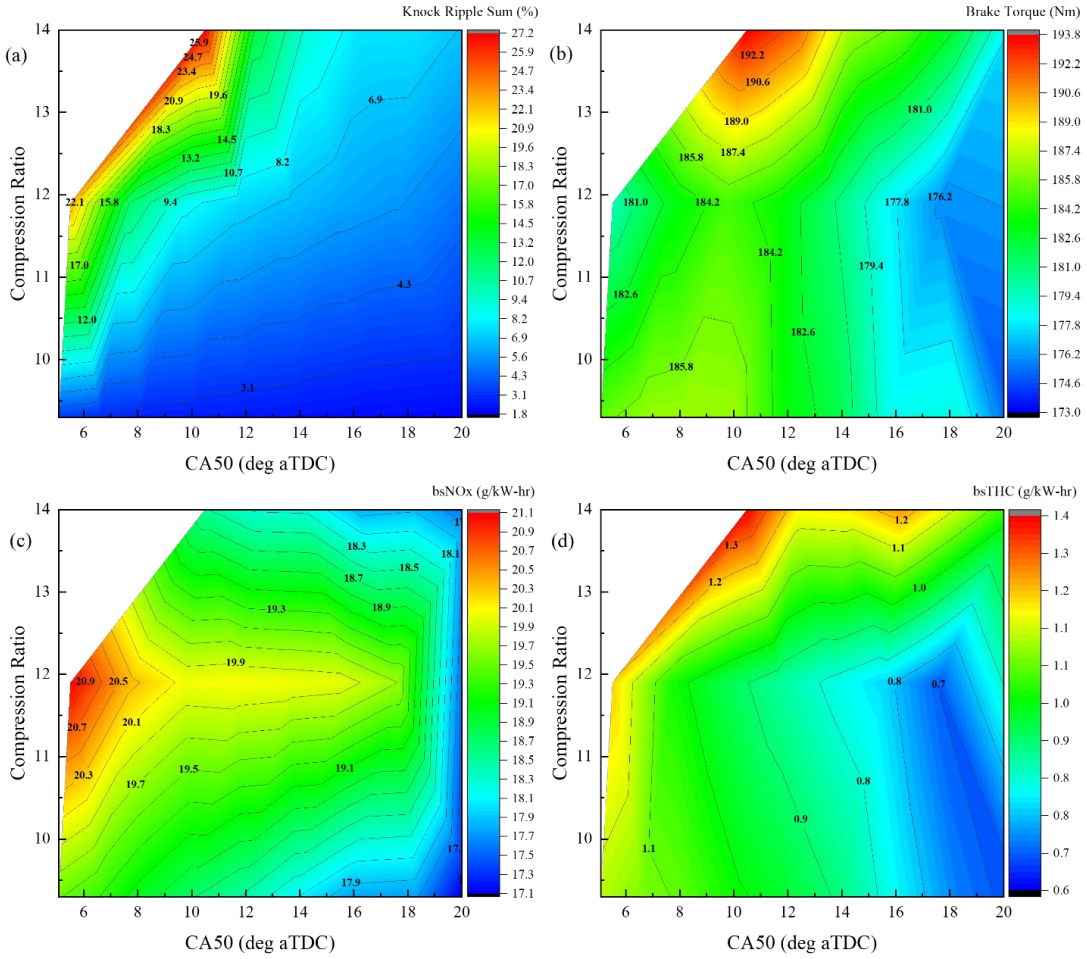

Figure 7.1-6: 3-D plots showing the relationship between combustion phasing and (a) KRS (%) (b) Brake Torque (Nm) (c) bsNOx (g/kW-hr) (d) bsTHC (g/kW-hr) and CR with the 5-hole DI configuration.

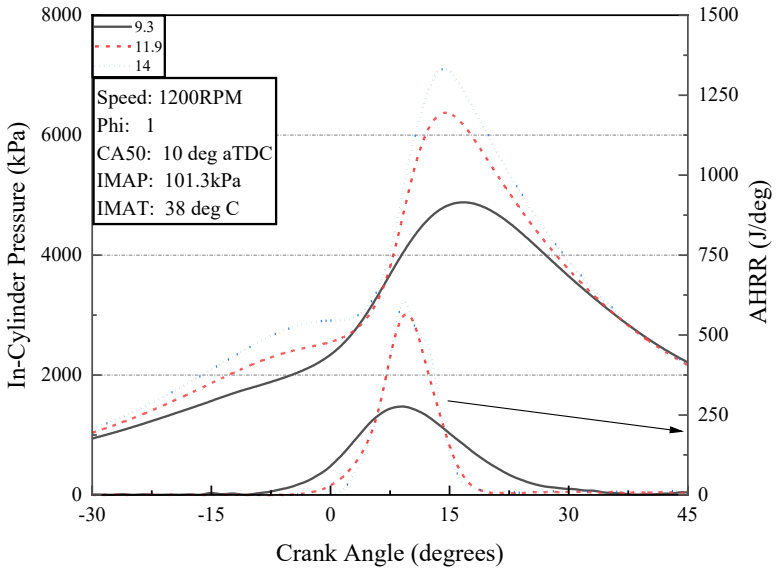

Figure 7.1-7: Combustion characteristics for the three compression ratio configurations on the engine

7.2 EGR Tolerance Testing

The EGR tolerance tests began with a redesign of the EGR measurement procedure to avoid the fluctuations encountered with the EGR flow measurements on the CFR engine. CO_2 concentrations were used to calculate the $\dot{m}_{EGR}$ on the heavy-duty X15 engine using Equation 7.2.2.

$$\dot{m}_{air} * X_{CO_{2_{air}}} + \dot{m}_{egr} * X_{CO_{2_{exh}}} = \dot{m}_{egr+air\_mix} * X_{CO_{2_{egr+air\_mix}}}$$

$$\dot{m}_{egr} = \dot{m}_{air} * \frac{X_{CO_{2_{air}}} - X_{CO_{2_{egr+air\_mix}}}}{X_{CO_{2_{egr+air\_mix}}} - X_{CO_{2_{exh}}}}$$

(7.2.1)

Where:

$X_{CO_{2_{air}}}$ is the mass fraction of CO2 in air

$X_{CO_{2_{egr+air\_mix}}}$ is the mass fraction of the CO2 in the intake air and EGR mixture

$X_{CO_{2_{exh}}}$ is the mass fraction of the CO2 in the exhaust

The main assumptions allowing this equation to be used were that the mole fraction of CO_2 in air was 410ppm, the LPG fuel had no CO_2 in its composition (confirmed by all gas chromatographs results) and that the CO_2 already in the intake charge does not participate in any further reactions. The EGR rates obtained with this method were in agreement with the calculated AGA report #3 values and showed the desired consistency.

EGR was introduced at low load conditions (900kPa BMEP) on the 11.9 'natural gas' piston with the baseline 5-hole modified injector and the 3-prong spark plug. The results are shown in Figure 7.2-1a for the EGR sweep at an early direct injection SOI timing (EDI) of 360 deg bTDC and a late direct injection SOI timing (LDI) of 120 deg bTDC. The EGR_{peak} is defined as the EGR rate at which the COV of peak pressure ~= 10% and the COV of IMEP < 3%. The key observation was that the EGR_{peak} at LDI was found to be around 7%, which was then more than tripled to over 22% at the early DI condition. This had a knock-on effect on BTE as the BTE at EGR_{peak} for the EDI case was 37.4%, ~11% relatively higher than the BTE at EGR_{peak} for the LDI scenario. Figure 7.2-1b shows the BTE, KRS and bsNOx as EGR was increased up to its limit at 360 deg SOI with the optimized PFI, the high squish 14:1 compression ratio piston and the prechamber spark plug configuration. The tests were conducted at low loads (1MPa BMEP). EGR has been shown to mitigate knock and NOx on the CFR engine and in the literature [5], however, it was imperative to demonstrate this on the heavy-duty LPG engine in order to understand the EGR limitations and define an EGR_{peak} value. The EGR_{peak} for this configuration was measured to be 29% shown in Figure 7.2-1b at the inflection point after which BTE starts to trend downwards. Similar values were measured for the high-flow DI injector using the 14:1 compression ratio and prechamber spark plug engine configuration at the same engine operating conditions. In terms of bsNOx and knock mitigation, the results showed an 88% and 68% reduction respectively as EGR was increased from 15% to

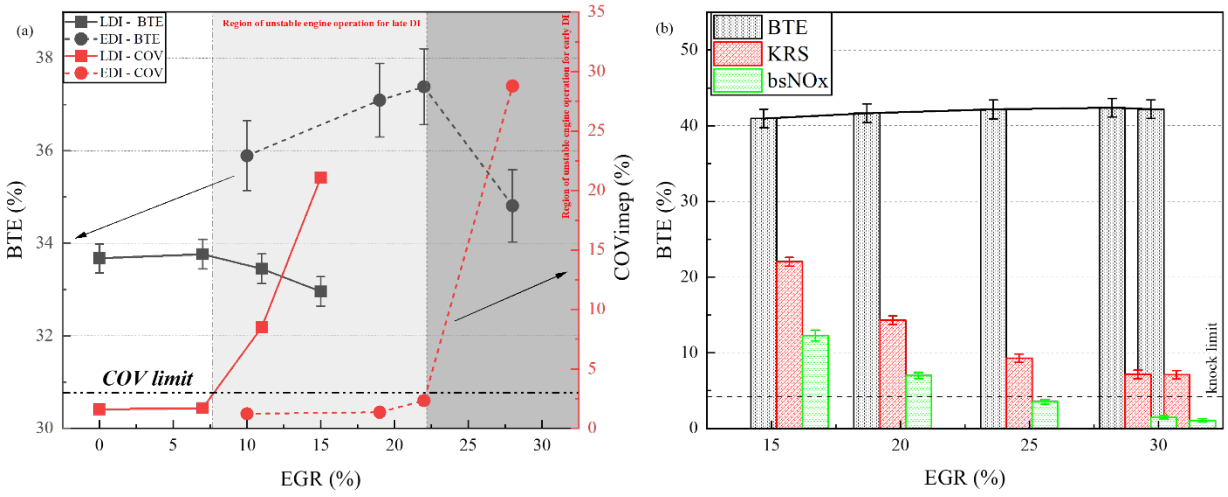

Figure 7.2-1: Plots of (a) BTE (%) and COV_{imep} (%) vs EGR (%) at late (120) and early (360) SOI timings (deg bTDC) for the 5-hole modified direct injector on the 11.9:1 compression ratio engine with the 3-prong spark plug and (b) BTE (%), KRS (%) and bsNOx (g/kW-hr)) vs EGR (%) for the 14:1 compression ratio engine with the prechamber spark plug, at early SOI 360 deg bTDC.

the EGR_{peak} value of 29%. This reduction continued beyond the EGR_{peak} point but BTE started to trend downwards as combustion stability began to suffer.

The preceding results showed that SOI 360 deg bTDC once again demonstrated superior performance but this time in terms of EGR operation. Figure 7.2-2 presents the combustion and emissions results at this optimized SOI timing. Figure 7.2-2a shows the pressure and AHRR traces as EGR was varied. Increasing EGR was shown to reduce the peak pressure and peak AHRR as well as increase the heat release duration. In terms of emissions, the brake specific NOx (bsNOx) trends were promising and consistent with the literature, with over 80% reduction in bsNOx at the EGR limit as a result of the reduced in-cylinder temperatures from introducing the exhaust gases. The bsCO trends were also encouraging with an overall reduction in bsCO as EGR was increased up to the EGR limit, however, unlike the bsNOx trends the bsCO increased drastically after the EGR limit by almost 100%. BsTHC demonstrated a steady rise as EGR was introduced into the cylinder. This was likely due to the deteriorating combustion at higher EGR dilution rates and the lower combustion temperatures associated with the recirculated exhaust gases which would then reduce the rate of oxidation of HCs that reenter into the cylinder from the crevice volume.

To mitigate the knocking propensity at high compression ratios and achieve the high-load conditions, the IMAP was increased and cooled exhaust gases recirculated into the engine with an attendant reduction in knocking intensity on the engine. The EGR was maintained at the EGR_{peak} for each load condition. In Figure 7.2-3 below, the knock ripple sum was monitored for several engine operating conditions and plotted in a contour plot with the engine load and BTE.

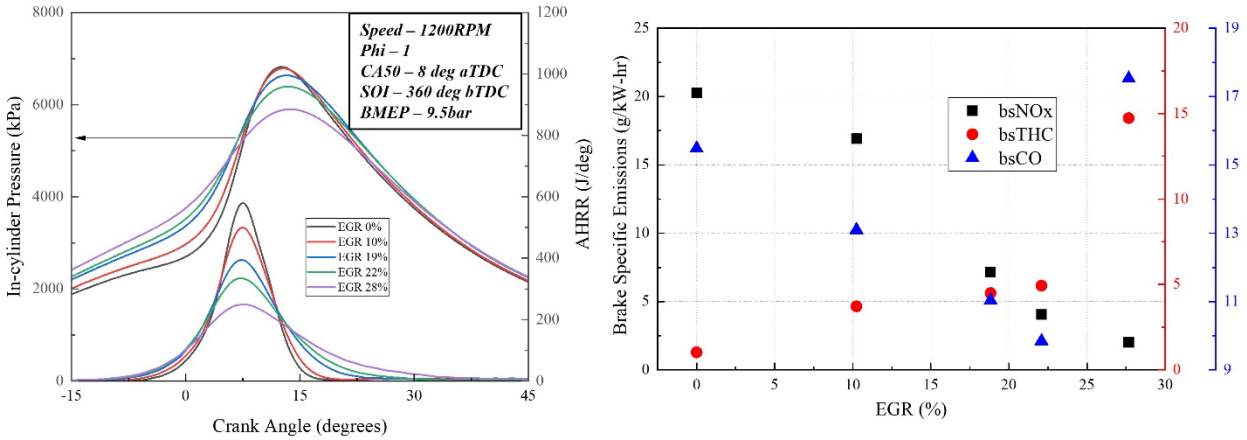

Figure 7.2-2: (a) In-cylinder Pressure (kPa) and AHRR (J/deg) traces and (b) Brake Specific Emissions (g/kW-hr) with varying EGR (0% to the EGR limit) on the engine

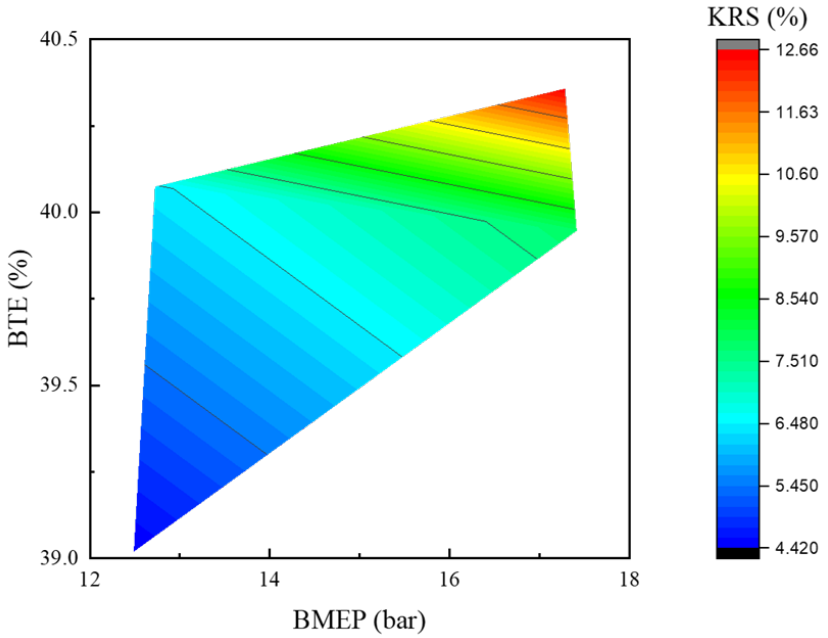

Figure 7.2-3: Contour plot showing the relationship between the Knock Ripple Sum (%), Engine load (bar) and BTE (%) for engine operation conditions: EGR_{peak}, 1200RPM, MAT: 38 deg C, Phi: 1 and variable CA50 (deg aTDC) for the XDI high flow injector engine configuration.

Figure 7.2-3 illustrates the importance of fine end-gas autoignition (EGAI) control on the engine as BTE was maximized at a KRS of ~13% and high load on the engine. This indicated that the CIM will become a critical tool in the optimization experiments and the achievement of the target efficiency in DI mode. Figure 7.2-4 shows the high load, EGR_{peak} operation of the engine with the optimized PFI configuration. In Figure 7.2-4a, an increasing trend of BTE with load was exhibited at a near constant EGR_{peak} of ~27%, until a maximum BTE of 43% (the highest recorded so far with LPG) was achieved at 15bar BMEP. After this point, the EGR tolerance started to diminish and the BTE suffered.

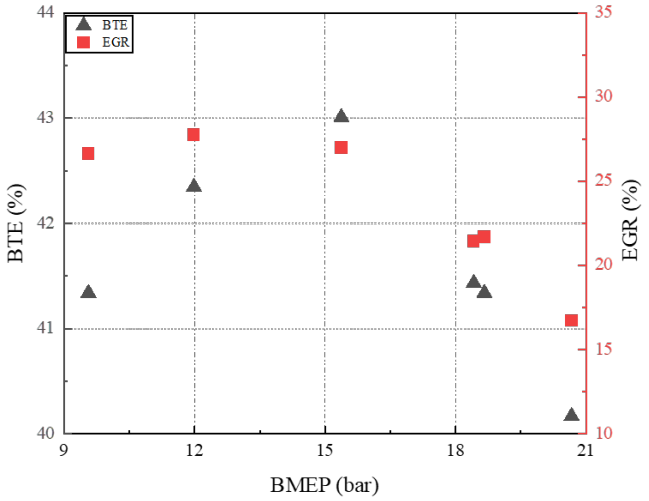

Figure 7.2-4: Plots of (a) BTE (%) and EGR (%) vs BMEP for each load condition at EGR_{peak}, 1200RPM, MAT: 38 deg C, Phi: 1 and CA50 determined by a KRS ~15%, for the optimized PFI engine configuration.

The ignition configurations were also tested at the CFD optimized 14:1 compression ratio piston and the high-flow DI configuration to determine their influence on EGR tolerances. Figure 7.2-5 shows the comparison between the 3-prong spark plug and the prechamber spark plug at 1.6MPa BMEP and EGR_{peak} as combustion phasing was advanced. The BTE was observed to be higher with the prechamber spark plug at all tested CA50 as presented in Figure 7.2-5a accounting for as much as a 1.2% absolute increase in BTE at the most advanced CA50 12.5 deg aTDC when compared to the 3-prong spark plug. The direct reason for this was the higher EGR_{peak} values demonstrated by the prechamber spark plug (~29%) compared to the ~26% EGR_{peak} for the 3-prong configuration. At stoichiometric conditions, this 3% increase in EGR reduces the in-cylinder temperatures further reducing heat losses and improves the gas exchange efficiency thus increasing efficiency. The operation of the passive prechamber spark plug involves forcing in-cylinder charge into the prechamber at high velocities, especially towards the end of the compression stroke, where mixing then happens rapidly. This mixture is then ignited and the combustion pressure differential between the prechamber and the main chamber forces flame jets to exit the prechamber, increasing the flame surface area that can now ignite the extremely EGR-diluted mixtures in the main chamber and maintain short enough combustion durations that guarantee stable combustion. Figure 7.2-5b is also a direct consequence of the difference in EGR tolerance. Due to the 3% difference in EGR_{peak}, there was improved knock mitigation at all tested CA50s pointing to the possibility of further advancing the combustion phasing with the prechamber configuration and achieving even higher brake thermal efficiencies. At the most advanced CA50 tested of 12.5 deg aTDC, the 3-prong configuration had begun to exhibit medium knock while the prechamber configuration which exhibited a 47% reduction in knocking intensities at the same CA50 was only experiencing light knock. As combustion phasing was retarded in both Figures 7.2-5a and b, BTE and KRS reduced. This relationship between knock, efficiency and combustion phasing has been shown to be one of the key design limitations for spark ignited engines. The bsNOx emissions are plotted in Figure 7.2-5c for both configurations. Another direct consequence of the improved prechamber spark plug EGR tolerance was the

higher level of mitigation of NOx emissions at the lower in-cylinder temperatures which effectively hampers the NOx formation chemistry. For both configurations, as combustion phasing was retarded in-cylinder pressures and temperatures are reduced which also effectively reduces engine out NOx. Finally, the bsTHC emissions are shown in Figure 7.2-5d. The passive prechamber ignition system can be seen to generate slightly higher HC emissions with the biggest difference at CA50 15 deg aTDC where it indicated ~9% higher bsTHC than the 3.01g/kW-hr measured for the 3-prong spark plug. The reason for this was believed to be three-fold. First, the higher EGR_{peak} was believed to contribute to more partial burns for the prechamber configuration. This effect was also responsible for the increase in bsTHC at retarded combustion phasing. Second, the lower temperatures associated with the higher EGR_{peak} for the prechamber configuration also could reduce late cycle temperatures which are critical for the oxidation of crevice volume HCs reintroduced into the combustion chamber. Third, the prechamber concept was passive and unscavenged and as such any HC left after the flame jets exit the prechamber could contribute to the total engine-out HC. In general, the results from this subsection point to the importance of the EGRpeak determination in achieving the target efficiency on the engine.

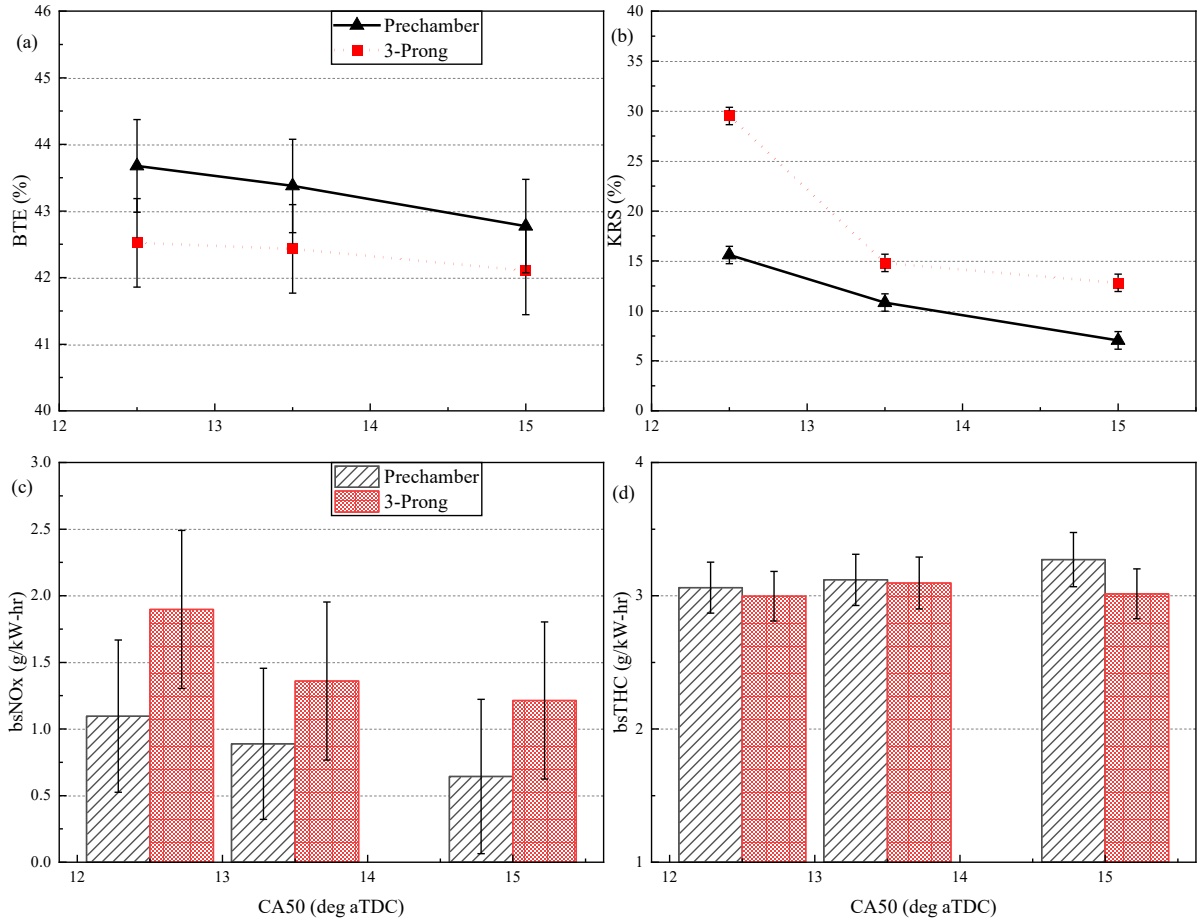

Figure 7.2-5: Plots of (a) BTE (%) (b) KRS (%) (c) bsNOx (g/kW-hr) (d) bsTHC (g/kW-hr) vs CA50 (deg aTDC) at 1600kPa BMEP + EGR_{peak} for the 3-prong Altronic and Woodward FTI prechamber spark plugs using the high flow DI and high squish 14:1 piston engine configuration.

7.3 BMEP/Knock Limit Testing

Having narrowed the compression ratio, ignition source, and injection configurations to the best possible candidates, the engine was operated using the strategies that have now been shown to improve efficiency i.e., at engine conditions with EGR_{peak} and early SOI timings (single injection strategy). Maintaining the EGR_{peak} at 26% < EGR_{peak} 29% for all tested engine loads and the SOI at 360 deg bTDC, the CA50 was advanced at each engine load (BMEP) until the knock limit was reached on the left and retarded until misfire region was approached on the right of the 3-D plots in Figure 7.3-1. This was done using the optimized double-injector PFI and high-flow DI injection strategies with the prechamber spark plug and the 14:1 piston engine configuration. As the CA50 was advanced in Figures 7.3-1a and e, the BTE was shown to increase as BMEP was increased up until the desired 44% BTE in the region between 1500 and 1700kPa and CA50 9 – 12.5 deg aTDC for both the high-flow DI and the optimized PFI configuration. As the CA50 was retarded the engine crossed into misfire for both injection configurations at such high EGR rates. A key feature of both 3-D plots for the BTE was the shortened region of operation at higher loads which could possibly be due to the longer time now required to mix the larger air, fuel and EGR mixture required to produce the higher loads. Thus, further shortening the injection durations for the LPG injection hardware could be advantageous in achieving even higher loads and expanding the region of operability of the LPG engine.

Figures 7.3-1b and f simply depict the trend towards end-gas auto-ignition as the region of operation of the LPG engine was shifted upwards and to the left (high BMEP, advanced CA50). In this regard, there was a possible competing effect of charge cooling with the direct injected liquid LPG spray for the high-flow DI configuration and the superior mixing of the optimized PFI configuration which would improve homogeneity in the combustion chamber. The DI charge cooling would likely reduce combustion temperatures and mitigate knock while the PFI mixing time and distance would possibly reduce the occurrence of locally rich regions at the cylinder and piston wall that would more easily auto-ignite. The better mixture preparation time and distance was also likely responsible for the slightly higher EGR_{peak} observed for the optimized PFI configuration at all tested BMEPs. Figures 7.3-1b and f would suggest that these PFI benefits slightly edged out the DI one as the PFI was able to achieve slightly more advanced CA50s and the knock intensities observed with the PFI mode at the same condition as the DI were also slightly lower. For example, at 1.4MPa BMEP and CA50 9, the optimized PFI recorded a KRS of 30.7%, 2.1% lower than the 32.8% recorded for the high-flow DI configuration.

The bsNOx emissions are presented in Figures 7.3-1c and g for the high-flow DI and the optimized PFI configurations respectively. Both 3-D plots show the previously discussed tendency of the NOx emissions to increase with advanced CA50. However, of the two injection modes, the high-flow DI configuration produced higher bsNOx emissions despite the described charge cooling effect of the LPG spray vaporizing in the combustion chamber. It is important to put the numbers into context however as the highest bsNOx shown in Figure 7.3-1c (3.33g/kW-hr) was still over 83% lower than the ~20g/kW-hr bsNOx reported for the baseline PFI configuration earlier. Even more significant was the fact that at the most efficient conditions on the engine the bsNOx reported was 1.7g/kW-hr for the high-flow DI configuration and 1.99g/kW-hr for the optimized PFI configuration. Finally, the bsTHC emissions are shown in Figures 7.3-1d and h for both

injection configurations. The bsTHC was observed to be maximized in the mirror opposite direction to the bsNOx for both configurations, at the most retarded timings and low engine loads. This was counterintuitive as the THC trends have been shown to reduce with retarded CA50 due to the higher late cycle temperatures and their more effective oxidation of the crevice volume HC. However, in this scenario the tendency for poor, partial burns and misfires as CA50 was retarded at such high EGR dilution rates was most likely responsible for the uptick in the bsTHC in the CA50 retard direction. In similar mirror opposite fashion to the bsNOx trends in Figures 7.3-1c and g, the bsTHC was minimized at higher loads and advanced CA50 for both configurations. Finally, the high-flow DI outperformed the optimized PFI configuration in terms of the bsTHC emissions, for example, at the most efficient operating condition for both configurations, the high-flow DI mode reported 9% lower bsTHC emissions than the optimized PFI configuration.

The emissions reported do not meet current emissions standards (e.g. Tier 4 final heavy duty emissions, 0.40 g/kW-hr NOx, 3.5 g/kW-hr CO, and 0.19 g/kW-hr NMHC). A three-way catalyst would be required for a production multi-cylinder engine. Development of a three-way catalyst system is beyond the scope of this work. However, preliminary sizing of a three-way catalyst for a 15 liter 6-cylinder LPG engine is provided in the appendix.

7.4 Response Surface Method Optimization

A response surface method technique was applied to optimize efficiency of the heavy-duty engine platform. The method involved a 2^k full factorial with center points design of experiments on the engine using the k = 5 variables shown in Figure 7.4-1. In this case, the experiments were non-randomized and without replication except for the center point which had multiple replicates to provide an estimate of the error and to check the time trends. The five variables were chosen based on experience with the engine and previous engine data and results. The variables were BMEP, SOI, EGR, Injection pressure and the CIM. The factor (variables) effects and their interactions, which typically account for the response surface curvature [7] were studied and a steepest ascent/descent technique (a gradient search method) was used to optimize the desired parameter [8]. The objective function was to minimize BSFC (desire parameter), which translates to an increase in BTE.

There were 32 corner points tested on the engine in the full factorial 2^5 design. The factor levels spacings were chosen to be as aggressive as possible due to the unreplicated factorial design [7] of the experiments while also ensuring that the engine operated within its limits by leveraging the experience of previous engine results, for example, in picking a center point that allowed engine operation within the limits of engine stability and practical EGR rate increments given hardware limitations. The half-cube plot in Figure 7.4-2 provides a visual representation of the experimental design where the “+” and “-” denote the high and low levels of a factor, respectively. The method involved two stages, experiments representing the 32 corner points which were combinations of the high and low factor levels of the five variables were run on the engine as well as several replicate runs of the center point (eight in this case). The responses (BSFC) from these 32 operating conditions formed the data that was used to quantify factor

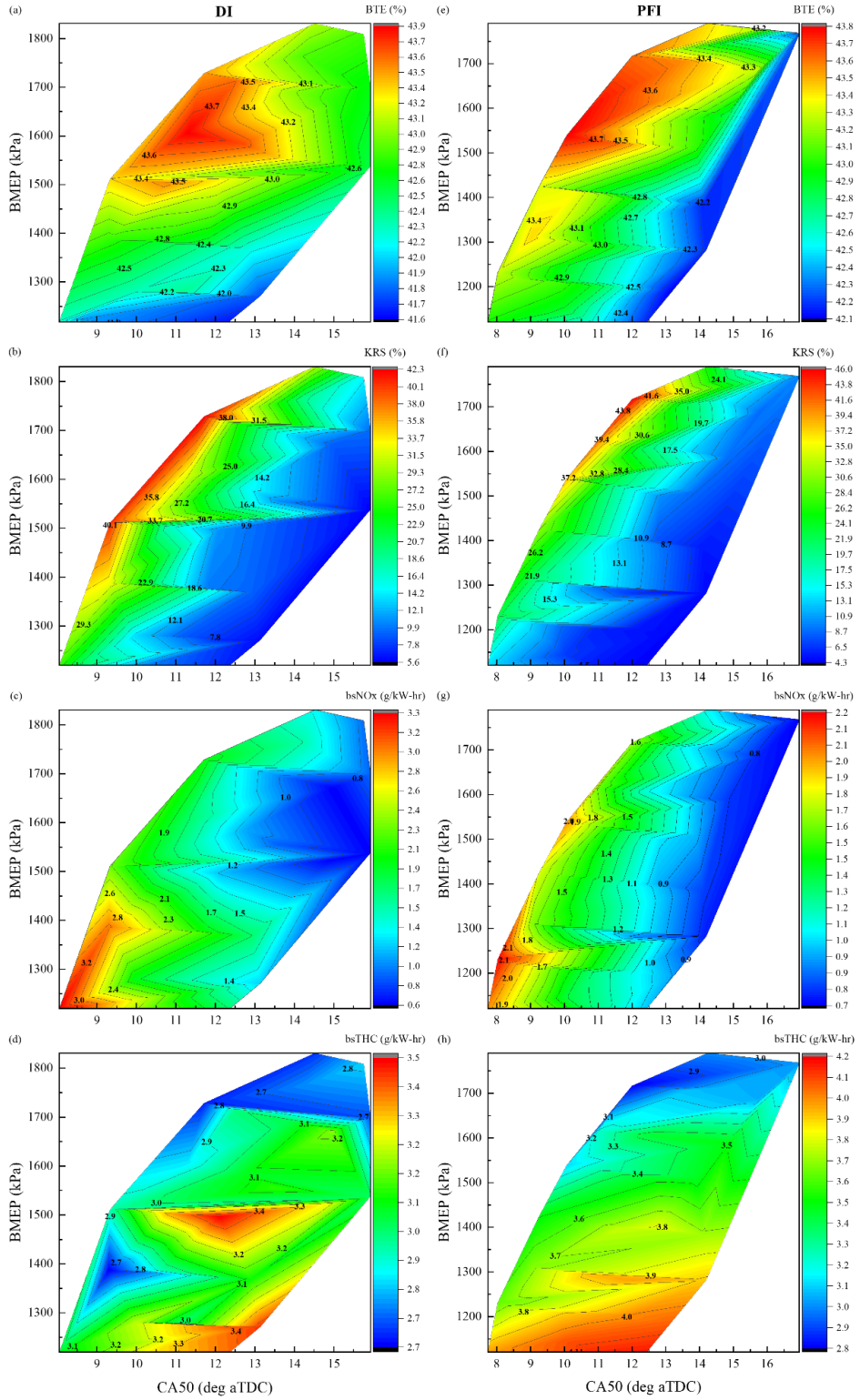

Figure 7.3-1: 3-D plots showing the relationship between BMEP (kPa) and (a) BTE (%) (b) KRS (%) (c) bsNOx (g/kW-hr) (d) bsTHC (g/kW-hr) for the high-flow DI configuration and (e) BTE (%) (f) KRS (%) (g) bsNOx (g/kW-hr) (h) bsTHC (g/kW-hr) for the optimized PFI configuration at EGRpeak and SOI 360 deg bTDC with the 14:1 and prechamber spark plug on the heavy-duty LPG engine.

Objective Function:						
Goal is to minimize BSFC.						
	Procedure					
1. Select centerpoint parameters.						
2. Select appropriate increments.						
3. Take data to complete cube.						
4. Follow optimization vector until q reaches minimum.						
5. Repeat process.						
Parameters at Center Point:						
BMEP =			12	bar		
SOI =			315	° bTDC		
EGR =			10	%		
Injection Pressure =			160	bar		
CIM =			20	%		
Increment Definition, Equivalent to +1 in Analysis:						
BMEP =			2	bar		
SOI =			15	° bTDC		
EGR =			5	%		
Injection Pressure =			20	bar		
CIM =			5	%		

Figure 7.4-1: Response surface method design template – Method of Steepest Descent.

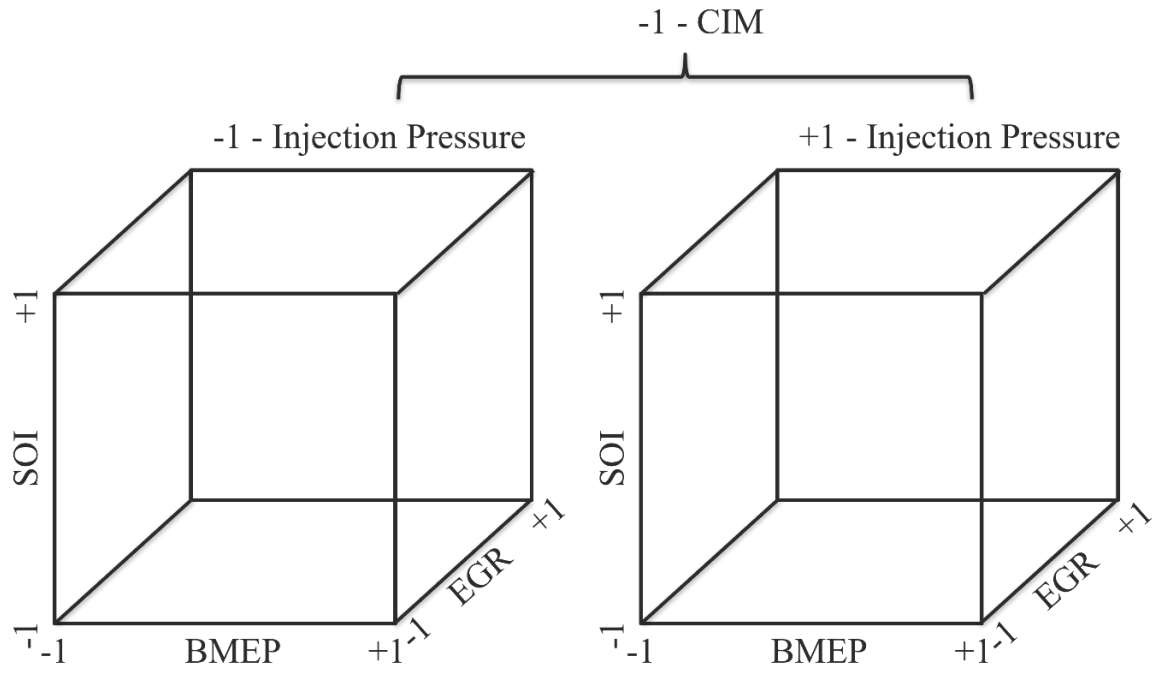

Figure 7.4-2: Half-cube plot of the five variables.

effects, statistically relevant factor interactions, and ulitmately generate a steepest descent vector of the five variables that would trend the response in the desired direction (reducing BSFC). The second stage involved following the vector, testing the engine operating conditions along the vector until an inflection point (optimum point) was reached in terms of the response (BSFC). This point then served as the new center point for the next iteration of the optimization routine.

The RSM optimization in this work was carried out in three phases. The first phase was with the 5-hole Delphi injector, the second phase was with the XDI high-flow injector, and the third phase was with the optimized PFI configuration which had only 4 variables. The vector of operating conditions for the three phases as well as the factor effects of the five variables from phase 1 and the four variables from phase 3 are shown in Figure 7.4-3. The key takeaway from phase 1 was that the direction of increasing efficiency for injection pressure was to reduce it. This was counterintuitive given the desire to reduce injection duration by increasing injection pressure, however, a possible explanation for this trend was that at higher injection pressures, the momentum of the fuel spray forces it to sit at the bottom of the piston bowl preventing beneficial mixing with the charge air. There was also the increased possibility of liner impingement and crevice volume filling at these higher injection pressures. This trend of optimizing efficiency with decreasing injection pressure was also observed in phase 2 with the high-flow direct injector configuration. Given that the optimization vector of phase I indicated that direction of increasing efficiency was towards lower BMEP contrary to the required project goals for high loads/peak torque efficiency and observing the limitations of the 5-hole Delphi injector in terms of flow rate and injection durations especially at high-loads, a subjective center point was chosen for the start of phase 2 and the injector changed to the high-flow XDI injector. The 32 corner points and replicated center points were tested once more and the vector of operating conditions followed until the inflection point. Due to the similarity of the high-flow XDI and the optimized PFI configurations as shown in subsection 8.3 as well as time limitations on the test cell, phase 3 was done in the optimized PFI configuration with four variables and 2^4 = 16 corner points. This cut down engine operating time and resources in half and still demonstrated the required optimization of the engine efficiency.

Figure 7.4-4 showed that the optimization technique was successful, as BTE increased by >16% from ~37% at the beginning of phase 1 to near-diesel efficiencies at ~43% at the end of phase 3. The EGR rate at the end of phase 3 had approached and exceeded the EGR_{peak} meaning that the engine would have begun to experience severe misfires and unstable combustion if the vector was followed any further. Thus, the EGR variable would need to be dropped and a 2^3 full or fractional factorial design of experiments run for phase 4. As mentioned in subsection 6.3, the CIM tool was susceptible to engine noise and discouraged the continuation of the RSM optimization technique after the successful demonstration of its potential in order to protect the engine from damage at the higher loads the engine was now being operated at. All three phases of the RSM engine operation were at 1200RPM, ϕ = 1, and MAT = 38 deg C with the pre-chamber spark plug and the 14:1 high-squish piston on the heavy-duty liquid LPG engine.

Optimization Vector – PHASE 1

Tested	BMEP	SOI	EGR	Injection Pressure	CIM	BSFC	
	12	315	10	160	20	207.5351	
1	12	319	11	157	22	203.8841	
2	11	323	13	154	24	198.0146	
	11	327	14	150	26		New center
3	10	331	16	147	28	196.1474	
	10	335	17	144	30		
4	9	339	19	141	32	193.2097	

Optimization Vector – PHASE 2

BMEP	SOI	EGR	Injection Pressure	CIM	BSFC	
11	327	14	150	26	194.7706	
11	331	17	149	28		
10	334	20	147	31	190.8722	
10	338	24	146	33	188.3637	new center
9	341	27	144	36	189.0592	
9	345	30	143	38		
8	348	33	142	40		

Optimization Vector – PHASE 3

BMEP	SOI	EGR	CIM	BSFC
10	338	24	33	184.5491
12	340	26	34	182.5843
14	343	28	35	182.1193
16	345	30	36	180.7142
18	347	**32**	37	
20	349	33	38	
22	352	35	39	

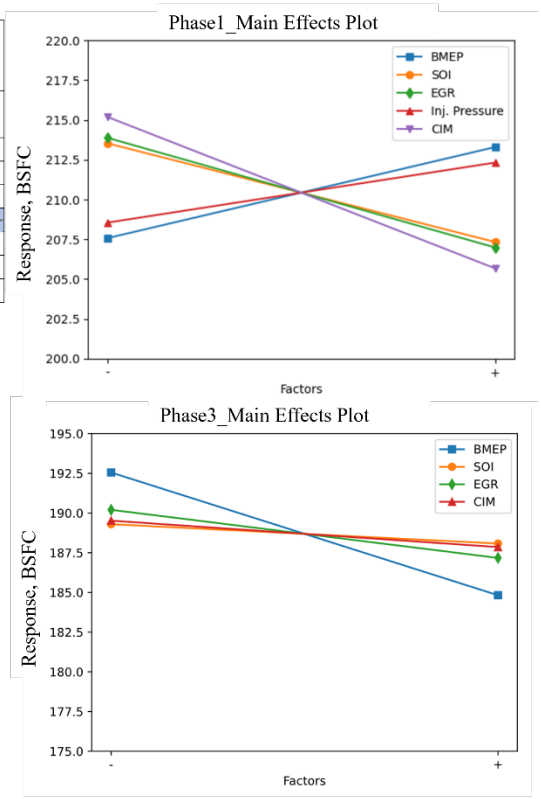

Figure 7.4-3: Optimization vectors for the three phases and the factor effects plot for phase 1 and 3.

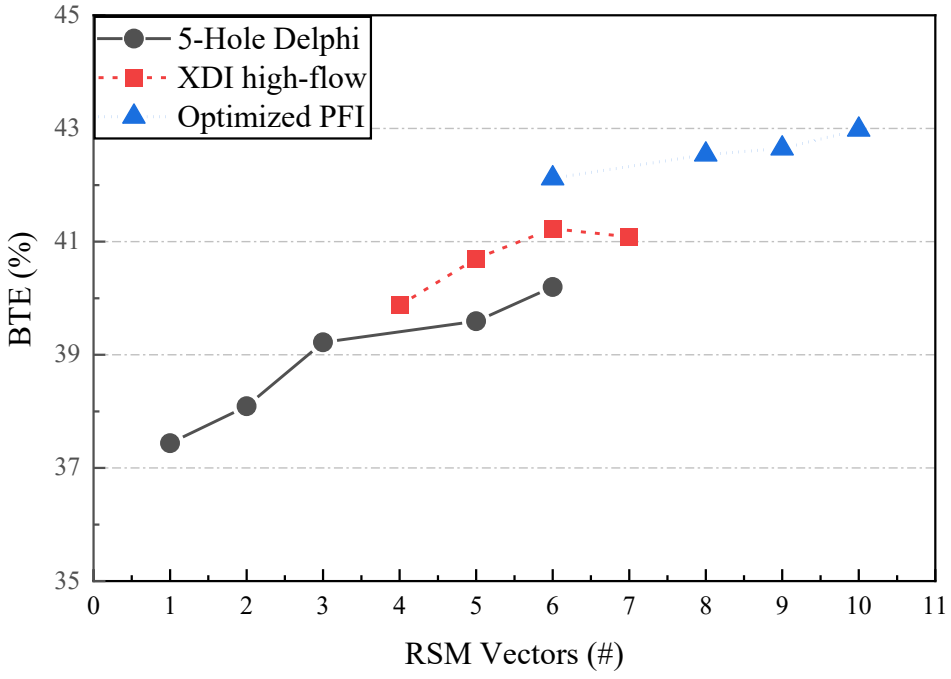

Figure 7.4-4: Response surface method efficiency optimization.

References

1. Fosudo, T., “Development of Advanced Combustion Strategies for Heavy-Duty LPG Engines to Achieve Near-Diesel Efficiency”, PhD Dissertation, Colorado State University, 2024.
2. Altronic, “Ignition Accessories,” [Online]. Available: https://www.altronic-llc.com/wp-content/uploads/Ignition-Accessories.pdf [Accessed 13-Jul-24]
3. Woodward Inc, "FTI-Family FAST TURBULENT IGNITER," [Online]. Available: https://www.woodward.com/en/shop/woodward44-electronic-controls/fti-family. [Accessed 13-Jul-24].
4. J. Wheeler, A. R. A. R. Ganji, Introduction to engineering experimentation / Anthony J. Wheeler, Ahmad R. Ganji; with contributions by V. V. Krishnan, Brian S. Thurow, 3rd Edition, Pearson Higher Education, Upper Saddle River, N.J., 2010.
5. J. B. Heywood, Internal Combustion Engine Fundamentals, 2nd Edition, McGraw-Hill Education, 2018.
6. J. P. Szybist, S. Busch, R. L. McCormick, J. A. Pihl, D. A. Splitter, M. A. Ratcliff, C. P. Kolodziej, J. M. Storey, M. Moses-DeBusk, D. Vuilleumier, M. Sjoberg, C. S. Sluder, T. Rockstroh, P. Miles, “What Fuel Properties Enable Higher Thermal Efficiency in Spark-Ignited Engines?”, Progress in Energy and Combustion Science 82 (2021).
7. Montgomery, D., Design and Analysis of Experiments: Fifth Edition, John Wiley and Sons, Incorporated, New York, 2001. ISBN: 0471316490
8. Brown, J., “On-Engine Investigation of a Micro-Liter Quantity Pilot Ignition System for a Large Bore Natural Gas Engine”, Master’s Thesis, Colorado State University, 2003.

8.0 Summary and Conclusions

Detailed conclusions related to technologies developed may be found in the preceding chapters. Some of the more important conclusions and results are repeated here:

- NUIGMech1.1 was found to be the best performing detailed mechanisms for LPG combustion under the thermodynamic conditions most relevant to the final application and to the expected validation data from the CSU RCM.
- A 153-species reduced mechanism (ALPINE 153) was developed that achieves flame speed error within 1% of the detailed mechanisms at most engine operating conditions. ALPINE 153 was deemed to be sufficiently accurate and small enough in size to use in the full three-dimensional simulations.
- A Lagrangian-Eulerian spray model was developed while accounting for the complex phase behaviour experienced in LPG sprays. The model was validated and tuned to experimental spray visualization data and shown to predict both vapor and liquid region spray penetration lengths. Modelling parameters were adjusted to account for varying degree of flash boiling, dependent on the superheat degree of the fuel entering the chamber and described by the fuel properties and the spray chamber pressures/temperatures. The developed spray model was implemented into engine simulations (run by CSU and Cummins) to identify optimized spray patterns and injection rates.
- Although it did not have an optimized spray pattern for the X15 engine and had to be modified to fit in the engine head, the XDI LT4 +65% injector was the only DI injector that could deliver the volume of fuel necessary to reach higher BTE %.
- The results showed that mixture preparation time was the most important factor in the heavy-duty LPG engine performance. Counterintuitively, the RSM optimization technique also showed that lower injection pressures were more beneficial for direct injection performance on the engine. The high-flow direct injector cut injection durations by about half at even lower injection pressures when compared to the 5-hole modified injector, while the optimized PFI configuration introduced longer mixing distances and shortened durations with the double-injector system. As a result, both the high-flow DI and optimized PFI configurations were able to achieve higher efficiencies.
- A BTE of 43.9% was achieved at 1.6MPa BMEP (320Nm) and CA50 11.3 deg aTDC for the direct injection heavy-duty single cylinder LPG engine. This was achieved with the high squish 14:1 compression ratio piston, the prechamber spark plug and 29% EGR. At this condition, the engine out bsNOx emissions were 1.73g/kW-hr, 91% lower than the baseline 9.3:1 bsNOx emissions. Similarly, the optimized PFI configuration achieved a BTE of 43.8% at 1.54MPa BMEP (306Nm) and CA50 10 deg aTDC.

Appendix: Low Emission Solution

Low Emission Solution: Preliminary Three-Way Catalyst Specification

Notes

- The engine development in this work was for stoichiometric combustion, and a three-way catalyst would be required to meet current emissions limits.
- The preliminary three-way catalyst specification from Johnson Matthey provided is for a 6-cylinder 15 liter LPG heavy duty engine, based on early data from single cylinder engine testing presented in the main body of this report.
- Although the catalyst design would require significant refinement for an LPG production engine, the specification provides a rough idea of the aftertreatment system size that would be required to meet current emission requirements.
- The catalyst analysis output sheet indicates the fuel is natural gas, but the input data that was provided was from commercial propane fuelled engine testing.
- To be conservative with catalyst sizing, Johnson Matthey scaled up the power and exhaust flow to more closely match the diesel version of the 15 liter engine.

Catalyst Sizing Data from Single Cylinder Engine Testing

Engine: Heavy Duty 15L LPG
Fuel: Commercial Propane (mole %)

CH4	0.04
C2H6	6.08
C3H8	93.33
C4H10	0.55
N2	0.01

Exhaust Flow: 692 kg/hr (6 cylinders)
Exhaust Temperature: 592 deg C
Lambda: 1.000

Exhaust Gas Composition (dry):

THC	1776 ppm
O2	0.497 %
NOx	529 ppm
CO2	12.6 %
CO	2051 ppm

Speed and Load:
1202 rpm
242 kW, brake power for 6 cylinders

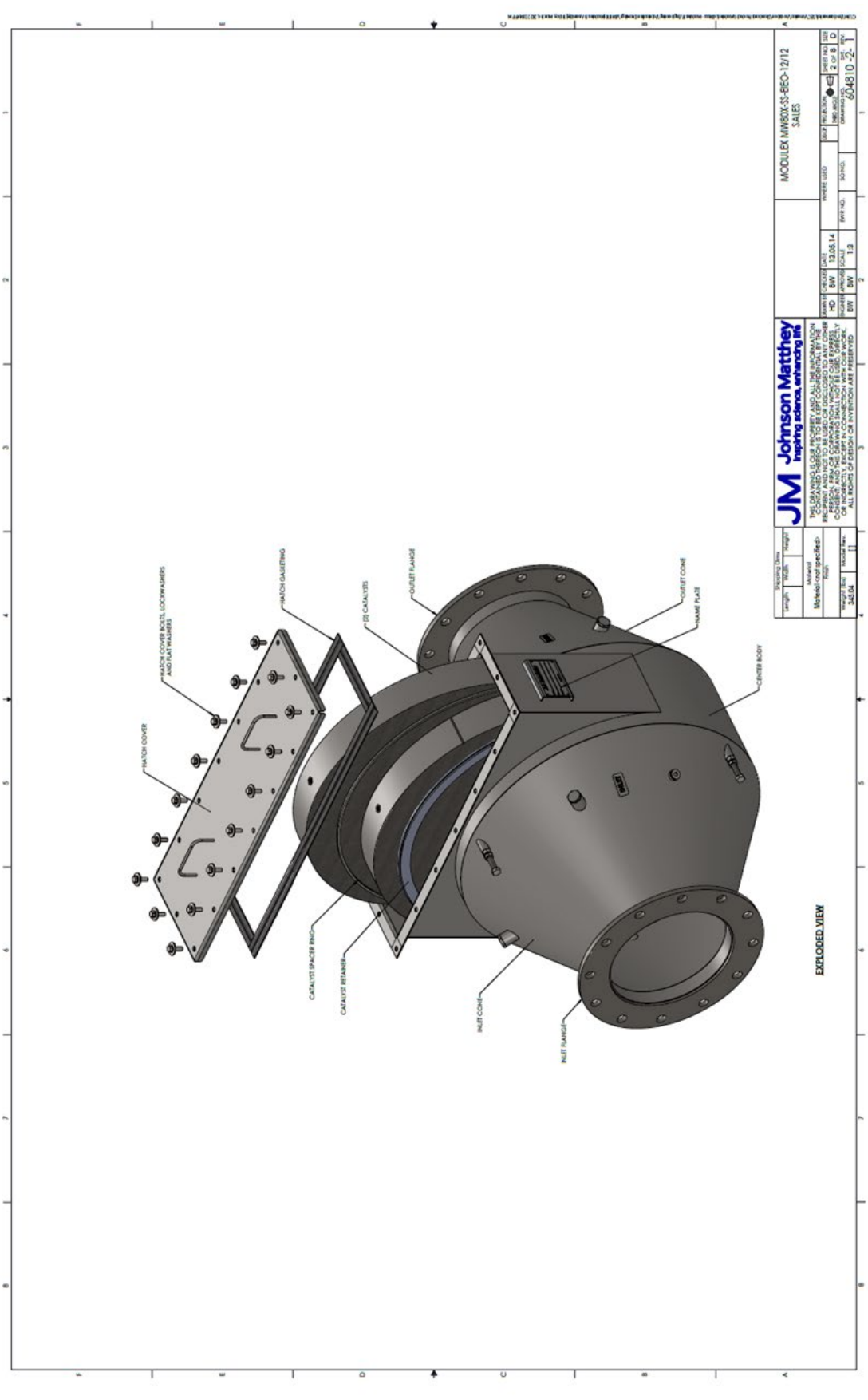
MODULEX MW80X-55-BEO-12/12
SALES
Johnson Matthey
Inspiring science, enhancing life
EXPLODED VIEW
MANHOLE COVER BOLTS, LOCKWASHERS AND FLAT WASHERS
MANHOLE COVER
MANHOLE GASKETING
[2] CATALYSTS
OUTLET FLANGE
OUTLET CONE
NAME PLATE
CENTER BODY
CATALYST SPACER RING
CATALYST RETAINER
INLET CONE
INLET FLANGE

ENGINE DATA	Rich Burn
Engine Mfg:	Cummins
Engine Model:	QSX15-G9 NR 2
Bhp:	680
RPM:	1800
Load:	100%
Fuel:	Natural Gas
Temp into Catalyst, °F:	1098
Operating Hours, hrs/yr:	8760

ENGINE PREFORMANCE	
Exhaust Flow, acfm:	3845
Exhaust Flow, scfm: Standard Cond.- 60F, 14.696 psi	1283
Exhaust Flow, scfh:	76999
Exhaust Flow, lb/hr:	5805
Exhaust MW:	28.6

TYPICAL (Rich Bu	MW		
Ar, vol %:	39.9		-
N2, vol %:	28.0		79.70
O2, vol %:	32.0		0.30
H2O, vol%:	18.0		10.00
CO2, vol %:	44.0		10.00

EMISSIONS DATA	PRE	POST	% Reduction
NOx as NO2, g/Bhp-hr:	10.33	0.50	95.2%
NOx as NO2, lb/hr:	15.48	0.75	
NOx as NO2, tons/yr:	67.82	3.28	
NOx as NO2, ppmv:	1,659.63	80.35	
NOx as NO2, ppmvd @ 15% O2:	529.00	25.61	
CO, g/Bhp-hr:	24.37	2.60	89.3%
CO, lb/hr:	36.54	3.90	
CO, tons/yr:	160.06	17.08	
CO, ppmv:	6,434.58	686.43	
CO, ppmvd @ 15% O2:	2,051.00	218.80	
VOC as NMNEHC (CH4), g/Bhp-hr:	12.060	0.140	98.8%
VOC as NMNEHC (CH4), lb/hr:	18.08	0.21	
VOC as NMNEHC (CH4), tons.yr.:	79.20	0.92	
VOC as NMNEHC CH4), ppm:	5,571.82	64.68	
VOC as NMNEHC CH4), ppm @ 15% O2:	1,776.00	20.62	

SCOPE OF SUPPLY	(1) JM - MW80S-SS-EIEO-3 Converter with (1) 30.25 x 3.5 300 CPSI Catalyst Element installed

Johnson Matthey
Inspiring science, enhancing life

Johnson Matthey
900 Forge Avenue
Suite 100
Audubon, PA 19403
T 1-484-320-2136

Three Way Catalysts Specification

- **The Three-Way Catalyst shall be designed to reduce NOx, CO, NMNEHC, and CH2O to pre-determined post catalytic emissions levels.**
- **Catalyst formulation shall be designed to resist poisoning.**
- **Catalyst to have a minimum service lifetime of 24,000 hrs.**
- **Catalyst will continue to be operational after (3) cleanings.**
- **Catalyst substrate is to consist of a robust metal foil design that is brazed to maximize performance and longevity.**
- **Catalyst Housing will to have an internal sealing flange designed to eliminate exhaust bypass of the catalyst.**
- **Catalyst housing to be of a gasket-less design.**
- **No gasketing material shall be used to seal the catalyst element inside the housing.**
- **Catalyst to have a welded in place threaded lifting lug to aid in the installation, removal, and handling of the catalyst element.**
- **Catalyst to be able to withstand 1250°F exhaust gas temperatures.**
- **Catalyst housing to be constructed by an ISO 9001 certified manufacturer.**
- **Catalyst housing to be welded in accordance with AWSD1.1 or ASME section IX.**
- **Manufacturer to have AWS-CWI certified inspectors.**
- **Catalyst housing shall be fabricated from either 304 stainless steel or carbon steel that is coated with high heat aluminium paint.**
- **Catalyst housing to have pre-installed test port on both the upstream and downstream ends.**
- **Catalyst housing to have a flat access panel to eliminate exhaust gas escape. A concave access panel will not be accepted.**
- **Catalyst housing to be of a dual catalyst design to allow for future emission control upgrades.**
- **Catalyst housing to be able to withstand 1250°F exhaust gas temperatures for stainless steel and 1,000 °F for carbon steel.**
- **An Installation and Operation Manual shall be provided at time of or before delivery.**
- **Supplier of the catalytic converter must also be the technology provider and manufacturer of the three-way catalyst so as to avoid potential warranty-related problems.**
- **Supplier must have at least twenty (20) years of experience providing three-way catalyst technology.**